8-2012

Engineering single-molecule, nanoscale, and microscale bio-functional materials via click chemistry

Michael Daniele
Clemson University, michaelangelo.daniele@gmail.com

Engineering single-molecule, nanoscale, and microscale bio-functional materials *via* click chemistry

---

A Dissertation
Presented to
the Graduate School of
Clemson University

In Partial Fulfillment
of the Requirements for the Degree
Doctor of Philosophy
Materials Science & Engineering (Polymers)

---

by
Michael Angelo-Anthony Daniele
August 2012

Accepted by:
Dr. Stephen Hans Foulger, Dissertation Supervisor
Dr. John Michael Ballato
Dr. Igor A. Luzinov
Dr. Olin Thompson Mefford IV

Abstract

To expand the design envelope and supplement the materials library available to biomaterials scientists, the copper(I)-catalyzed azide-alkyne cycloaddition (CuCAAC) was explored as a route to design, synthesize and characterize bio-functional small-molecules, nanoparticles, and microfibers. In each engineered system, the use of click chemistry provided facile, orthogonal control for materials synthesis; moreover, the results provided a methodology and more complete, fundamental understanding of the use of click chemistry as a tool for the synergy of biotechnology, polymer and materials science.

Fluorophores with well-defined photophysical characteristics (ranging from UV to NIR fluorescence) were used as building blocks for small-molecule, fluorescent biosensors. Fluorophores were paired to exhibit fluorescence resonant energy transfer (FRET) and used to probe the metabolic activity of carbazole 1,9a-dioxygenase (CARDO). The FRET pair exhibited a significant variation in PL response with exposure to the lysate of *Pseudomonas resinovorans* CA10, an organism which can degrade variants of both the donor and acceptor fluorophores. Nanoparticle systems were modified *via* CuCAAC chemistry to carry affinity tags for CARDO and were subsequently utilized for affinity based bioseparation of CARDO from crude cell lysate. The enzymes were baited with an azide-modified carbazolyl-moiety attached to a poly(propargyl acrylate) nanoparticle. Magnetic nanocluster systems were also modified *via* CuCAAC chemistry to carry fluorescent imaging tags. The iron-oxide nanoclusters were coated with poly(acrylic acid-*co*-propargyl acrylate) to provide a clickable surface. Ultimately, alternate Cu-free click chemistries were utilized to produce biohybrid microfibers. The biohybrid microfibers were synthesized under benign photopolymerization conditions inside a microchannel, allowing the encapsulation of viable bacteria. By adjusting pre-polymer solutions and laminar flow rates within the microchannel, the morphology, hydration, and thermal properties of the fibers were easily tuned. The methodology produced hydrogel fibers that sustained viable cells as demonstrated by the encapsulation and subsequent proliferation of *Bacillus cereus* and *Escherichia coli* communities.

Acknowledgments

"And it's not enough to be smart, lots of people are very bright and get nowhere in life. To succeed in science, you have to avoid dumb people... Even as a child, I never liked to play tag with anyone who was as bad as I was. If you win, it gives you no pleasure. And in the game of science or life, the highest goal isn't simply to win, it's to win at something really difficult. Put another way, it's to go somewhere beyond your ability and come out on top. If you are going to make a big jump in science, you will very likely be unqualified to succeed by definition.

So be sure you always have someone up your sleeve who will save you when you find yourself in deep shit."

James Dewey Watson, 1962 Nobel Laureate of Physiology and Medicine

Table of Contents

List of Tables

List of Figures

CHAPTER 1

Introduction

Click chemistry is a paradigm of organic synthesis, in which new compounds or combinatorial libraries are constructed from primary, chemical building blocks with "built-in high-energy content drive a spontaneous and irreversible linkage reaction with appropriate complementary sites in other blocks."[1, 2] Directed by natural synthetic routes for building macromolecules from elementary blocks, Nobel Laureate Karl B. Sharpless *et al.* conceived this synthetic philosophy and described a set of stringent criteria for a reaction to qualify as click chemistry; a click reaction must be (1) stereospecific (not necessarily enantio-selective), (2) wide in scope, (3) modular, and result in (4) high-yield products and (5) inoffensive by-products if any at all, where these byproducts should be easily removable by non-chromatographic methods like crystallization and or distillation. In addition, the synthetic process must include simple reaction conditions, *i.e.* the reaction should be insensitive to oxygen and water, use readily available starting materials and reagents, and if necessary, use a benign, easily removable solvent.[2] These guidelines delineate an organic reaction which is essentially modular, and employs small molecules that can be quickly joined together to form complex functional compounds, mimicking the natural production of nucleic

acid chains, proteins and complex carbohydrates.

Click chemistry has affected diverse applications, from drug synthesis and polymer chemistry, to materials and surface science. Click chemistry gained immediate attention in the biomedical sciences, as a route for bioconjugation.[3–6] Bioconjugation is the process of covalently linking a synthetic label, *e.g.* fluorophores, ligands, chelates, or radioisotopes, to a biomolecule, *e.g.* proteins and nucleic acids; furthermore, bioconjugation has recently incorporated methods for the fusing of two or more biomolecules.[4, 5, 7–9] Because biosystems contain an array of inherent chemical functionalities, bioconjugation requires orthogonality and benign reaction conditions (tenets of click chemistry). For biochemists, click chemistry is a route to label and detect biomolecules in a live cell or a complex cell lysate with greater selectivity and specificity.[10, 11] For diagnosticians, click chemistry allows a physician or a radiologist to label biomarkers to track the progression of disease or the efficacy of a treatment.[12]

The continuing success of click chemistry as a biochemical strategy has increased the desire for tightly defined, engineered materials and surfaces to mimic natural products. The controlled synthesis of materials, at the molecular scale of natural products, introduces new synthetic challenges; materials chemists have struggled to achieve the elaborate structural and functional properties of natural macromolecules, such as complex carbohydrates, proteins and DNA. These challenges have become a beacon, calling materials scientists. Between 2005-2009, materials science publications citing click chemistry have outpaced biochemical and pharmaceutical applications, nearly 3:1.[13]

Designer materials produced *via* click chemistry are constantly under development to modify and mimic natural materials; however, it is the position of this work, that the click chemistry paradigm should be slightly altered when examining its role

and application to materials synthesis. Although efforts to recreate natural materials have been fruitful, there may be greater success in the juxtaposition of click chemistry and materials science to harness and directly repurpose biosystems. Recognizing the limitations for recreating natural materials, the role of click chemistry in materials science can be focused on the development of materials to monitor (biosensors), extract (bioseparation) and harness (cell encapsulation/immobilization) the complexity of biosystems for engineering applications.

1.1 Cu(I)-catalyzed cycloaddition of azides and terminal alkynes

Since 2001, click chemistry has highlighted a series of reactions with different reaction mechanisms but commonly high efficiency and modular nature. Figure 1.1 presents a selection of reactions that have qualified as click chemistry. Initially, three classes of reactions were identified as candidates for the label, "click reactions": 1) nucleophilic opening of highly-strained electrophiles, *e.g.* epoxides and aziridines, 2) mild condensation reactions of carbonyl compounds, *e.g* hydrazones and oximes from aldehydes, and 3) cycloaddition reactions.[2] The mechanisms for each of these reactions can be envisioned as "spring-loaded" for single trajectory because they are driven by a high thermodynamic driving force ($\geq$ 20 kcal·mol^{-1}), resulting in rapid completion and regio-selective synthesis of a single product. Ultimately, K.B. Sharpless *et al.* championed the copper-(I) catalyzed variant of Huisgen's 1,3-dipolar cycloaddition of azides and terminal alkynes (CuCAAC), which has become the archetype of click chemistry reactions (Figure 1.2).[1, 2, 14] The CuCAAC reaction is regio-selective, forming only 1,4-substituted triazoles, insensitive to solvents, can be performed at

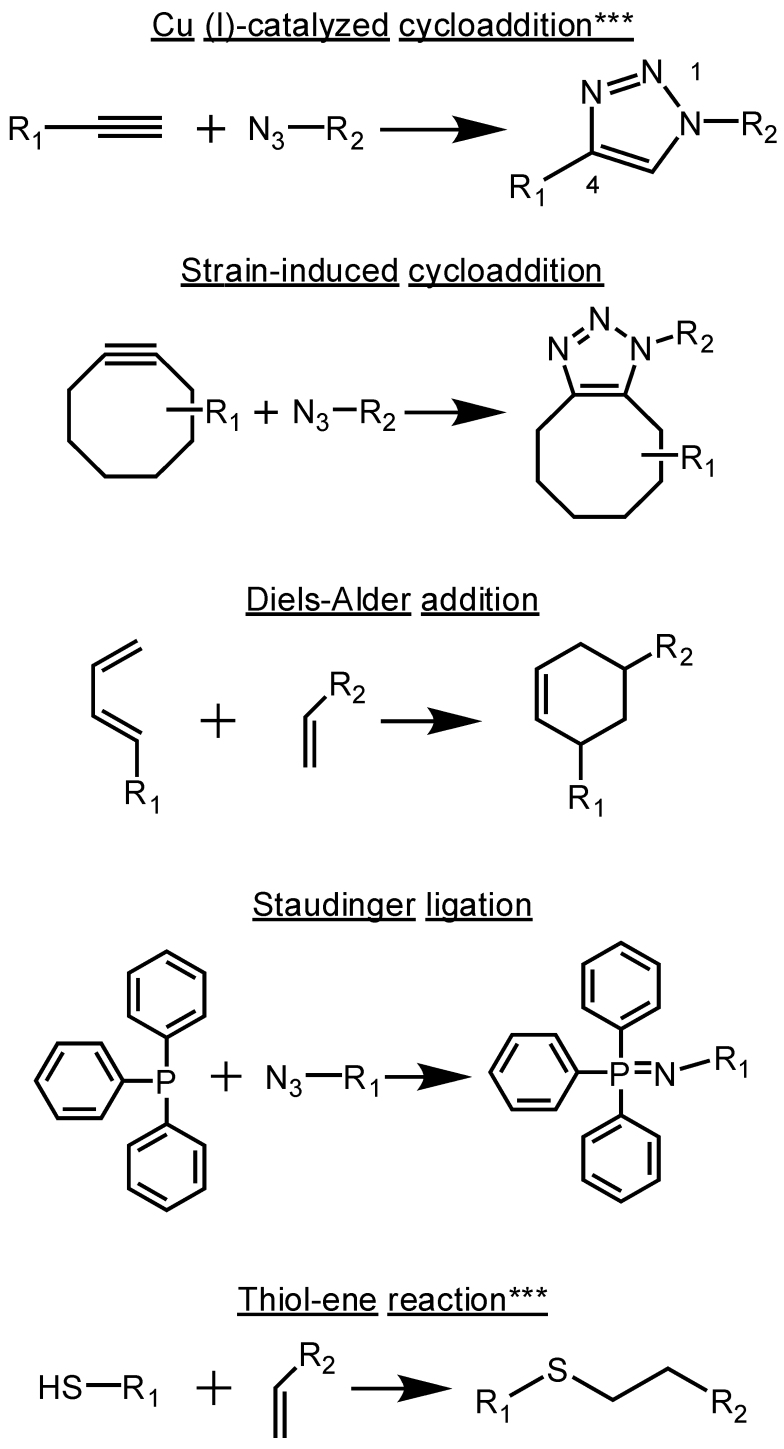

Figure 1.1: Common reaction mechanisms that meet the requirements for classification as "click reactions". Click chemistry is not limited to a specific type of reaction, but comprises of a range of efficient, modular reactions. ***The Cu(I)-catalyzed cycloaddition and thiol-ene reactions are explored in this work.

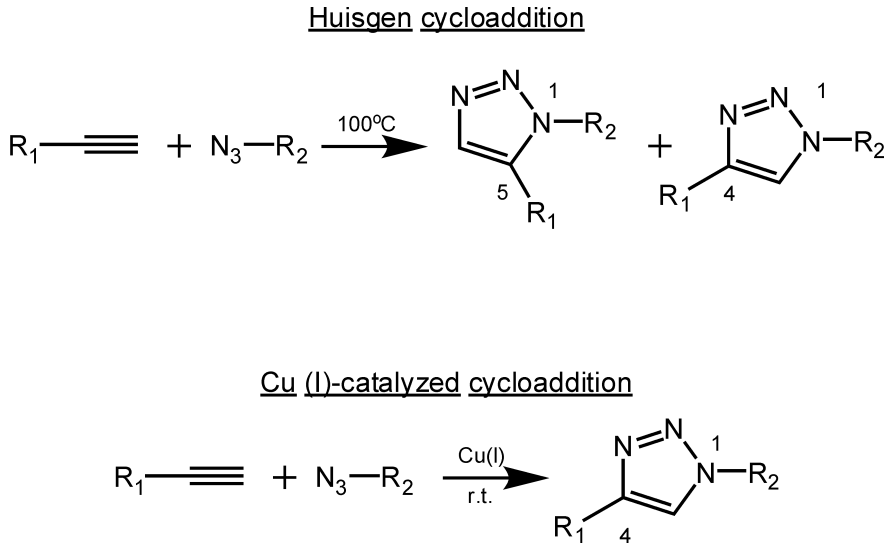

Figure 1.2: The traditional Huisgen 1,3-dipolar cycloaddition and "click" Cu(I)-catalyzed cycloaddition of azides and terminal alkynes.

room temperature, and proceeds with high yields.[14]

The CuCAAC reaction was developed from Huisgen's cycloaddition of azides and terminal alkynes (Figure 1.2). This 1,3-dipolar cycloaddition reaction was extensively studied in early 1960's by Rolf Huisgen.[15] In 2002, a more reliable Cu(I)-catalyzed stepwise variant was independently discovered by Valery V. Fokin with K.B. Sharpless, and Morten Meldal. M. Meldal *et al.* first reported a method for triazole synthesis on solid phases, closely followed by the report of V.V. Fokin and K.B. Sharpless describing a water-based catalyzed reaction with copper (II) sulfate ($Cu(II)SO_4$) and sodium ascorbate.[14, 16] The Cu(I) catalyst accelerates the reaction to minutes at room temperature, and the catalyzed process was found to have an unprecedented level of regio-selectivity, producing an isolated 1,4-triazole product. A mechanistic picture of the Cu(I)-catalyzed reaction (Figure 1.3) was first proposed by M. Meldal and later verified by computational methods.[17] The proposed catalytic mechanism (calculated by density functional theory (DFT) calculations) relies

on the initial formation of a Cu-acetylide between the Cu(I) species and the terminal alkyne, which subsequently proceeds with an initial *p*-complex formation between the Cu(I) and the alkyne, lowering the pK_a of the terminal acetylene and enabling the attack of the C-H bond. A variety of copper-based catalytic systems have been used to affect the 1,3-dipolar cycloaddition process. Methods can use Cu(I) salts, generate the copper(I) species by reduction of Cu(II) salts using a reducing agent, or direct incorporation of metallic copper. Many functional groups are compatible with the CuCAAC process, excluding those that are a) either self reactive, or b) able to yield stable complexes with the Cu(I) during catalyst deactivation. Interfering functional groups are strongly activated azides (*i.e.*, acyl- and sulfonyl azides) as well as cyanides, which are able to compete in purely thermal cycloaddition processes. With the exception of the aforementioned inhibitory functional groups, this catalytic mechanism results in a 100x rate acceleration and absolute regio-selectivity.[18, 19]

It is noted that other metals which catalyze the dipolar cycloaddition of terminal alkynes and azides have been reported. K.B. Sharpless *et al.* found that a variety of Ru complexes ($C_pRuCl(PPh_3)$, $[C_pRuCl_2]_2$, $C_PRuCl(NBD)$, and $C_PRuCl(COD)$) promote this click reaction.[20] The type of Ru-catalyst also determines the preferred triazole variant, where the 1,4-adduct is favored by $Ru(OAc)_2(PPh_3)_2$ and other catalysts result in the the 1,5-adducts.[21, 22] A catalytic cycle that relies on a pathway similar to the cyclo-trimerization reaction of alkynes *via* a six-membered Ru-cycle has been proposed.[23, 24] Krzysztof Matyjaszewski also reported the use of Ni, Pd, and Pt salts to catalyze this reaction.[25] The considerable flexibility of the catalyzed variant of Huisgen's 1,3-dipolar cycloaddition of azides and terminal alkynes has led to the broad application in materials science and biotechnology.

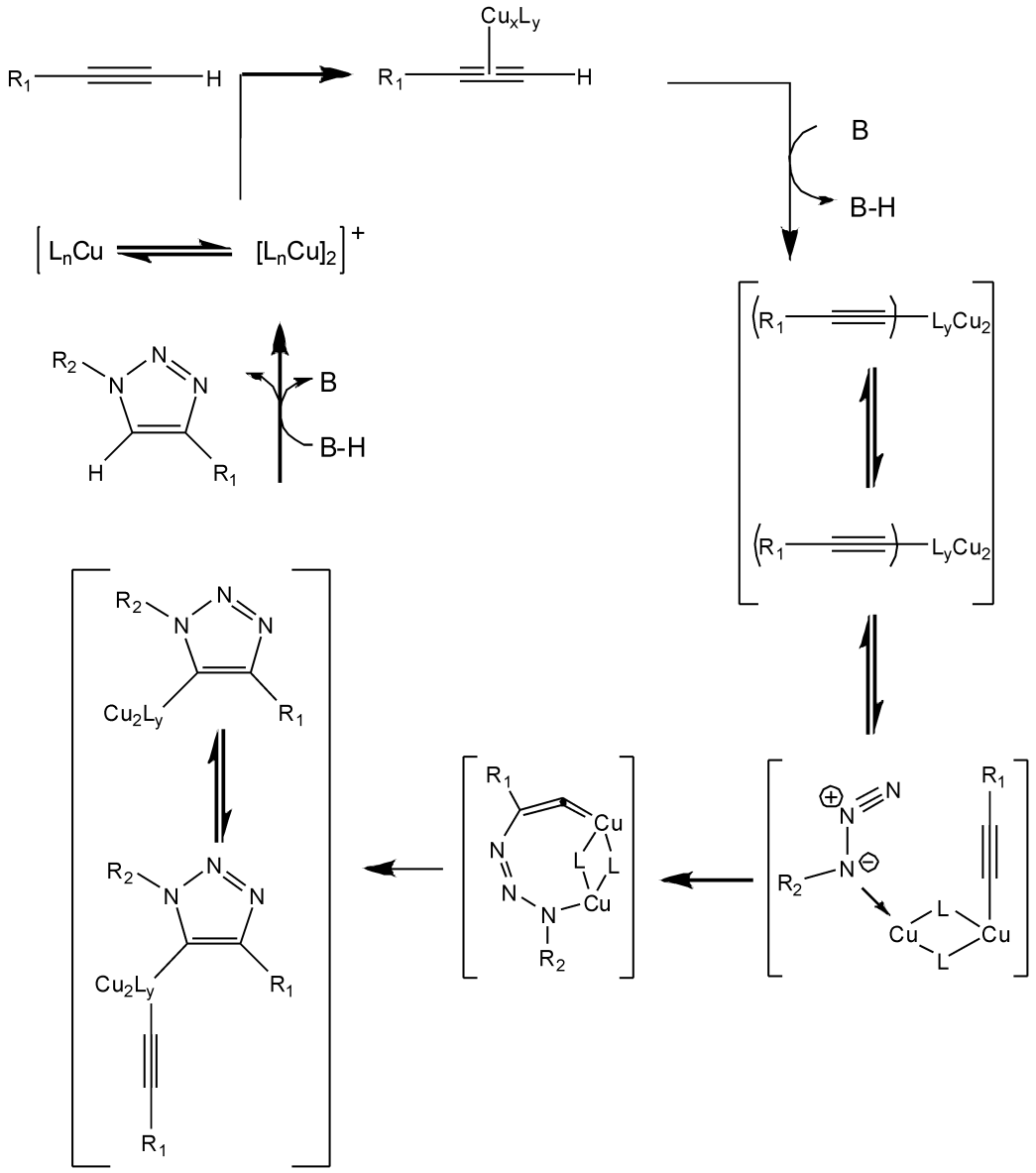

Figure 1.3: Mechanism for the catalysis of the 1,3-dipolar cycloaddition of azides and terminal alkynes with Cu(I) as determined by DFT.[17]

1.2 Building Soft Materials with Click Chemistry

Despite some noteworthy restrictions of CuCAAC, such as the need for metal catalysts and the limitation to terminal alkynes, a wide range of novel materials were realized soon after the adoption of the CuCAAC click reaction by materials scientists. Figure 1.4 illustrates the most common scenarios in which click chemistry has made an impact in materials science. By highlighting specific examples of click chemistry being employed in macromolecular synthesis and functionalization, the following sections will give context to the application and particular utility of click chemistry as a materials synthesis paradigm.

1.2.1 Polymer Synthesis

The synthesis of complex macromolecules often requires the use of efficient and specific post-polymerization modification techniques to incorporate functionality, potentially incompatible with the polymerization, characterization, or processing conditions. Click reactions are especially suited for advanced macromolecular design. Numerous reviews have describe the application of click chemistry, specifically the CuCAAC reaction, for the synthesis of dendrimers, brushes, branched, linear, or cyclic polymers.[26–32] Early examples of materials synthesis *via* click chemistry were demonstrated by the research groups of Craig J. Hawker, V.V. Fokin and K.B. Sharpless.[31, 33] In their approach, triazole-based dendrons were divergently synthesized using the CuCAAC as the dendrimer-growth step; these dendrons were then anchored to a variety of poly(acetylene) cores to generate dendrimers.[30, 34] Jean M.J. Fréchet also constructed dendrimers by side-chains cycloadditions.[35] The application of click strategies for the preparation of dendrimers proved highly benefi-

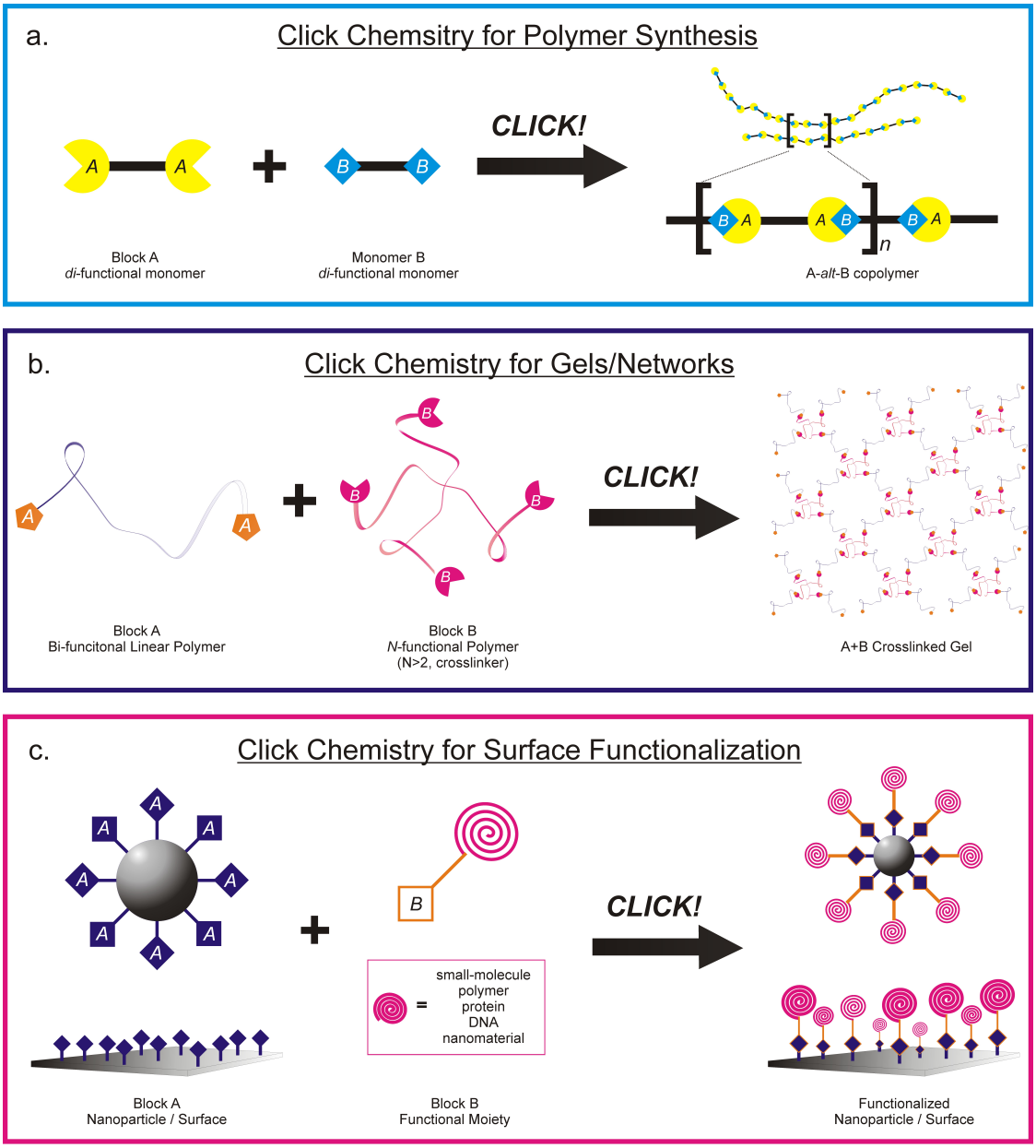

Figure 1.4: Common applications of the Cu(I)-catalyzed cycloaddition of azides and terminal alkynes by materials scientists: (a) polymer synthesis, (b) polymer crosslinking/gel formation, (c) nanoparticle and surface modification.

cial, as there is perhaps no other area of polymer synthesis that relies so heavily on near-quantitative reaction conversions. Accordingly, the CuCAAC reaction has been employed to synthesize or modify various polymer systems.

Efficient monomer conversion is a fundamental requirement for obtaining high molecular weight polymer by routine step-growth polymerization; therefore, many applications of click chemistry to polymer synthesis exploited the high-yield of the CuCAAC reaction by polymerization of azide- and alkyne-containing monomers to form high-molecular weight linear polymer.[35, 36] In these cases, the resulting structures contain multiple triazole repeating units formed by difunctional azide and alkyne monomers (Figure 1.4a). Due to the efficient kinetics of the CuCAAC, linear polymerizations of aliphatic-backbone difunctional azide and alkyne monomers are driven by high activation energy, $E_a \approx 45$ kJ mol^{-1}.[37] In addition to polymerization of low molecular weight azides and alkynes, the high activation energy, rapid polymerization, and the remarkable functional-group tolerance of click reactions enable the facile introduction of reactive groups, such as hydroxyl and carboxyl groups, by monomer or polymer modification. K. Matyjaszewski *et al.* demonstrated that linear polymers with alkyne or azide end groups could be further polymerized, with the chain extension leading to high molecular weight homopolymers, multi-block copolymers and crosslinked gels.[38] Interestingly, the rate of azide-alkyne coupling of these polymers was significantly higher than that for the corresponding monomers, an effect attributed to auto-acceleration by anchimeric assistance, a beneficial by-product of the rapid kinetics of the CuCAAC reaction. These reports demonstrated poly(triazoles) to be excellent ligands for Cu(I); thus, triazoles formed along the polymer backbone complex with the catalyst, leading to a higher local catalyst concentration in the immediate vicinity of neighboring unreacted azide groups.[39, 40]

The high yield and specificity of click chemistry have not only allowed the

quantitative introduction of various functional groups onto polymer backbones, but also enabled both simultaneous and cascade functionalization of a variety of macromolecules. The relative rates of polymerization and click functionalization can be conveniently tuned by varying the catalyst concentration, solvent and temperature. Triblock copolymers of poly(ethylene glycol), polystyrene, and poly(methyl methacrylate) have been synthesized in a one-pot method by a combination of Diels-Alder and the CuCAAC reaction, where block-arrangement was controlled by the differing reaction rates.[41] Click strategies are also fruitful when applied as complements of living polymerization techniques, such as ring-opening polymerization (ROP), ring-opening metathesis polymerization (ROMP), cationic polymerization, atom transfer radical polymerization (ATRP), and reversible addition fragmentation chain transfer polymerization (RAFT).[42–44] Whether isolated as co-monomers of a linear polymerization or as conjugates of sequential polymerizations, azide- and alkyne-terminated monomers and polymers have been utilized in an array of polymer synthesis methods.

1.2.2 Surface Functionalization

Building in scale from polymer synthesis, click chemistry has been applied to the chemical functionalization of surfaces and interfaces by preparing azide- or alkyne-modified surfaces. Because of the high surface:volume ratio inherent in nanomaterials, the control of appropriate surface chemistry (precise engineering of location, ordering, and self-assembly of surface moieties) is a critical component of nanoparticle design. Accordingly click chemistry has been applied to the engineering of the surface of nanoparticles, including Au, CdSe, Fe_xO_y, SiO_2, carbon nanotubes, and bioparticulates (whole viruses and capsids).[45–51] A plethora of methodologies have been used to address surface modifications of nanoparticles, often metal complexation-

based and covalent-modification methodologies; however, none of these methods is universal in that a preliminary surface modification step allows the attachment of small molecules (polar and non-polar molecules), polymers (either via grafting-from and grafting-to methods) and complex ligands, such as biological recognition elements (proteins, carbohydrates, DNA, RNA); therefore, click chemistry represents a valuable contribution to affect universal modification of nanoparticle surfaces. The presence of the alkyne or azide groups at the material surface enables highly specific post-synthesis modification. Surface functionalization *via* click chemistry provides a greater level of control over the orientation and the density of the moiety attached to the surface, while reducing the risk of side reactions (Figure 1.4c). Stephen H. Foulger reported the development of a standard alkyne-incorporating nanoparticle platform and illustrated the application of the CuCAAC to modify alkyne-terminated nanoparticle surfaces with photoluminescent moieties. S.H. Foulger *et al.* demonstrated the attachment of azide-modified chromophores to ordered poly(propargyl acrylate) particles (crystalline colloidal arrays) afforded loading levels of nearly 105 dye molecules per nanoparticle, resulting in improved optical gain.[52, 53]

In addition to nanoparticles, the CuCAAC reaction has proven to be an excellent tool for functionalizing inert polymer, gold, silicon and quartz substrates.[54–58] Joerg Lahann combined the efficiency of the CuCAAC reaction with high-throughput printing techniques and reported the spatial control of click cycloadditions on flat surfaces using microcontact printing. Defined biotin functional surface patterns were prepared using a poly(dimethylsiloxane) (PDMS) stamp that was inked with $Cu(II)SO_4$. The stamp was used to locally catalyze the CuCAAC of an adsorbed alkyne-modified polymer and azide-modified biomacromolecule.[59, 60] The CuCAAC reaction has also been used to pattern the surface of bulk materials (microbeads and thick films) by post-processing modification.[61] Overall, a very wide variety of functional molecules

(synthetic or biological) have been attached to surfaces using a the CuCAAC reaction and click strategies, opening a wide range of opportunities for materials applications such as molecular optoelectronics, catalytic systems and biosensors.

1.2.3 Bio-functional Materials

Structural and surface design capabilities afforded by click chemistry have provided materials scientists a platform to explore an array of biotechnological challenges. The application of click chemistry in drug discovery, ranges from lead finding through combinatorial chemistry and target-templated *in situ* chemistry, to proteomics and gene therapy, using bioconjugation reactions.[12, 62] The reactions used for biosystems modification must not only fulfill the criteria of an efficient click reaction, such as high yields, selectivity and compatibility with an aqueous environment, but the reaction must also be bio-orthogonal to avoid interruption or modification of the biomacromolecules' native function. Bio-orthogonality refers to the necessity of exploiting reactants that are non-interacting towards the functionalities present in biological systems. These properties, inherent in the CuCAAC reaction, have been highlighted for the development of potent inhibitor drugs of acetylcholineesterases, carbonic anhydrase, HIV-protease and chitinase.[63–66] Benjamin F. Cravatt *et al.* most notably introduced a method to label enzymes *in vivo* and *in vitro* with an activity-based protein profiling probe and detect the labelled proteins in whole proteomes by the CuCAAC reaction with an alkyne-modified fluorophore.[67, 68] The CuCAAC reaction was also demonstrated for viable DNA coupling, and oligonucleotides have been labelled with fluorescent dyes, sugars, peptides and other reporter groups through modified nucleobases and phosphate backbones.[13, 69, 70] Most amazingly, researchers have succeeded in performing site-specific, fast, reliable and irreversible bioconjugation by

the genetic incorporation of azide and alkyne-containing non-natural amino acids into proteins, resulting in the direct CuCAAC modification of live cells.[6, 71, 72]

The introduction of bioactive moieties, which can both be tracked and detected *in vivo* as well as *in vitro* conditions are also a popular technique for modification of synthetic materials, such as tailor-made biopolymers and bio-functional surfaces. Polymer-block-oligopeptide bioconjugates have been prepared by click-ligation of azido-modified poly(ethylene glycol) (PEG) and alkyne-modified oligopeptides.[73] A number of mannose- and galactose-containing polymers with protein-binding studies have also been prepared by reacting different azide-modified sugars onto into the biopolymer backbone; "clickable" sugars were later exploited in the design of protein biohybrid materials by adding azide-modified mannopyranoside and galactopyranoside to poly-alkyne peptide scaffolds.[74] The CuCAAC reaction also offers mild reaction conditions that circumvent the biodegradation of aliphatic polyesters by hydrolysis or trans-esterification, when attempting to modify with biomacromolecules. These polyester can be generated by the use of azide- or alkyne-modified cyclic monomers that can be polymerized by ROP, *e.g.* azido-caprolactone and propyn-1-yl-valerolactone, and many bioactive moieties, such as maltose and glucose, could be attached onto these functionalized polyesters by the CuCAAC reaction. The application of CuCAAC click chemistry has also been used for the synthesis of several rotaxanes, catenanes and molecular shuttles using passive as well as active template strategies with biological applications in mind.[45, 75] The practical ligation under neutral reaction conditions and the fact that several compounds containing 1,2,3-triazole displayed a broad spectrum of biological activities, such as antibacterial, herbicidal and fungicidal, anti-allergenic and anti-HIV, have been emphasized in recent reviews.[76–78]

As more "clickable" bio-functional moieties are developed, novel nanomate-

rials are also being explored as scaffolds to carry bio-functional moieties through biosystems. Self-assembled protein capsids are a promising class of nanoparticles for biomedical applications due to their uniform (monodisperse) nature and versatile genetic and chemical design.[79] The tobacco mosaic virus (TMV) surface was employed as a scaffold when an alkyne was introduced by chemo-selective modification of the tyrosine residue on the surface of the viral capsid. The CuCAAC reaction was then used to couple azide-functionalized compounds including small molecules, peptides and polymers onto the TMV surface with a variety of groups that promote or inhibit cell binding. Synthetic nanoparticles have also be utilized as carriers for bio-functional moieties.[80] When nanoparticles are surface-functionalized with contrast agents or ligands, they can become imaging platforms for the tissue of interest or highly specific targeted therapies to a disease site. S.H. Foulger has reported on the preparation of CuCAAC-modified nanoparticles which were used as biocompatible carriers both imaging and therapeutic delivery. Nanoparticles were prepared with surface-attached indocyanine green (ICG) and PEG by the CuCAAC reaction. Proteins complexed with the surface-attached moieties, resulting in fluorescence enhancement. The surface-attached ICG also provide a photodynamic therapeutic, resulting in a statistically significant reduction in tumor cell growth.[81] Click-nanoparticles have also been developed as targeted delivery vehicles, for both synthetic and gene therapeutics. Molly S. Shoichet *et al.* reported the attachment of nearly 400 targeting-peptides per poly(lactide) nanoparticle by the CuCAAC reaction, and Theresa M. Reineke utilized a similar approach to attach DNA-harboring β-cyclodextrins to nanoclusters for targeted-delivery.[75, 82–84]

From these few selected examples, it is apparent why click reactions have been so popular and successful for the synthesis and modification of macromolecules and nanomaterials. The need to effectively decorate biomaterials and biointerfaces,

the ability to drive covalent reactions inside living organisms and the promise of constructing large macromolecules through complimentary junctions present in their constituents will be important materials science and biotechnology drivers for decades to come.

1.3 Overview

Although click chemistry was introduced as a synthetic route to expand drug libraries, its application to materials synthesis and biotechnology have been a resounding success. After a decade of developing basic polymeric materials by click chemistry and in light of the increasing synergy between the physical and life sciences, it is necessary to rethink the use of click chemistry in materials sciences as the ideal methodology for engineering "bio-hybrid tools" ***Bio-hybrid tools are materials that are designed and engineered to be utilized as specific sensors within biosystems or traps to harness and convert biosystems complexity into commercial technologies; thus, the work presented in the following chapters explores the basic science required to develop a series of bio-hybrid tools, by joining click chemistry and materials science in a paradigm which materials are developed to extract and harness the inherent complexity and efficiently of biosystems.***

The chapters of this dissertation can be summarized as follows:

- Chapter 1 offered an introduction to the concept of click chemistry and its current uses as a materials synthesis strategy; moreover, examples were provided in which click chemistry has been employed to either recreate or modify biosystems. The proceeding chapters present work conducted to examine the extent of click materials as a strategy for developing biotechnologies at various scales,

in which the engineered material is designed to exploit a specific component of a complex biosystem.

- Chapter 2 explores a direct correlate to the early uses of click chemistry as a combinatorial drug development strategy. Small-molecule chromophores are modified and combined to form a library of energy transfer dyads with spectral characteristics ranging from the ultraviolet to near infrared. Energy transfer systems were modeled by *ab initio* and semi-empirical calculations to estimate optimal geometries, synthesized, characterized, and ultimately used as an biosensor of a bioremediation enzyme.

- Chapter 3 and 4 explore click chemistry as a surface ligation tool by modifying both polymer and organic/inorganic composite nanoparticles. The functionalized polymer and magnetic nanoparticles were utilized as bioseparation and bioimaging devices, respectively.

- Chapter 5 culminates in the synthesis of materials *via* click chemistry to encapsulate and repurpose an entire biosystem (bacteria). The rapidly emerging field of copper-free click chemistry is explored, and an old reaction is rebranded as a member of the click family. This reaction is employed for the design and production of a biohybrid, hydrogel fiber with a microfluidic shaping system. The click hydrogel chemistry and microfluidic production process allowed for the encapsulation of viable bacteria *in situ*.

CHAPTER 2

Single-molecule FRET: Bridging chromophores via click chemistry

---

2.1 Introduction

Photobiological sensing is often affected by either a native photoreceptor protein or an exogenous molecule introduced by bioconjugation, which then undergoes a photochemical reaction, *e.g.* photoisomerization or excitation transfer, signaling the biological event. Bioconjugation techniques are often applied to selectively modify cellular components with signaling probes for *in vivo* imaging, proteomics, cell biology and functional genomics. A multistep procedure is usually required: 1) the *in vivo* target is tagged with a detectable chromophore, 2) purification of the ligated target and 3) the detection of the chromophore-target pair. Commercially available fluorogenic probes are able to tag biomacromolecules containing an array of functional groups, *e.g.* primary amines, thiols or carbonyls; however, since amine, thiol and carbonyl groups are the most abundant functional units in biosystems, these reagents can hardly provide selective modification of a targeted species under the complicated intracellular conditions. Genetically encoded tags such as green fluores-

cent protein (GFP) and its variants are routinely applied as fluorescent probes, but GFP is perturbative because its size (238 amino acids) is often larger than the target of interest. Small-molecule fluorogenic devices are required for more accurate probing of biosystems, specifically the analysis of the array of small-molecule ligating proteins.

To date, a wide variety of fluorescent sensors and switches have been synthesized to probe environmental and biological events. For example, selective ligands and ionophores for cations and anions are well established, commercial products for *in vivo* sensing. More recently, excimer, exciplex, and FRET fluorescent probes have offered a number of advantages over common single-emitter designs.[85–89] As an alternative to genetically-incorporated fluorophores, *i.e.* in leiu of GFP, RFP, and Sanger nucleobases, small-molecule energy transfer probes can be introduced to biosystems by click chemistry. Alkyne and azide groups are very small in size, highly energetic, and have a particularly narrow distribution of reactivity; furthermore, they can be conveniently introduced to organic compounds and are quite insensitive to solvent and pH. A pertinent example is the development of fluorogenic "clickable" coumarins, where upon formation of a triazole between azide-modified coumarins and alkyne-modified reagents, the fluorescence increased because the quenching effect of the electron-rich azides is reduced.[90, 91]

Similarly, the organic chromophores explored in Chapter 2 are combinatorially paired by azide and alkyne-modification to display the appropriate spectral characteristics to act as a permanent donor:acceptor pair in an energy transfer mechanism when the triazole-linkage is formed. Energy transfer can take place through a Coulombic interaction (Förster) or electron exchange (Dexter) mechanism and occurs when an excited donor (a higher energy fluorophore) transfers energy over to a ground state acceptor (a lower energy fluorophore). In order to be an effective means of energy transfer, both the Förster and Dexter mechanisms are dependent on

spatial separation between the donor and acceptor and the spectral characteristics of the donor's emission and the acceptor's absorption. A Förster-type transfer can be potentially effective up to $\approx$ 10 nm, while a Dexter-type transfer, though highly dependent on the electronic configuration of the donor-acceptor, is roughly limited to distances $\approx$ 2 nm. The distance dependance of both energy transfer mechanisms make Förster and Dexter energy transfer very precise "molecular rulers." Any perturbation at the molecular scale would cause decay in the energy transfer mechanism, signaling a molecular event. In addition, both modes of energy transfer require a high level of spectral overlap of the donor's emission and the acceptor's absorption. Being able to modify, enhance or suppress the molecular mechanisms that modulate the response of the energy transfer would provide a route to produce orthogonal, exogenous bioprobes.

2.1.1 Energy transfer: Förster resonance mechanism

The simplified process of photon emission by excited state relaxation involves exciting an electron in an atom from the valance band to the conduction band by introducing enough energy into the ground-state electron. The excited electron and its corresponding hole are electrostatically bound, forming an exciton. Entropic forces dictate the excited electron's return the ground state, recombination with its corresponding hole, and release of excess energy, as a photon, phonon or other non-radiative decay.

For organic small-molecule or polymeric systems, excitation and emission occurs in the electron orbitals of the molecules. Electrons found in the highest occupied molecular orbitals (HOMO), can be excited to the lowest unoccupied molecular orbital (LUMO), corresponding to the valence and conduction band of single-crystal mate-

rials, respectively. Figure 2.1 is the Jablonski diagram illustrating the excitation, fluorescence and Förster resonance energy transfer (FRET) processes. S_0, S_1, and S_2 correspond to the ground, first, and second electronic singlet states, respectively. T_1 is the first excited triplet state. The corresponding 0-5 bands are the vibronic states at each energy level. In the case of fluorescence, absorption of a photon induces an electronic transition from the S_0 to a high-energy vibronic band in either, S_1 or S_2. In organic molecules, an electron is promoted from the HOMO to the LUMO. The fastest relaxation mechanism is vibrational relaxation, a non-radiative process that allows the relaxation of an excited electron from a higher vibrational level within the same excited state. Internal conversion is a similar non-radiative transition, which occurs when an excited electron relaxes between two excited states of the same multiplicity. Intersystem crossing is a slower non-radiative transition, which occurs when an electron relaxes from an a singlet to triplet state. Ultimately, a radiative transition (fluorescence) can be achieved, *i.e.* relaxation to S_0 causing the emission of a photon.

FRET is an alternate, intersystem relaxation mechanism; it is a virtual Coulombic interaction between an emissive excited-state donor molecule and an absorptive ground-state acceptor molecule resulting from long range dipole-dipole or quadripole-quadripole interaction. The transfer arises from the resonance between donor and acceptor and is largely dependent on the alignment of the dipole moments of the two molecules. This form of non-radiative energy transfer is relatively slow, suggesting there is a weak coupling between the transition dipole moments of both molecules. From Theodor Förster's kinetic expressions, the FRET rate (k_D) can be described as a function of inter-molecule donor/acceptor distances (2.1), where R is the intermolecular distance, R_0 is the idealized FRET distance when the rate of the energy transfer becomes the same rate as the decay of the excited state donor, and τ_0 is the fluorescence decay time of the excited-state of the donor. Equation 2.1 illustrates

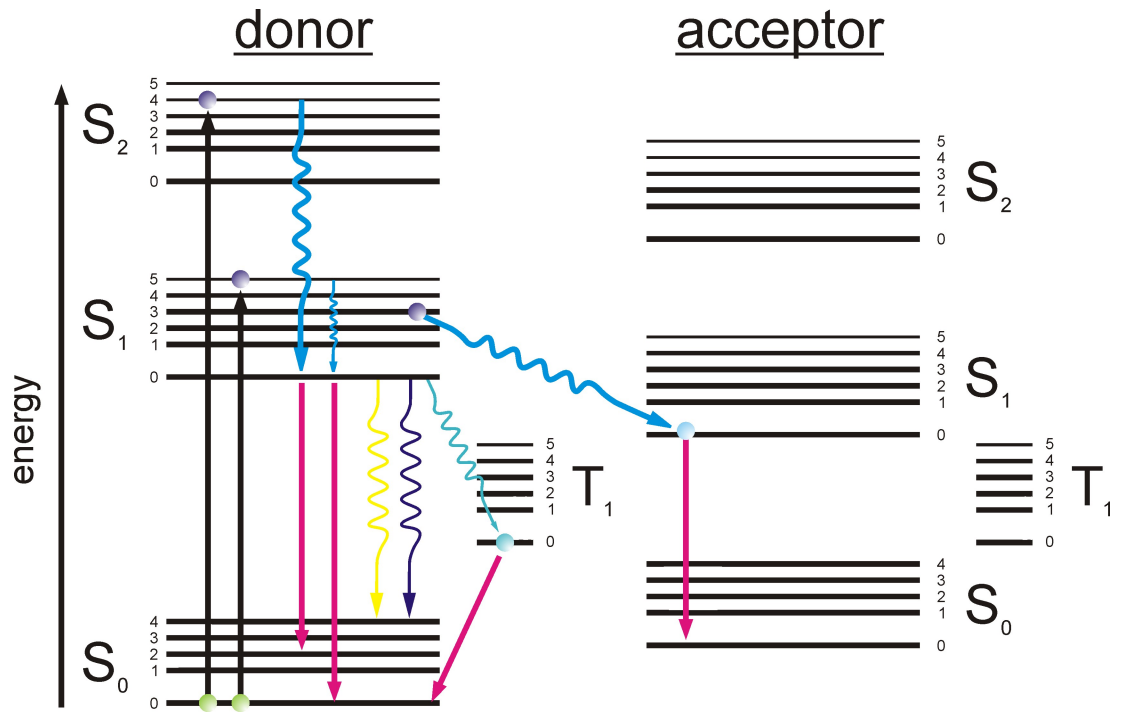

Figure 2.1: Jablonski diagram illustrating electronic excitation (black arrow) when a ground-state electron absorbs energy and is excited to a higher singlet state, internal conversion (blue arrow) when the excited electron relaxes to a vibronic state within the S_1 or S_2 levels, intersystem conversion (cyan arrow) when the excited electron relaxes to a triplet state, and fluorescence (magenta arrow) when the excited electron relaxes to a ground state. FRET relaxation is also pictured, when the excited electron transitions to the excited state of the acceptor molecule and consequently relaxes to the ground state.

FRET's extreme sensitivity to any distance changes between 1 - 10 nm. Equations 2.2 and 2.3 define the critical donor/acceptance distance based on the absorbance and emission spectral overlaps of the interacting molecules, where κ is the orientation factor of the dipole moments, N is Avagadro's number, q is the quantum efficiency of the donor, n is the refractive index of the matrix, and λ is the wavelength in nm, and ϵ_a is the molar extinction coefficient of the acceptor. Since FRET is a resonant transfer and does not rely on charge propagation, the critical Förster radius is practically taken as when the transfer efficiency is $\approx 50\%$ and is typically in the range of 2-10 nm. Additionally, the transition dipole moments of the interacting molecules play a significant role in the transfer efficiency, though an average orientation factor (0.66) is often used for calculations.

$$k_{FRET} = \frac{1}{\tau_0}\left(\frac{R_0}{R}\right)^6 \tag{2.1}$$

$$R_0 = \left[\frac{9000(ln10)\kappa^2 q}{128\pi^5 n^4 N}\int f(\nu)\epsilon_A(\nu)\frac{d\nu}{\nu^4}\right]^{1/6} \tag{2.2}$$

The expression, $\int f(\nu)\epsilon_q(\nu)\frac{d\nu}{\nu^4}$, is defined as the integrand **J** ($M^{-1}cm^{-1}nm^4$):

$$J = \int F_D(\lambda)\cdot\epsilon_A(\lambda)\cdot\lambda^4 d\lambda \tag{2.3}$$

The integral **J** is the spectral overlap of the donor and acceptor, where $F_D(\lambda)$ is the normalized spectrum and ϵ_A is the maximum molar extinction coefficient.

2.2 Results and Discussion

The chromophores presented in Figure 2.2 were synthesized and combined to produce permanent FRET dyads. Absorbance and photoluminescence spectra were

experimentally analyzed to predict possible energy transfer pairs; moreover, to better design click chromophores quantum chemistry calculations were performed to model intra-chromophore spacing and placement of the chromophore band gap.

2.2.1 Calculated geometries and molecular orbitals of single-molecule FRET systems

FRET dyads were modeled and characterized by quantum chemical calculations. The first principle for calculations of the molecular states is the general time-dependent Schrödinger Equation (2.4, where $\Psi(\mathbf{R,r},\mathrm{t})$ is the wavefunction of nuclei positions ($\mathbf{R} = (\mathbf{R}_1,\ldots,\mathbf{R}_n)$) and electron positions ($\mathbf{r} = (\mathbf{r}_1, \ldots, \mathbf{r}_n)$. The Hamiltonian operator, $\hat{H}$, accounts for the kinetic and potential energy operators for all nuclei and electron interactions. Ultimately, the complete set of solutions for the Schrödinger wave equation would provide the ground state geometry and expected electron distributions for both absorbance and fluorescence of the FRET dyads.

$$i\hbar\frac{\partial}{\partial t}\Psi(\mathbf{R},\mathbf{r},t) = \hat{H}\Psi(\mathbf{R},\mathbf{r},t) \tag{2.4}$$

In the reported calculations, the following assumptions are made:

- The Born-Oppenheimer approximation is inherently assumed. The approximation posits that the motion of electrons or infinitely faster that the motions of the nuclei do to their mass difference and the electrons instantaneously follow the nuclei, thus the nucleus position becomes a parameterized value.

- Relativistic effects are neglected. The momentum operator is assumed to be classical.

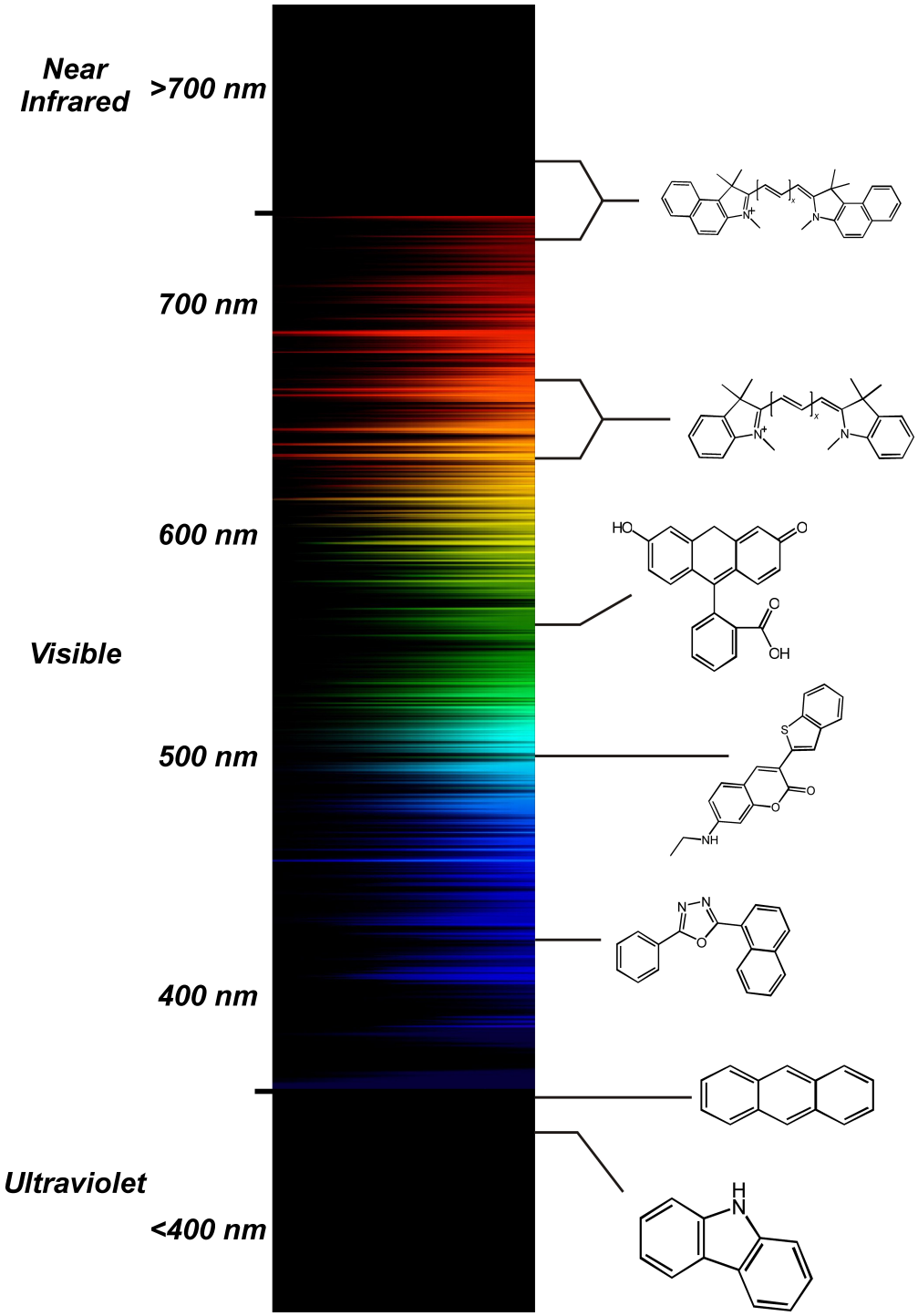

Figure 2.2: Spectral range of organic chromophores spanning from the Ultraviolet, through the visible, to the NIR. By pairing chromophores with conjugate click functionality, single-molecule FRET dyads can be synthesized by the CuCAAC reaction.

- The basis set is composed of a finite number of orthogonal functions. (In reality, the wave function is a linear combination of functions from an infinite basis set.
- The energy eigenfunctions are assumed to be products of one-electron wave functions.
- The effects of electron correlation are neglected.

The simplest type of *ab initio* calculation is the Hartree-Fock (HF) method, in which the instantaneous Coulombic electron-electron repulsion is not specifically taken into account and the Schrödinger Equation is treated as a simple eigenvalue equation of the Hamiltonian operator, with a discrete set of solutions. This is a variational procedure; therefore, the obtained approximate energies, expressed in terms of the system's wave function, are always equal to or greater than the exact energy, and tend to a limiting value called the HF-limit as the size of the basis is increased. The simplest approach for the description of a system of N interacting electrons is the the Hartree-Fock (HF) method, where the ground-state many-body wavefunction is approximated as the optimal non-interacting solution, *i.e.* a Slater determinant of single-particle spin-orbitals $\{\Phi_i\}$:

$$\Psi_{HF}(x_1, ..., x_N) = \frac{1}{\sqrt{N!}} \begin{vmatrix} \Phi_1(x_1) & \Phi_1(x_2) & ... & \Phi_1(x_N) \\ \Phi_2(x_1) & \Phi_2(x_2) & ... & \Phi_2(x_N) \\ \vdots & \vdots & \vdots & \vdots \\ \Phi_N(x_1) & \Phi_N(x_2) & ... & \Phi_N(x_N) \end{vmatrix} \tag{2.5}$$

The optimal molecular orbitals are determined by minimizing the interacting Hamiltonian operator on the wavefunction, Ψ_{HF}, and if the spin-orbitals are written as the product of a spatial and a spin components (Eq. 2.6), the spatial orbitals must satisfy

the solutions of Ψ_{HF}.

$$\Phi_i(x) = \phi_i\ (\boldsymbol{r})\ \chi_{si}\ (\sigma) \tag{2.6}$$

Each orbital experiences the external potential, the Hartree electrostatic component, and the non-local HF exchange potential. The HF potential cancels the interaction of the electron with itself, that is the self-interaction contribution coming from the the Hartree potential, and keeps the electrons of the same spin apart so that each electron has a hole around it, known as the exchange hole, containing unit positive charge. For molecular systems, the orbitals are expanded as a linear combination of atomic orbitals (LCAO) centered on the nuclear positions:

$$\phi_i(\mathbf{r}) = \sum_{\mu}^{nuclei} \sum_{j} a_{ij}^{\mu} \eta_{j\mu}(\mathbf{r} - \mathbf{r}_{\mu}) \tag{2.7}$$

where $\mathbf{r}_{\mu}$ denotes the position of a nucleus. The LCAO coefficients, a_{ij}^{μ} and $\eta_{j\mu}$, are optimized to yield the lowest variational energy. In general, the HF operators will be input with a Gaussian atomic basis set:

$$\eta(\mathbf{r}) = x^m y^n z^k e^{-\alpha r^2} \tag{2.8}$$

as this set allows all integrals to be computed analytically. Since relativistic effects are neglected and the Born-Oppenheimer approximation is applied, it is assumed that a non-relativistic system of N interacting electrons is described by the Hamiltonian:

$$H = -\frac{1}{2} \sum_{i=1}^{N} \nabla_i^2 + \sum_{i=1}^{N} \nu_{ext}(\mathbf{r}_i) + \sum_{i<j}^{N} \frac{1}{|\mathbf{r}_i - \mathbf{r}_j|} \tag{2.9}$$

where the atomic units apply ($\hbar$ = m = e = 1). The external potential $\nu_{ext}(\mathbf{r})$ is given either by the bare electron-ion Coulomb potential Z/r where Z is the charge of

the ion, or by a pseudopotential describing the ion plus the core electrons which have been eliminated from the calculation, **r** is the 3N particle coordinates with x = (r, σ) (the 3 spatial and 1 spin coordinates of one electron where $\sigma = \pm 1$).

Initially, the performance of the theoretical basis and available computational power was tested on simplified molecular models. The quantum chemical investigation of the FRET systems was initialized with the computation of the electronic excitations of discrete chromophores *in vacuo* since the lower level of complexity of these systems allow us to push the limits of the available computational tools and better understand their limitations. Moreover, calculations using highly-correlated techniques are available for discrete chromophore models; whereas, the FRET dyads will require un-correlated, small-basis set calculations. Calculations began with a HF model and subsequently were corrected for electron-electron repulsion. Möller-Plesset perturbation theory was the utilized post-HF methods. Second order Möller-Plesset (MP2) calculations are standard levels used in calculating small systems and were implemented in these simulations. The density matrix for the first-order and higher MP2 wavefunction is of the type known as response density, which differs from the more usual expectation value density. The eigenvalues of the response density matrix (which are the occupation numbers of the MP2 natural orbitals) can therefore be greater than 2 or negative, but unphysical numbers are a sign of a divergent perturbation expansion.

Figure 2.3 shows the calculations of the HOMO and LUMO for the isolated chromophores paired to produce the FRET dyads, within an all-electron HF, 6-311+G(d,p) basis set and the MP2 correlation. As discrete chromophores, many of these pairs have been exploited for FRET.[92] The resultant HOMO and LUMO accurately predicted the maximum absorbance energy for each chromophore; however, it is apparent in the calculation is lacking for the fluorescein moiety, The HOMO

and LUMO should mirror each other, as represented in Figure 2.3 carbazole and anthracene, but for the fluorescein calculation the HOMO is shifted toward the higher electron density of the double-bonded oxygen which is a common error produced by small basis set *ab initio* calculations.[93] The clicked models were analyzed for both geometry optimization, excited states and molecular orbitals by *ab initio*, where possible, and semi-empirical calculations (MOPAC) for charged chromophores (to reduce calculations costs). Theoretical calculations of the optical properties of the FRET dyads complement spectroscopic characterization by providing an atomistic description of the molecules' ground and excited states. Quantum chemical calculations should provide an accurate quantum-mechanical description of the ground state and electronic excitations; furthermore, the relative positions of the donor and acceptor frontier molecular orbitals is a predictor of the preferred energy transfer mechanism. When the HOMO and LUMO of the acceptor are located within the energy level of the donor's band gap, FRET dominates; whereas, if the acceptor's HOMO or LUMO lies outside the donor's band gap a Dexter or nonradiative mechanism is observed.[93, 94] Table 2.1 summarized the HOMO/LUMO and molecular bandgap calculations for the discrete chromophores. Accordingly the carbazole HOMO/LUMO levels bracket the HOMO/LUMO levels of anthracene, suggesting they can be donor and acceptor, respectively. The same is true for C6 and Cy3; however, the LUMO of Cy3 falls above the LUMO of Fl suggesting their FRET efficiency may be diminished.

For *ab initio* simulations of the larger FRET dyads, electron-electron correlation needed to be scaled for computational efficiency. Ground state properties of large systems can be reliably and efficiently computed from first principles by density functional theory (DFT). In the FRET dyad calculations, high-dimensionality problems are circumvented by employing one-electron Kohn-Sham DFT, which replaces the electron-electron interactions by an effective potential. In the KohnSham system, elec-

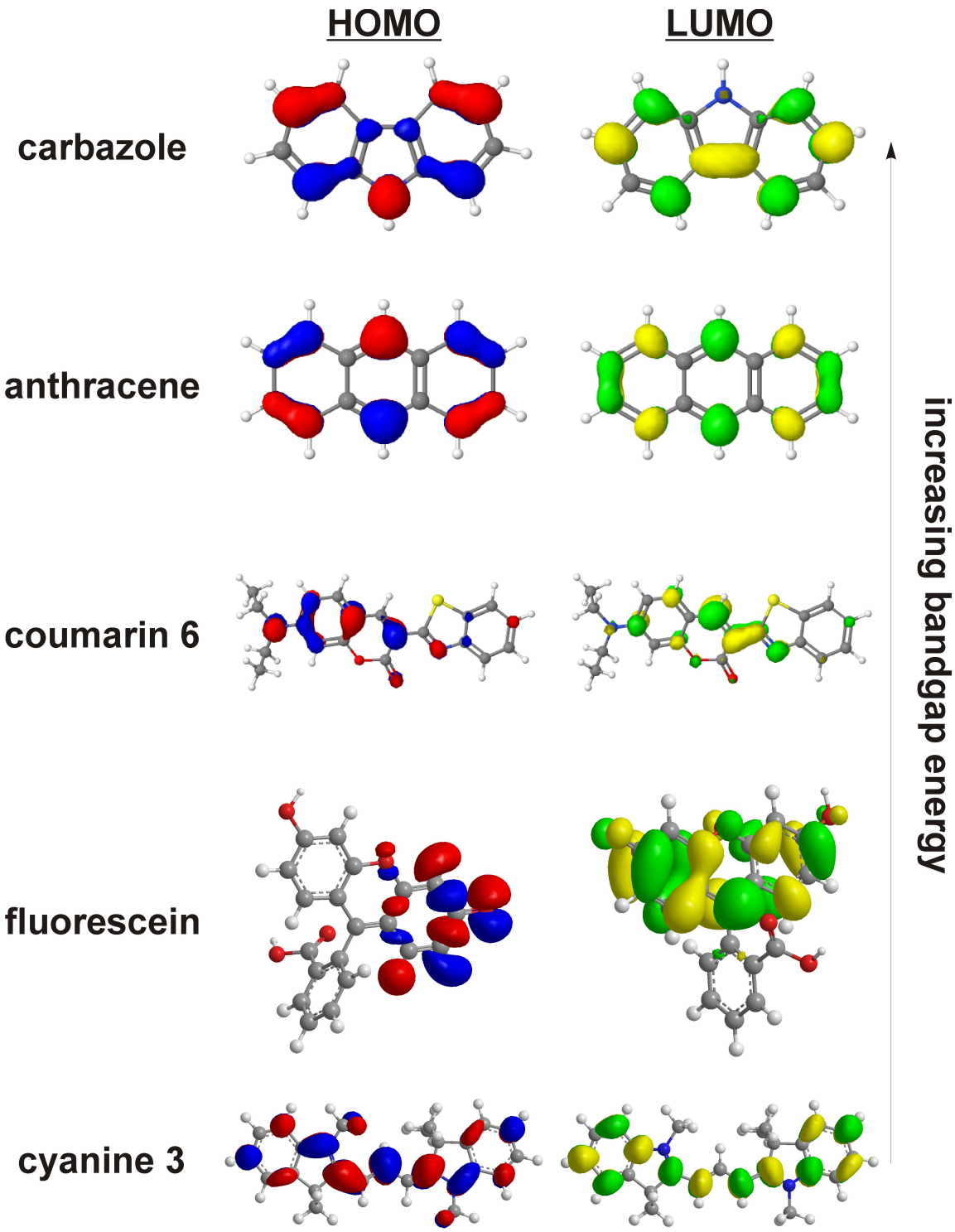

Figure 2.3: The HF/6-311+G(d,p)/MP2 calculations of HOMO and LUMO for the discrete chromophores utilized to build the FRET dyads. Shown are the HOMO (red^{+}/blue^{-}) and LUMO (green^{+}/yellow^{-}) orbitals which are responsible for molecular fluorescence.

chromophore	HOMO	LUMO	bandgap (ΔE)	λ_{abs} (nm)
carbazole	-0.284	-0.105	0.179	255
antrhacene	-0.218	-0.087	0.131	348
coumarin 6	-0.277	-0.151	0.125	364
fluorescein	-0.206	-0.106	0.100	456
cyanine-3	-0.198	-0.113	0.085	537

*** energy reported in Hartree

Table 2.1: Highest occupied molecule orbital (HOMO) and lowest unoccupied molecular orbital (LUMO) calculations for individual components of the FRET dyads. The molecular bandgap is reported as the energy differential from the ground state to first excited state.

trons are non-interacting fermions, so the KohnSham wavefunction is a single Slater determinant, unlike the series required for HF-models. Geometry optimization and molecular orbital models for the FRET dyads were calculated with the B3LYP correlation The B3LYP hybrid functionals are approximations to the exchange-correlation energy functional that only incorporate a portion of exact exchange from HF methods. Figures 2.4, 2.5, and 2.6 show the calculated HOMO/LUMO for the ATBC, C6Cy3 and FlCy3 FRET dyads, respectively. The HOMO/LUMO positions of C6Cy3 and FlCy3 are expected for the donor and acceptor interactions of a FRET pair; the HOMO is located on the donor, C6 and Fl, while the LUMO is located on the acceptor, Cy3. In the ATBC model, both the HOMO and LUMO are located at the anthracene component, suggesting direct stimulation of the anthracene molecule may be the dominant energy transfer mechanism, as opposed to FRET.

In summary, the HF calculations of discrete chromophores suggested the pairing carbazole/anthracene, C6/Cy3, and Fl/Cy3, and corresponding DFT calculations of the FRET dyads showed differing HOMO/LUMO locations that will need to be defined experimentally. While the FRET features will also be largely dependent on structural features of the dyads in solution, the molecular orbital calculations suggest the resultant photoluminescent response will come from the acceptor chromophore.

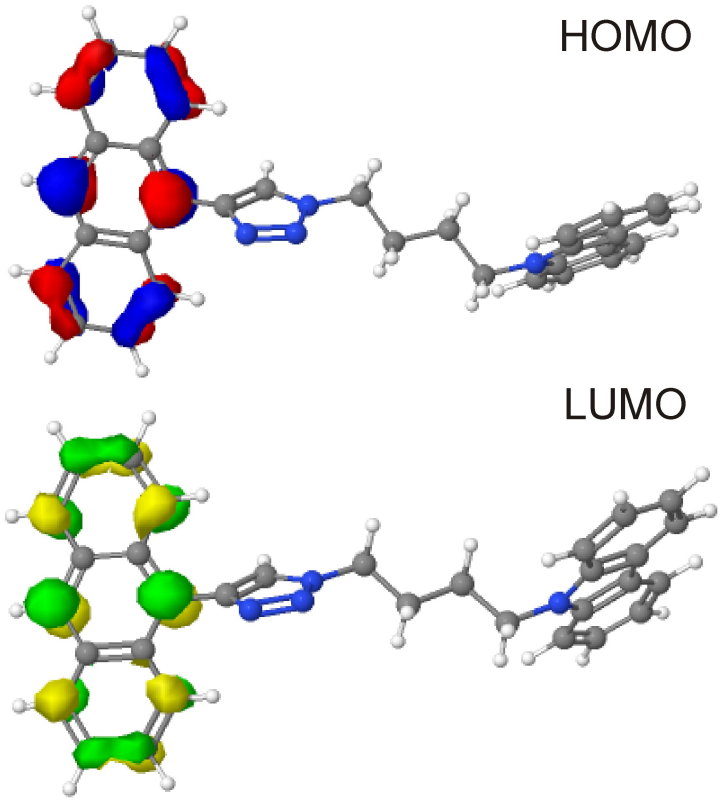

Figure 2.4: The B3LYP(DFT)/6-31G(d) orbitals for the ATBC chromophore. Shown are the HOMO (red$^+$/blue$^-$) and LUMO (green$^+$/yellow$^-$) orbitals which are responsible for molecular fluorescence.

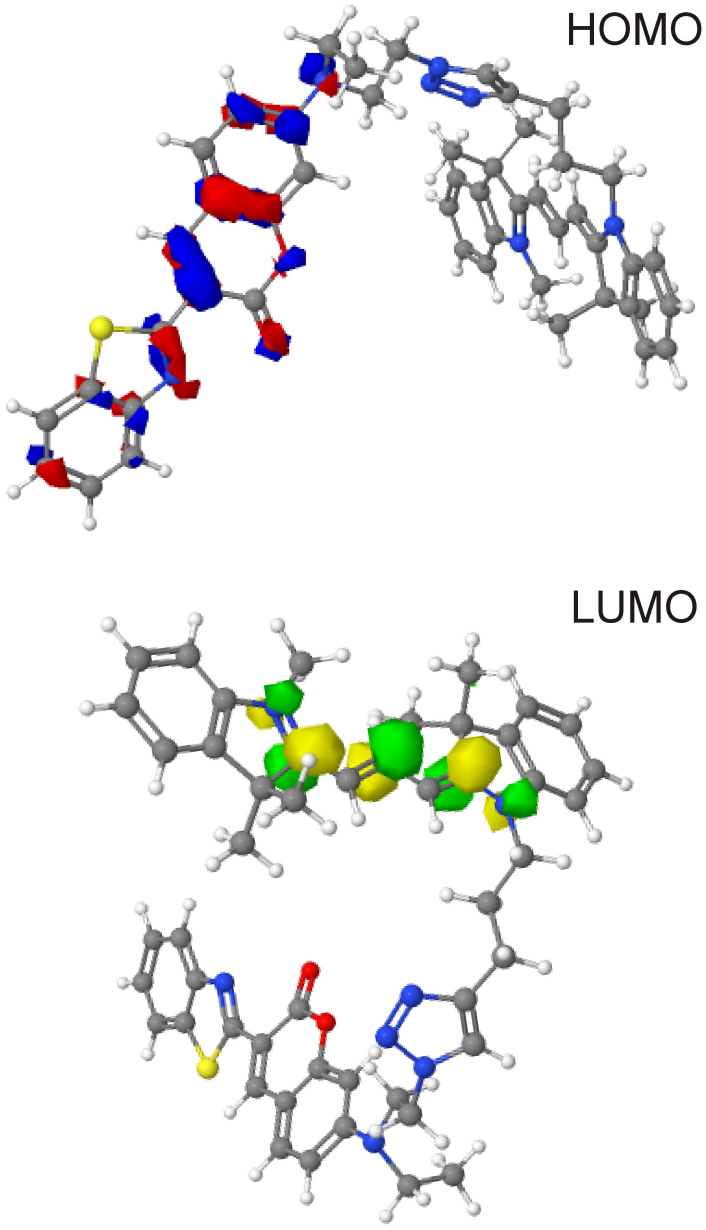

Figure 2.5: The B3LYP(DFT)/6-31G(d) orbitals for the C6Cy3 chromophore *in vacuo*. Shown are the HOMO (red$^+$/blue$^-$) and LUMO (green$^+$/yellow$^-$) orbitals which are responsible for molecular fluorescence.

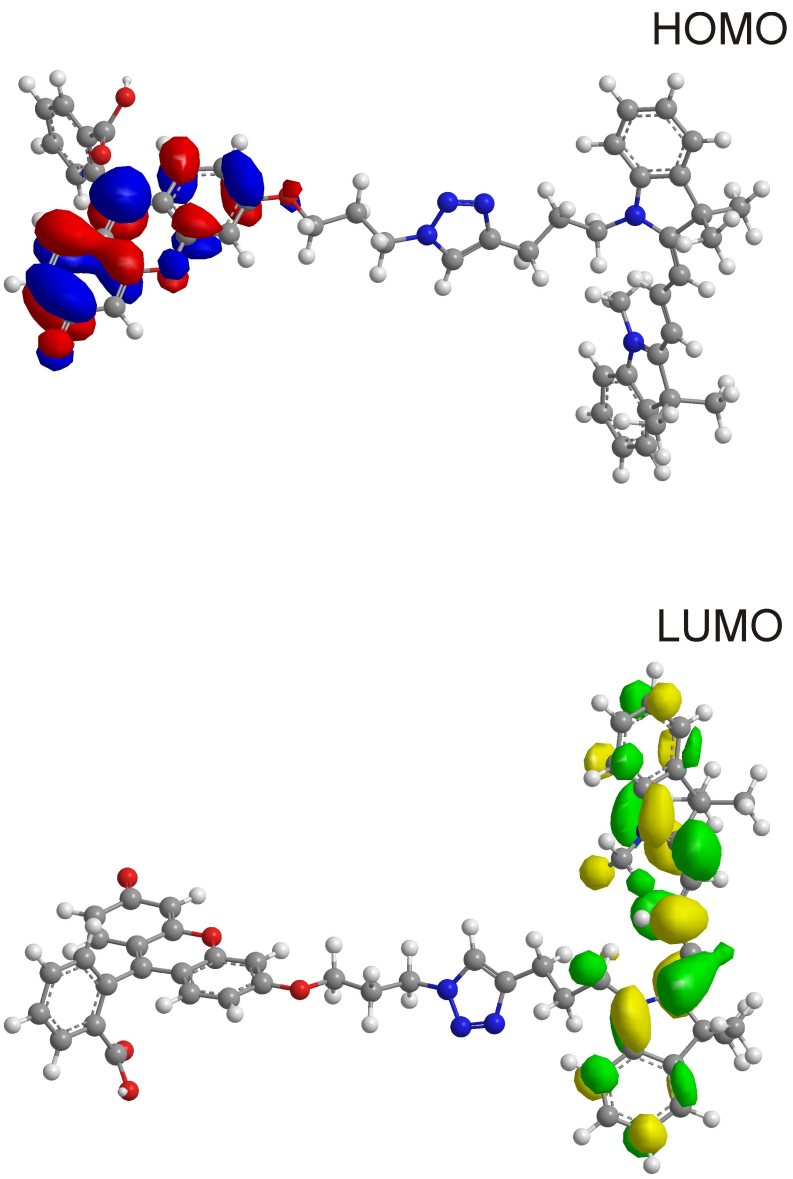

Figure 2.6: The B3LYP(DFT)/6-31G(d) orbitals for the FlCy3 chromophore *in vacuo*. Shown are the HOMO (red^+/$blue^-$) and LUMO ($green^+$/$yellow^-$) orbitals which are responsible for molecular fluorescence.

donor	acceptor	quantum yield, ϕ_D	molar extinction, ϵ_A (M^{-1} cm^{-1})	**J** (A^6 mol^{-1})	R_0 (A)
AC	ABC	0.41	9.7 x 10^4	1.08 x 10^{15}	4.34
C6	Cy3	0.78	1.5 x 10^5	5.6 x 10^{15}	6.36
Fl	Cy3	0.79	1.5 x 10^5	5.93 x 10^{15}	6.44

Table 2.2: Spectral constants for donor and acceptor, quantum yield (ϕ_D) and molar extinction (ϵ_A), respectively. Calculated spectral overlap (**J**) and critical Förster radii for FRET dyads utilizing dipole orientation factor, κ=0.66, and refractive index, n = 1.4.

As will be reported in the following sections, the calculated geometry and molecular orbitals are promising harbingers for the critical FRET distance and spectral characteristics, the J-integral.

2.2.1.1 Spectral properties of single-molecule FRET systems

As an initial approach to experimentally examine the FRET efficiency in the small-molecule dyads, FRET is assumed to be the dominant transfer mechanism and the spectral overlap integrals are used to calculate the FRET parameters. The FRET efficiencies dependent on the spectral characteristics of the donor and acceptor can be calculated from Eq. 2.1 and Eq. 2.2. The dipole orientation factor, κ, can adopt any value between 0 and 4, and its value is often chosen as 0.666666. This limiting situation is valid when the molecular dipoles are rapidly rotating at a speed much faster than the FRET rate.[95] The refractive index, n, of the medium is taken at n = 1.4, which can be idealized as buffer salts dissolved in water. The quantum yield of the donor, ϕ_D, and molar extinction coefficient of the acceptor, ϵ_A, are values taken from the literature.The output of Eq. Table 2.1 and Eq. 2.2, *i.e.* the FRET efficiencies of the synthesized FRET dyads are summarized in 2.2.

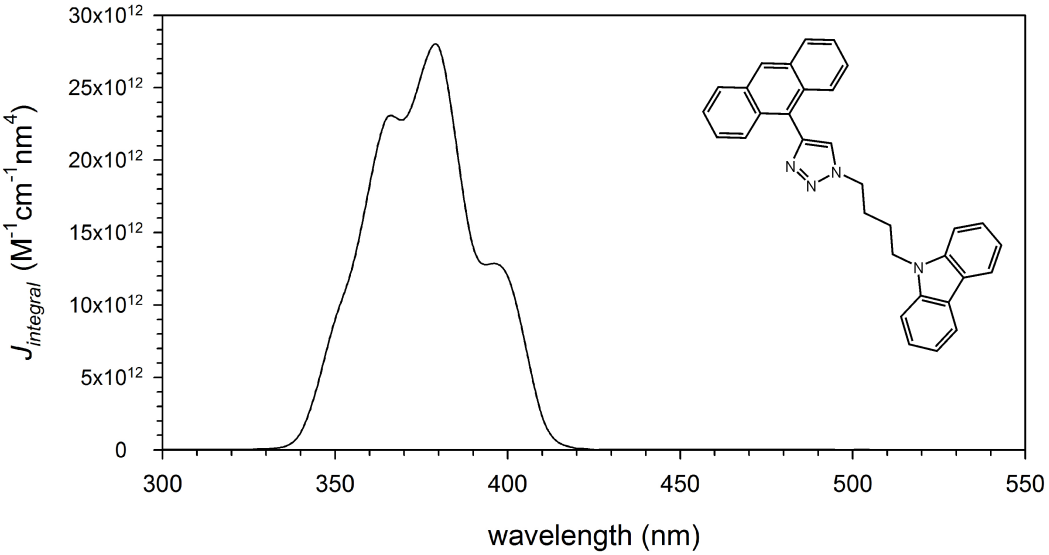

Figure 2.7: Calculated spectral overlap of ATBC dyad.

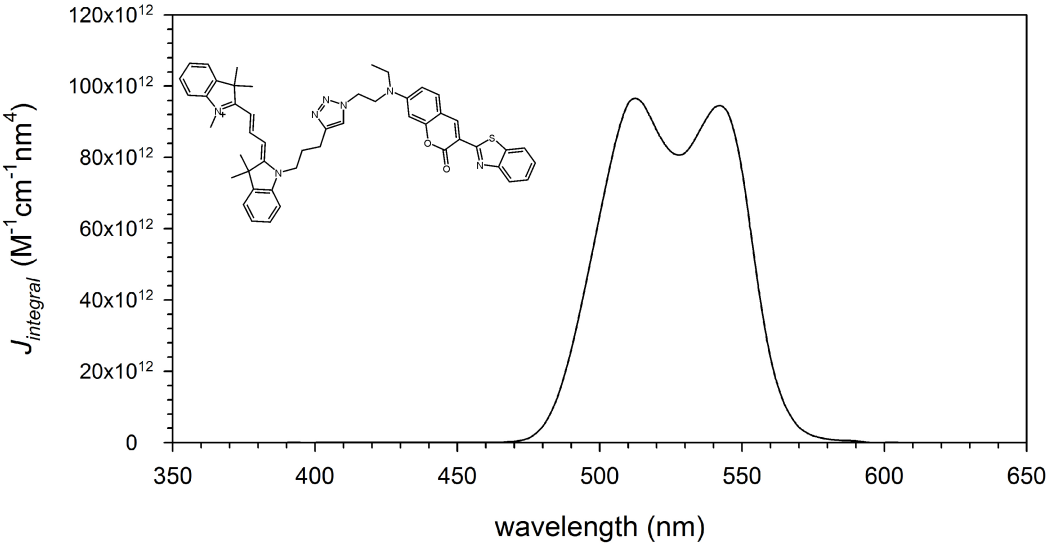

Figure 2.8: Calculated spectral overlap of C6Cy3 dyad.

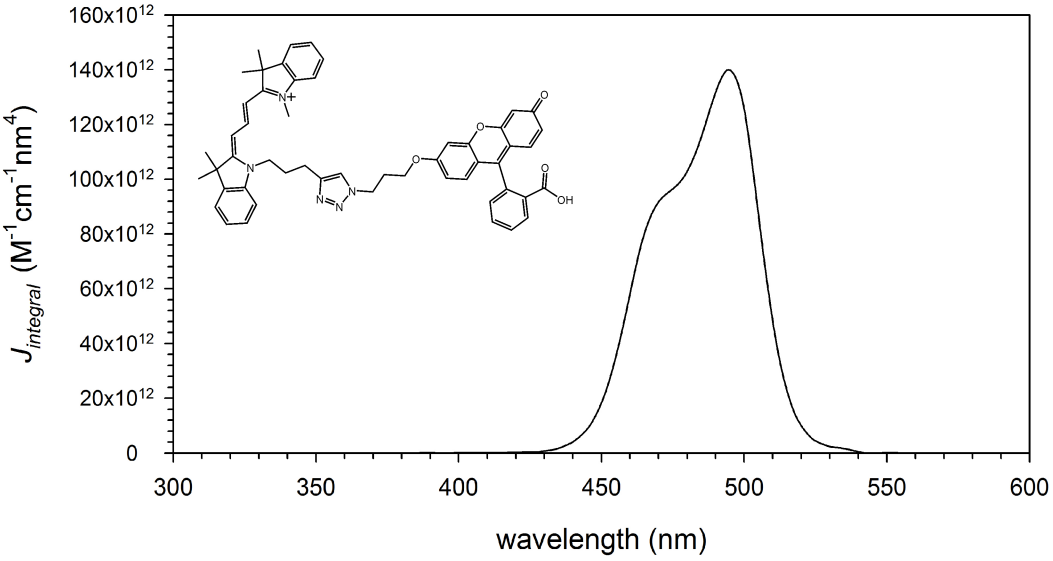

Figure 2.9: Calculated spectral overlap of FlCy3 dyad.

2.2.2 Engineering and application of a single-molecule FRET system as an enzymatic biosensor

The most widely utilized technique for the detection and targeting of endogenous proteins through fluorescence relies on the labeling of the protein with a primary antibody and subsequent attachment of a complementary, emitting dye, protein, or particle.[96] For decades, employing a chromophore pair that can participate in fluorescence resonance energy transfer (FRET) has been the operational basis for studying protein dynamics. For example protein conformational changes, protein-protein interactions, and protein synthesis are measurable due to the dependence of the FRET efficiency on the separation distance and orientation of the donor and acceptor.[97] Recently, techniques employing FRET have been employed in metabolomics, which focuses on the collection of metabolites (metabolome) in a biological cell, tissue, organ or organism, which are the end products of cellular processes.[98] Establishing

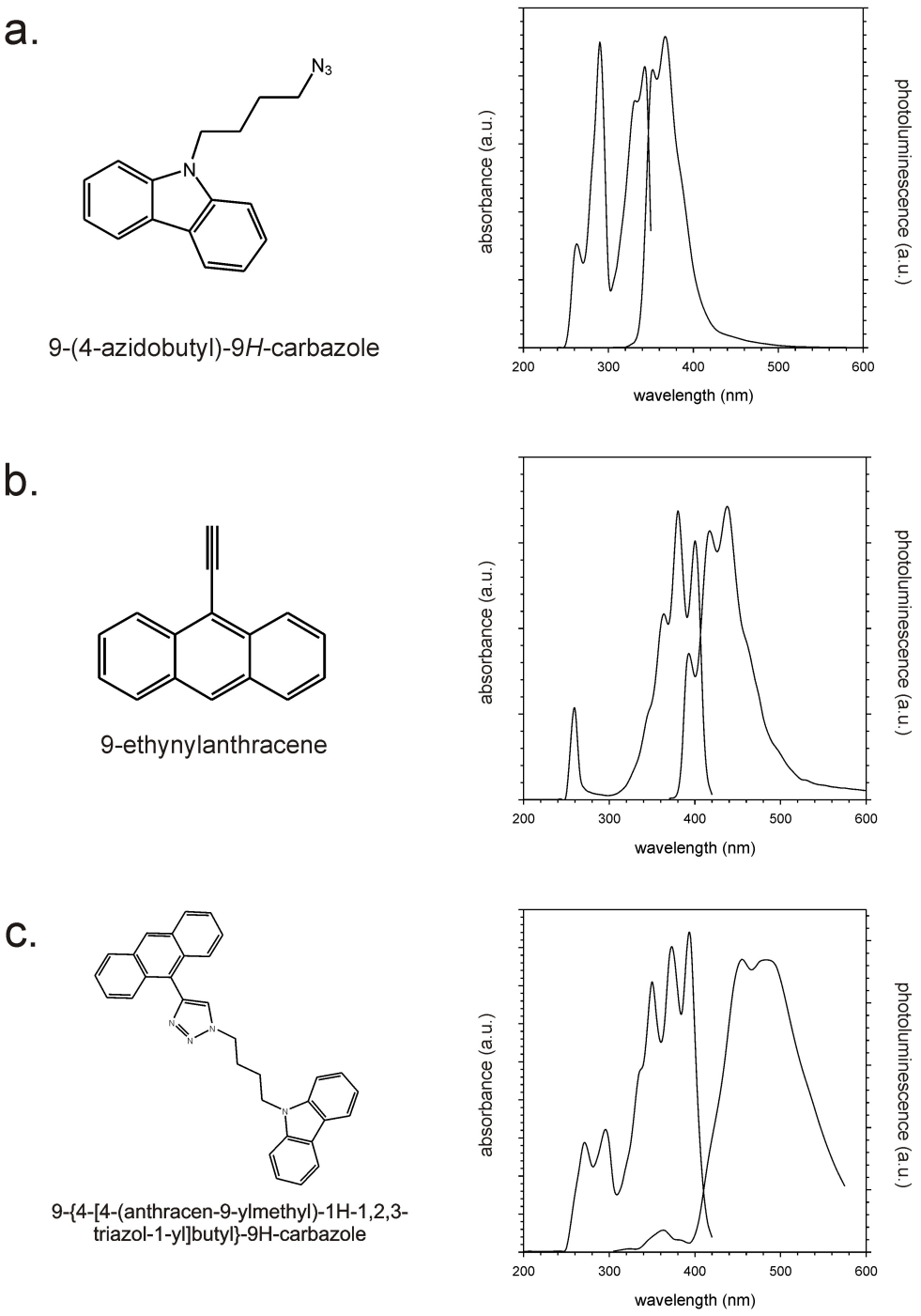

Figure 2.10: Absorbance and photoluminescence spectra of (a) azide-modified carbazole (ABC) ($\lambda_{ex} = 295$ nm), (b) alkyne-modified anthracene (EA) ($\lambda_{ex} = 360$ nm), and (c) carbazole/anthracene FRET dyad (ATBC)($\lambda_{ex} = 295$ nm). All samples in 90:10 water:DMSO solution.

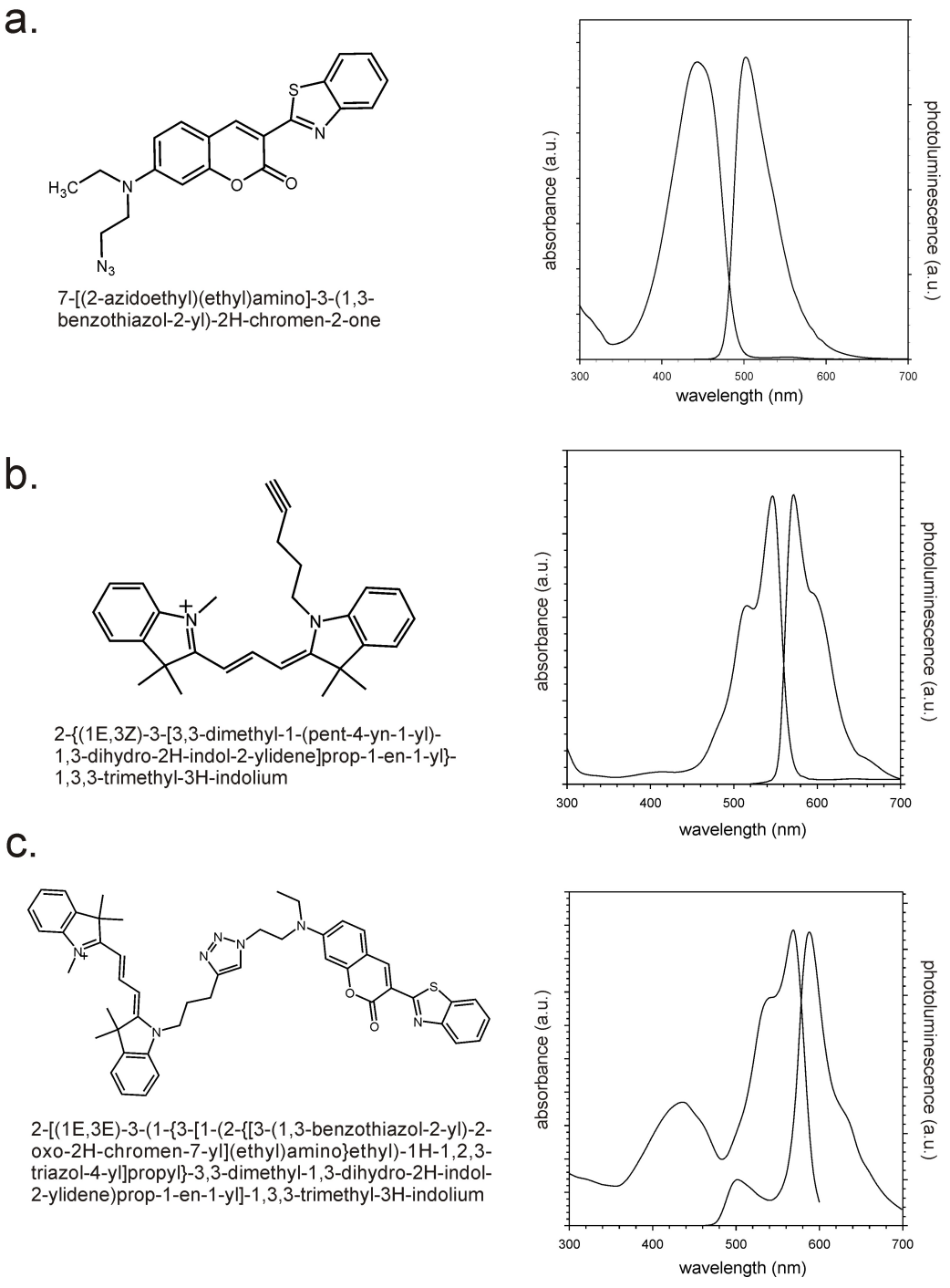

Figure 2.11: Absorbance and photoluminescence spectra of (a) azide-modified coumarin (C6) (λ_{ex} = 425 nm), (b) alkyne-modified cyanine (Cy3) (λ_{ex} = 550 nm), and (c) coumarin/Cy3 FRET dyad (λ_{ex} = 425 nm). All samples in 90:10 water:DMSO solution.

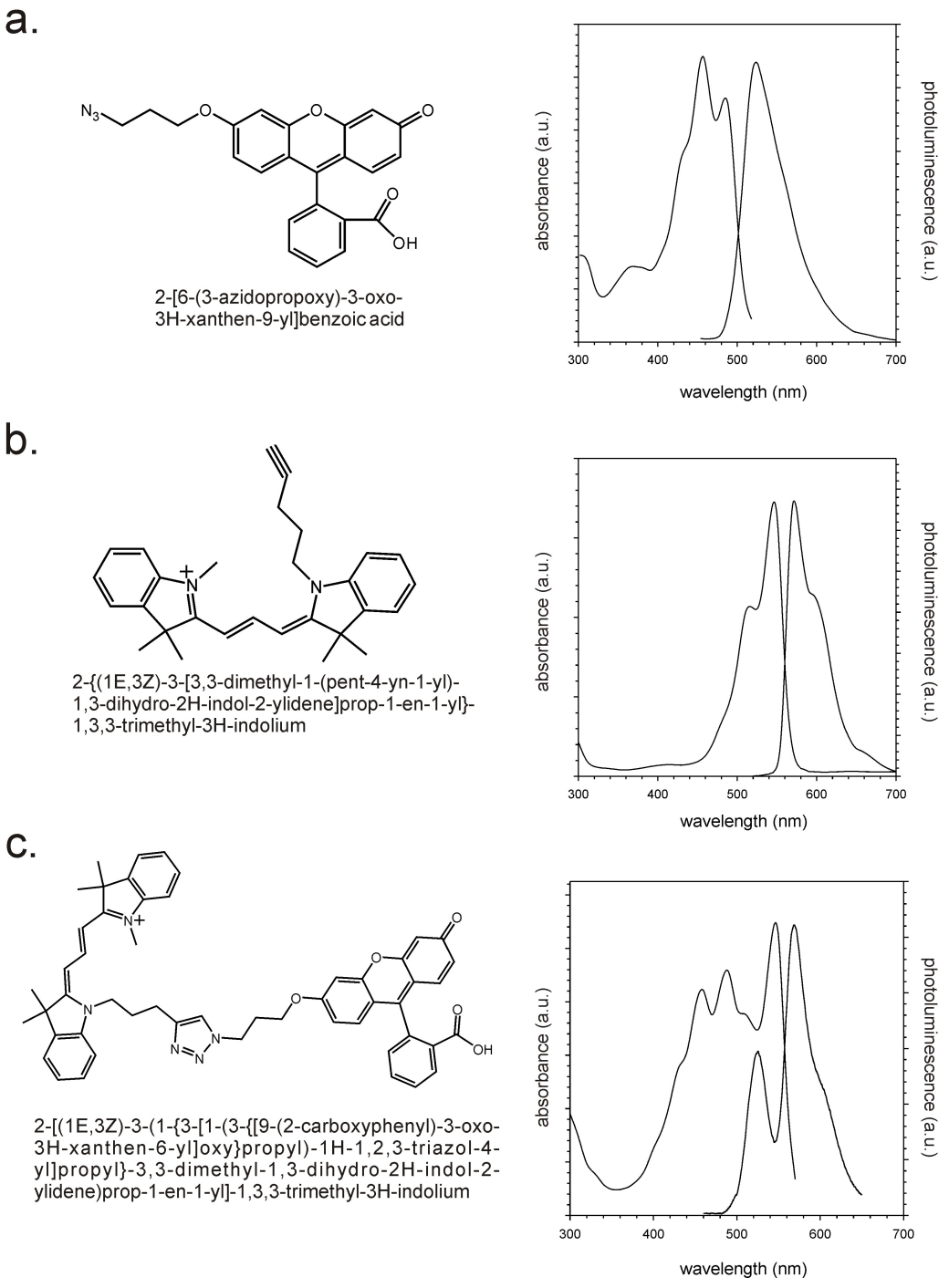

Figure 2.12: Absorbance and photoluminescence spectra of (a) azide-modified fluorescein (Fl) (λ_{ex} = 425 nm), (b) alkyne-modified cyanine (Cy3) (λ_{ex} = 550 nm), and (c) Fl/Cy3 FRET dyad (λ_{ex} = 425 nm). All samples in 90:10 water:DMSO solution.

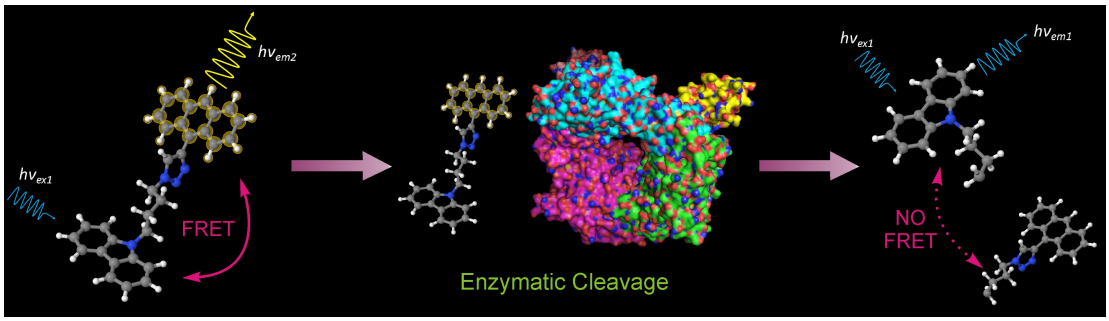

Figure 2.13: Schematic of the biotransformation of 9-4-[4-(9-anthryl)-1H-1,2,3-triazol-1-yl]butyl-9H-carbazole (ATBC), a coupled donor and acceptor pair, with exposure to the lysate of *P. resinovorans* CA10. FRET between moieties of ATBC is interrupted by enzymatic breakdown of ATBC by carbazole 1,9a-dioxygenase.

the processes that generate the metabolome provides insights into the biochemical diversity of cell populations. To achieve this level of understanding requires a method for single-cell metabolomic studies.[99] To this end, a donor/acceptor pair were covalently linked and their FRET characteristics employed in the detection of a metabolic transformation. Enzymes are traditionally considered remarkably specific catalysts; nonetheless, promiscuity is the inherent ability of an enzyme to catalyze multiple reactions. Recent experimental evidence suggests that promiscuity, in the actual protein function, is not as rare or detrimental as was previously thought [100–102]. Promiscuous activity, substrate ambiguity and cross reactivity, in an existing protein can cause a selective advantage, resulting in survival and further evolution; thus, gene duplication would drive the divergent evolution of a new protein.[103–107] Studies on enzyme evolvability have given convincing evidence that the mechanism of functional evolution is due to the fact that many proteins have promiscuous functions in addition to their native functions. In the proposed mechanism, a weak promiscuous function arises due to neutral evolution, the ability of proteins to tolerate mutations without compromising fitness and plasticity. Under the right selection pressure, natural selection can improve the new function once it has arisen until, at some point, the protein

may become specialized for the new function.[105, 106, 108–111] In many cases, the pairing of native and promiscuous function is smaller than expected. This allows for several generations of "generalist" proteins that are able to perform both functions and suggests that gene duplication acts after the new function has appeared.[103, 112] These "generalist" proteins lead to the promiscuous enzymes capable of degrading multiple primary metabolites through different pathways.

Specifically, *Pseudomonas spp.* are the most predominant group of soil microorganisms that degrade carbazole[113] and were utilized in this effort. Differing species of carbazole degraders all appear to follow a similar carbazole degradation pathway that begins with the oxidative cleavage of the heterocyclic nitrogen ring of carbazole, catalyzed by carbazole 1,9a-dioxygenase (CARDO); subsequent breakdown of carbazole requires the degradation of one of the aromatic rings, meaning *Pseudomonas spp.* also produces a *meta*-cleavage enzyme, 2-aminobiphenyl-2,3-diol-1,2-dioxygenase.[113] Previous studies indicate that CARDO can catalyze diverse oxygenation reactions and has a broad substrate range including polyaromatic compounds, such as dibenzothiophene, biphenyl, and polycyclic aromatic hydrocarbons and is attributed to flexibility in binding of the substrates to the active site of CARDO.

The focus of this study was to modulate the Förster energy transfer of coupled fluorophores through their biotransformation (Figure 3.1).

Specifically, an alkyne-functionalized anthracene and azide-functionalized carbazole derivative were employed as the donor/acceptor pair and linked through a copper-catalyzed azide/alkyne cycloaddition ("click" transformation) performed in a water:isopropanol (5:4) mixture.[2] CARDO catalyzes the angular dioxygenation of carbazole to yield an unstable dihydroxylated intermediate which is considered to be instantly converted to 2'-aminobiphenyl-2,3-diol, while CARDO transforms

anthracene into cis-1,2-dihydroxy-1,2-dihydroanthracene[113]. Figure 2.14 presents the photoluminescence (PL) spectra and structures employed in this effort. Specifically, Figure 2.14a presents the emission characteristics of both 9-(4-azidobutyl)-9H-carbazole (ABC) and 9-ethynylanthracene (EA) in a water:DMSO (90:10) mixture. The carbazole containing moiety (ABC) exhibits an emission that is characteristic of 9*H*-carbazole containing compounds with two major peaks at 351 nm and 363 nm and a shoulder at ≈380 nm.[114] Similarly, the anthracene containing moiety (EA) indicates vibronic bands in the region 410 - 500 nm typically seen with this chromophore when excited at 360 nm.[115] In contrast to these isolated chromophores, Figure 2.14b presents the emission characteristics under various excitation energies of the resulting molecule when ABC and EA have undergone a click transformation to form 9-4-[4-(9-anthryl)-1*H*-1,2,3-triazol-1-yl]butyl-9*H*-carbazole (ATBC). With an excitation energy at a wavelength of 295 nm, there is only a small emission contribution attributed to the carbazole moiety, while with an excitation at 360 nm, all contributions of the carbazole are absent. Nonetheless, at both excitation energies, the emission of the linked carbazole/anthracene molecule is similar and reminiscent of an aggregated anthracene.[115] The lack of a significant carbazole signature in the linked moiety with an excitation of 295 nm is indicative of energy transfer from the carbazole to anthracene.

For the current system, the Förster radius was calculated to be ≈ 19 Å, while a similar system composed of 9-phenyl carbazole and 9-cyano anthracene fabricated into Langmuir-Blodgett films with interlayers of stearic acid indicated a Förster radius of 12.5 Å[116].The calculated Förster radius is comparable to the ≈13 Å maximum separation distance of the linked chromophores in ATBC. A molecular dynamics simulation of ATBC was performed *in vacuo* utilizing the MM2 force field and indicated that the most probable conformations for ATBC at room temperature result in a

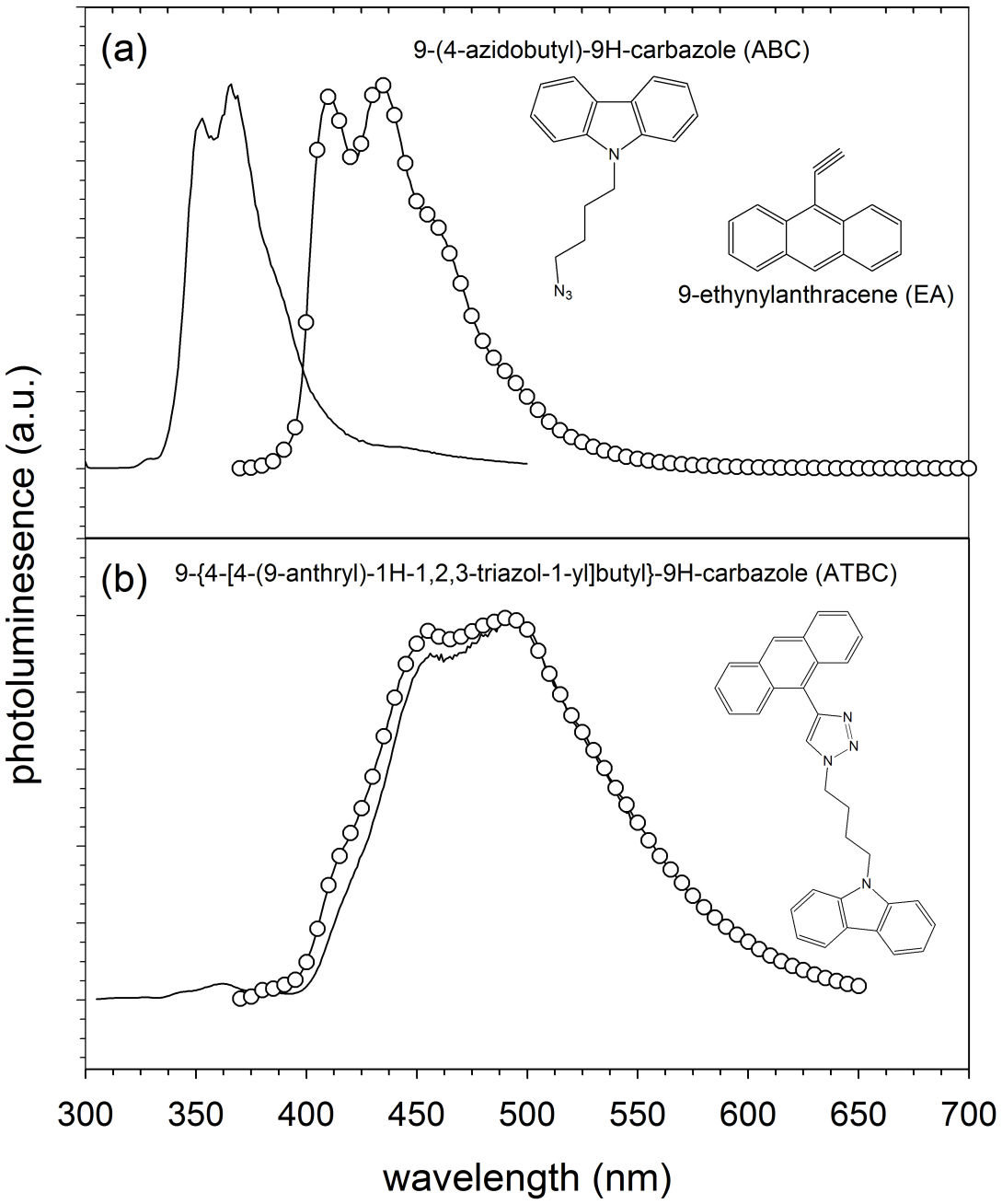

Figure 2.14: Photoluminescence of (a) 9-(4-azidobutyl)-9H-carbazole (ABC) (—) (λ_{ex} = 295 nm) and 9-ethynylanthracene (EA) (◯) (λ_{ex} = 360 nm); (b) 9-4-[4-(9-anthryl)-1*H*-1,2,3-triazol-1-yl]butyl-9*H*-carbazole (ATBC) with λ_{ex} = 295 nm (—) and λ_{ex} = 360 nm (◯). All samples in 90:10 water:DMSO solution.

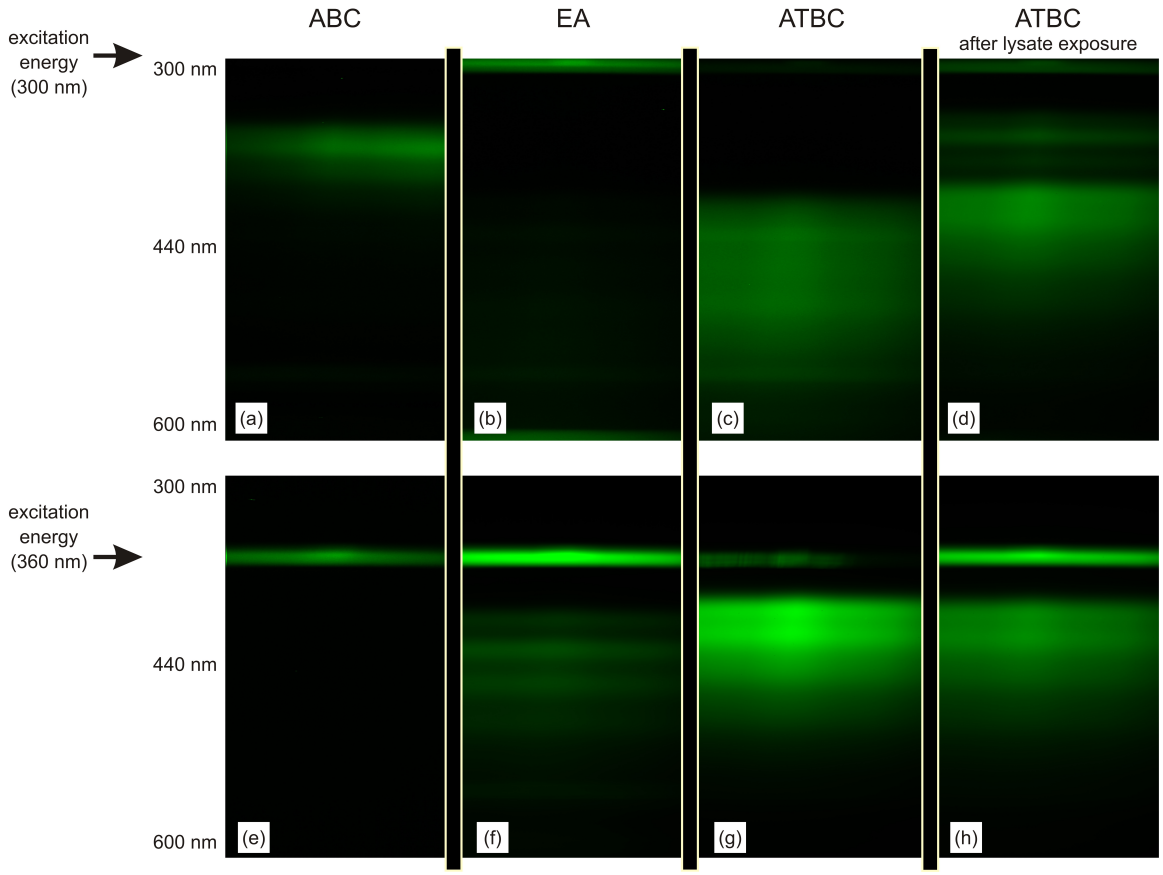

Figure 2.15: Spectral photoluminescence images of neat (a,e) ABC, (b,f) EA, (c,g) ATBC and (d,h) ATBC after exposure to the lysate of *Pseudomonas resinovorans* CA10. Upper band of images (a-d) corresponds to an excitation at a wavelength of 300 nm, while the lower band (e-h) corresponds to 360 nm.

slightly folded back configuration that puts the anthracene and carbazole ring centers within a separation distance 5 - 8 Å, indicating that energy transfer from carbazole to anthracene should dominate at this temperature. A serial dilution of ATBC was also performed which indicated the concentrations of ATBC used in this study were sufficiently dilute that the observed PL spectra was due to individual chromophores, *i.e.* PL at $\lambda_{ex} = 295$ nm and $\lambda_{ex} = 360$ nm. The normalized serial dilution spectra are provided in Fig. 2.17.

Figure 2.15 presents the PL spectral image at differing excitation energies of the initial compounds and the variation in emission of ATBC with exposure to the lysate of *Pseudomonas resinovorans* CA10. As was indicated previously (Figure 2.14), ABC and EA emit at differing excitation wavelengths, 295 nm and 360 nm, respectively (Figures 2.15a,b,e,f). Initially, the PL spectrum of ATBC exhibits no signature from the carbazole moiety by the absence of any appreciable emission between 340 nm and 400 nm with either excitation energy in Figure 2.15c,g, but with the introduction of the lysate, the characteristic PL signature of the carbazole moiety re-emerges as a high energy band in Figure 2.15d. As a simple diagnostic tool, the reappearance of this band in the PL image is a clear indication that some of the coupled chromophores have been separated. This was confirmed in Figure 2.16a which presents the spectral characteristics of this emission and indicates a carbazole emission coupled with a shoulder at ≈ 420 nm and an enhancement of emission intensity of the peak at ≈ 440 nm. These latter changes are suggestive of the reemergence of the isolated anthracene emission being coupled to the ATBC emission, likely due to the separation of linked carbazole and anthracene moieties with the lysate degradation of the triazole linking unit.

The solution utilized in Figures 2.15 and 2.16a includes both the reactants (proteins and ATBC) and products (residues of ABC and EA) of the enzymatic

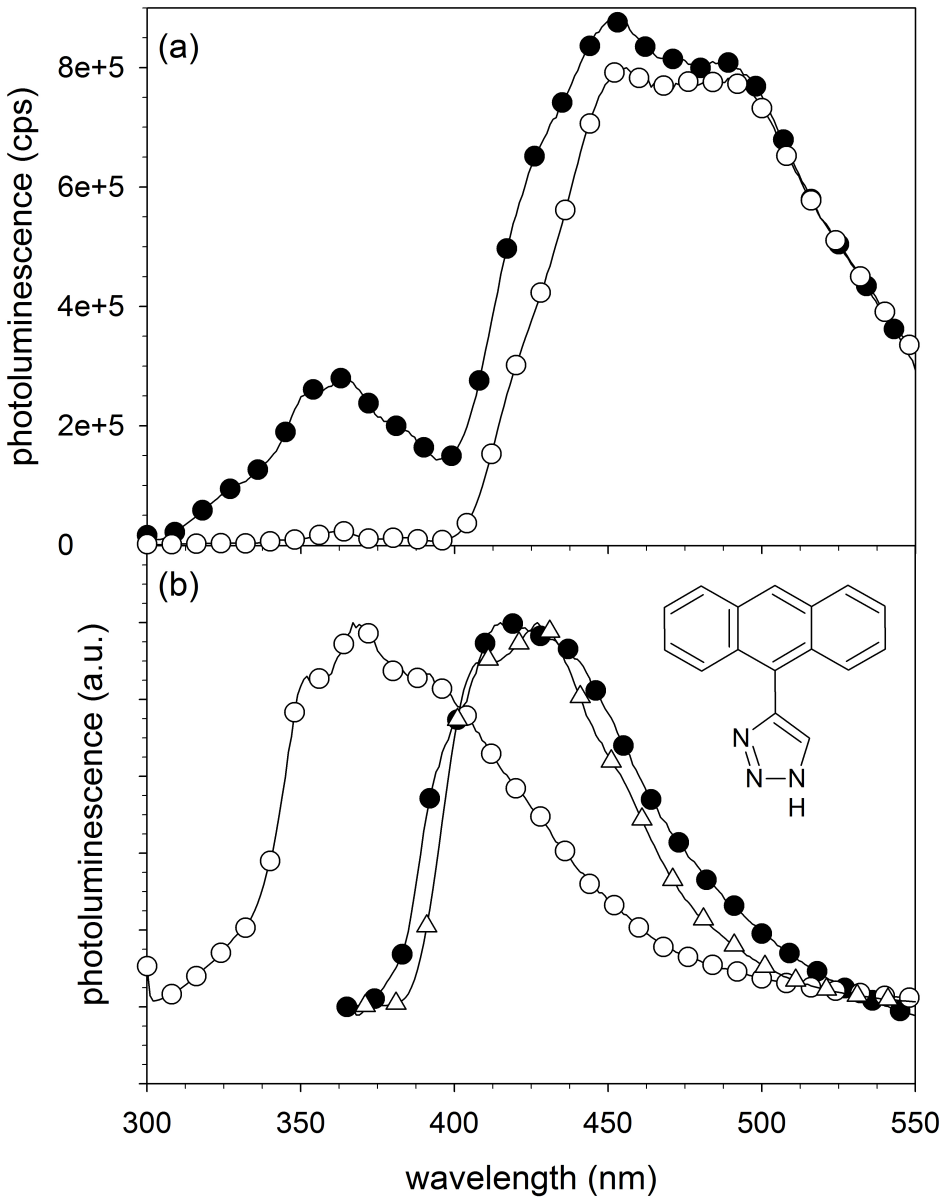

Figure 2.16: Photoluminescence of (a) ATBC (λ_{ex} = 295 nm) initially (◯) and after a one hour exposure to lysate (•) in 90:10 Tris-HCl aqueous buffer (50mM) : DMSO and of (b) supernatant (product residues) with excitation of λ_{ex} = 295 nm (◯) & λ_{ex} = 360 nm (•) and 4-(9-anthryl)-1*H*-1,2,3-triazole (structure in inset) with excitation of λ_{ex} = 360 nm (△). Samples in DMSO.

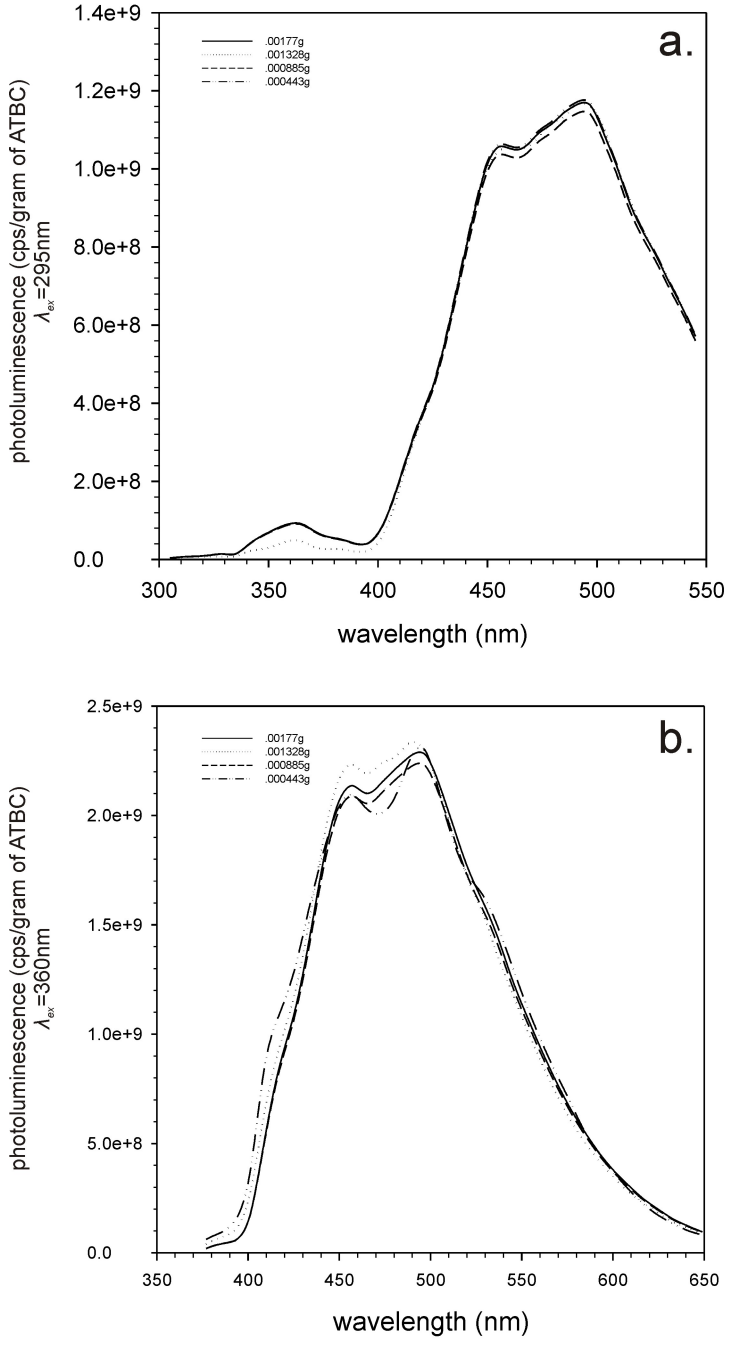

Figure 2.17: Normalized serial dilution photoluminescence spectra of ATBC at (a) $\lambda_{ex} = 295$ nm and (b) $\lambda_{ex} = 360$ nm which indicated the concentrations of ATBC used in this study were sufficiently dilute that the observed PL spectra was due to individual chromophores.

degradation and was centrifuged and redispersed multiple times in an attempt to isolate moieties. The PL spectrum of the supernatant produced in this cleaning process is presented in Figure 2.16b under various excitation energies. The use of 295 nm and 360 nm excitation wavelength was an attempt to isolate the contributions from the various chromophores that may be present in the solution after the enzymatic degradation of ATBC. With an excitation at 295, it is apparent that the supernatant incorporates a significant quantity of a carbazole containing residue by the appearance of the signature 9*H*-carbazole PL emission, with peaks at 351 nm and 366 nm. In addition, in Figure 2.16b, the carbazole PL emission has a small shoulder at 393 nm, a peak attributed to the anthracene moiety. With an excitation wavelength of 360 nm, the PL characteristics of the supernatant exhibit characteristics of ATBC as well as an aggregated anthracene. For comparison, in Figure 2.16b, the PL spectra of 4-(9-anthryl)-1*H*-1,2,3-triazole (AT) is presented. This compound serves as a reference acceptor assuming that the carbazole moiety was cleaved from ATBC in the biotransformation. This reference acceptor and supernatant have closely matched PL characteristics when excited at 360 nm. The separated reaction products were also subject to mass spectroscopy analysis. ATBC incubated with *P. resinovorans* CA10 lysate and resultant metabolites were extracted from the incubation medium and products were identified by comparing mass peaks with those of pure ATBC, ABC and EA. The former showed significant fragments at m/z 167, 205, and 200. These metabolites can be tentatively identified as 9-H carbazole, EA, and ATBC fragment respectively. A comparative plot of mass spectra is provided in Figure 2.18. Results verified the biotransformation of ATBC by *P. resinovorans CA10*; however, there was no overt preference indicated for the degradation of either ABC or EA moieties.

In order to further identify the contributing components to the PL signatures in Figure 2.16, the photoluminescence excitation (PLE) at various emission wave-

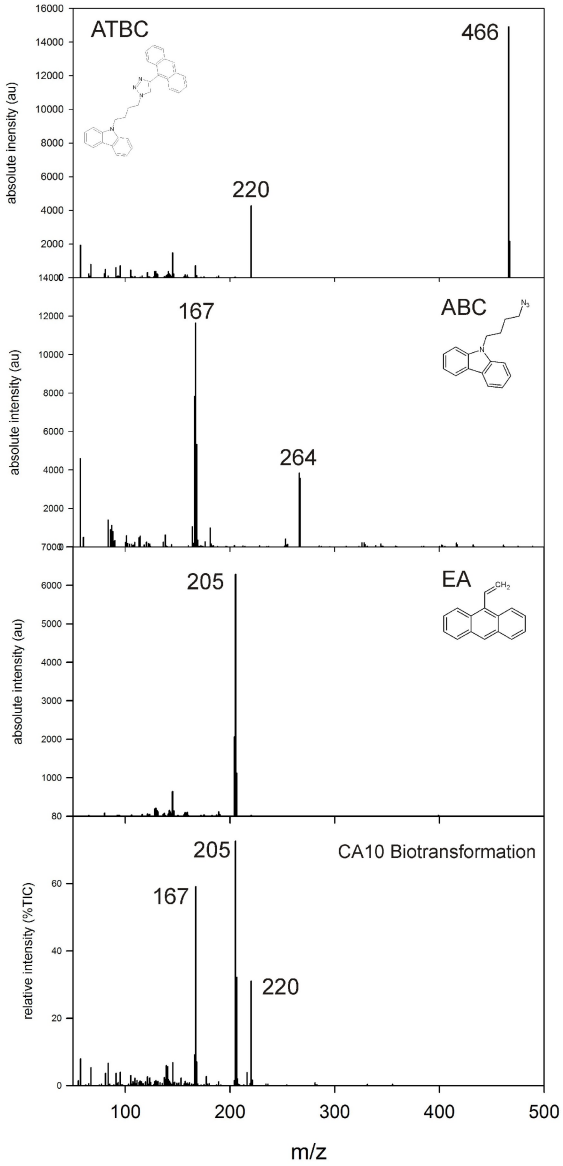

Figure 2.18: Mass spectroscopy comparison for donor-acceptor system (ATBC), paired moieties (ABC, EA) and biotransformation residues of ATBC (CA10 Biotransformation).

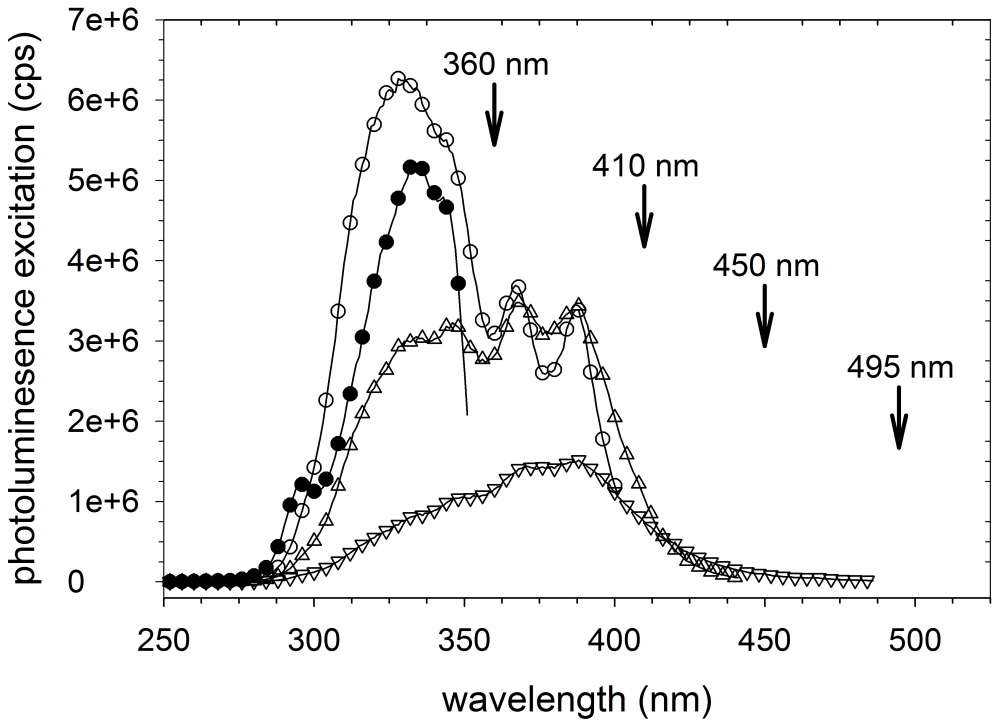

Figure 2.19: Photoluminescence excitation of supernatant with emission at λ_{em} = 360 nm (•), λ_{em} = 410 nm (◯), λ_{em} = 450 nm (△), and λ_{em} = 495 nm (▽). All samples in 90:10 Tris-HCl aqueous buffer (50mM) : DMSO.

lengths was studied and is presented in Figure 2.19. Setting the emission wavelength to 360 nm results in an excitation profile, as expected, that is indicative of the absorbance spectrum of carbazole with two main peaks centered at $\approx$ 332 and 343 nm. Raising the emission wavelength to 410 nm results in a enhanced contribution from residues containing the carbazole moiety, as well as residues that incorporate an anthracene fluorophore. The anthracene signature, as indicated by the two peaks at 381 nm and 403 nm, is significantly less than the contribution from carbazole containing residues, which occurs at wavelengths under 360 nm. This indicates that the emission at 410 nm can be efficiently achieved by exciting the carbazole moiety and transferring energy over to the anthracene moiety, suggesting that the supernatant has a mixture of residues that incorporate ABC and EA, as well as ATBC. Increasing the emission wavelength to 450 nm is sufficient to remove contributions that are directly attributed to the carbazole moiety, though this wavelength is in the middle of the emission spectrum for both EA and ATBC. Nonetheless, the PLE spectrum at this emission wavelength indicates a contribution from the carbazole fluorophore, suggesting that either the supernatant contains (1) ATBC and/or (2) carbazole and anthracene flourophores that are not chemically linked but spatially within the Förster radius for energy transfer. Extending the emission wavelength to 495 nm verifies that the the supernatant must contain ATBC since this fluorophore would be the dominating emitter at this wavelength.

2.3 Conclusions

In summary, a simple diagnostic tool was presented that employed a coupled donor/acceptor pair that was formed through a click transformation. The FRET pair exhibited a significant variation in PL response with exposure to the lysate of

Pseudomonas resinovorans CA10, an organism which can degrade variants of both the donor and acceptor fluorophores. This general approach can be tailored for a range of metabolic processes and be employed as a method for single-cell metabolomic studies.

2.4 Experimental Details

2.4.1 Synthesis of "clickable" fluorophores and FRET dyads

2.4.1.1 Synthetic scheme for synthesis of ATBC

Compounds (1) and (5) were synthesized according to published methods.[117, 118]

2.4.1.2 4-(9H-carbazol-9-yl)butyl methanesulfonate (2)

To a cooled solution of 4-(9H-carbazol-9-yl)butan-1-ol (1) (3.0 g, 12.5 mmol) and triethylamine (2.53 g, 25.0 mmol) in dichloromethane (30 ml) was added dropwise to the solution of methanesulfonyl chloride (2.01 g, 17.6 mmol) in dichloromethane (2 ml). The solution was stirred for 8 hours at room temperature and then washed with water. The organic layer was separated, dried with Na_2SO_4 and then filtered. The solvent was removed under reduced pressure to give a clear-brown oil (3.3 g). Yield 83%. This product was used in the next step without further purification. ^{1}H NMR ($CDCl_3$) δ 1.76 (m, 2H, $^3J_{HH}$=6.3 Hz), 2.00 (m, 2H, $^3J_{HH}$=6.8 Hz), 2.88 (s, 3H), 4.13 (t, 2H, $^3J_{HH}$=6.3 Hz), 4.36 (t, 2H, $^3J_{HH}$=6.8 Hz), 7.22-7.28 (m, 2H, $^3J_{HH}$=7.9 Hz), 7.37-7.51 (m, 4H), 8.12 (d, 2H, $^3J_{HH}$=7.9 Hz).

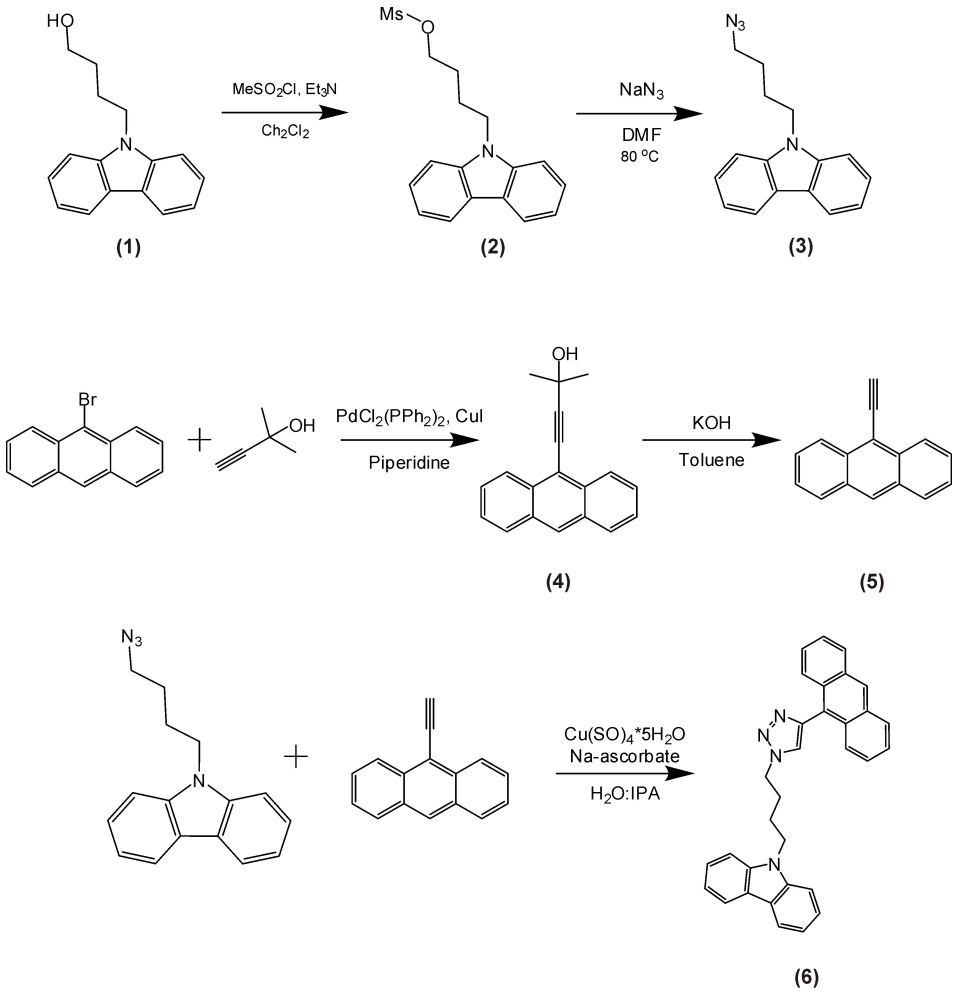

Figure 2.20: Reaction scheme for synthesis of ATBC and starting compounds.

2.4.1.3 9-(4-azidobutyl)-9H-carbazole (3)

A mixture of 3-(9H-carbazol-9-yl)butyl methanesulfonate (2) (3.3 g, 10.4 mmol) and sodium azide (1.35 g, 20.8 mmol) in dimethylformamide (10 ml) was heated and stirred at 80 °C for 7 hours. After cooling, the mixture was quenched with water and extracted with dichloromethane. The organic solution was washed with water, dried with Na_2SO_4, filtered and filtrate was evaporated under vacuum to give a red-brown oil. After purification by flash column chromatography (silicagel, hex-

ane : dichloromethane 9:1, R_f=0.2) was obtained 1.8 g of clear oil. Yield 65%. ^{1}H NMR ($CDCl_3$) δ 1.65 (m, 2H), 1.98 (m, 2H), 3.27 (t, 2H, $^3J_{HH}$=6.9 Hz), 4.36 (t, 2H, $^3J_{HH}$=7.2 Hz), 7.21-7.27 (m, 2H, $^3J_{HH}$=7.9 Hz), 7.38-7.51 (m, 4H), 8.10 (d, 2H, $^3J_{HH}$=7.9 Hz). ^{13}C NMR ($CDCl_3$) δ 26.44, 26.86, 42.56, 51.32, 108.65, 119.08, 120.57, 123.01, 125.85, 140.41. EI-Mass (m/z; rel. intensity %): 265 (M^++1; 5), 264 (M^+; 25), 193 (90), 180 (100), 167 (46), 152 (48), 139 (11).

2.4.1.4 4-(anthracen-10-yl)-2-methylbut-3-yn-2-ol (4)

9-Bromoanthracene (2 g, 7.8 mmol), 2-methyl-but-3-yn-2-ol (1.3 g, 15.6 mmol), $Pd(PPh_3)_2Cl_2$ (55 mg, 0.078 mmol), PPh3 (20 mg, 0.076 mmol) and CuI (15 mg, 0.079 mmol) were dissolved in piperidine (20 ml). This mixture was refluxed for 24 h under N_2 atmosphere, then cooled to room temperature. The residue was extracted with dichloromethane and washed with water. Organic layer was separated and dried with Na_2SO_4, filtered and evaporated. The crude product was purified by flash column chromatography (silicagel, hexane : dichloromethane 1:2, R_f=0.4) to give 1.32 g of yellow solid, m.p. 116-117 °C. Yield 65%. ^{1}H NMR ($CDCl_3$) δ 1.85 (s, 6H), 2.26 (s, 1H), 7.47-7.60 (m, 4H, $^3J_{HH}$=8.5 Hz, $^3J_{HH}$=6.6 Hz $^4J_{HH}$=1.4 Hz, $^4J_{HH}$=1.7 Hz), 8.00 (d.m, 2H, $^3J_{HH}$=8.5 Hz), 8.42 (s, 1H), 8.50 (d.m, 2H, $^3J_{HH}$=8.5 Hz).

2.4.1.5 9-4-[4-(9-anthryl)-1*H*-1,2,3-triazol-1-yl]butyl-9*H*-carbazole (6)

Compound (3) (157 mg, 0.59 mmol) and compound (5) (120 mg, 0.59 mmol) were dissolved in mixture of isopropanol (5 ml) and water (3 ml). A water solution (0.5 ml) of $CuSO_4$*$5H_2O$ (8 mg, 0.03 mmol) was added to this solution under N_2 atmosphere. After 5 min of stirring at room temperature sodium L-ascorbate (20 mg, 0.1 mmol) in water (0.5 ml) was added to the reaction. Obtained mixture was stirred at 50 °C for 17 h. After cooling to the room temperature, the mixture was extracted

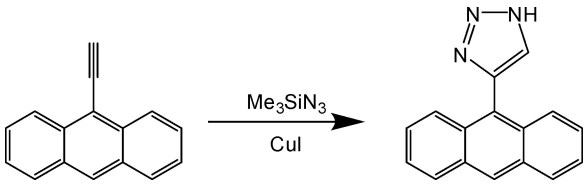

Figure 2.21: Reaction scheme for synthesis of proposed metabolite residue 4-(9-anthryl)-1*H*-1,2,3-triazole.

with dichloromethane and washed with water. Organic layer was separated and dried with Na_2SO_4, then filtered and evaporated. The residue was crystallized with diethyl ether, filtered and dried to give 147 mg of white solid, m.p. 182-183 °C. Yield 53%. ^{1}H NMR (DMSO-d6) δ 1.85 (m, 2H), 2.08 (m, 2H), 4.52 (t, 2H, $^3J_{HH}$=7.0 Hz), 4.62 (t, 2H, $^3J_{HH}$=6.8 Hz), 7.2 (m, 2H, $^3J_{HH}$=7.2 Hz), 7.36-7.47 (m, 4H, $^3J_{HH}$=7.2 Hz, $^3J_{HH}$=8.3 Hz), 7.54 (m, 2H, $^3J_{HH}$=7.2 Hz), 7.66 (m, 4H, ^{3}JHH=7.2 Hz, $^3J_{HH}$=8.3 Hz), 8.15 (m, $^3J_{HH}$=7.2 Hz, $^3J_{HH}$=8.3 Hz), 8.45 (s, 1H), 8.73 (s, 1H). ^{13}C NMR ($CDCl_3$) δ 26.1, 28.2, 42.4, 50.1, 108.6, 119.2, 120.6, 123.0, 124.5, 124.7, 125.3, 125.9, 126.0, 126.2, 128.4, 128.6, 131.3, 131.4, 140.6 EI-Mass (LC/MS) (m/z; rel. intensity): 267.27 (M^++1; 100), 222.27 (80), 180.20 (28).

2.4.1.6 4-(9-anthryl)-1*H*-1,2,3-triazole

4-(9-anthryl)-1*H*-1,2,3-triazole was obtained from 9-ethynyl-anthracene (5) and $TMSN_3$ according to the literature.[3] The product was purified on column with silicagel, CH_2Cl_2, then MethOH. R_f=0.1 in CH_2Cl_2. m.p. 243-244 °C. Yield 59%. ^{1}H NMR (DMSO-d6) δ 7.47-7.58 (m, 4H, $^3J_{HH}$=8.3 Hz), 7.66 (m, 2H), 8.17 (d, 2H, $^3J_{HH}$=8.3 Hz), 8.76 (s, 1H). ^{13}C NMR (DMSO-d6) δ 125.5, 126.4, 128.5, 130.6, 130.8 EI-Mass (ESI) (m/z; rel. intensity %): 246.27 (M^++1; 100), 215.33 (9).

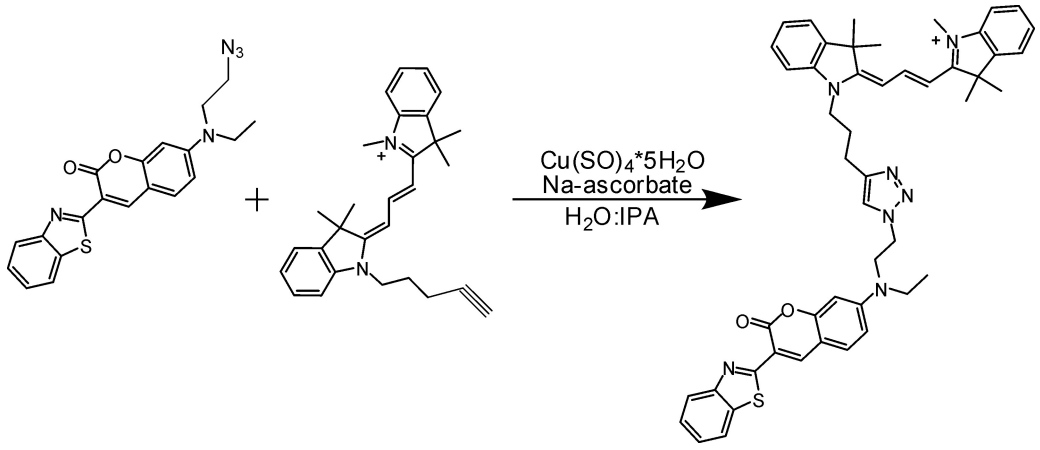

Figure 2.22: Reaction scheme for synthesis of C6Cy3.

2.4.1.7 Synthetic scheme for synthesis of C6Cy3 and starting compounds

2.4.1.8 1,2,3,3-Tetramethyl-3H-indolium iodide (1)

2,3,3-Trimethyl-3H-indole (0.5 g, 3.14 mmol) and iodomethane (1.34 g, 9.42 mmol) were dissolved in acetonitrile (5 ml) and refluxed for 5 hours. After cooling, the precipitated solid was filtered and washed with acetone then dried to give white crystalline product (940 mg). Yield 99%. ^{1}H NMR (DMSO-d6) δ 1.53 (s, 6H), 2.76 (s, 3H), 3.97 (s, 3H), 7.60-7.64 (m, 2H), 7.81-7.84 (m, 1H), 7.90-7.93 (m, 1H).

2.4.1.9 1-(3-Azido-propyl)-2,3,3-trimethyl-3H-indolium iodide (2)

2,3,3-Trimethyl-3H-indole (1 g, 6.28 mmol) and 1-azido-3-iodo-propane (2 g, 9.48 mmol) were dissolved in acetonitrile (10 ml) and refluxed for 14 hours. Solvent was evaporated and the residue was dissolved in dichloromethane (4 ml), obtained solution was added drop-wise to the stirred diethyl ether solution. Precipitated dark solid was separated and the same purification was done one more time. Obtained hygroscopic solid was dried under reduced pressure to give 1.85 g of product. Yield

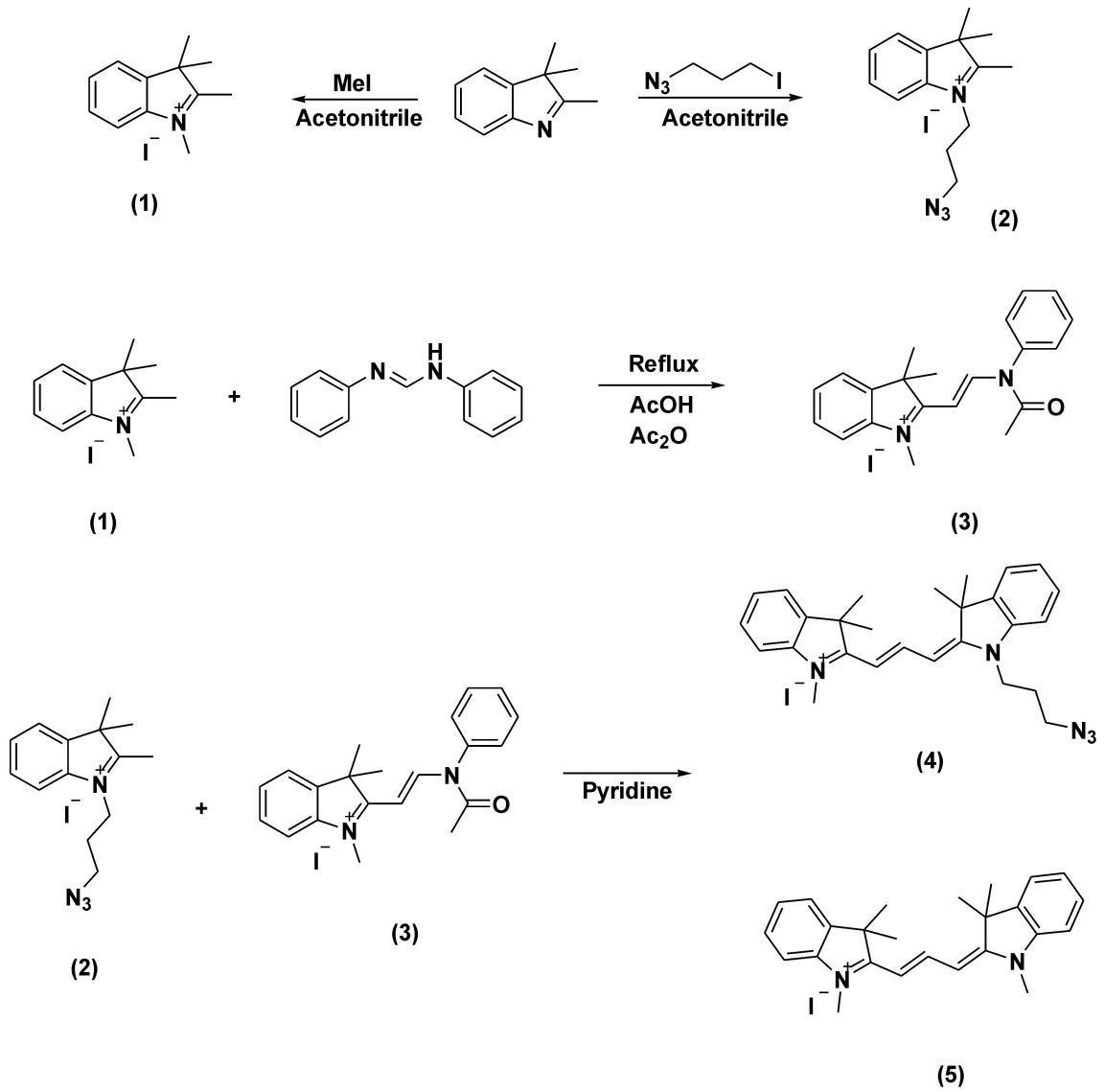

Figure 2.23: Reaction scheme for synthesis of Cy3 and starting compounds.

80%. ^{1}H NMR ($CDCl_3$) δ 1.65 (s, 6H), 2.32 (m, 2H, $^{3}J_{HH}$=5.7 Hz, $^{3}J_{HH}$=7.2 Hz), 3.19 (s, 3H), 3.73 (t, 2H, $^{3}J_{HH}$=5.7 Hz), 4.91 (t, 2H, $^{3}J_{HH}$=7.2 Hz), 7.54-7.62 (m, 3H), 7.83-7.86 (m, 1H).

2.4.1.10 2-[2-(Acetyl-phenyl-amino)-vinyl]-1,3,3-trimethyl-3H-indolium iodide (3)

1,2,3,3-Tetramethyl-3H-indolium iodide (1) (0.65 g, 2.16 mmol) and N,N'-diphenyl-formamidine (0.51 g, 2.60 mmol) were mixed with acetic acid (8 ml) and acetic anhydride (4 ml). Obtained mixture was refluxed and stirred for 1 hour. After cooling, the solvent was evaporated, the residue was dissolved in dichloromethane (2 ml) and added to diethyl ether solution. Precipitated dark solid was separated by centrifugation. This crude product was dissolved in dichloromethane and washed with water. Organic layer was separated and evaporated, obtained residue was dissolved in dichloromethane and precipitated with diethyl ether once again. The dark-brown solid was filtered and dried to give 0.87 g of product. Yield 90%. ^{1}H NMR ($CDCl_3$) δ 1.83 (s, 6H), 2.11 (s, 3H), 3.85 (s, 3H), 5.59 (d, 1H, ^{3}JHH=14.3 Hz), 7.46-7.50 (m, 4H, $^{3}J_{HH}$=5.2 Hz, $^{4}J_{HH}$=1.4 Hz), 7.53-7.55 (m, 2H, $^{3}J_{HH}$=5.2 Hz, $^{4}J_{HH}$=1.4 Hz), 7.63-7.73 (m, 3H, $^{3}J_{HH}$=7.4 Hz, $^{4}J_{HH}$=1.4 Hz), 9.17 (d, 1H, $^{3}J_{HH}$=14.3 Hz).

2.4.1.11 2-3-[1-(3-Azido-propyl)-3,3-dimethyl-1,3-dihydro-indol-2-ylidene]-propenyl-1,3,3-trimethyl-3H-indolium iodide (4), (5)

Compound (2) (0.16 g, 0.43 mmol) and compound (3) (0.175 g, 0.39 mmol) were dissolved in pyridine (4 ml) and stirred at 50 °C for 2.5 hours. After cooling, the solution was extracted with dichloromethane and washed with water. Organic layer was separated and solvent was evaporated under reduced pressure. Obtained dark-red residue was dissolved in minimum of dichloromethane (1 ml) and added

drop-wise to diethyl ether solution to precipitate a brown solid, which was separated by centrifugation. Separated solid was purified by precipitation from ether once again. Obtained brown solid (0.12 g) is the mix of compounds (4) and (5) with ratio 2:1 correspondingly. This mix is id difficult to separate by column chromatography because two compounds have very similar structure and usually go together on silica gel. Obtained mixture was used for the next click reactions without further purification. ^{1}H NMR ($CDCl_3$) δ 1.70 (s, 12H), 2.16 (m, 2H, $^{3}J_{HH}$=6.0 Hz), 3.81 (s, 3H), 3.81 (t, 2H, $3J_{HH}$=6.0 Hz), 4.36 (t, 2H, $^{3}J_{HH}$=7.7 Hz), 7.13 (d, 1H, $^{3}J_{HH}$=7.7 Hz), 7.22-7.27 (m, 3H), 7.34-7.43 (m, 4H), 7.53-7.58 (d.d, 2H, $^{3}J_{HH}$=13.4 Hz, $^{4}J_{HH}$=3.2 Hz), 8.44 (t, 1H, $3J_{HH}$=13.4 Hz). ^{13}C NMR ($CDCl_3$) δ 26.93, 28.20, 28.29, 32.88, 42.22, 48.89, 48.92, 48.95, 104.90, 105.58, 110.89, 110.97, 122.14, 122.24, 125.38, 125.52, 129.01, 129.13, 140.55, 140.64, 142.10, 142.77, 151.03, 173.59, 174.48. EI-Mass (ESI) (m/z; rel. intensity %): 426.33 (M^{+} +1; 68), 277.33 (100).

2.4.1.12 Synthetic scheme for synthesis of FlCy3

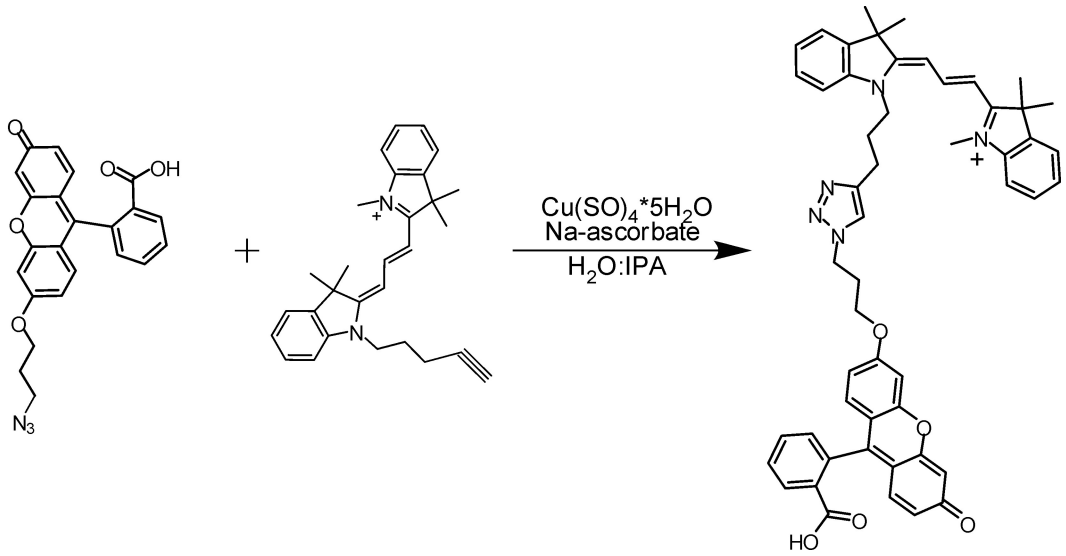

Figure 2.24: Reaction scheme for synthesis of FlCy3.

2.4.1.13 5-Amino-2-[3-(3-azido-propoxy)-6-hydroxy-9H-xanthen-9-yl]-benzoic acid 3-azido-propyl ester

The mixture of 5-aminofluorescein (0.2 g, 0.58 mmol.) and K_2CO_3 (0.16 g, 1.15 mmol.) in DMF (5 ml.) was stirred at 80 °C for 10 minutes, then 1-azido-3-Iodopropane (0.3 g, 1.42 mmol.) was added and obtained mixture was stirred at 80 °C for 4 hours. After cooling, the mixture was added drop-wise to diethyl ether solution (30 ml) to precipitate a crude product. Precipitated residue was mixed with water (20 ml) and acidified with hydrochloric acid (2 ml), extracted with dichloromethane. Organic extract was dried with Na_2SO_4, filtered and evaporated to give a crude product (orange oil). Crude product was crystallized from diethyl ether, filtered and dried. 0.265 g was obtained. Orange oil. Yield 90%. ^{1}H NMR ($CDCl_3$) δ 1.67 (m, 2H, $^2J_{HH}$=6.5 Hz, $^2J_{HH}$=6.1 Hz), 2.15 (m, 2H, $^2J_{HH}$=6.5 Hz, $^2J_{HH}$=6.1 Hz), 3.16 (t, 2H, $^2J_{HH}$=6.5 Hz), 3.56 (t, 2H, vJ_{HH}=6.5 Hz), 4.02 (t, 2H, $^2J_{HH}$=6.1 Hz), 4.28 (t, 2H, vJ_{HH}=6.1 Hz), 6.98-7.06 (m, 3H, $^3J_{HH}$=2.5 Hz) 7.11-7.15 (m, 2H, $^3J_{HH}$=2.2 Hz), 7.18 (d, 1H, $^3J_{HH}$=2.2 Hz), 7.34 (d.d, 2H, $^2J_{HH}$=6.5 Hz), 7.57 (d, 1H, $^3J_{HH}$=2.2 Hz).

2.4.1.14 2-[3-(3-Azido-propoxy)-6-hydroxy-9H-xanthen-9-yl]-5-(3-carboxy-acryloylamino)-benzoic acid 3-azido-propyl ester

To the solution of compound 5-Amino-2-[3-(3-azido-propoxy)-6-hydroxy-9H-xanthen-9-yl]-benzoic acid 3-azido-propyl ester (120 mg, 0.23 mmol) in dichloromethane (8 ml) was added maleic anhydride (40 mg, 0.41 mmol). Was obtained 0.14 g of orange solid which was used without further purification. Yield 98%. ^{1}H NMR (DMSO-d6) δ 1.51 (m, 2H, $^2J_{HH}$=6.6 Hz, $^2J_{HH}$=6.1 Hz), 2.02 (m, ^{2}H, $^2J_{HH}$=6.1 Hz), 3.06 (t, 2H, $^2J_{HH}$=6.6 Hz), 3.52 (t, 2H, $^2J_{HH}$=6.6 Hz), 3.99 (m, 2H, $^2J_{HH}$=6.1 Hz), 4.22 (t, 2H,

$^{2}J_{HH}$=6.1 Hz), 6.26 (d, 1H, $^{3}J_{HH}$=1.9 Hz), 6.39 (m, 1H, $^{3}J_{HH}$=1.9 Hz), 6.43 (d, 1H, $^{3}J_{HH}$=1.9 Hz), 6.55 (d, 1H, $^{2}J_{HH}$=12.1 Hz), 6.93 (m, 3H), 7.26 (d, 1H, $^{3}J_{HH}$=2.2 Hz), 7.45 (d, 1H, $^{2}J_{HH}$=8.3 Hz), 8.10 (d.d, 1H, $^{2}J_{HH}$=8.3 Hz, $^{3}J_{HH}$=2.2 Hz), 8.50 (d, 1H, $^{3}J_{HH}$=2.2 Hz), 10.81 (b.s, 1H). ^{13}C NMR (DMSO-d6) δ 27.25, 27.86, 47.14, 47.60, 62.37, 65.90, 101.03, 104.64, 113.93, 114.53, 117.01, 121.10, 123.13, 128.03, 129.13, 129.42, 130.19, 130.37, 130.55, 131.47, 131.84, 140.18, 149.88, 153.58, 158.33, 163.06, 163.96, 164.84, 166.95, 183.85. EI-Mass (ESI) (m/z; rel. intensity %): 610.07 ($M^{\pm 1}$; 100), 604.33 (12), 384.87 (11), 326.87 (5).

2.4.2 Preparation of CA10 lysate

Pseudomonas resinovorans CA10 was grown in minimal media M9 minus glucose at 30°C for 48 hrs. The cells were harvested using a Beckman JLA 16.250 at 10000Xg at 4°C. The cell pellet (20 g) was resuspended in five volumes of the lysis buffer (20 mM K_2HPO_4 (pH 7.4), 0.5 mM DTT, 10% sucrose, 0.250 M KCl, protease inhibitors: pepstatin, leupeptin, chymostatin and aprotinin 5 μg/ml final concentration, 1 mM PMSF and 1 mM EDTA) and incubated with 1 mg/ml lysozyme at 4°C. The resuspended cells were sonicated and subjected to ultracentrifugation using a T-1270 Sorvall rotor for 45 min at 100,000xg. The clarified supernatant was frozen in aliquots using liquid nitrogen and stored at -80°C. The total protein concentration was measured using Bradford's assay.[119]

2.4.3 Degradation of ATBC with CA10 lysate

The functionality of CARDO present in CA10 lysate to transform ATBC was confirmed by the reaction of ATBC with CA10 lysate. ATBC (75 μmol) in DMSO and NADH (100 μmol) were used in the sonicated lysate (500 μL) with 50 mM Tris-HCl

buffer (pH 7.5). DMSO was added to aid the dispersion of ATBC in water. NADH was added to ensure CARDO reactivity was the limiting factor in the metabolism of ATBC. PL measurements were taken after 1 h of incubation at 30°C.

2.4.4 Separation and analysis of product residues

After exposure to lysate for 72 h, samples were centrifuged using the Sorvall Legend Micro21 at 14800 rpm for 30 min. Pellet was removed and decanted supernatant was redispersed in DMSO to separate ATBC degradation residues. PL measurements were taken of the resultant supernatants at 295 and 360 nm excitation wavelengths. The ATBC, ABC, EA and biotransformation residues were assayed by gas chromatography-mass spectroscopy (model Shimadzu Q2010). GC-MS samples were dissolved in tetrahydrofuran and clarified by centrifugation (5 min at 10,000 x *g*). The inlet temperature was 200 °C. The injection volume was 1 μL with a 1:1 split and helium flow of 1 mL/min. The temperature program was 60 °C, 3 min; 20 °C/min, 300 °C, 5 min.

2.5 Attributions

The synthesis of the azide and alkyne modified chromophores was conducted or aided by Dr. Iurii Bandera at Clemson University. CA10 Lysate was prepared by Dr. Deepti Sharma and Dr. Michael G. Sehorn at Clemson University. Portions of this chapter have been published as Daniele *et al.*, *Manipulation of Förster energy transfer of coupled 1 fluorophores through biotransformation by Pseudomonas resinovorans CA10.* Photochemistry and Photobiology (39), 2012. Content has been reproduced with permission from Wiley Publishing Co.

CHAPTER 3

Clickable Platforms I: Polymer nanocarriers for bio-functional moieties utilized for bioseparations

---

3.1 Introduction

As materials engineers design materials with molecular precision, materials are exhibiting properties very distinct from their bulk counterparts. At 100 nm and below, scientists qualify materials as nanostructures; the surface:volume-ratio dramatically increases and properties are dominated by quantum and interfacial effects. These effects lead to the well known characteristics of quantum dots, superparamagnetic nanoparticles, and Pickering emulsions. Click transformations, specifically the CuCAAC reaction, have found widespread acceptance in the nanoparticle community. Through this facile method of modifying the surface of aqueous-phase particles, a range of potential substrates and metabolites can be attached to particles at high grafting densities that are only limited by the steric interactions of the attached moieties.The novel properties afforded by nanoscale engineering with the CuCAAC reaction are a driving force for the use of nanoparticles in basic fields of chemical and molecular biology; moreover, designer nanomaterials will play a larger role in applied

fields of bioanalytics and bioprocessing.

Biological systems exhibit astounding chemical complexity, which is harnessed for the production of biochemicals, biopharmaceuticals, foods, nutraceuticals, and agrochemicals. A single bacterial or mammalian cell contains thousands of proteins, DNA, RNA, glycans, lipids, a myriad of small-molecule metabolites, and metal ions, all in varied aqueous environments. Each of these components displays many chemical functionalities, including nucleophiles, electrophiles, oxidants, and reductants. Within this environment, enzymes choreograph the innumerable chemical transformations that together constitute the life of the cell: catabolic conversion of metabolites into energy, biosynthesis and post-translational modification of proteins, replication of DNA, and many other biochemical processes.[120] Chemical biologists have attempted to study the molecular intricacies of living systems by labeling and extracting individual components or groups of components, within the complexity of the living system, with fluorophores and affinity assays. A critical aspect of any strategy for labeling a target biomolecule inside a living cell or organism using a chemical reaction is that the reaction must be exquisitely chemoselective; thus, click chemistry provides an ideal platform for analysis of cellar constituents. Click approaches permit both the tracking of biomolecules within the living cell by imaging and also the determination of their exact molecular identities and compositions after purification from a cell lysate; nonetheless, bioprocessing is often tedious and inefficient. Click nanomaterials now allow a route for up-processing biomolecule extraction and library building.

3.1.1 Bioseparations and nanoparticles

The ability to exploit metabolomics and develop novel technologies from an advanced repertoire of genomic data requires the evolution of high-throughput bioseparation techniques. Bio-derived products need to be extensively purified before they can be used for their respective applications, so bioseparation technology requires both target-specific sensors and target-extraction materials. Bioseparation is largely based on chemical separation processes. A plethora of well established separation techniques is used in the chemical industry.[121] A number of these techniques were found to be suitable for carrying out biological separations; however, while borrowing from chemical separations, the fundamental differences between synthetic chemicals and biological substances need to be kept in mind. Some biologically derived substance such as antibiotics and other low molecular weight compounds such as vitamins and amino acids are purified using conventional separation techniques such as liquid-liquid extraction, packed-bed adsorption, evaporation and drying with practically no modifications being necessary.[122] Substantially modified separation techniques are required for purifying more complex molecules such as proteins, lipids, carbohydrates and nucleic acids; moreover, an unprecedented level of gentility and specificity is required for extracting multicomponent systems, *e.g.* antibodies, enzymes, and organelles.[123]

After sensing, of a targeted biomolecule, extraction and concentration would provide unlimited opportunities for both chemical and biological analysis. Biological products are present in very low concentrations in the starting material from which they are purified. For example, monoclonal antibodies are typically present in concentrations around 0.1 mg/ml in the mammalian cell culture; therefore, large volumes of dilute product streams have to be processed for obtaining even modest

amounts of pure products.[124] Impurities or by-products frequently have chemical and physical properties similar to those of the target product, so bioseparation has to be very selective in nature. Biological products are susceptible to denaturation and other forms of degradation, so bioseparation techniques have to be gentle in terms of avoiding extremes of physicochemical conditions such as pH and ionic strengths, hydrodynamic conditions such as high shear rates, and exposure to gas-liquid interfaces. Organic solvents also have relatively limited usage in bioseparation due to their tendency to promote degradation of many biological products. Many biological products are thermolabile and hence many bioseparation techniques are usually carried out at sub-ambient temperatures.

Because biochemical pathways are often distributed between several compartments and even neighboring cells, non-destructive sensing is an imperative start to bioseparation, so current biotechnology trends use functionalized nanoparticles to study the metabolism of large microbial communities, compare enzymes present in different strains, and recognize metabolic compounds with niche specificity.[125–131] Fluorescence nanoparticles are non-destructive and capable of imaging spatial heterogeneity. To provide a set of tools for real-time, sub-cellular measurements of metabolite levels, fluorescent nanoparticles for various metabolites have been developed.[132, 133] Fluorescent nanoparticle assays allow for diverse functionalization, metabolic substrate specificity, and photosensitivity, which enhances the ability to visualize a number of cellular processes and the decouples often convoluted metabolic pathways and extracts enzymes.[134, 135]

In a 2009 study, researchers attempted to produce fluorescence sensors to probe bacterial metabolic pathways by extracting active enzymes with a synthetic cobalt-thiol trap. Ana Beloqui *et al.* produced metabolite "fingerprints" for different organisms by probing, extracting and cataloguing metabolic enzymes, but this method

resulted in a collective of greater than 1500 metabolites, that needed to synthesized and attached to particles.[136] Although this technique showed promise, the capability to produce an entire metabolomic set of nanosensors is unwieldy and commercially impractical. Due to the generalized metabolite functionality of the particles, decoupling the series of metabolic pathways and environmental variants present ultimately proved to be impossible. As opposed to proteomic data sets, metabolic databases, which can predict metabolite structure from a genome sequence, are not available; therefore, introduction of a deduced metabolome does not account for metabolites resulting from promiscuous function or adaptation. Specific metabolite recognition and pathway determination is essential to understand the capabilities of flexible enzyme metabolism by combining sub-cellular sensing and metabolomics. Consequently, a reduction in the scope of metabolites introduced may be required to better recognize and characterize flexible enzyme behavior.

3.2 Results and Discussions

3.2.1 Catch and release strategy for bioseparation

The isolation of a single type of protein from a complex mixture is vital for the characterization of the function, structure, and interactions of the protein of interest and is typically the most laborious aspect of the protein purification process. A model system was utilized to show the efficacy of synthesizing a "baited" nanoparticle to capture and recycle enzymes (proteins that catalyze chemical reactions) from crude cell lysate. Enzyme trapping and recycling was illustrated with the CARDO system, an enzyme important in bioremediation and natural product synthesis. The enzymes were baited with azide-modified carbazolyl-moieties attached to poly(propargyl acry-

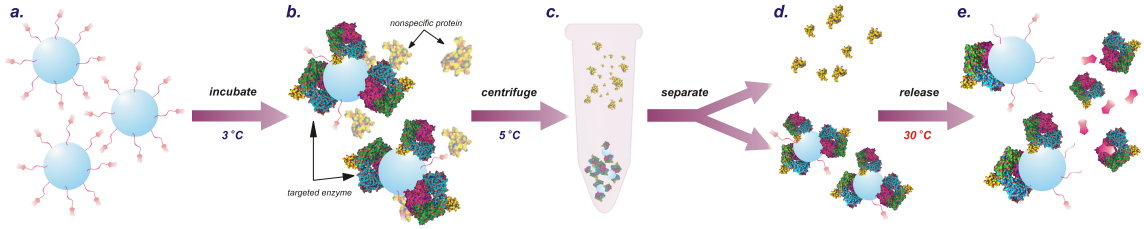

Figure 3.1: Schematic illustration of the baited-particle enzyme extraction method: (a) the nanoparticles consist of poly(propargyl acrylate) (PA) and their surface modification with 9-(3-azidopropyl)-9*H*-carbazole (AC); (b) after adding particles to the protein solution, the CARDO enzyme is attracted and binds to the bait; (c) centrifugation is used to remove the particles with immobilized enzyme. After decanting and resuspension of the particles, the enzyme can be (d) separated by decanting, (e) released and assayed for its carbazole-degrading activity by elevation of temperature and introduction of cofactors.

late) nanoparticles through a click transformation. MALDI-TOF and SDS-PAGE analysis indicated the single step procedure to immobilize the enzymes on the particles was capable of significantly concentrating the protein from raw lysate and sequestering all required components of the protein to maintain bioactivity. These results establish a universal model applicable to concentrating and extracting known substrate protein pairs, but it can be an invaluable tool in recognizing unknown protein-ligand affinities.

There is widespread interest in developing robust, flexible platforms which can be employed in both the verification of proposed metabolic pathways for specific enzymatic chemical reactions and as a means to harvest these specific enzymes from a mixture. Ligand-immobilization techniques represent a powerful tool for downstream processing of enzyme biotechnologies, both in terms of enzyme identification and recovery.[137–139] However, the most common methods to concentrate and deliver these enzymes use covalent immobilization of the enzyme to a bulk surface.[140–142] Covalent binding of enzymes to the substrate aids in immobilization, but it hinders the recovery & recycling of the enzymes.[143] Core-shell particles are also a common

covalent-immobilization filter for low molecular weight proteins, but these methods require complex chemistries and fine control of shell porosity to allow proteins to access their specific ligand.[144, 145] In addition, many of these covalent immobilization methods employ an indiscriminate binding chemistry, *e.g.* thiol-reactivity, which results in a non-specific enzyme immobilization, resulting in the neglect of unknown members of the proteome.[146] An alternative approach would employ substrate or metabolite infused particles which would be capable of treating dilute solutions or mixtures containing only minute amounts of target molecules in the presence of other accompanying compounds. The only report employing a metabolite-surface modified particle utilized commercial amine-reactive linkers with agarose beads to probe metabolic pathways.[147]

Expanding on that effort, a general strategy is presented that employs sub-100 nm particles on which a substrate for a unique protein is "tethered". These "baited" nanoparticles can immobilize a specific protein type then release them for subsequent analysis without a loss of bioactivity. The principle of this substrate-baited separation method is general and applicable to many systems. Particulate carriers bearing a general substrate or metabolite are mixed with a solution or mixture, *e.g.*, crude cell lysates, plasma, cultivation media, or environmental samples, containing the target or unknown metabolic enzymes. Following an incubation period during which the target compounds bind to the decorated particles, the particles with the immobilized target compounds are easily removed from the mixture using centrifugation. After washing out the contaminants, the isolated target protein can be eluted or reactivated from the particles and used for further work. Due to the simple synthesis and rapid decoration of the particles employed in this approach, this process can be tailored for a range of primary substrate/metabolites and their corresponding target proteins and produced in quantities appropriate for applications in large scale separation technologies, *e.g.*,

fluidized-bed systems.

3.2.2 Carbazole 1,9a-dioixygenase (CARDO)

Because of the large pathway deviations and network combinations inherent in metabolism, it is imperative to focus on a simple metabolic pathway and well-characterized genome of value. Metabolic enzymes are a large class of proteins in which their biochemical functions are often veiled behind flexible reaction kinetics and a myriad of applicable substrates, yet there is a critical need to establish their proposed functions as well as discover unforeseen activities, as metabolic enzymes link biological structure to ultimate function.[146, 148, 149]

Xenobiotic metabolism is a good example of a complicated, unknown metabolic network that would elucidate the complications of metabolomics, specifically the inordinate number of metabolites as compared to metabolic enzymes.[150, 151] Xenobiotic metabolism includes microbial biodegradation pathways and drug metabolism in mammals.[152, 153] Xenobiotics, such as polycyclic aromatic hydrocarbons and heterocyclic aromatics (HCAs), play a unique role in environmental science and current biotechnology. As common environmental pollutants HCAs are prime candidates for bioremediation, and in pharmaceutics, they supply a unique substrate for drug development.[154–157] Given HCAs' robust structures, conventional synthetic approaches have given way to biological methods, and a series of microorganisms have the capacity to degrade HCAs. This property results from exposure to foreign substances that instigate new metabolic pathways.[158, 159] In recent decades, HCA-degrading gene clusters have been characterized, and in a few cases, the genes are located on plasmids [113, 160–166]. For example, bacterial degradation of a HCA, 9H-carbazole (CAR), has proven its worth in both fields of biore-

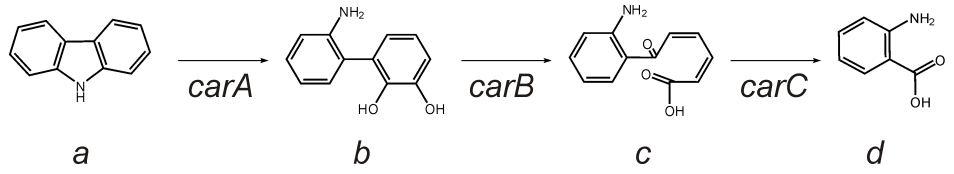

Figure 3.2: Degradation pathway of carbazole by Pseudomonas sp. strain CA10. Gene designations: (carA) carbazole 1,9a-dioxygenase; (carB) 2,9-amino-biphenyl-2,3-diol 1,2-dioxygenase; (carC) 2-hydroxy-6-oxo-6-(29-aminophenyl)-hexa-2,4-dienoic acid (meta-cleavage compound) hydrolase. Compounds: (a) carbazole; (b) 29-aminobiphenyl-2,3-diol; (c) 2-hydroxy-6-oxo-6-(2,9-aminophenyl)-hexa-2,4-dienoic acid; (d) anthranilic acid.

mediation and biotransformation.[155, 157, 167, 168] *Pseudomonas spp.* bacteria are able to survive with catabolic activity necessary to degrade carbazole at a sufficient rate, but often, the expressed carbazole degrading enzymes have multiple and distinct functionalities *ex vivo*.[169] One strain, *Pseudomonas resinovorans* CA10 (CA10) has the capability to use CAR as its sole source of energy, but the enzyme of interest, carbazole 1,9a-dioxygenase (CARDO), also catalyzes a variety of HCA metabolisms.[113, 160, 162, 170–173] CARDO's successful adaptation to multiple metabolic niches requires extraordinary physiological capabilities and reflects the broad technological capacity of this organism and enzyme.

The model system employed to demonstrate this strategy for extraction of xenobiotic metabolizing enzymes utilized *Pseudomonas resinovorans* CA10. This specific bacterial strain is a source of heterocyclic aromatic degrading enzymes, a critical biotransformation for numerous bioremediation and natural product synthesis processes.[174–181] CARDO has been identified as a multicomponent enzyme system which consists of three components: CARDO-O (terminal oxygenase), CARDO-F (ferredoxin), and CARDO-R (ferredoxin reductase).[182]

To verify the CAR degradation activity of CARDO, the purified enzyme was exposed to CAR and required cofactors. The degradation of carbazole fluorescence signals, shown in Figure 3.3. The decrease in the characteristic carbazole fluorescence

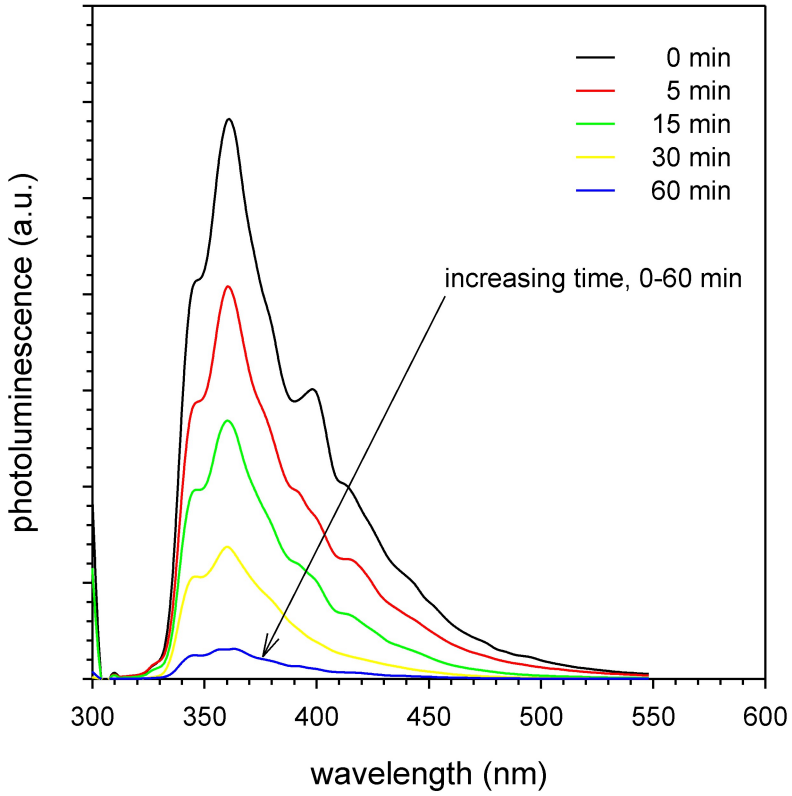

Figure 3.3: Photoluminescence spectra (λ_{ex} = 295 nm) of 9H-carbazole incubated with CARDO complex for 60 minutes at 30 °C. Decrease in PL intensity coincides with enzymatic breakdown of 9H-carbazole.

signaled the degradation of carbazole by the purified CARDO complex. Like many ligating enzymes, the CARDO complex activity can be controlled by temperature deactivation. The activity of the CARDO complex to degrade carbazole was explored by monitoring carbazole fluorescence at various incubation temperatures; at 5 °C, the conversion of carbazole was significantly retarded as shown in Figure 3.4.

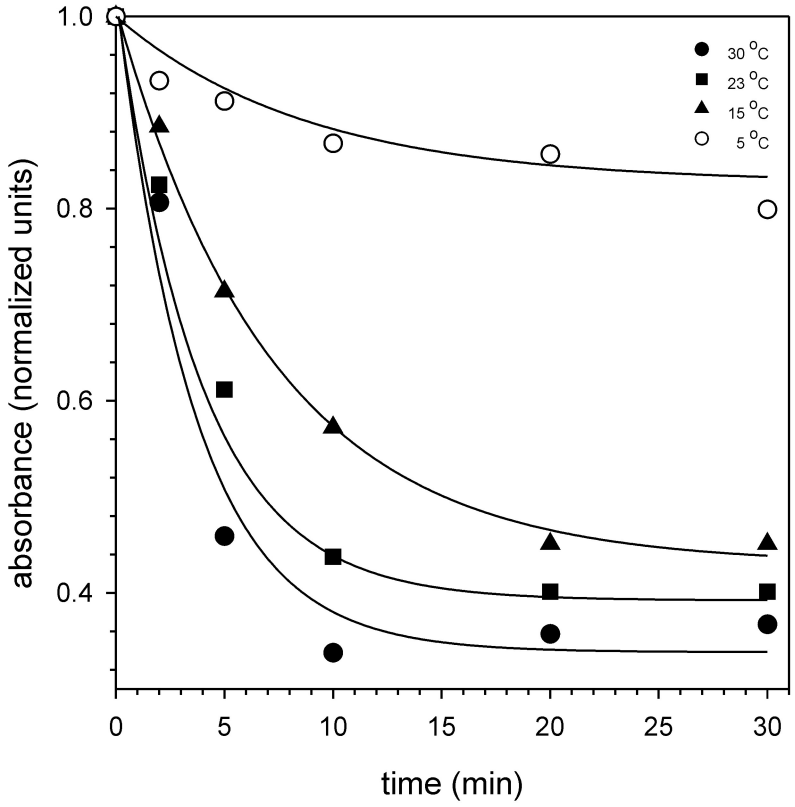

Figure 3.4: Normalized absorbance at 295 nm (peak absorbance of 9H-carbazole) after exposure to purified CARDO complex. Samples were incubated at 30, 23, 15, and 5 °C.

3.2.3 Preparation and testing of affinity-based bioseparation nanoparticles

An azide-modified carbazole was attached to crosslinked, inert poly(propargyl acrylate) (PA) particles following a previously presented procedure.[53] Briefly, the preparation of aqueous-phase nanoparticles that are surface-functionalized with a carbazole substrate was achieved through the CuCAAC reaction.[2, 33, 183] The carbazole decorated particles (PA/AC) were utilized to bind and harvest CARDO from *P. resinovorans* CA10 lysate. The specificity of the PA/AC method was then compared to traditional nickel-bead extraction methods. This method illustrates the power that can be harnessed from the diversity of a "clickable" protein harvesting substrate. The subsequent steps of the enzyme recognition and harvesting can then take place in a single test tube, in which the immobilization of the enzyme on the particle and release is studied to assess the affinity of the enzyme for the substrate and the ability to ultimately harvest and recycle the enzyme.

Figure 3.1 presents the schematic of the "catch and release" strategy for protein harvesting. The PA colloids were prepared using a standard aqueous emulsion polymerization technique. The copper catalyzed click transformations with the azide-terminated carbazole (AC) were done in water. Moieties which incorporate carbazolyl groups are blue emitters, which allows for spectroscopic measurement of their constitution.[184, 185] The biotransformation of the small molecule 9*H*-carbazole (CAR) by *P. resinovorans* CA10 results in non-fluorescing intermediate metabolites which include 2'-aminobiphenyl-2,3-diol (ABP), 2-amino-benzoic acid (ABA), and pyrocatechol (PC).[113, 162, 170, 174] These characteristics were utilized to monitor the degradation of carbazole by *P. resinovorans* CA10 and to analyze the interaction of PA/AC particles with *P. resinovorans* CA10 lysate. Figure 3.3 shows the idealized

the loss of 9H-carbazole fluorescence during incubation with the purified CARDO complex.

Detailed synthesis procedures of the AC molecule and PA/AC particles are presented in the experimental section (Figure 3.1a). The PA/AC particles underwent a 48 hour click transformation, which results in a surface grafting density of $\approx$ 3.5 AC groups/nm^2 and corresponds to a 100 % coverage if the distance of a carbazole ring at its widest point ($\approx$7 Å) can be assumed to define the diameter of a cylinder enclosing the moiety and attached to the PA surface; each particle (diameter = 83 $\pm$ 12 nm) has then $\approx$76k AC moieties.[186] The modified particles underwent multiple methanol and water washes with centrifugation to remove any remaining reactants or copper catalyst. The cleaned PA/AC colloids were then incubated at 5 °C for 1 hour with the lysate of *P. resinovorans* CA10 (Figure 3.1b).

Differing species of carbazole degraders (such as *P. resinovorans* CA10) all appear to follow a similar carbazole degradation pathway that begins with the oxidative cleavage of the heterocyclic nitrogen ring of carbazole, catalyzed by CARDO.[113] This reaction results in the cleavage of one of the two carbon nitrogen bonds; however, subsequent biodegradation of carbazole by all characterized cultures involves the degradation of one of the aromatic rings, meaning these degraders also contain a carbon-carbon cleavage capabilities.[187] For example, *P. resinovorans* CA10 has the capability to utilize carbazole as its sole source of carbon, nitrogen and energy, but the CARDO, present in all carbazole-degrading bacteria, also catalyzes diverse oxygenations of a variety of aromatic compounds, *e.g.* dioxin and fluorene, at reduced efficiency.[113] These enzymes typically consist of two or three components that comprise an electron-transfer chain that mobilizes electrons from NADH or NADPH by flavin and the [2Fe-2S] redox center of the oxygenating activation site.The activation of this catalytic chain can be slowed by temperature reduction. This was verified by

an enzyme activity assay measuring 9*H*-carbazole degradation with purified CARDO at various temperatures (Fig. 3.4). Thus, low temperature incubation allows for the immobilization of the enzyme onto the particles through the bioaffinity of CARDO for the attached carbazole but reduces the kinetic rate in which this enzyme catalyzes the biotransformation.[147]

First, the enzymatic degradation of the attached carbazole was performed at 30 °C. Figure 3.5 presents the change in the photoluminescence (PL) spectra of PA/AC particles after a 12 hour incubation with various concentrations of *P. resinovorans* CA10 lysate. Initially, the spectral characteristics of the modified particles exhibit peaks at ≈350 nm and 366 nm which are attributed to the monomeric emission of the carbazole rings. In addition, the particles exhibit two additional peaks centered at 405 nm and 430 nm and are routinely attributed to excimer emission stemming from carbazole ring dimers.[114, 188] The appearance of these lower energy peaks in the PL spectra suggest that the carbazolyl groups are in close proximity and can energetically couple. When the particles are incubated at a ratio less than 6.12 x 10^9 particles : 1 μg *P. resinovorans* CA10 lysate, the PL signature is completely destroyed and replaced by a broad & weak peak centered at 360 nm. Like the degradation of 9H-carbazole by CARDO, this enzymatic degradation can be slowed by reducing the incubation temperature. Figure 3.6 shows the fluorescence characterization of the degradation of PA/AC by CA10 lysate at different temperatures. There is ≈50% decrease in the 351 nm peak at 25 °C, as compared to ≈13% at 12 °C, and only ≈5% decrease at 5 °C over 12 h. At 5 °C, significant AC degradation was slowed beyond 1 h, allowing enough time for incubation and extraction of the CARDO enzyme. The advantage of the slowed reaction can then be exploited to extract immobilized enzymes. The bioavailability of the hydrophobic metabolites is also critical to understanding metabolic enzymes that bind to them.[189] Prior efforts have indicated that

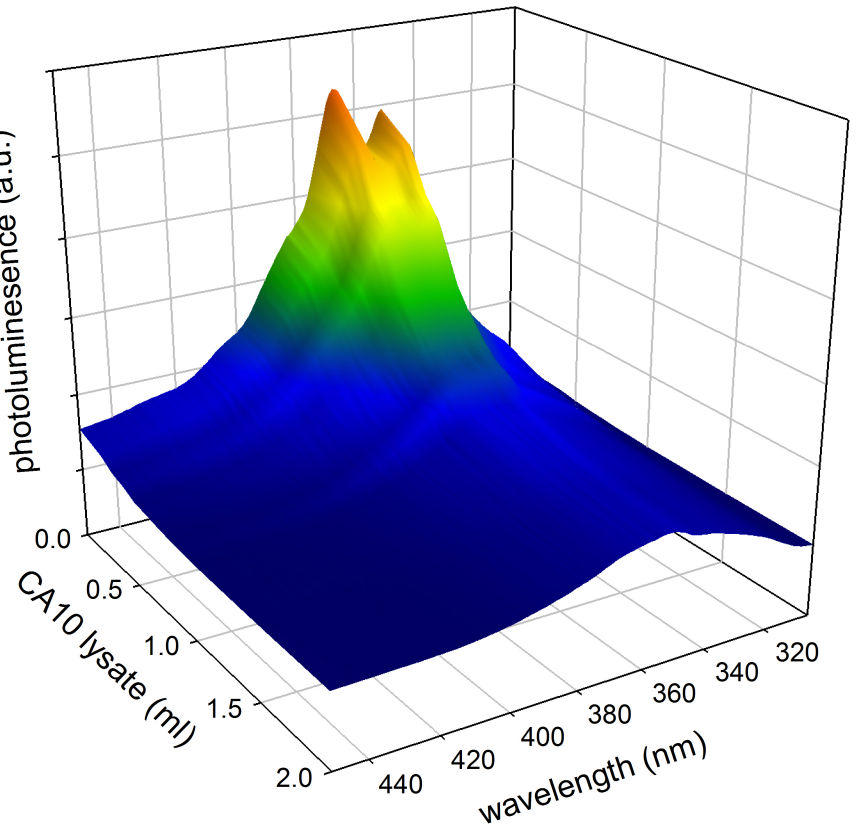

Figure 3.5: Change in photoluminescence spectra of PA/AC particles after 12 hour incubation at 30 °C with various concentrations of *P. resinovorans* CA10 lysate. Particle density was 3.43 x 10^{13}cm^3 (diameter = 83 ± 12 nm) and (100 μL in 2.9 mL water) were combined with *P. resinovorans* CA10 lysate (5.6 μg/μL). Excitation wavelength at 295 nm.

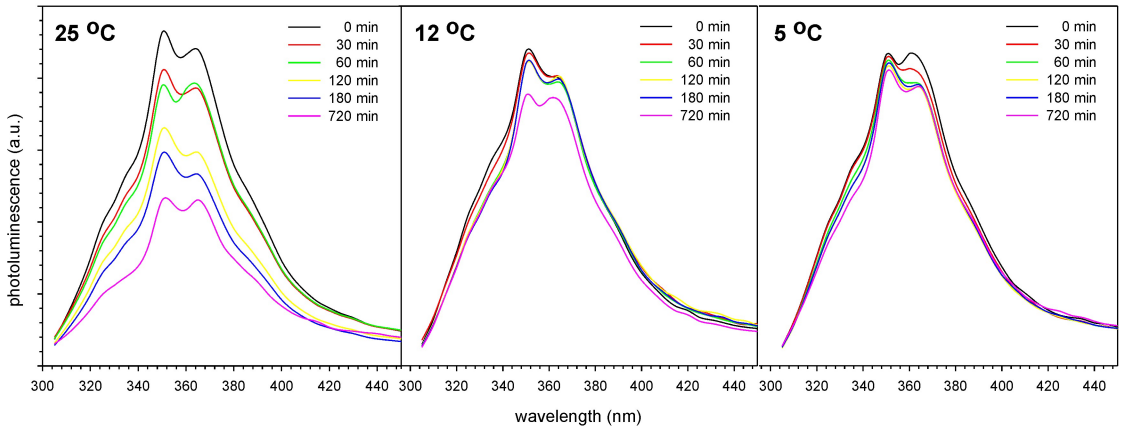

Figure 3.6: Fluorescence at λ_{ex} = 295 nm for PA/AC incubated with CA10 lysate for 12 h at various temperatures to illustrate the slowing of degradation by temperature decrease. From left to right, 25, 12, and 5 °C.

P. resinovorans CA10 can degrade the small molecule *H*-carbazole.[174, 190, 191] The modification of this small molecule with an aliphatic chain attached to the nitrogen (9-(3-azidopropyl)-9H-carbazole) does not alter the ability of CA10 to employ it as a substrate.

Figure 3.7 presents the proliferation of *P. resinovorans* CA10 with both 9H-carbazole and PA/AC particle based media during a 96 hour incubation. The consistent growth between free carbazole and PA/AC shows the flexibility of CA10 to degrade carbazolyl moieties sequestered to particles. The growth curves show that attachment of metabolites to PA colloids did not hinder bioavailability or activity. The low temperature incubation of the particles with the lysate of *P. resinovorans* CA10 allows for the immobilization of the protein on the particle (Figure 3.1b). Once immobilized, the particles can be centrifuged and effectively capture the enzymes, filtering them from non-specific proteins (Figure 3.1c). To assess the specificity of the immobilization on the particles, the centrifuged particles were washed with a mild NaCl solution to remove non-specifically bound proteins and then were subjected

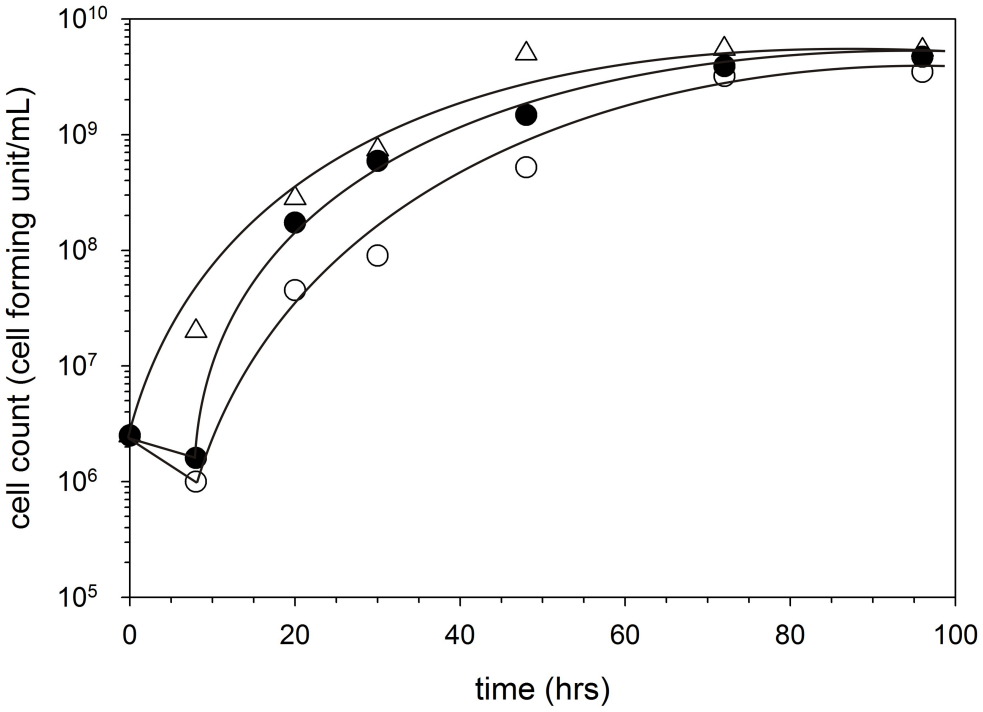

Figure 3.7: Proliferation of *P. resinovorans* CA10 with small molecule CAR (◯) and PA/AC particle (•) based media during a 96 hour incubation at 23 °C. Control growth performed with glucose medium (△).

to matrix-assisted laser desorption/ionization (MALDI) time-of-flight (TOF) mass analysis in order to identify the sequestered enzymes.

Figure 3.8 presents the predicted mass spectrum of the neat CARDO protein constituents and the observed PA/AC particles with immobilized protein.[137, 192] The components CARDO-F (12-kDa monomer) and CARDO-R (37-kDa monomer) function as a ferredoxin and a ferredoxin reductase, respectively, to transport electrons from NADH to terminal oxygenase. The CARDO-O is a 132-kDa homotrimeric terminal oxygenase made up of 44-kDa monomeric units. The experimentally observed mass spectrum (Figure 3.8 (b)) exhibits high intensity peaks at 12, 24, 37, and 44 kDa, as well as two lesser peaks at 49 and 74 kDa. These majority peaks

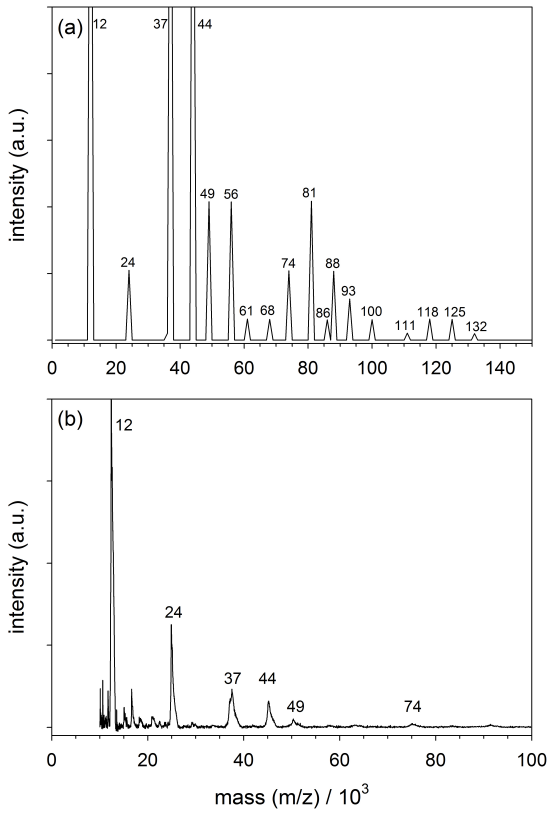

Figure 3.8: (a) Predicted matrix-assisted laser desorption/ionization (MALDI) time-of-flight (TOF) mass spectrum of neat CARDO protein and (b) observed PA/AC particles with immobilized protein.

are consistent with the predicted mass spectrum, while the peaks at masses over 74 kDa are in the noise level of the instrument. To further demonstrate that correlation between the observed and predicted mass spectrum, the component proteins of CARDO were purified employing traditional multistep affinity purification methods using a polyhistidine-tag/nickel pair and their mass spectrum acquired. Figure 3.9 presents the MALDI mass spectrum of CARDO-O, CARDO-F, and CARDO-R. All of the peaks observed in these component proteins are observed in Figure 3.8 (b) except for the masses greater than 74 kDa due to the signal to noise ratio in the spectrum.

Sodium dodecyl sulfate polyacrylamide gel electrophoresis (SDS-PAGE) was employed in order to assess the molecular weights of the immobilized proteins and visually confirm the extraction of the CARDO components from whole-cell *P. resinovorans* CA10 lysate. In Figure 3.10, the proteins immobilized on the PA/AC particles is presented in lane 3 while the raw lysate is presented in lane 2 (lane 1 is the molecular weight markers). The immobilized proteins produced two distinct bands corresponding to a molecular mass of 44 and 37 kDa. These molecular masses correspond to CARDO-O and CARDO-R respectively.[182] This identification was corroborated by comparison with the electrophoretic mobility of purified CARDO-O and CARDO-R as shown in lanes 4 and 5. The high intensity of the bands indicates that this methodology has advantages in the selective harvesting and concentrating of these proteins from the crude lysate in a single step. The purified CARDO-F protein (Figure 3.10 lane 6) exhibits multiple bands and appears to run slower than its actual molecular weight, characteristics which have been presented in previous reports.[182, 193] Faint bands similar to the purified CARDO-F are present in the immobilized proteins. The presence of this protein can be verified by a bioactivity assay with the immobilized proteins because in the CARDO *P. resinovorans* CA10 system, CARDO-F is essential

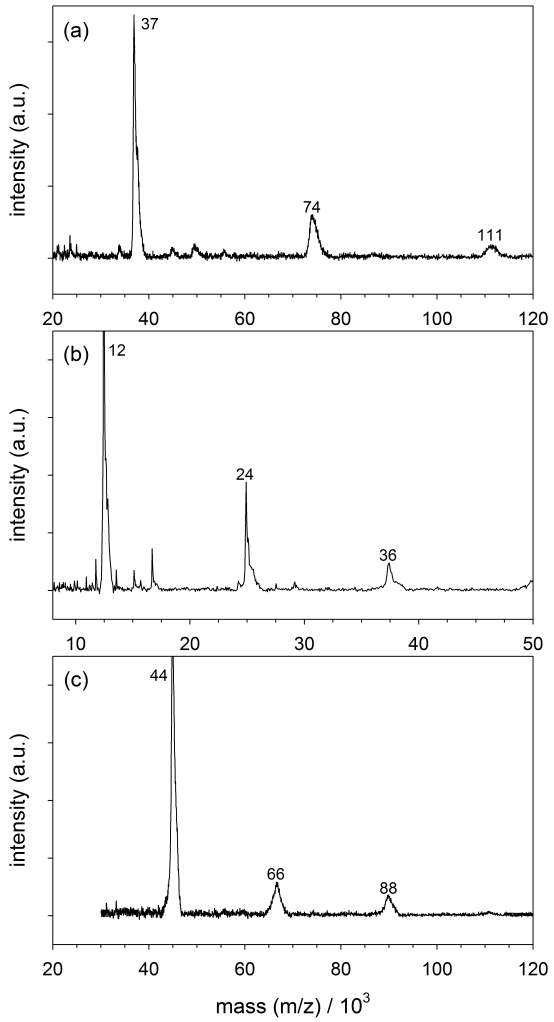

Figure 3.9: Matrix-assisted laser desorption/ionization (MALDI) time-of-flight (TOF) mass spectrum of purified (a) CARDO-R (b) CARDO-F, and (c) CARDO-O.

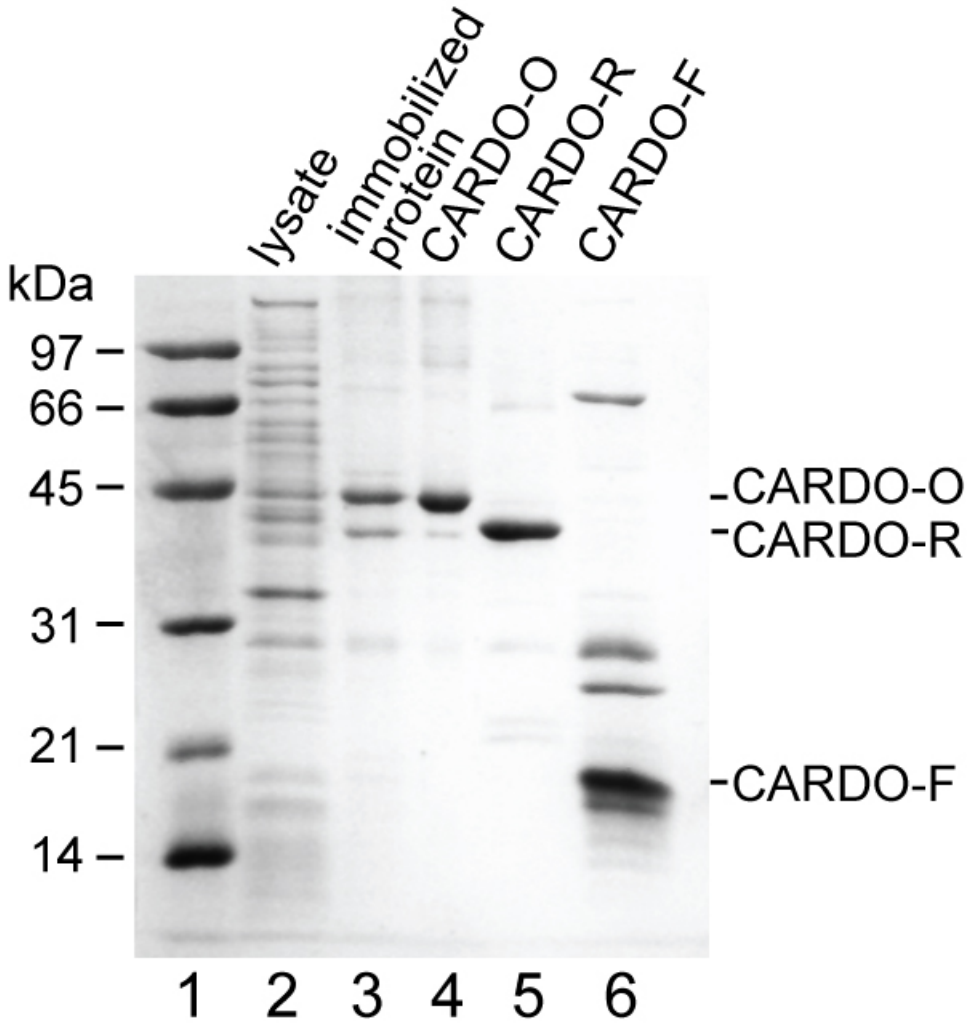

Figure 3.10: Sodium dodecyl sulfate polyacrylamide gel electrophoresis of whole cell lysate from *P. resinovorans* CA10 (**2**) and PA/AC particle immobilized proteins (**3**). For comparison, the purified CARDO components of CARDO-O (**4**, 1 μg), CARDO-R (**5**, 1.5 μg), and CARDO-F (**6**, 2 μg) obtained through traditional multistep affinity purification methods using a polyhistidine-tag/nickel pair is presented. Lane **1** is the molecular weight marker.

for electron transfer to CARDO-O and must be present for bioactivity.[182]

To assess the bioactivity of the proteins attached to the particles, a modified affinity assay was carried out in which the addition of NADH, FAD, and Fe^{2+} reconstituted the enzyme electron transport system and activity was promoted by the addition of carbazole and an increase in temperature to 30 °C.[182] Figure 3.11 presents the measurement of activity with incubation time for these harvested protein as well as CA10 lysate incubated with PA/AC particles, neat CA10 lysate, and non-specific proteins.

The ability of PA/AC particles to harvest desired enzymes was assessed by the conversion of NADH to NAD^+. This conversion was monitored through the loss of an absorption peak at 340 nm of the supernatant over a specified incubation period. Under all activity studies, the carbazole concentration was kept constant. As was expected, the neat lysate exhibited the fastest conversion, with the NADH oxidized to NAD^+ within a 2 hour incubation period. This is due to the high protein content of the neat lysate relative to the substrate concentration. Similarly, the lysate incubated with the PA/AC particles exhibited a high level of NADH to NAD^+ conversion, confirming the PA/AC's ability to trap and remove carbazole degrading enzymes. The proteins immobilized on the particles were released and capable of the biotransformation of carbazole as determined through the oxidation of NADH (Figure 3.1 (e)). The degradation of carbazole by extracted proteins verifies the PA/AC particles capabilities to extract the entire CARDO complex, including CARDO-O, CARDO-R, and CARDO-F. Without each component of the enzyme, bioactivity could not be restored. Although, the activity of the proteins sequestered on the particles was similar to the neat lysate, it was reduced in rate due to the lower ratio of protein to substrate. In contrast, the non-specific proteins exhibited no activity towards the carbazole.

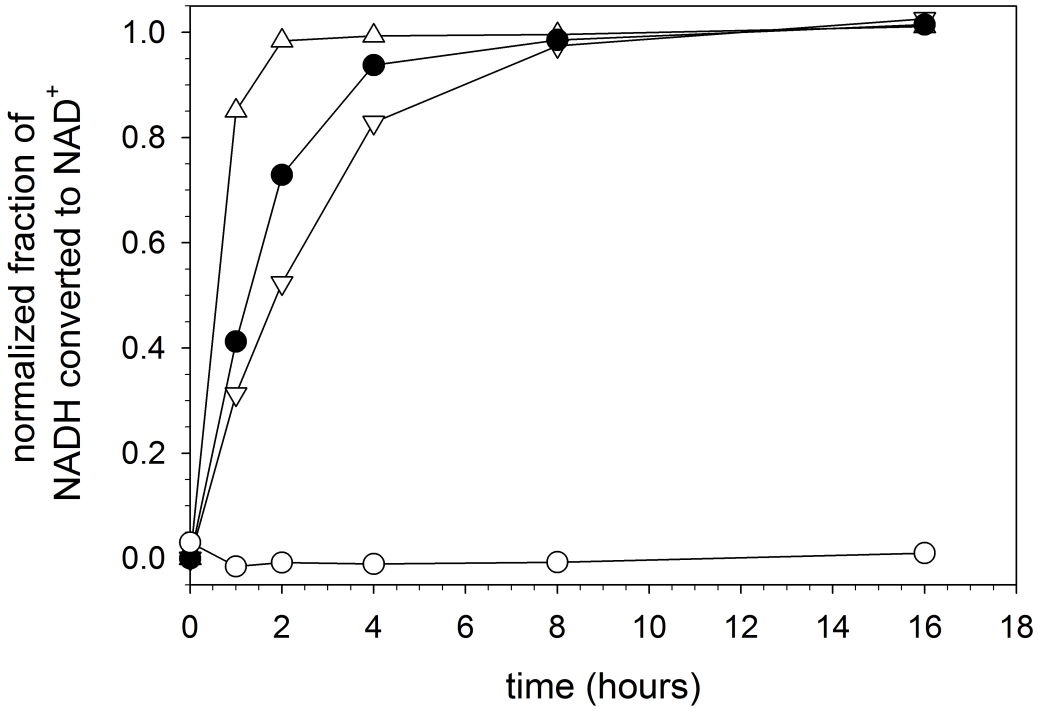

Figure 3.11: Measurement of activity with incubation time for proteins immobilized on PA/AC particles (•), CA 10 lysate incubated with PA/AC particles (▽), neat CA 10 lysate (△), and non-specific proteins (○). Activity measured by the oxidation of NADH to NAD^+ and assessed through the change in absorption of the supernatant at 340 nm.

Clearly, the immobilization of the CARDO proteins on the particles still allows them to function as a carbazole degrader once removed from the particles. In the CARDO *P. resinovorans* CA10 system, an unrelated reductase can be substituted for CARDO-R and still maintain activity, but CARDO-F is indispensable for electron transfer to CARDO-O.[182] The observed activity of the sequestered proteins indicates that all three components have been harvested.

3.3 Conclusions

In this effort, a model system was utilized to show the efficacy of synthesizing a "baited" nanoparticle to capture and recycle enzymes from lysate. Enzyme trapping and recycling was illustrated with the CARDO systems, an enzyme important in bioremediation and natural product synthesis. The enzymes were baited with an azide modified carbazolyl-moiety attached to a PA nanoparticle. The bait products is well dispersed in water and buffers, a property that is independent of selected ligand, but a result of their attachment to PA particles. These results establish a universal model applicable to concentrating and extracting known substrate protein pairs, but it can be an invaluable tool in recognizing unknown protein-ligand affinities. Despite the widespread availability of genome sequences, according to the shear multitude of metabolites the selectivity of many metabolic enzymes are still veiled, this procedure goes a long way toward cultivating large banks of recyclable metabolic enzymes and probing enzyme selectivity.

3.4 Experimental Details

3.4.1 Reagents and solvents

All the commercial reagents were used without further purification. All the solvents were dried according to standard methods. Deionized water was obtained from a Nanopure System and exhibited a resistivity of ≈18.2x10^{18} ohm^{-1}cm^{-1}.

3.4.2 Characterization

^{1}H and ^{13}C NMR spectra were recorded on JEOL ECX 300 spectrometers (300MHz for proton and 76MHz for carbon). Chemical shifts for protons are reported in parts per million downfield from tetramethylsilane and are referenced to residual protium in the NMR solvent ($CDCl_3$: δ 7.26 ppm, DMSO-d6: δ 2.50 ppm). Chemical shifts for carbons are reported in parts per million downfield from tetramethylsilane and are referenced to the carbon resonances of the solvent ($CDCl_3$: δ 77.16, DMSO-d6: δ 39.52 ppm). Electron impact (EI) (70 eV) ionization mass spectra were obtained using Shimadzu GC-17A mass spectrometer. LC/MS mass spectra were obtained using Finnigan LCQ spectrometer and HP 1100 (HPLC). Photoluminescence (PL) spectra were collected using a Jobin-Yvon Fluorolog 3-222 Tau spectrometer.

3.4.3 Materials

3.4.4 Synthesis of 9-(3-azidopropyl)-9*H*-carbazole (AC)

3-(9*H*-Carbazol-9-yl)propyl methanesulfonate (2) Methanesulfonyl chloride (0.84 g, 7.32 mmol) was added dropwise at room temperature to a stirred solution of 3-(9*H*-carbazol-9-yl)propan-1-ol (1.5 g, 6.66 mmol) **(1)** (synthesized according to

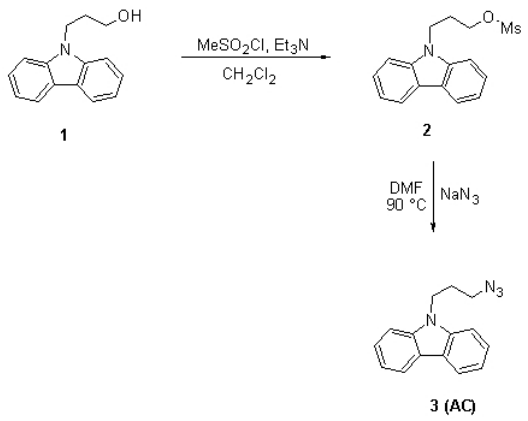

Figure 3.12: Reaction scheme for 9-(3-azidopropyl)-9*H*-carbazole (AC).

Ref. [117]) and triethylamine (0.74 g, 7.32 mmol) in dichloromethane (25 mL). The solution was stirred for 8 hours and then washed with water two times. The organic layer was separated, dried with Na_2SO_4 and then filtered. The solvent was removed under reduced pressure to give the clear-yellow oil. Yield: 1.96 g (97%). ^{1}H NMR ($CDCl_3$) 2.36 (m, 2H, *J* 6.5, 5.9), 2.86 (s, 3H), 4.14 (t, 2H, *J* 5.9), 4.50 (t, 2H, *J* 6.5), 7.25 (m, 2H), 7.40-7.52 (m, 4H), 8.10 (d, 2H, *J* 7.9).

9-(3-Azidopropyl)-9*H*-carbazole (AC) (3) A mixture of 3-(9*H*-carbazol-9-yl)propyl methanesulfonate **(2)** (1.96 g, 6.46 mmol) and sodium azide (0.46 g, 7.14 mmol) in dimethylformamide (25 mL) was heated and stirred at 90 °C for 4 hours. After cooling to room temperature, the mixture was quenched with water and extracted with dichloromethane. The organic solution was washed with water, dried with Na_2SO_4 and filtered. The solvent was removed under reduced pressure to give the clear-brown oil, which was purified by flash chromatography (10% ethyl acetate/hexane; R_f=0.4). A clear-yellow oil was obtained. Yield: 1.34 g (82%). ^{1}H NMR ($CDCl_3$) 2.13 (m, 2H, *J* 6.5, 6.2), 3.30 (t, 2H, *J* 6.2), 4.42 (t, 2H, *J* 6.5), 7.24 (m, 2H), 7.41-7.50 (m, 4H), 8.10 (d, 2H, *J* 7.6). ^{13}C NMR ($CDCl_3$, 75.6 MHz) δ 28.3, 39.8, 48.8, 108.6, 119.2, 120.6, 123.1, 126.0, 140.4. EI-Mass (m/z; rel. intensity%)

251 (M^++1; 5), 250 (M^+; 35), 194 (12), 180 (100), 167 (65), 152 (46), 139 (21).

3.4.5 Preparation of baited particles

Monodisperse poly(propargyl acrylate) (PA) particles were prepared using a modified emulsion polymerization procedure. The propargyl acrylate (PA) (4.6 ml) and divinylbenzene (DVB) (0.8 ml) were passed through a packed alumina column while all other materials were used as-received. A 500 mL three necked jacketed reactor was charged with 140 mL of deionized water and 0.08 g of sodium dodecyl sulfate (SDS, 99% Aldrich) was added and the solution was stirred for 1 h at 83 °C under a nitrogen atmosphere. The PA and DVB were mixed and slowly dropped into the reaction vessel. Once the addition of the PA:DVB mixture was completed, 0.2 mL of 3-alloxy-2-hydroxy-1-pro- panesulfonic acid sodium salt (COPS-1, 40wt % soln. Aldrich) in 5mL deionized water was added drop-wise to the solution. After the COPS-1 was completely added, the solution was stirred for an additional 5 min before 0.16 g potassium persulfate (KPS, 99+ % Aldrich), that was mixed with 5 mL deionized water, was added to the solution. The emulsion polymerization was carried out under a nitrogen atmosphere for at least 2 h. The resulting PA latex was dialyzed against deionized water for 5 days at 60 °C using a dialysis bag with a molecular weight cut-off of 50,000. The dialyzed dispersion was then shaken with an excess of mixed bed ion-exchange resin (Bio-Rad Lab AG 501-X8, 20-50 mesh) to remove excess electrolyte. After the cleaning procedures, the particle diameter was measured to be 83 ± 12 nm (average and standard deviation) with a Coulter N4Plus dynamic light scatter (DLS). Reported DLS diameters are based on intensity distribution. Drying a known mass of the suspension in an oven at 90 °C overnight and then in a vacuum oven for 2 days, resulted in a particle density of 3.43 x 10^{13}

particles/mL.

For a typical surface modification of the particles, for example, the grafting of AC onto the particles, 1 mL PA particles and 4.5 mg AC were added to a 2 mL deionized water. Solutions of 0.0644 g copper(II) sulfate (99.999% Aldrich) in 10 mL deionized water and 0.17 g sodium ascorbate (99% Aldrich) in 10 mL deionized water were made. Initially, 0.2 mL of the Cu_2SO_4 solution was added to the PA/AC solution, followed by 0.3 mL of the sodium ascorbate solution. The resulting mixture was maintained at a temperature of 28 °C for 48 h. The resulting clicked particles were dialyzed against deionized water for 3 days at 60 °C using a dialysis bag with a molecular weight cut-off of 50,000.

3.4.6 Preparation of *P. resinovorans* CA10 lysate

P. resinovorans CA10 was grown in minimal media M9 minus glucose at 30 °C for 48 hrs. The cells were harvested using a Beckman JLA 16.250 rotor at 10000 x g at 4 °C. The cell pellet (20 g) was resuspended in five volumes of Buffer A (20 mM K_2HPO_4 (pH 7.4), 0.5 mM DTT, 10% sucrose, 0.250 M KCl, protease inhibitors: pepstatin, leupeptin, chymostatin and aprotinin 5 μg/ml final concentration, 1 mM PMSF and 1 mM EDTA) and incubated with 1 mg/ml lysozyme at 4 °C. The resuspended cells were sonicated and subjected to ultracentrifugation using a T-1270 Sorvall rotor for 45 min at 100,000x g. The clarified supernatant was frozen in aliquots using liquid nitrogen and stored at -80 °C. The total protein concentration was measured using Bradford's assay.[119]

3.4.7 Purification of CARDO proteins

All the resins and chemicals were from GE healthcare and American Bioanalytical, respectively, unless otherwise mentioned.

3.4.7.1 Expression of CARDO-F, CARDO-O and CARDO-R

Each plasmid was transformed separately in the BL21(*DE3*) Rosetta strain of *Escherichia coli*. The transformed bacterial cells were grown in 2X LB media (yeast extract 5 g/L, tryptone 10 g/L and NaCl 5g/L) supplemented with kanamycin (50 μg/ml) at 37 °C to an OD of 0.8. Isopropyl-D-1-thiogalactopyranoside (IPTG) was added to the cultures (final concentration of 0.4 mM) and the culture was further incubated for 16 hrs. The cells were harvested by centrifugation at 6000 rpm at 16 °C for 10 min in a Beckman 8.1000 rotor.

3.4.7.2 Purification of CARDO-F, CARDO-O and CARDO-R

Lysate from bacterial cell pellets for each of CARDO-F, CARDO-O and CARDO-R was separately prepared using the same protocol at 4 °C. A 30 g cell pellet of each bacterial culture was resuspended separately in 150 ml Buffer A and incubated at 4 °C for 30 min in the presence of lysozyme (1 mg/mL) followed by sonication. Each individual lysate was centrifuged at 40,000 rpm in a Beckman Ti-45 rotor for 1 hr at 4 °C. The supernatant from each lysate was further subjected to affinity and conventional column chromatography as described below.

3.4.7.3 CARDO-F purification

The supernatant from the CARDO-F lysate was incubated with Ni-NTA sepharose (GE Healthcare) for 1 hr. The supernatant-Ni-NTA slurry was collected

and poured into a column (0.7 cm inner diameter X 0.5 height). The Ni-NTA column was washed with Buffer B (20 mM K_2HPO_4 pH 7.4, 300 mM KCl, 10% glycerol, and 1 mM EDTA) followed by elution of CARDO-F with Buffer B containing 500 mM imidazole. Peak fractions were diluted to match conductivity of Buffer C (20 mM K_2HPO_4 pH 7.4, 10% glycerol, and 1 mM EDTA) containing 100 mM KCl and loaded on a 1 mL Source 15Q column (GE Healthcare). The bound protein was fractionated using Buffer C containing 100 mM - 800 mM KCl. The peak fractions containing the protein (∼700 mM KCl) were pooled, diluted to match conductivity of Buffer C containing 100 mM KCl and loaded onto a 1 mL Source 15S column (GE Healthcare). The bound protein was fractionated using Buffer C containing 100 mM 800 mM KCl. The peak fractions (∼150 mM KCl) containing CARDO-F were pooled, concentrated and stored at -80 °C.

3.4.7.4 CARDO-O purification

The supernatant containing CARDO-O was subjected to Ni-NTA affinity chromatography as described for CARDO-F. The eluent from the Ni-NTA column was diluted to match conductivity of Buffer C containing 100 mM KCl then loaded on a 1 mL Source 15Q column. The bound protein was fractionated as described for CARDO-F. Peak fractions containing the CARDO-O (∼360 mM KCl) were pooled, diluted to match conductivity of Buffer C containing 100 mM KCl and loaded onto a 1 mL Source 15S column. The bound protein was fractionated as described for CARDO-F. The peak fractions (∼100 mM KCL) containing CARDO-O were pooled, concentrated and stored at -80 °C.

3.4.7.5 CARDO-R purification

The supernatant containing CARDO-R was subjected to Ni-NTA affinity chromatography as described for CARDO-F. The eluent from the Ni-NTA column was diluted to match conductivity of Buffer C containing 100 mM KCl then loaded on a 1 mL Source 15Q column. The bound protein was fractionated as described for CARDO-F. Peak fractions containing the CARDO-R (∼400 mM KCl) were pooled, diluted to match conductivity of Buffer C containing 100 mM KCl and loaded onto a 1 mL Source 15S column. The bound protein was fractionated as described for CARDO-F. The peak fractions (∼100 mM KCL) containing CARDO-R were pooled, concentrated and stored at -80 °C.

3.4.7.6 Denaturing polyacrylamide gel electrophoresis

The protein samples (whole cell lysate, 5 μg; purified lysate, 1 μg; CARDO-O, 1μg; CARDO-R, 1.5μg; and CARDO-F, 2μg) were loaded on a 12% SDS-polyacrylamide gel and subjected to electrophoresis for 50 min at 200V. The gel was stained using Commassie Brilliant Blue. The image was taken using Gel-Doc (Bio-Rad).

3.4.7.7 Fluorescence measurement of 9H-carbazole degradation by purified CARDO complex

The purified enzymes CARDO-F, CARDO-O and CARDO-R were incubated in 500 μL buffer (50 mM Tris-HCl pH 7.5, 100 nmol/μL Mohrs Salt, 200 pmol/μL FAD+ and 100 nmol/μL NADH) at 30 °C. All buffer cofactors were in excess as suggested by previous reports.[182] The reaction was started with the addition of 50 nmol/μL 9H-carbazole dissolved in DMSO. The sample was incubated in a water jacketed cuvette to maintain a constant temperature. Samples were gently stirred

with a magnetic stir plate. The photoluminescence spectra were collected λ_{ex} = 295 nm.

3.4.8 Temperature dependence of CARDO catalysis on 9H-Carbazole and PA/AC

Purified CARDO complex activity was monitored using a modified enzymatic assay previously described.[194] The purified enzymes CARDO-F, CARDO-O and CARDO-R were incubated in 20 μL Buffer D (25 mM Tris-HCl pH 7.5 and 1 mM NADH) containing 1 mM carbazole dissolved in DMSO at varying temperatures from 30 °C to 5 °C. An aliquot was removed from the reaction at the indicated times and the absorbance of the reaction was determined with a NanoDrop spectrophotometer (Thermo Scientific) at 295 nm.

CA10 lysate interaction with PA/AC was monitored by fluorescence. CA10 lysate (1 mL at 5.6 μg protein/μL) and 100μL PA/AC (3.43 x 10^{13} particles/mL) was incubated in a water jacketed cuvette to maintain a constant temperature. Samples were stirred with a magnetic stir plate. Temperature dependence was evaluated at 25 °C, 12 °C, and 5 °C. Fluorescence measurements were made at t = 0, 30, 60, 120, 180, and 720 min. The PL spectra were collected at λ_{ex} = 295 nm.

3.4.9 Enzyme trapping and affinity activity assay

The enzyme trapping and affinity of the bound proteins were assessed through the following procedures. Initially, 100 μL PA/AC particles in an aqueous buffer (3.43 x 10^{13} /cm^3 and (100 μL in 0.8 mL water)) were added to 100 μL neat lysate of CA 10 and incubated at 5 °C for 1 hour. This solution of particles and lysate was centrifuged (10,000 x g, 5 °C, 10 min.) and the supernatant was decanted. The

particles were washed with 1 mL of a 100 mM NaCl solution and the tube was inverted 10 times followed by incubation for 30 min at 5 °C. After the incubation, the particles were centrifuged (10,000 xg, 5 °C, 10 min) (PA/AC particles with bound proteins) and the salt solution decanted. To assess the activity of the various components (PA/AC particles with bound proteins, incubated lysate, non-specific proteins, and neat lysate), each was individually added to an aqueous buffer in which 5 μL of a 10 nmol carbazole / DMSO solution was added.To initiate bioactivity, 1 nmol flavin adenine dinucleotide (FAD), 100 nmol ammonium iron(II) sulfate, and 100 nmol NADH, were added, resulting in a total buffer volume of 1 mL, and the temperature raised to 30 °C. All cofactors were added in excess. After either 30, 60, 120, 240, 320, or 960 min., the temperature of the samples was lowered to 5 °C, the tubes centrifuged (10,000 x g, 5 °C, 10 min), and the supernatant decanted and the oxidation of NADH to NAD^+ assessed through the change in absorption of the supernatant at 340 nm.

3.4.10 MALDI/TOF measurements

All samples were analyzed in a saturated 3,5-dimethoxy-4-hydroxycinnaminic acid solubilized in 1:1 water:acetonitrile, 0.1% TFA. A sandwich method of 1 μL matrix, followed by 1 μL acid solubilized sample, capped with 1 μL matrix was prepared on the plate. A desalting step of 1 μL water was utilized for all samples. The samples were analyzed with the Bruker OmniFlex III.

3.5 Attributions

The synthesis of the azide-modified chromophores was conducted or aided by Dr. Iurii Bandera at Clemson University. Production of CARDO enzymes and traditional purification was conducted by Dr. Deepti Sharma and Dr. Michael G. Sehorn

at Clemson University. Plasmids harboring genes for CARDO-F-$(HIS)_6$, CARDO-O-$(HIS)_6$ and CARDO-R-$(HIS)_6$ vectors were a kind gift from Hideaki Nojiri at the University of Tokyo.The results presented in Chapter 3.3.2 were previously published: Daniele *et al.*, *Substrate-baited nanoparticles: A catch and release strategy for enzyme recognition and harvesting.* Small, 2012.

CHAPTER 4

Clickable Platforms II: Magnetic field-affected composite carriers for bio-functional moieties

---

4.1 Introduction

As introduced in Chapter 3, nanomaterials have unique properties because of exaggerated surface: volume ratio and quantum effects realized at the nanoscale. Comparable to polymer nanoparticles, inorganic nanoparticles have many surprising characteristics, ranging from novel optical response and semiconducting properties to superparamagnetic behavior. Quantum dots (CdS, CdSe, InAs) have semiconducting properties due to quantum confinement of excitons, resulting in partially formed valence and conduction bands. The QD electronic bandgap is directly proportional to the size of the nanocrystal. Adjusting the bandgap tailors the absorption and emission wavelengths, where larger QD reduce the band gap for a bathochromic shift and smaller QD increase the band gap for a hypsochromic shift. The continuous, tailored absorption and emission spectra of QD have led to their popularity as multiplex imaging, cell targeting and FRET sensors. At the orthogonal-end of the electromagnetic spectrum, nano-sized magnetic materials (Fe, Co, Ni) have unique

characteristics based on the size of the nanocrystals. Iron oxide nanoparticles, Fe_3O_4 and γ-Fe_2O_3, have attracted interest due to their superparamagnetic properties dependent on particle size. Applications include magnetic storage devices, catalysts, sensors and magnetic resonance imaging(MRI) contrast agents, but unlike QD, iron oxide nanoparticles require organic coatings for stability, such as synthetic polymers or biomacromolecules.[195–197] The requirement of well-defined surface chemistries, tailored at the nanoscale, make iron oxide nanoparticles a prime platform for the application of click chemistry and the topic of Chapter 4.

4.1.1 Magnetism and nanomaterials

Magnetic materials can be classified into three classes based on their susceptibility to external magnetic fields: 1) diamagnetic, 2) paramagnetic, and 3) ferromagnetic. Diamagnetism is dominant in materials with unpaired electrons. Paramagnetic materials have unpaired electrons, but there is no coupling between their spins. Ferromagnetic materials also have unpaired electrons, but all spins are coupled and parallel. Diamagnetic materials have a very small repulsion to external fields. Paramagnetic materials have exhibit small attraction response to applied fields, and ferromagnetic materials have strong attraction upwards of 100x paramagnetic response. More importantly, ferromagnetic materials show a permanent magnetic moment after removal of the applied field.

The most common materials formed into nanoparticles are magnetite and maghemite (Fe_3O_4 and γ-Fe_2O_3, respectively) which in the bulk form are a unique type of ferromagnetic; they are ferrimagnetic. Ferrimagnetic materials have unpaired electrons with paired spins; however, their pairs have some anti-parallel arrangements. When these ferrimagnetic materials are confined to $<$50 nm, they exist as

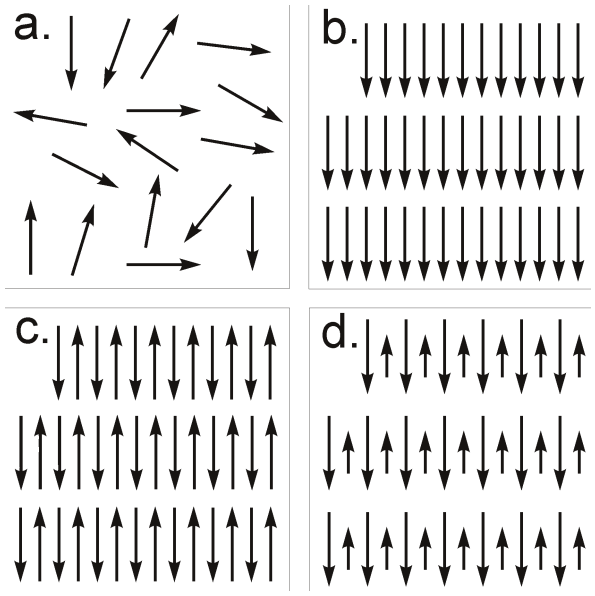

Figure 4.1: Diagrams illustrate the arrangement of magnetic dipoles in (a) paramagnetic, (b) ferromagnetic, (c) anti-ferrimagnetic and (d) ferrimagnetic materials.

single-domain magnets. Each ferrimagnetic nanoparticle has a permanent magnetic moment which can be reoriented in an applied field, but due to thermal energy at ambient temperatures, the magnetic moment is perturbed and the magnetic moment of each nanoparticle can constantly switch orientation. On the macroscopic scale, there is no net magnetization, and these nanoparticles are considered superparamagnetic (SPION).The difference in magnetization in response to an applied field is significant between different magnetic materials as shown in Figure 4.2. In the presence of an applied field, SPION are readily and strongly attracted to the field because of reorientation of each nanoparticle, but unlike ferromagnetic materials, there is not remnant magnetization or coercive field realized, *i.e.* hysteresis in the magnetization curve. Superparamagnetism results from the confined magnetic domain in the SPION can be easily inverted by thermal energy great enough to overcome an energy barrier, resultant from the magneto-crystalline and shape anisotropy of the material. Both magneto-crystalline and shape anisotropy are dependent on SPION volume, as is the

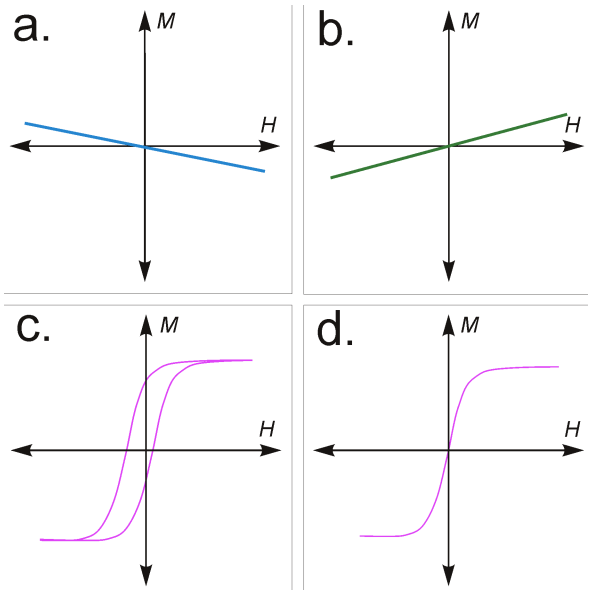

Figure 4.2: Diagrams illustrate the Magnetization response to external field in (a) diamagnetic, (b) paramagnetic, (c) ferromagnetic and (d) superparamagnetic materials.

superparamagnetic behavior.

4.1.2 Magnetic nanoparticles and biotechnology

Superparamagnetism allows SPION to be utilized in biosystems because they display colloidal stability absent of an applied magnetic field. Accordingly, SPION with designer surface chemistries are candidates for the next-generation of cancer theranostics, including diagnostic assays, MRI contrast agents, cell-tracking, immune-stimulation, hyperthermia, and drug delivery; however, agglomeration of nanoparticles with a large surface-to-volume ratio inside biosystems of varying pH and ionic concentration.[198–205] Any agglomeration of SPION will result in the loss of superparamagnetic characteristics, decrease of surface activity, short blood half-life and rapid elimination from circulation. In light of the aforementioned benefits and hurdles, a major challenge in medical applications is to devise a methodology to maintain

superparamagnetism which avoids ferrimagnetic agglomeration, stabilize SPION to prevent surface-energy agglomeration, and include sufficient functionality on the surface of these nanodevices.

Immobilization of enzyme, antibodies, oligonucleotides and other bio-functional moieties onto SPION are an efficient tool for bioseparation by the application of an external magnetic field. SPION have been covalently coupled with lectins, enzymes or antibodies using thiol chemistry. Dextran-coated SPION have been commercially produced with covalently immobilized antibodies and fluorescent moieties. SPION have also found a promising role in applied biomedical sciences, specifically as MRI contrast agents and and cancer therapeutics. MRI results depend on the variation in proton density and magnetic relaxation times of various tissues; therefore, localization of SPION in targeted-tissue would produce increased contrast against native tissue. Hyperthermia is a promising cancer therapy based on the heating of tumor tissue to temperatures between 40-50 °C, reducing the viability of the cancerous cells. Magnetic fluid hyperthermia results from subdomain magnetic particles that produce heat through energy loss during the application of an external, alternating current (AC) magnetic field. From these few examples, SPION represent an extremely interesting group of nanomaterials for biotechnology applications, but *in vitro* applications require designer particles for bioseparation and *in vivo* applications require uniform surface coatings to prevent agglomeration and cloak particles from natural immune response.

The most common route to SPION surface-functionalization includes ligand-exchange reactions, but due to the inconsistencies and difficulties associated with ligand exchange, researchers have also explored click chemistry routes. In an early example, researchers coated the surface of maghemite SPION with azide-functional ligands, which were evidenced to be highly versatile platforms for further function-

alization with alkyne-terminated organic moieties.[48] More recently, azide-modified SPION have been coated with short-chain peptides and massive biomacromolecules, *e.g.* enhanced green fluorescent protein (EGFP), maltose binding protein (MBP) and human serum albumin (HSA), by the CuCAAC reaction.[198] Although, the ultimate functionalization step utilizes the rapid and efficient CuCAAC reaction, conversion of the SPION surface to be amenable to click chemistry requires complex reaction schemes similar to ligand-exchange methods. An alternate approach to synthesizing "click-ready" SPION utilizing alkyne-functionalized polymer stabilizers is reported herewith.

4.2 Results and Discussion

To synthesize SPION, Fe_3O_4 nanoparticles smaller than 20 nm are commonly produced by co-precipitation of ferric and ferrous salts (Eq.4.1).[206] Unfortunately broad polydispersity and aggregation result from the co-precipitation process; nevertheless, recent efforts have utilized this method to synthesize biocompatible ferrofluids.[207, 208] A wide variety of surfactants have been utilized to stabilize the materials in both polar and non-polar media. Although these discrete particles are superparamagnetic, the force acting on a nanoparticle in a magnetic field is proportional to the particle size; thus, smaller particles result in smaller forces that can be reasonably affected on the SPION. To generate high applied forces for magnetic steering, nanoclusters can be formed. Nanoclusters are packed particles of adjacent SPION. This leads to a superparamagnetic material that will exhibit a significant mechanical response in the presence of a magnetic field. To stabilize and functionalize the SPION, polymers are often attached to the surface. The size and shape of polymer stabilized nanoclusters have been controlled with block copolymers, and proteins; however, the

degree of functionality has been limited because of the need for a large amount of stabilizing agents. To attain novel surface chemistries, discrete nanoparticles are usually treated with sophisticated ligand exchange reactions to modify the surface moiety for subsequent covalent immobilization of desired molecules. Ligand exchange reactions commonly require non-aqueous solvents, harsh conditions, and multi-step protection sequences that are not amenable to high-efficiency functionalization and high-throughput production. Unlike direct covalent attachment to the nanoparticles, polymer coatings have the potential to incorporate a myriad of of surface functional groups in a single step by designing novel copolymers. An ideal magnetic nanocluster functionality that has been difficult to achieve is to modify the surface of SPION for ready use in the CuCAAC reaction. Few efforts have been made to modify magnetic nanoparticles for click chemistry without direct ligand-exchange on the surface of the particles. In an early example, researchers coated individual nanoparticles with poly(acrylic acid) (PAA) and proceeded with EDC coupling to exchange carboxylates for polymer-stabilized, alkyne-functionalized SPION. Although, they required numerous synthesis steps to develop an alkyne functionality, this work is harbinger for our methodology.[209] To meet the demand for the rapid development and potential clinical application of SPIONs, high-throughput surface coating procedures, like attachment of poly(acrylic acid), and functionalization can be synchronized into one-pot methods.

$$5NaOH + 2FeCl_3 + FeCl_2 = Fe_3O_4 + 5NaCl + 5H_2O \tag{4.1}$$

Herein, a one-pot route to synthesize stable superparamagnetic nanoclusters that deliver a functional surface is developed and the resultant nanoclusters are characterized . Although PAA-capped nanoparticles have been previously reported, this

study is the first to prepare functional, magnetic nanoclusters in one-pot; moreover, the frequency dependent susceptibility is utilized to characterize the cluster formation. Unlike previous studies which covalently decorate the SPION surface, CuCAAC functionality is achieved through the design of the copolymer stabilizer. The nanocluster characteristics are tuned through the design of copolymers based on a PAA chemisorbed stabilizer with an alkyne-bearing, propargyl acrylate comonomer. The nanoclusters are modified by the control of molecular weight, comonomer concentration, and the use of a chain transfer agent. Acrylic acid binds to the SPION surface, and propargyl acrylate was utilized as the functional comonomer due to its general application in the click reactions, including the CuCAAC reaction and thiol-yne addition. The nanoclusters are described by common characterization techniques (DLS, TEM, TGA), and the complex susceptibility of the nanoclusters, which provides a simple measurement of the magnetic cluster size and an insight into the packing of SPION in the nanocluster. Due to the applicability of this technique for generating particles useful in biomedical imaging or drug delivery applications, the nanoclusters were ultimately surface modified with a NIR theranostic moiety, indocyanine green.

Recently, S.H. Foulger *et al.* proposed a method for the click functionalization of nanoparticles by concurrent co-polymerization of a "clickable" copolymer shell onto a polystyrene core.[210] To this end, a functional copolymer is utilized to form functional magnetic nanoclusters. Figure 4.3(a1) presents a schematic of the procedure employed to synthesize fluorescent, magnetic nanoclusters. The iron oxide nanoparticles were prepared using a modified chemical co-precipitation of iron salts with a strong base. To form stable nanoclusters, the synthesized copolymers were incorporated as aqueous solutions with the iron salts. Subsequently, the surface of the nanoclusters were modified *via* the CuCAAC reaction between the alkyne-functionalized surface of the nanoclusters and the azICG fluorophore. Due to the

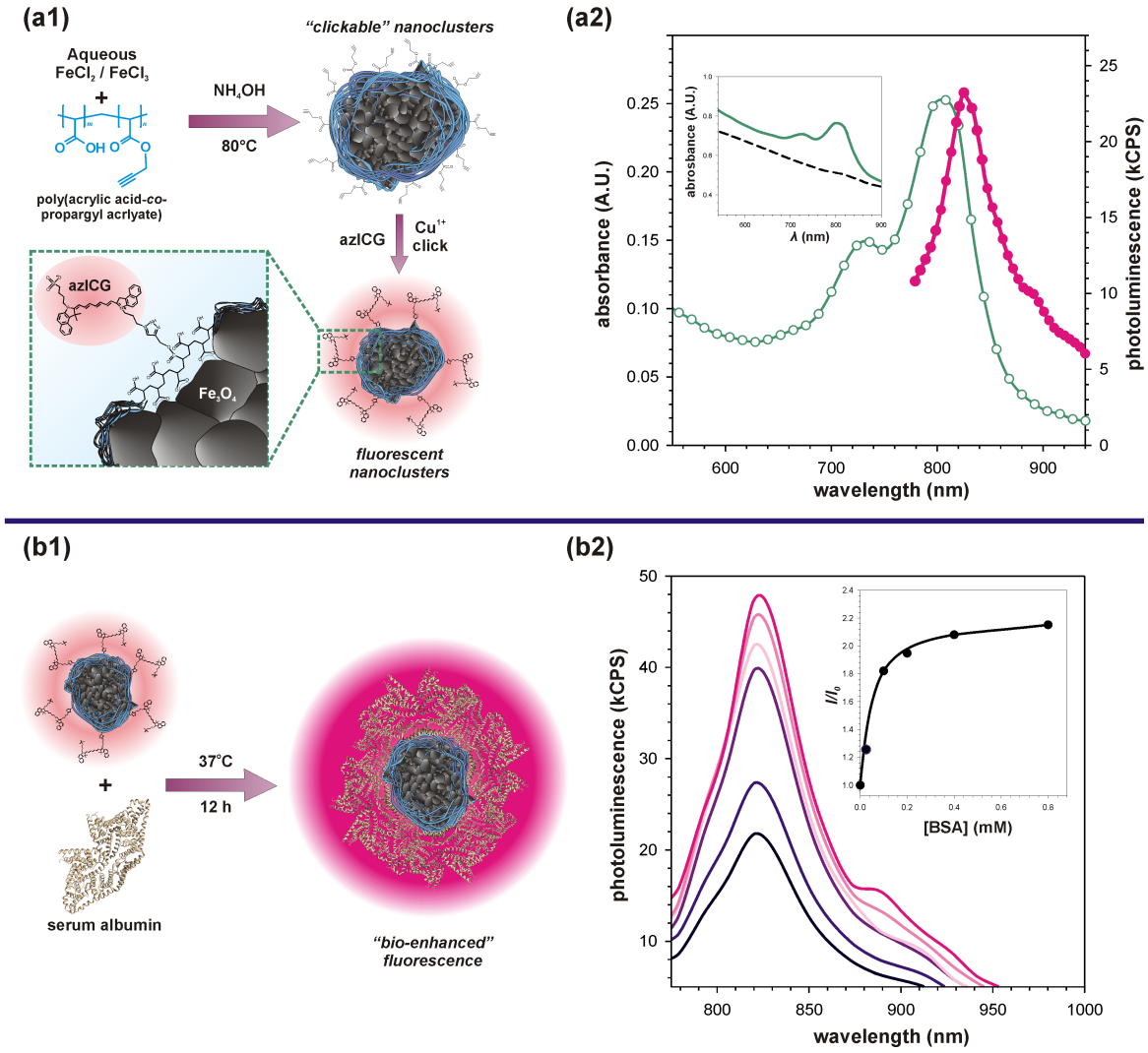

Figure 4.3: (a1) Schematic of the production of polymer-stabilized nanoclusters by chemisorption of poly(acrylic acid-*co*-propargyl acrylate) to Fe_3O_4 nanoparticles and functionalized with an azide-modified indocyanine green derivative (azICG) attached by CuAAC. (a2) Attachment of azICG provides absorption (◯) and photoluminescence (•) response in the NIR wavelengths (aqueous, λ_{ex} = 725 nm). (b1, b2) Subsequent fluorescence enhancement is exhibited after incubation and complexation with bovine serum albumin, (b2, inset) reaching a 2x increase in peak fluorescence.

mild reaction conditions, high conversion rate and chemoselectivity, click reactions are a powerful strategy for magnetic-fluorescent nanocomposite preparation. We therefore carried out the attachment of a popular theranostic agent, indocyanine green (ICG). The CuCAAC click reaction offers a good alternative to other more conventional SPION functionalization schemes that often rely on the reactivity of amide, ester, or thio-ether with naturally abundant carboxyl, amine, and thiol groups. The azICG-conjugated nanoclusters were characterized using absorption and fluorescence measurements. Figure 4.3(a2) shows the absorption and fluorescence (λ_{ex} = 725 nm) spectra of the azICG-conjugated nanoclusters suspended in PBS (pH = 7.4, 0.1 M). The inset shows the convoluted absorbance spectrum of azICG-nanoclusters with a significant response from particle-induced light scattering. Both spectra indicate the presence of conjugated azICG. The absorption spectra of the azICG-nanoclusters indicate an absorption maximum at a wavelength of 800 nm. The emission peak is at a wavelength of 827 nm, with a resulting Stokes shift for the nanocluster-attached dyes of 27 nm. The fluorescent nanoclusters show a bathochromic shift from the absorbance and emission of solvated ICG. This shift is expected from surface-conjugated azICG.[81] These results demonstrate that the CuAAC reaction successfully coupled azICG to the stabilizing polymer, yielding a novel fluorescent nanocluster complex. These results clearly confirm the potential of our method to produce stable, functional magnetic nanoclusters for multimodal theranostic applications.

Figure 4.3(b1) illustrates the subsequent fluorescence *bio-activation* by binding of bovine serum albumin to the surface attached azICG. It has been well established that the fluorescence of high concentration of ICG, whether aggregated in aqueous media or on a surface, is greatly diminished;[211] however, the fluorescence quantum yield of ICG can be promoted by the adsorption of the molecule onto a macromolecule or the analogous binding of ICG to a protein.[81, 212] Accordingly,

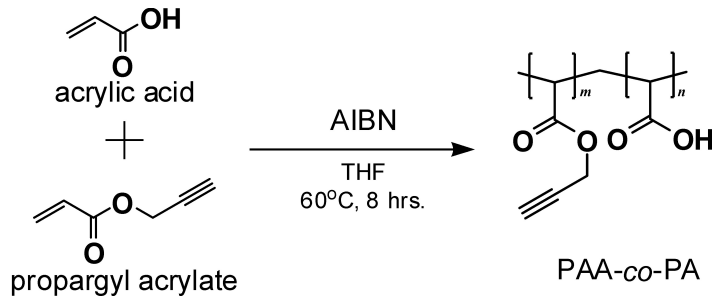

Figure 4.4: Synthetic scheme for production of for poly(acrylic acid-*co*-propargyl acrylate) stabilizer. The same reaction conditions were used to synthesize all stabilizers with the addition of a chain transfer agent (1-nonanethiol) or for acrylic acid, the absence of propargyl acrylate comonomer.

the az-ICG modified nanoclusters were mixed with bovine serum albumin (BSA) at increasing concentrations, and the fluorescent response was monitored after a 12 h incubation period. The observed fluorescence intensity increased with additional BSA, with the rate of increase slowing at [BSA] $>$ 0.25 mM (cf. Figure 4.3 (b2)). The inset of Figure 4.3 (b2) presents the intensity ration (I/I_0) for the azICG-modified nanoclusters at different BSA concentrations. The nanoclusters exhibit a long term 2x increase in fluorescence, where the ultimate fluorescence intensity was monitored after 60 h. The observed fluorescence enhancement with BSA is attributed to the ability of the protein to isolate the hydrophobic azICG moiety from the aqueous environment. The enhancement of the NIR fluorescence by the ubiquitous serum albumin protein greatly increased the potential of utilizing the azICG-modified nanoclusters for directed *in vivo* imaging.

4.2.1 Synthesis and characterization of polymers

In the design of functional copolymers to form iron oxide nanoclusters, both the adsorption properties, integration of bi-functional monomers and, most importantly, the ability to form particle clusters was considered. The intelligent incor-

poration of functional moieties into copolymer coatings will short cut the multistep ligand exchange reactions, while providing a biocompatible, stable surface. It has been established that the carboxylates strongly complex with metal atoms in metal oxides through bidentate resonance bonding. [213–215] Adsorption of acrylic acid-based copolymers have been vetted as nanocluster stabilizers, but to date there has been no efforts to incorporate a functional moiety.[216, 217] Copolymer containing a carboxylic acid groups (acrylic acid) were chosen to serve as anchors which will complex with the Fe atoms at the surface of the Fe_3O_4 nanoparticles. Figure 4.4 shows the general synthetic scheme for producing copolymer stabilizers. Poly(acrylic acid) (AA) and poly(acrylic acid-*co*-propargyl acrylate) (AA-PA) polymers were synthesized to form stable, magnetic nanoclusters. To incorporate an alkyne functionality, the simple free-radical copolymerization of acrylic acid with propargyl acrylate (PA), an acrylic monomer containing alkyne functionality was exploited; however, this copolymerization proved challenging because the use of even small amounts of PA can result in crosslinked gels, since PA is able to act as a bifunctional monomer in free radical polymerizations.[218] Crosslinking during co-polymerization is avoided by balancing the amount of the bifunctional PA monomer, polymerization time and concentration of an incorporated chain transfer agent (CTA), 1-nonanethiol, which curtailed the molecular weight of the copolymers. The synthesized polymers were analyzed by FTIR spectroscopy in order to verify the presence of the polymer stabilizer and incorporated alkyne functionality. The characteristic stretching frequencies of PAA at include O-H stretching at 3431 cm^{-1}; C=O stretching at 1728 cm^{-1}, and the C-O stretching at 1100-1200 cm^{-1}. Figure 4.5 shows the FTIR spectra for stabilizer used in this study: citric acid and the variants of AA and AA-PA. All spectra show the series of broad peaks between 2500 and 3500 cm attributed to the O-H stretching and bound water. The defined, strong peak at 1750 cm^{-1} is directly attributed to

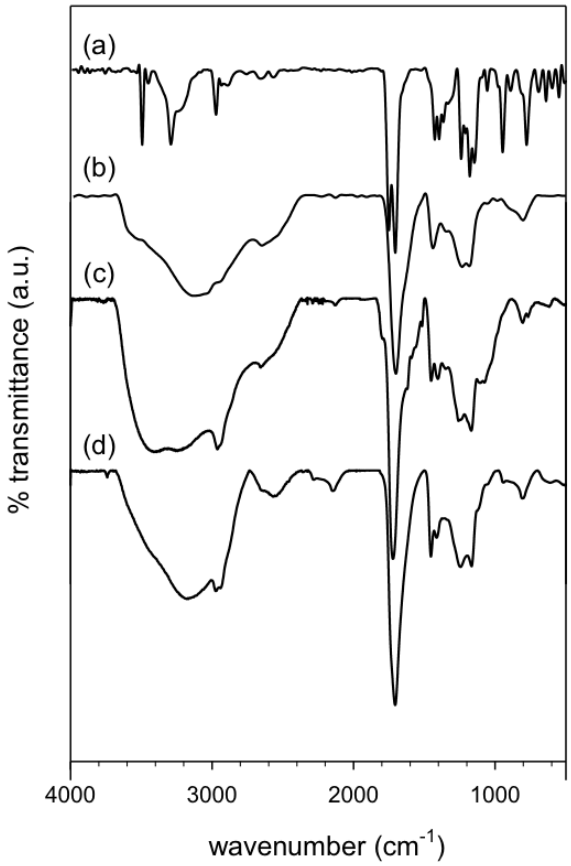

Figure 4.5: FTIR spectra of (a) citric acid, (b) poly(acrylic acid), (c) poly(acrylic acid-*co*-propargyl acrylate), and (d) poly(acrylic acid-*co*-propargyl acrylate)$_{CTA}$. Inset shows expanded view of spectra (2500-1000 cm^{-1}) to emphasize presence of 2130 cm^{-1} peak attributed to the alkyne functionality of propargyl acrylate. Spectra are shifted for clarity.

the C-O stretching in the carboxylates of each polymer. The Figure 4.5 inset clearly shows the peak at 2130 cm^{-1}, attributed to the alkyne functionality and is present in the copolymer that used CTA (AA-PA$_{3\%,CTA}$), while the signal in AA-PA without CTA (AA-PA$_{3\%}$) was within the noise level and diffcult to discern.

Gel permeation chromatography (GPC) was performed on synthesized polymers used to form nanoclusters and molecular weights are presented in Table 4.1. Polymers that did not employ CTA (AA, AA-PA$_{1\%}$ and AA-PA$_{3\%}$) exhibited number averaged molecular weights that range from 16,000-29,000 and have a polydis-

	Mw/Mn	PDI
AA	16.6k/12.6k	1.32
AA_{CTA}	12.8k/4.3k	2.97
$AA\text{-}PA_{1\%}$	22.7k/13.9k	1.64
$AA\text{-}PA_{1\%,CTA}$	17.1k/4.5k	3.79
$AA\text{-}PA_{3\%}$	29.1k/13.0k	2.23
$AA\text{-}PA_{3\%,CTA}$	14.3k/3.2k	4.48

Table 4.1: Molecular weight characteristics of synthesized poly(acrylic acid) (AA) and poly(acrylic acid-co-propargyl acrylate) (AA-PA) determined by gel permeation chromatography. Subscript denotes molar percent PA and use of chain transfer agent (1-nonanethiol).

persity index (PDI) between 1.32-2.23. In contrast, the polymers which employed the CTA exhibited significantly lower molecular weights of 12,800-17,100 and broader PDIs between 2.97-4.48. These results are expected from the incorporation of the CTA.[219] In reference to the seminal work by Robert Ditsch *et al.*, the molecular weights were tailored to produce polymer-stabilized nanoclusters that would form by bridging between polymer coated particles; moreover, the broader PDI will allow for the uniform coating and stabilization of the magnetic nanoparticles.[217] A high-percent of polymer incorporation and uniform coating is critical for maintaining colloidal stability and to achieve an accessible alkyne functionality.

4.2.2 Preparation and characterization of nanoclusters

Iron oxide nanoparticles were synthesized by a standard co-precipitation technique, modified to include the addition of the nanocluster stabilizing polymers. As a reference, iron oxide nanoclusters were also prepared with citric acid, which acts as a small-molecule stabilizer with analogous carboxylate complexation with the Fe_3O_4 nanoparticles.[220–222] Figure 4.6 shows the bare Fe_3O_4 nanoparticles and citric acid formed nanoclusters. HR-TEM was utilized to examine the crystallinity of the Fe_3O_4 nanoparticles and Figure 4.6(c) shows the expected lattice spacing for the [311] plane

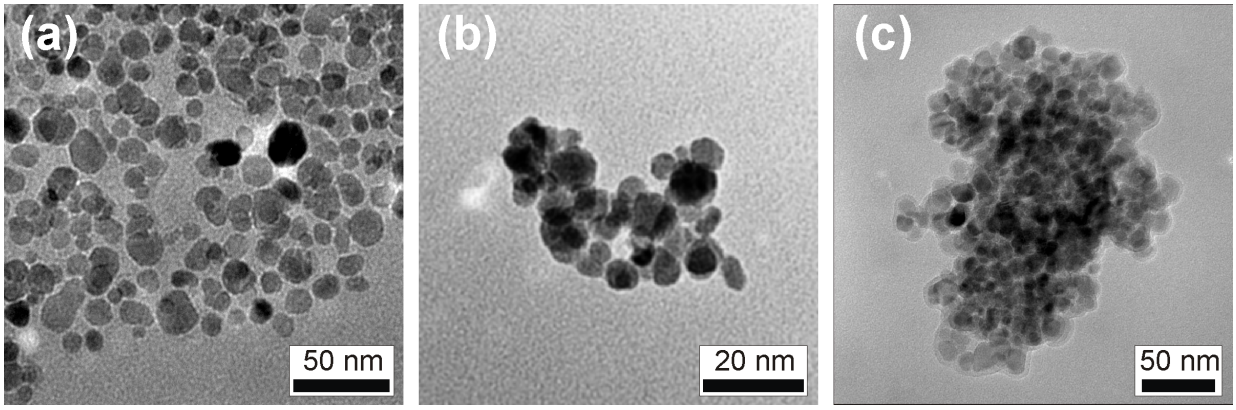

Figure 4.6: TEM micrographs of (a) bare Fe_3O_4 particles, (b) citric acid formed nanoclusters, and (c) AA-$PA_{3\%,CTA}$ formed nanoclusters.

of Fe_3O_4. To form larger nanoclusters and explore the copolymer coatings, both AA and AA-PA replaced citric acid to stabilize the Fe_3O_4 particles and form functional nanoclusters.The prepared nanoclusters were analyzed with FTIR spectroscopy in order to verify the presence of the AA or AA-PA polymers. Figure 4.7 shows the FTIR spectra for the prepared nanoclusters. The peaks between 400 and 600 cm^{-1} can be associated with the stretching and torsional vibration modes of the Fe_3O_4; these assignments are concordant with Keiser *et al.* who described two broad bands at 580 and 400 cm^{-1} associated with magnetite.[223] All nanoclusters show peaks at 2900 cm^{-1} (the stretching vibration of C-H groups), 1442-1400 cm^{-1} (the bending vibration of C-H groups and asymmetric stretching of C-O groups). The broad, intense band at 3500 cm^{-1} is exhibited by the citric acid and polymer-stabilized nanoclusters and is attributed to structural -OH groups and incorporated water. The 1700 peak is attributed to the CanalO vibration (symmetric stretching) of the COOH group present in the stabilizers, which shifts to broader band at 1600 cm^{-1} revealing the binding of a carboxylate to the magnetite surface.[213, 214] In both cases, the position of the carboxylate asymmetric and symmetric stretching frequency exhibits a

	$d_{DLS}{}^a$ (nm)	polymer (w/w)%	$d_X{}^b$ (nm)	f_{max} (kHz)	τ_{eff} (s)	$\tau_{B_{water}}$ (s)
Citric Acid	59 ± 9	-	35.16	15.62	0.00001	0.00001
AA	278 ± 17	18.0	233.78	0.013	0.01136	0.00487
AA_{CTA}	225 ± 19	37.6	213.18	0.015	0.01224	0.00369
$AA\text{-}PA_{3\%}$	162 ± 10	11.7	124.46	0.206	0.00077	0.00073
$AA\text{-}PA_{3\%,CTA}$	136 ± 6	31.3	92.36	1.330	0.00012	0.00030

Table 4.2: Clustering characteristics of magnetite nanoparticles synthesized in the presence of citric acid, poly acrylic acid, and poly (acrylic acid-co-propargyl acrylate). Subscript denotes molar percent PA and use of chain transfer agent (CTA). (a) Dynamic light scattering derived hydrodynamic diameter of nanoclusters. (b) Complex susceptibility derived magnetic volume diameter. (c) Maximum absorption frequency of imaginary component of complex susceptibility.

hypsochromic shift when attached to the magnetite particle surface compared to the un-adsorbed PAA. Non-significant differences between the IR spectra of the nanoclusters were observed, suggesting a uniform mechanism of carboxylate complexation for both citric acid, AA, and AA-PA polymer-particle binding.

The polymer content of the nanoclusters is also a critical parameter in tailoring the stability and size of the nanoclusters. The polymer content of the AA and AA-PA nanoclusters was determined by thermogravimetric analysis (TGA). Figure 4.7 shows the thermograms of polymer stabilized nanoclusters. The degradation between 200 and 400 °C is attributed to the documented thermal degradation of poly(acrylic acid). The polymer content ranged between 11 and 38 (w/w)%, with the highest polymer content in systems that utilized CTA. Both the lower molecular weight and higher polydispersity of polymers containing CTA contributed to higher polymer content of the nanoclusters. It is suggested that the lower molecular weight and polydispersity forms a more uniform, denser coating of the nanoparticles and nanoclusters.[217]

The control of the polymer coating and nanocluster size also effects the nanocluster's stability in an array of aqueous environments. The stability of the nanoclusters is dependent on them remaining strongly charged over a range of pHs,

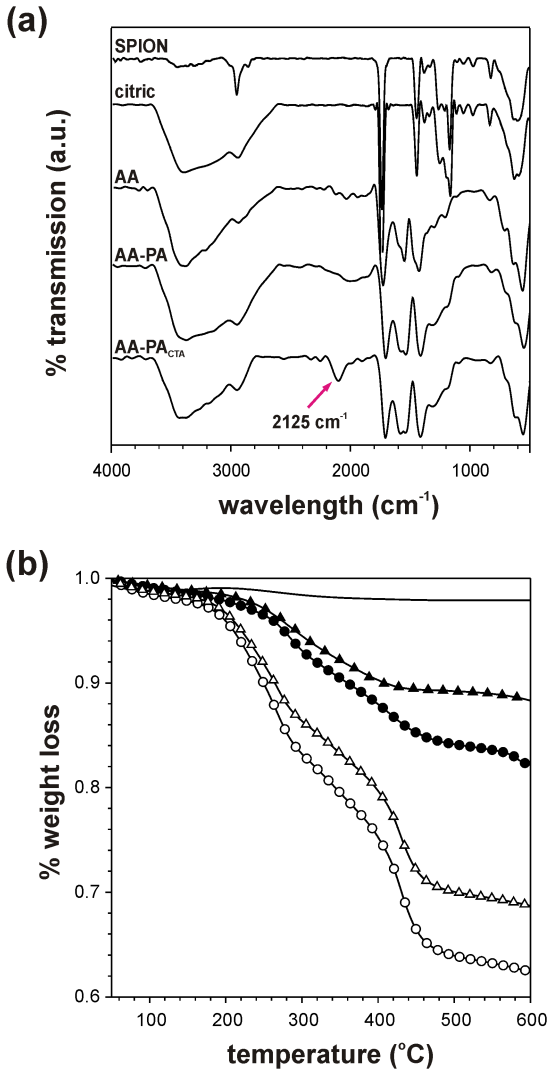

Figure 4.7: (a) FTIR spectra of bare iron oxide nanoparticles and stabilized nanoclusters. (b) Thermogravimetric analysis of bare magnetite nanoparticles (-), poly(acrylic acid-*co*-propargyl acrylate) (▲), poly(acrylic acid) (●), poly(acrylic acid-*co*-propargyl acrylate)$_{CTA}$ (△), and poly(acrylic acid)$_{CTA}$ (○).

which would be encountered for both *in vitro* and *in vivo* applications. SPION, while capable of being suspended in water, are better dispersed in organic solvents; thus, we investigated the stabilizing effects of the copolymer for nanoclusters suspended in a range of aqueous buffers. The stability of the nanoclusters formed with different molecular polymer stabilizers was assessed by ζ-potential analysis. The nanoclusters were considered stable, due to the mutual electrostatic repulsion of the particles, when the absolute ζ-potential is greater than 30 mV. In the case of the nanoclusters, the acid groups of all stabilizers would provide a negative surface charge and particle repulsion. Figure 4.8 presents the ζ-potential of the citric acid, AA, and AA-PA formed nanoclusters. Salt concentration was maintained at a relatively high level, 0.01 M, to ensure a high ionic strength at the extremes of the pH range. Excellent stability is exhibited for all nanoclusters at 5<pH<9, with the ζ-potential values in this range of pH falling below -30 mV. An isoelectric point is clearly realized for citric acid formed nanoclusters (Figure 4.8a) at pH<2. At pH < 6, there is a sharp increase in the ζ-potential for the citric acid stabilized nanoclusters. The destabilization is caused when the carboxylate group in the citric acid nanoclusters is protonated at pH $\leq$ 5.5.[213] The polymer coated nanocluster show a similar effect at pH < 5.5, however the abundance of polymer maintains ζ-potential values less than -30 mV until a pH<3 is reached. Being highly stable in a range of aqueous buffers due to high polymer loading, these nanoclusters are suitable for any number of surface-conjugation reactions and applications.

4.2.3 Characterization of Cluster Formation

Fe_3O_4 nanocluster formation can be initiated by two mechanisms: (1) reduction of surface energy of the nanoparticles followed by the chemisorption polymer to

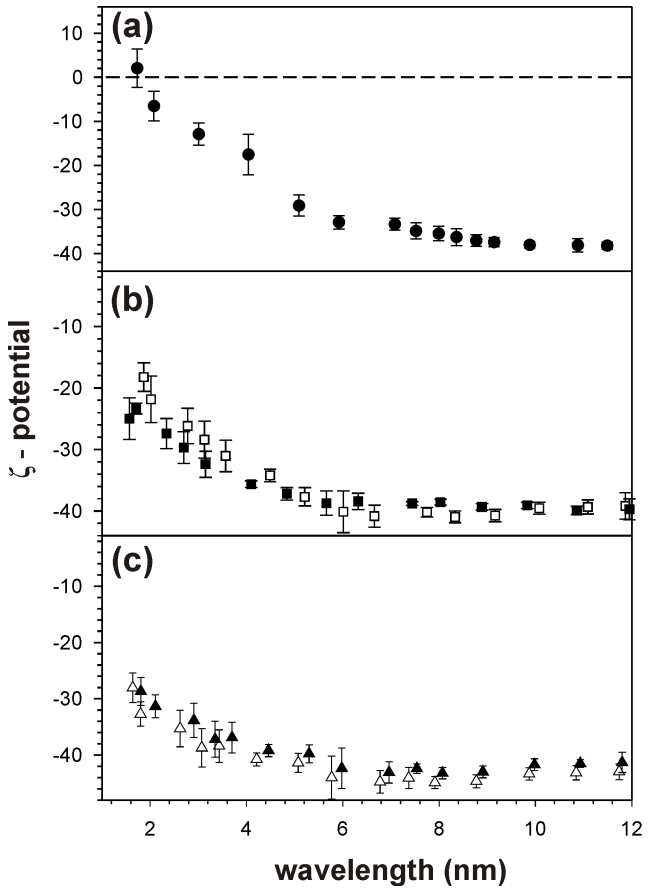

Figure 4.8: ζ-potential of (a) citric acid, (b) AA, and (c) AA-PA formed magnetic nanoclusters, polymerized with and without chain transfer agent. The samples used 2 mol% PA in the polymerization, and polymers were synthesized with (filled) or without (open) CTA.

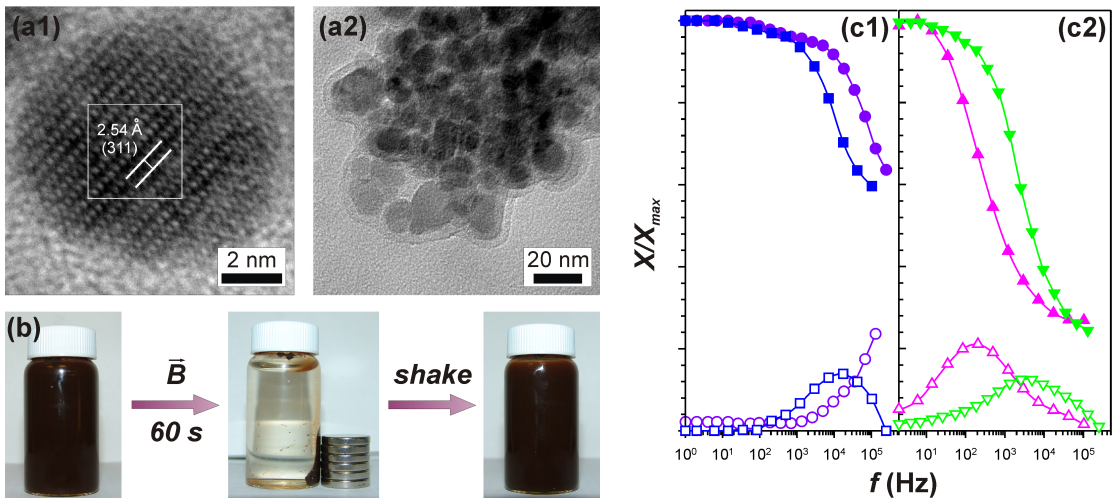

Figure 4.9: (a1) HR-TEM micrographs of AA-PA stabilized nanoclusters showing the the crystallinity of the Fe_3O_4 particles and the [3 1 1] plane with lattice spacing 2.54 $\mathring{A}$, and (a2) the copolymer stabilizer coating on the surface of the nanocluster. (b1, b2) AC susceptibility measurements in the range 1-100 kHz, $X'(\omega)$ (filled) and $X''(\omega)$ (open), versus for (b1) bare-SPION ($\bigcirc$, purple), citric acid stabilized nanoclusters ($\square$, green) and (b2) AA-PA ($\triangle$, pink) and AA-PA_{CTA} ($\triangledown$, green) nanoclusters.

the nanocluster surface or (2) bridging of an extended network of hydrated polymers between individually coated nanoparticles. The predominant bridging effects is dependent on molecular weight, where a minimum in nanocluster size is exhibited by individually coated nanoparticles, followed by a sharp rise in nanocluster diameter as molecular weight increases and bridging occurs.[217]

The clustering of the iron oxide nanoparticles was studied with TEM, DLS and frequency dependent susceptibility measurements. The characteristic cluster size and susceptibility is summarized in Table 4.2. Figure 4.6 shows TEM micrographs of an illustrative AA-PA$_{3\%,CTA}$ nanocluster. TEM micrographs show the nanoclusters were composed of primary crystals between 5 - 20 nm (well within the superparamagnetic regime) and a 5-10 nm stabilizing cap of copolymer. Figure 4.9(a1) presents HR-TEM micrographs of an illustrative AA-PA$_{3\%,CTA}$ nanocluster. The stabilized nanoclusters are comprised of densely aggregated Fe_3O_4 nanoparticles, as illustrated in Figure 4.9-a1 (the characteristic 2.54 $\AA$ lattice spacing corresponds to the d-value of the [3 1 1] plane of Fe_3O_4).

DLS was utilized to determine the hydrodynamic radius of the stabilized nanoclusters. The mean hydrodynamic diameter and standard deviation are provided in Table 4.2. The nanoclusters ranged from 50-300 nm dependent on molecular weight of the agent used for stabilization and cluster formation. The citric acid stabilized nanoclusters showed the smallest hydrodynamic diameter of 59 nm. The clustering of citric acid coated nanoparticles is solely due to minimization of surface energy. The small-molecule stabilizer does not form bridges between particles. The mean hydrodynamic diameter was 278 and 189 nm for PAA and PAA-co-PA polymer coated clusters, respectively; whereas the average diameter for nanoclusters formed with AA$_{CTA}$ and AA-PA$_{CTA}$ was significantly smaller, 228 and 136 nm. The hydrodynamic radius of the nanoclusters incorporates both the size of the clustered particles

and polymer cap. The changes in stabilizer molecular weight and PDI most significantly affect the hydrodynamic radius. The larger molecular weight polymers show a larger hydrodynamic radius which is commensurate with the coating solvated to a higher degree in the water. More of the small molecular weight polymer is attached to the iron surface, reducing its solubility and subsequent hydrodynamic radius. Use of CTA generates polymers with higher PDI, where the smaller chains may rapidly coat the nanoparticles, resulting in enhanced steric stabilization and minimization of cluster formation. As the molecular weight increases, and PDI decreases, the bridging predominates between the unstable nanoparticles and the hydrodynamic diameter of AA and AA-PA nanoclusters approach 300 nm.

The magnetization properties, specifically characteristic relaxation times, can be a useful signal for recognizing SPION interactions and surface properties.[198, 204] There are two distinct mechanisms by which the magnetization of the nanoclusters may relax after an applied magnetic field has been removed:1) bulk rotation of the particle within the carrier liquid (Brownian relaxation) or by rotation of the magnetic vector within the particle (Néel relaxation). The former relaxation process is characterized by a Brownian rotational diffusion time given by Eq. 4.2, and the latter is characterized by an internal Néel relaxation given by Eq. 4.3:

$$\tau_B = 4\pi\eta r^3/kT \tag{4.2}$$

$$\tau_N = \tau_0 e^{\sigma} \tag{4.3}$$

where the magnetic anisotropy is assumed uniaxial, η is the kinematic viscosity, r is the hydrodynamic radius, σ is the anisotropic energy constant, and a damping

constant, τ_0, is approximated as 10^{-9} s.[224, 225] In a ferrofluid with a distribution of particle and nanocluster size, both relaxation mechanisms will contribute to the magnetization, with an effective relaxation, τ_{eff}, defined in Eq. 4.4.[226] If the nanoclusters are formed by surface energy minimization of particles clustering before polymer stabilization minimally sized clusters will form and, due to tight packing of the nanoparticles, the magnetic properties of the particles will affect each other and Néel relaxation would dominate.[227] Otherwise, the iron oxide nanoparticles would be stabilized within the polymer matrix, not interfere with each other and the nanocluster would relax through a Brownian mechanism.[228–230] In the case of the reported nanoclusters, the polymers coat particles, then form clusters which would results in a Brownian relaxation at low frequency.

$$\tau_{eff} = \tau_N \tau_B / (\tau_N + \tau_B) \tag{4.4}$$

The frequency dependent susceptibility of the nanoclusters was measured at low frequency , 1 Hz - 250 kHz. The frequency dependent susceptibility may be written in terms of its real and imaginary components (Eq. 4.5).

$$X\,(\omega) = X'(\omega) - iX''(\omega) \tag{4.5}$$

Accordingly, the complex susceptibility has a frequency dependence modeled from Debye's form on dielectric dispersions,[231] as given by Eq. 4.6,

$$X(\omega) - X_\infty = (X_0 - X_\infty)/(1 + i(\omega)\tau_{eff}) \tag{4.6}$$

where

$$\tau_{eff} = 1/2\pi f_{max} \tag{4.7}$$

and

$$X_0 = nm^2/3kT\mu_0. \tag{4.8}$$

In Eq. 4.7, τ_{eff} is the effective relaxation time and f_{max} is the frequency at which $X''(\omega)$ is a maximum. In Eq. 4.8, X_0 is the static complex susceptibility at $\omega = 0$, n is the particle number density, m is the magnetic moment, k is Boltzmann's constant, T is absolute temperature and μ_0 is the absolute permeability. In the ideal case, the predicted intersection of the real and imaginary components occurs at the maxima of X$''$, when $\omega\tau = 1$. In the real case,the polydispersity of the particles results in a significant shift of the frequency dependent susceptibility which accounts for the distribution of particle sizes, Brownian, and Néel relaxation.

When Fe_3O_4 nanoclusters are formed by surface-energy minimization of nanoparticles prior to polymer stabilization, the proximity of the nanoparticles cause non-discrete magnetic response, the nanoparticles become confined and Néel relaxation dominates.[227] However, the polymer stabilized nanoclusters would exhibit segregated magnetic propertes, where the nanoclusters would relax by the Brownian mechanism.[229, 230] The effective relaxation times were calculated from Eq. 4.7 and summarized in Table 4.2. The effective relaxation times for polymer stabilized nanoclusters are within the expected range for Brownian relaxations (0.00005-0.02 s). Brownian relaxation dominates due to the size and mobility of the nanoclusters.[229] The bare nanoparticles show minimal clustering due to surface energy minimization, and they clearly exhibit a much faster relaxation time, with a distribution measurable at higher frequencies, attributed to Néel relaxation of individual particles (Fig. 4.9c1). The citric acid stabilized nanoclusters also exhibit a fast relaxation time, suggesting the distribution of relaxation mechanism is skewed toward characteristic Néel relaxation; however, a particle size distribution could be attained at the mea-

sured frequencies.. This distribution can be expected from the large gap between real and complex susceptibility, suggesting the imaginary component may peak at a higher frequency (Fig. 4.9(c1, c2). Upon the addition of the stabilizing polymers and copolymers, the imaginary absorption peak is shifted toward lower frequencies as shown in Figure 4.9(c2). The shift toward low frequency absorption is indicative of larger nanocluster diameter and desired cluster formation.

To verify the effect of Brownian relaxation in the polymer stabilized nanoclusters, the complex susceptibility was measured at an increased viscosity, by changing the carrier liquid from water (0.00088 Pa·s) to glycerol (50 (v/v)%, 0.00669 Pa·s) at 25 °C.[228] The AA-PA stabilized nanoclusters show a significant shift in the f_{max} due to viscosity change (Fig.4.10b). All Brownian relaxation times are within the expected time domain, confirming that the nanoclusters are discrete nanoparticles coated by polymer, which do not effect their neighboring particles magnetic properties. This also explains the comparably high loading of polymers in the nanoclusters, *i.e.* the polymers penetrate throughout the nanocluster. As a comparison, non-stabilized clusters and citric acid stabilized nanoclusters were suspended in glycerol and show little to no change in f_{max} in relation to viscosity. Brownian relaxation is directly proportional to viscosity and this confirms that Brownian relaxation is responsible for relaxation in the polymer stabilized clusters; whereas, in citric acid and bare particles, Néel relaxation may be the dominate mechanism. The large difference between real and imaginary susceptibility in the citric acid and bare nanoparticles suggests there is a high frequency absorption peak that is not monitored. The ideal maximum susceptibility is 0.5 relative to a real susceptibility maximum of 1.[229, 230] Our measurements show that in primary agglomerates of nanoparticles the magnetic coupling between crystallites is quite low and the agglomerates can retain the superparamagnetic character of individual crystallites in combination with much larger

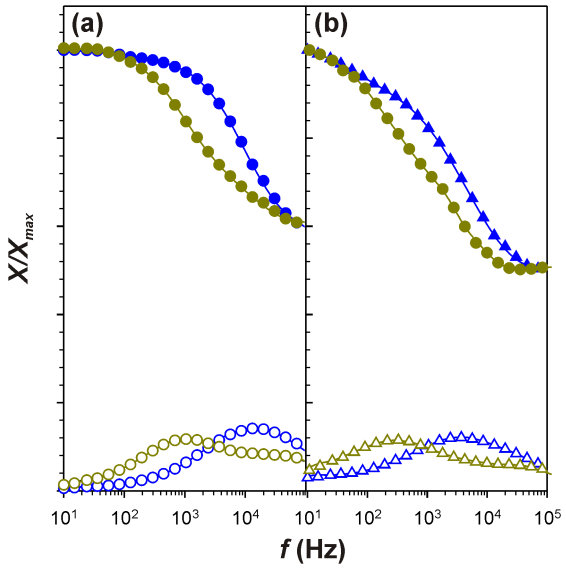

Figure 4.10: Plot of normalized magnetic susceptibility, X′(ω) (filled) and X′′(ω) (open), versus frequency for (a) citric acid and (b) AA-PA$_{CTA}$ nanoclusters in water (◯, black) and glycerol solution (△, red).

density of magnetic material and higher magnetic force compared to the individual crystallite. This has beneficial consequence for applications like magnetic hyperthermia or magnetic drug delivery where superparamagnetic particles are preferred but larger particles could improve magnetic steering and heat generation.

4.3 Conclusions

In this effort, a general methodology for producing magnetic nanoclusters with an elevated alkyne functionality was demonstrated and the production of SPIOn in the presence of different chelating-copolymers was studied to better understand nanocluster formation behavior. The functional nanoclusters were formed by the adsorption of poly(AA-co-PA), which provides both colloidal stability and surface functionality. Complicated synthesis routes previously required for the surface func-

tionalization of SPIONs are circumvented by designing the copolymer stabilizer prior to nanocluster formation. By copolymerizing acrylic acid with propargyl acrylate, a click-ready coating was synthesized, that would anchor itself to the SPION. The size of the nanoclusters and thickness of the polymer coating was controlled by tailoring the molecular weight of the adsorbed polymer with the use of a chain transfer agent during synthesis. For the first time, the complex susceptibility measurements of the particles was utilized to investigate the nanoparticles clustering formation. Nanoclusters exhibited a relaxation time dominated by Brownian relaxation, confirming that the particles coat with polymer and then bridge to form clusters. The availability of accessible alkyne groups on the surface of the aqueous-phase nanocluster allowed for the surface modification of the particles CuCAAC click reaction with an azide-modified ICG. It is predicted that this method can be extended to the synthesis of clinically viable hyperthermia nanoclusters, which exploit the CuCAAC click reaction for the targeting of nanoclusters, and direct delivery of therapeutic agents.

4.4 Experimental Details

4.4.1 Materials

Ferrous chloride tetrahydrate ($FeCl_2$), ferric chloride hexahydrate ($FeCl_3$), ammonium hydroxide, copper (II) sulfate ($Cu(II)SO_4$), sodium ascorbate, azobisisobutyronitrile (AIBN), 1-nonanethiol, acrylic acid (99%) and propargyl acrylate (98%) were purchased from Sigma-Aldrich (St. Louis, MO). Inhibitor was removed from all monomers with a column of Alumina Basic (60-325 Mesh). Tetrahydrofuran (THF) (HPLC grade) and dialysis tubing (SPECTRA, 10000 and 50000 MWC) were purchased from Fisher Scientific (Waltham, MA). THF was dried using a Innovative

Technologies Inc. Pure Solv MD-2 solvent purification system prior to use. Deionized water was obtained from a Thermo Scientific Barnstead Nanopure System and exhibited a resistivity of $\sim 10^{18}$ ohm^{-1}cm^{-1}.

4.4.2 Synthesis of poly(acrylic acid) and poly(acrylic acid-*co*-propargyl acrylate)

Standard acrylic acid and propargyl acrylate incorparating copolymers were synthesized by solution, free-radical polymerization. All polymerizations were performed in dry THF (2 mL) under a nitrogen atmosphere.An amount of monomer (2 g) and initiator (AIBN, 2 mg) was charged into the reaction vessel, and polymerization was allowed to proceed for 8 hrs. A chain transfer agent (CTA), 1-nonanethiol, was used in the polymerization reaction to tailor the molecular weight and polydispersity of the polymers. Polymers were precipitated in cold methanol, filtered and collected. The precipitation cleaning was repeated 3x in order to remove all excess monomer, initiator and CTA.

4.4.3 Preparation of magnetic nanoclusters

Iron oxide nanoparticles were synthesized by a modified co-precipitation method. Aqueous solutions of ferric chloride ($FeCl_3$) and ferrous chloride ($FeCl_2$) were mixed in a 2:1 molar ratio in a three-necked round bottom flask, fitted with a paddle stirring mantle, thermocouple and nitrogen purge. $FeCl_3$ (2.703 g) and $FeCl_2$ (0.9946 g) were dissolved in deionized water (50 mL), then vigorously stirred and purged with nitrogen for 10 min. The solution was purged with nitrogen to prevent unwanted oxidation. The solution was heated to 80 °C before the drop-wise addition of ammonium hydroxide (20 mL) until the solution reached pH $\sim$13. Stirring continued for 30 min.

and the solution turned from brown to black, before the reaction was stopped by cooling and magnetic precipitation of the nanoparticles. For nanocluster formation, 0.5 g (∼13 (w/w)%) citric acid or polymer stabilizer was added to the suspension of nanoparticles and the mixture was stirred for 90 minutes before cooling and cleaning. The formed nanoparticles or nanoclusters were removed from solution by repeated magnetic separation and dispersion in deionized water. The final concentration of nanoparticles and nanoclusters was prepared at ∼50 mg/mL.

4.4.4 Surface modification of magnetic nanoclusters

Synthesis of an azido-modified ICG (azICG) was reported elsewhere.[81] For a typical surface modification of the nanoclusters, azICG (5 mg), sodium ascorbate (15 mg), AA-PA formed nanoclusters (10 mg) and deionozed water (10 mL) were combined in a round bottom flask. The solution was purged with nitrogen for 10 min. before the addition of $Cu(II)SO_4$. The resulting mixture was maintained at a temperature of 28.8 °C for 1 hr. The reaction was stopped by the removal of unreacted azICG, sodium ascorbate, and $Cu(II)SO_4$ through a repeated particle washing procedure consisting of magnetic collection and dispersion in water. The resulting particles were dialyzed against deionized water for 48 hrs. at 4 °C using a dialysis bag with a 10,000 MWCO.

4.4.5 Characterization methods

Molecular weights of the polymers (diluted to 1 mg/mL in chloroform) were determined by gel permeation chromatography (GPC) (chloroform at 1.0 ml/min), using a Waters 515 pump, four 7.8 x 300 mm Styragel columns (HR 2, 3, 4, 6), a Waters 2414 refractive index detector and a Waters 2487 tunable absorbance detector.

Reported molecular weights are relative to narrow distribution polystyrene standards (Mw = 2,330 - 980,000). Transmission electron microscopy was conducted with a Hitachi H7600T TEM. Hi-resolution TEM (HR-TEM) was conducted with a Hitachi 9500. The infrared spectra were recorded at room temperature in the wavenumber range of 400-4000 cm^{-1} and referenced against air with a Nicolet 6700 FTIR spectrometer. Thermogravimetric analysis was conducted with a TA Hi-res TGA 2950 Thermogravimetric Analyzer. Dried powder samples were heated at a constant rate of 20°C/min from 30-700° under a nitrogen purge. The loss in mass after heating indicated the polymer component of nanoclusters. Hydrodynamic diameter was measured using a Coulter N4 Plus dynamic light scattering (DLS) analyzer. ζ-potential measurements were made with a Brookhaven Instruments Corporation ZetaPlus Zeta Potential Analyzer. Complex susceptibility measurements were made using an Imego DynoMag AC Susceptometer. UV/Vis/NIR absorbance spectra were collected using a Perkin-Elmer 900 spectrometer. Photoluminescence (PL) spectra were collected using a Thermo Oriel xenon arc lamp (Thermo Oriel 66-902) mated with a Thermo Oriel Cornerstone 7400 1/8m monochromator (Thermo Oriel 7400) and a Horiba Jobin-Yvon MicroHR spectrometer coupled to a Synapse CCD detector.

4.5 Attributions

The synthesis of the azide-modified ICG and PAA-PA was conducted by Dr. Iurii Bandera and Ryan D. Roeder, respectively, at Clemson University. Magnetic susceptibility measurements were made with the aid of Dr. Olin Thompson Mefford IV and Steven R. Saville at Clemson University. Portions of this work are in preparation for publication as Daniele *et al.*, *Copolymer stabilizers as a facile route to functional nanocluster surfaces exhibiting bio-activated fluorescence*, 2012.

CHAPTER 5

Microfluidic Micromaterials: A "photo-click" route to hydrogel fibers for cell encapsulation

---

5.1 Introduction

Biosensors are self-contained devices which utilize biological elements, *e.g* proteins, DNA, or whole cells, in conjunction with a transducer to convert biological expressions into an electronic signal.[232–234] Biosensors need to be rugged, incorporate a large number of sensing components to ensure a large signal, and operate remotely with little maintenance. Cellular immobilization is the key to the complex design and integration problems of viable biosensors. Immobilization schemes need to be tailored for structural, biological, and chemical stability in the presence of environmental conditions, and designed to transport analytes rapidly enough to allow for short response times.[232] Immobilization schemes must also co-localize the biological element with the transducer to ensure proper signal output. Common immobilization methods are physical adsorption to a surface, covalent binding to a surface, and entrapment in hydrogels.[235, 236] The goal of the work in this chapter was to design and produce viable hydrogel scaffolds for use in whole-cell biosensors. Presented and compared is

a new technique for high-throughput production of cell-containing hydrogel fibers by a benign method which does not adversely affect the viability of entrapped cells.

The choice of biological element used in a biosensor depends on the analytes being monitored, the storage capacity of the element, and the environmental and operational stability of the element. Biological elements include enzymes, DNA, antibodies, antigens, and whole cells.[232, 234] Whole-cell biosensing, unlike small-molecule and protein-based detectors, are capable of detecting an array of general upsets in their environment. Viable whole cells are particularly valuable as they utilize respiratory and metabolic functions to sense analytes. They also have the capability of demonstrating the potential effects of certain analytes to living organisms.[237] Cell signal expression can be positive as in the case of cell growth or mitosis; adverse expressions can also be observed as in the case of protective responses or cell death. Microbial cells are low cost, have large population sizes, grow rapidly, and require little maintenance.[238] Most importantly, microbial communities easily adapt to their environment, metabolize a wide range of chemicals, and can be genetically engineered to produce a desired signal.

Applications for immobilized bacteria include controlled delivery of biofertilizers or biopesticides, bioreactors, bioremediation, environmental sensors, and microbial fuel cells.[239–244] A popular method for bacterial attachment is the growth of biofilms on suspended particles or solid substrates.[245, 246] However, biofilm-mediated immobilization does not protect the cells from mechanical or chemical damage; consequently, sustaining high levels of viable bacterial cells within these systems for extended periods is tenuous at best.[239, 247] Synthetic materials that encapsulate cells offer more protection from damage during use than immobilizing the cells on a surface, but may block transport of nutrients or targeted chemicals to the cells. Hydrogels have been widely explored for encapsulation because of biocompatibility and

facile control of analyte transport; bioactive constituents encapsulated in hydrogels include complementary enzymes, bacterial, and mammalian cells.[248–250]

The combination of hydrogel chemistry and fiber morphology provides an ideal platform for the encapsulation of cells for many large-scale applications, *e.g.* biofertilizers and biopesticides. While the surface area-to-volume ratio (SA:V) of the hydrogels is inherently high, organizing the hydrogels into fibers can be used to promote the spatial distribution of cells and flux of liquids containing essential nutrients or chemical targets to the cells. Depending on the application, the fibers can be used as individually as tubes or in concert as woven mats for applications such as sensing, filtration, tissue engineering or wound healing.

5.1.1 Copper-free click chemistry

In spite of the success of click chemistry within the past decade, there are limitations associated with its application when designing biosensors. The CuCAAC reaction employed extensively in the various biomedical materials may show cytotoxic side-effects attributed to residual copper; therefore, much effort has been devoted to copper-free click cycloaddition reactions in chemical biology. For click reactions to be used in contact with living systems, the copper catalyst must be completely removed or alternatives, such as Staudinger ligation, strain-promoted hetero-cycloadditions, or thiol-based reactions must be employed. One feasible solution is the introduction of a strained cyclo-octyne as a source of the alkyne as originally enveloped and recently reviewed by Carolyn R. Bertozzi; the review also reminds of the importance of bio-orthogonality to applications *in vivo* and *in vitro*.[251, 252] These chemical modifications of course add to the complexity of the introduction of alkyne but this presently seems to be an unavoidable payload if copper-free click cycloaddition is

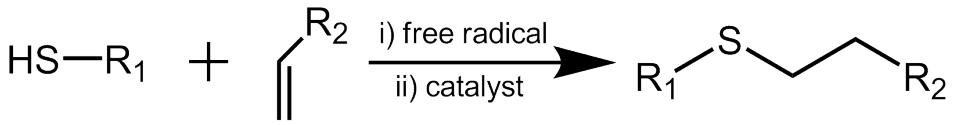

Figure 5.1: Free-radical or catalyst mediated thiol-ene click reaction.

necessary. Alternate reactions, avoiding cycloaddition, have been promoted as click reactions, most favorably the thiol-based addition reactions.

5.1.1.1 Thiol-ene Click Reactions

The favored Cu-free click reaction are radical or catalyst mediated thiol-based polymerizations.[253, 254] The thiol-ene reaction, used industrially since the 1970's, has recently demonstrated its importance[255] employed as a click method between small molecules and larger biomacromolecules, such as collagen and proteins.[256, 257] This approach has also been used to build complex nanostructures such as dendrimers, star polymers, and inorganic composites.[258–260] The thiol-ene process is also attractive for making bulk materials because it is insensitive to oxygen, gives low shrinkage, imparts high thermo-stability, and proceeds to relatively high conversion, all while crosslinking at a rate that is as rapid as traditional UV-crosslinking.[254, 261, 262]

The thiol-ene (Figure 5.1) reaction was first explored by Theodor Posner in 1905.[263] An ideal thiol-ene reaction revolves around the alternation between thiyl radical propagation across the -ene functional group and the chain-transfer reaction, which involves abstraction of a hydrogen radical from the thiol by the carbon-centered radical.[264] The addition of the thiol across the -ene double bond is exothermic, with reaction enthalpies ranging from 10.5 kcal·mol^{-1} for the electron-rich vinyl-ether double bond to 22.6 kcal· mol^{-1} for the electron-poor double bond of an N-alkyl maleimide.[265, 266] For a given thiol, electron-rich enes polymerize much more

rapidly than electron-poor -enes. Reduced rates and conversions are obtained for 1,2-substituted internal -enes, which is presumably due to steric considerations and a reversible addition of the thiyl radical to the internal -ene. For ideal thiol-ene reactions, such as those observed for norbornenes and vinyl ethers,no homopolymerization or chain growth is observed, thus implying that the overall rates of chain transfer and propagation must be essentially identical.[267] The thiol-ene reaction is the only known free-radical addition reaction in which various chemical groups (*e.g.* phenolic rings, ethylene glycol groups, ester groups) can be incorporated into the main chain backbones, potentially allowing for a greater amount of property variation. The thiol-ene polymer is not restricted by the presence of pure carbon-carbon chains, though these can be included if needed. The thiol-ene free radical addition polymerization reaction, assuming the thiol-ene cannot homopolymerize. Termination is generally thought to occur by radical recombination, and shows how inhibition by oxygen is avoided in this reaction by the peroxy radical still shows significant affinity for hydrogen abstraction from the thiol group, propagating the radical and allowing the reaction to continue. In the ideal purely step-growth thiol-ene reaction, no homopolymerization, in which the carbon-centered radical propagates through the -ene moiety occurs, and conversion approaches 100%. The net reaction is the combination of the thiol and -ene functional groups, which causes the molecular weight and network structure to evolve in a manner that is identical to other step-growth polymerization reactions whilst simultaneously enabling all of the benefits of a rapid, photoinitiated radical mediated process.[255]

Acrylates can be incorporated into the thiol-ene system because the acrylate group contains pendant unsaturated carbons. These, too, must be difunctional in order to avoid premature chain termination, but acrylates can homopolymerize, adding another step to the above reaction scheme. This added step increases the complica-

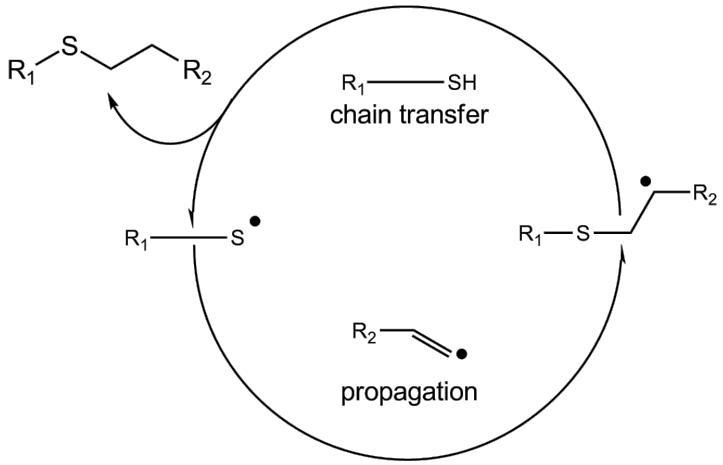

Figure 5.2: Free-radical initiated thiol-ene reaction mechanism.

tion of both the kinetics, because the -ene and acrylate compete for thiyl radicals, and the network structure, since methacrylate carbon-centered radicals can abstract a hydrogen from a thiol in the normal fashion or it can homopolymerize as illustrated in Figure 5.3. The relative rates of these cycles, which are dictated by the chemical properties of the thiol and acrylate, the component concentrations tailor the final network structure and mechanical/physical properties. Some of the most comprehensive studies on the photopolymerization of the thiol-ene system determined how various neighboring groups to both the -ene and the thiol affect their reactivities. It was found that an -ene with a neighboring vinyl ether is much more reactive than one with an allylic structure, which itself is more reactive towards hydrogen abstraction from a thiol than a plain alkene. Also, methacrylates are less reactive than acrylates due to the methyl group. The most reactive thiol type is mercaptopropionate esters followed by mercaptoacetates, and the least reactive type is alkane thiols. Some researchers have even investigated the unique ability of thiols to radicalize without photoinitiators, creating polymers without potential contaminants. By combining methacrylates

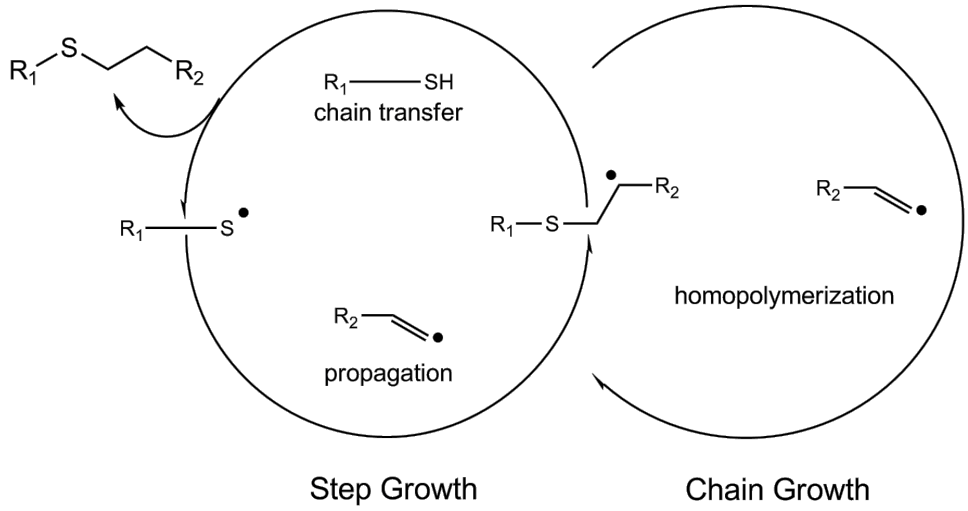

Figure 5.3: Thiol-ene/acrylate polymerization mechanism, showing the additional reaction step for homopolymerization of acrylates.

and thiols, a broad range of material properties are accessible from the large number of commercial methacrylates that are available.

5.1.1.2 Acrylate *photo-flow*: Another Click Reaction from Old Parts and a New Process

A practical limitation of developing thiol-click reactions for viable biosensors, and the excessive supply of thiols in biological systems renders them non-orthogonal in biological applications. As the click chemistry philosophy continues to spread through the area of materials science, polymers and biotechnology, more and more clickable building blocks can be expected to become easily available; nonetheless, there is a common constituent of materials repository that can be viewed as a click reaction. Traditional polymer science offers a potential click reaction: acrylate photopolymerizations.

Acrylate photopolymerizations are high yield, modular, produce no bi-products,

can be conducted in benign or no solvent (depending on starting ligands); however, to be considered click reactions, acrylate photopolymerizations must overcome the apparent oxygen sensitivity. Acrylate polymerizations are free-radical, solvent-less, radiation induced, and are step or chain growth reactions, very similar to the thiol-ene click reactions. In the free-radical polymerization scheme, an initiator sensitive to the wavelength of incident radiation, such as the ultraviolet (UV) initiator 2,2-dimethoxy-2-phenylacetophenone (DMPA), is cleaved into free radicals which begin the polymerization reaction. The free radical from the initiator then breaks a nearby double bond, creating a new covalent bond to the nearby molecule and propagating the radical further along the newly-forming chain. The propagation step involves the newly propagated radical attacking other nearby double bonds in succession, and termination involves various pairs of radicals interacting with each other to cause mutual extinction by either coupling, where two small chains meet up to become one larger chain, or disproportionation, resulting in the two smaller chains remaining separate and in the regeneration of a double bond. Free radical photopolymerization is popular because of it relatively low energy requirements, ability to be performed at ambient temperatures, and rapid speed. They are popular because of their relatively low cost, ready availability, rapid polymerization kinetics, optical clarity, toughness, the broad range of achievable properties, and the relative ease of monomer synthesis and polymer manufacture and processing. Methacrylates are popular materials for biomedical engineering because of their potential biocompatibility, the ability to photopolymerize them *in situ*, and the ability to tune the mechanical and degradative properties of the network.

To achieve click status, the acrylate materials need to be cured without the need for a nitrogen atmosphere, expensive initiator combinations, or the extremely high light intensities that are frequently required to overcome oxygen inhibition in

purely methacrylate polymerizations. This report will show that at relatively small volumes, methacrylate photopolymerization can be considered a click reaction. The enhanced ability to overcome oxygen inhibition and the control over the network structure facilitates the implementation of methacrylate polymerization in the formation of hydrogels and tissue engineering matrices, for which polymerizations in the presence of oxygen are necessitated by the clinical environment and the requirement for cell viability.Thereby reducing the photoinitiator concentration required to obtain a fast, high-conversion polymerization process with a rate acceleration of a factor of about 10. The structure of methacrylate polymers can vary from a thermoplastic to a thermoset, depending on the concentration and structure of the monomers added. A copolymer of purely mono-functional monomers results in a thermoplastic by definition, while the addition of di- or higher-functionality monomers results in thermosets ranging in behavior from lightly-crosslinked elastomers to highly-crosslinked, three-dimensional networks.

5.1.2 Poly(ethylene glycol) hydrogels and *click-gels*

Although the biological element can be spared the the cytotoxic effects of Cu(I)-catalyzed reactions by exploiting either thiol-ene or acrylate photopolymerization, developing an inert encapsulation medium is critical to ensure the benign immobilization of the bacterial community. Immobilization matrices must prevent cells from dislodging from the matrix during production and transport, yet still enable cellular trafficking and analyte diffusion with the environment and signal transduction. An ideal immobilization matrix would be functional at ambient temperatures, survive harsh environmental conditions including contaminated zones and turbidity, and allow the flow of cells, nutrients, oxygen and analytes through the matrix along

with wastes and signals out.

Hydrogels are applicable immobilization matrices due to their high water content, pliability, biocompatibility, and easily controlled diffusion characteristics.[268, 269] Common immobilization matrices include naturally occurring alginates, copolymers consisting of (1-4) linked D-mannuronic acid and L-guluronic acid.[270] Alginates are ionically crosslinked between the carboxylic acid elements through divalent ions, usually Ca^{+2}. Natural immobilization hydrogels typically have poor structural stability; their crosslinks are ionic as opposed to covalent, which are easily broken apart by cationic scavengers such as sodium citrate and chelators such as ethylenediaminetetraacetic acid (EDTA).[271] In addition to the weak bonding structure, natural hydrogels are also susceptible to biodegradation, making their use somewhat limited depending upon the cell type being immobilized. Alternative synthetic hydrogels include poly(ethylene glycol, poly(vinyl alcohol), poly(methacrylic acid), and poly(2-hydroxyethyl methacrylate). Poly(ethylene glycol) (PEG)-based hydrogels have attracted broad interest as a scaffold material for biohybrid applications because PEG is well hydrated in an aqueous environment, minimizing minimizes the adsorption of proteins and cell-scaffold interactions.[272] A variety of approaches have been utilized to form PEG hydrogels, including radiation cross-linking, modification with fumarate, acrylate, or methacrylate groups followed by free radical photopolymerization, and linking sulfone terminated multiarm-PEG with di-sulfhydryl cross-linkers by click Michael's addition.[73, 272–274] In particular photopolymerization using a suitable free radical photoinitiator allows hydrogels to be formed into a variety of shapes *in situ* under relatively mild polymerization conditions and aqueous environments compatible with living cells. Photopolymerization, including photolithography, of PEG dimethacrylate (PEGDMA) has been employed specifically for tissue engineering applications.[275–278]

The unique design parameters for viable biohybrid scaffolds have garnered attention for the use of click chemistry as a route to novel gels and polymer networks. Multivalent azide and alkynes can be directly reacted, generating networks with a high level of cross-linking density due to the high efficiency of the azide-alkyne click reaction. By appropriate choice of the corresponding building block (examples of small monomer, oligomeric or polymeric) azides-alkynes, the corresponding properties of the networks, such as swelling character, hydrophobic/hydrophilic properties, density or functionality, can be controlled. An early example was the production of crosslinked polymeric adhesives synthesized from polyvalent azide and alkyne building blocks, which owe their adhesiveness to the strong affinity of triazoles for metal ions and surfaces. Jöns Hilborn *et al.* first reported the synthesis of "clicked" poly(vinyl alcohol) (PVA)-based hydrogels by combining azide-modified PVA and acetylene-modified PVA in the presence of a Cu(I) catalyst.[279] Well-defined PEG-based hydrogels with improved properties were later prepared by C.J. Hawker *et al.*, also using the CuCAAC reaction.[280] Because of their tolerance towards a wide range of unprotected chemical groups, the CuCAAC formation of hydrogels has been widely used to immobilize sugars, proteins, DNA, and even cells, and this capability is owed to the relatively controllable network densities afforded by the precision of click reactions.[281] The robustness and simplicity of the thiol-ene, thiol-yne, and thiol-acrylate photopolymerizations have also led to their widespread use in a number of hydrogel applications, particularly in controlled drug delivery and tissue engineering. At the fore-front of thiol-click hydrogels is the photopolymerizations of either thiol-ene or thiol-acrylate components. Both reaction types are generally performed in aqueous media, with one or both components in the reaction frequently containing poly(ethylene glycol) (PEG) cores modified to contain thiol and vinyl groups.[281–283] The utilization of the thiol-acrylate reaction to form hydrogel biomaterials was

pioneered by Jeffrey Alan Hubbell; these hydrogels were readily formed in an aqueous environment from PEG-containing multi-acrylates or vinyl-sulfones and a variety of thiols, and particularly those from cysteine units in peptide sequences.[73, 273] Most recently, the the thiol-click reaction has been popularized by the reported efforts of Robert S. Lange and K.S. Anseth, both researchers having reported on the post-funcitonalization of hydrogels by incorporating remnant thiol sites [284, 285]

5.1.3 Microfluidic production of materials

Flow microreactors gained popularity through the efforts of George M. Whitesides and his use of poly(dimethylsiloxane) (PDMS) to create inexpensive microfluidic devices.[286] More recently, microfabrication techniques have been used to generate hydrogel microparticles and microfibers with various sizes and shapes.[287–289] Polymeric microparticles have been developed by *in situ* photopolymerization techniques. Immiscible fluids were merged at the entrance of a microfluidic device, droplets were formed and subsequently crosslinked by a UV light exiting the microchannel. Microfluidic microparticles are formed by the surface tension and shear forces generated at the junction of the microfluidic channel. This process results in the formation of monodisperse microparticles that could be manipulated by controlling the flow rates. As the sheath flow rates increased, the resulting particles were smaller.[249] Microcapsules can also be similarly generated in a continuous flow by introducing alternate immiscible fluids, and given their ability to encapsulate various chemicals and cells in monodisperse and shape-controlled particles, these microfluidic platforms hold great potential for generating delivery vehicles for various types of applications. In addition to photocrosslinkable microparticles, monodisperse hydrogel (alginate) microparticles have been chemically crosslinked in a microfluidic device, where cells

were encapsulated inside the microparticles with higher cell viability.[249] Hydrogel-based microfibers have also been created by laminar flow-based multiple phase coaxial flowing systems and are of benefit for creating biohybrid materials. To generate hydrogel-based microfibers, conventional wet spinning techniques are commonly used. For example, a triple-orifice spinneret was employed to generate hollow and solid fibers of gelatin-hydroxyphenylpropionic acid.[290, 291] Hollow microfibers have also been created using a similar spinning method. In this approach, the inner diameter of the alginate hollow fibers was controlled by a coaxial triple fluid flow. Furthermore, heterogeneous hydrogel microfibers have been produced by converging coaxial flows, and cells seeding and growth were monitored within the hollow alginate microfibers to mimic the formation of tubular tissue constructs.[292] However, the conventional spinning methods have some limitations, such as the inability to generate symmetric or asymmetric Janus microfibers containing different pore size or mechanical stiffness. To address the limitations imposed by the conventional spinning techniques, new microfluidic devices will be presented here in, and have been recently used to fabricate hydrogel microfibers and provide an optimal platform for generating biohybrid fibers.

5.2 Results and Discussion

5.2.1 Microfluidic device design and flow simulations

Figure 5.4 illustrates the production method for biohybrid microfibers infused with bacteria that utilizes hydrodynamic focusing and rapid UV polymerization. A pre-polymer solution including the cells was introduced into the microchannel adjacent to the sheath fluid. Five diagonal grooves recessed into the top and bottom surfaces of the microchannel at 45° angles directed the sheath fluid across the channel;

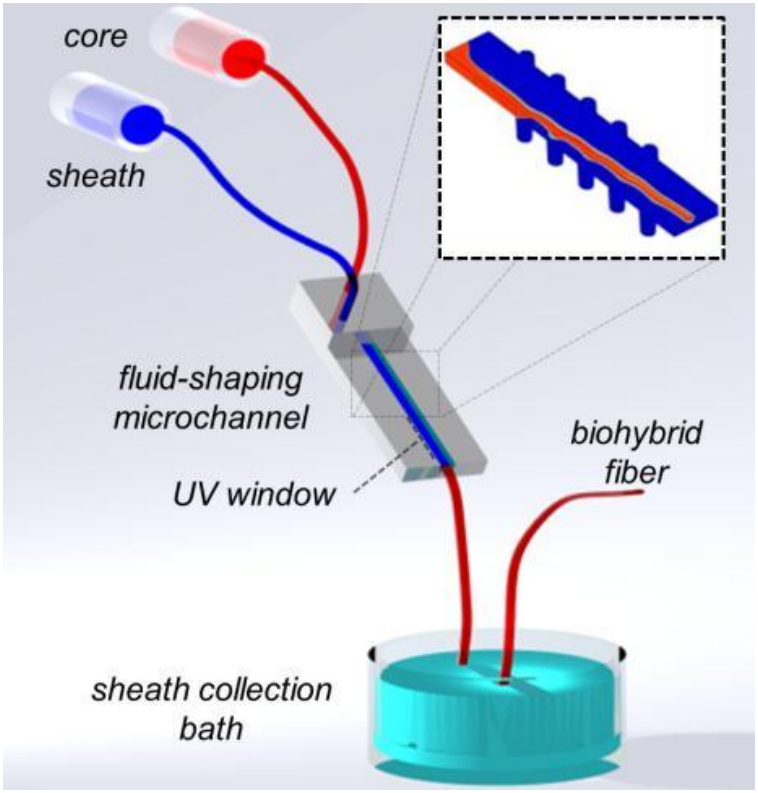

Figure 5.4: An illustration of the method for the fabrication of fibers. Sheath and core solutions are introduced in parallel to the channel. Recessed grooves hydrodynamically shape the sheath fluid (blue) around the core fluid (red). A detailed schematic of the microchannel is provided in Figure 5.20. (inset) Simulation of fluid shaping by recessed diagonal geometries.

thereby, enveloping and shifting the core fluid toward the center of the microchannel, allowing for continuous in-flow polymerization and production of microfibers. The concept of geometric shaping of core-sheath laminar flow was developed by Frances S. Ligler *et al.*, and was initially utilized to affect micro-mixing and produce novelty nanofibers. To design a version of this device capable of producing fibers with desired size and shape for cell encapsulation, microchannel flow simulations were carried out with the COMSOL Multiphysics modeling tool. Taking advantage of the device's symmetry, only half of the microchannel was modeled (Figure 5.4, inset). Figure 5.5 shows a simulation of the vertical cross-section down the length of the 5-groove

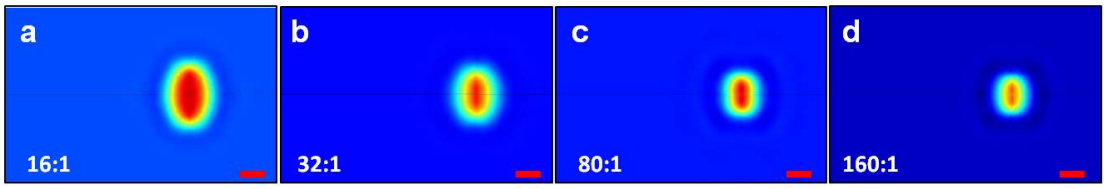

Figure 5.5: COMSOL Multiphysics simulations of the different flow-rate ratios. A vertical cross-section down the length of the channel showing the fluid shape after passing through the geometric-shaping zone. The core component (red) is surrounded by a diffusion layer (yellow/green) and the sheath fluid (blue). The dimensions of the microchannel were 2.54 x 1.68 mm. All scale bars: 500 μm.

channel. The simulation indicated the formation of an elliptical core flow. By varying the number and geometry of the shaping grooves, different fiber morphologies can be produced.[17] A detailed description of the design, fabrication and operation of the microchannel device, simulation procedure and additional models are provided in the Experimental Details. Photoinitiated polymerization of the core fluid was achieved by irradiating the fluid in situ with a UV curing lamp (λ_{peak} = 365 nm, 100 mW/cm^2) as it traversed the microchannel. The residence time of the fluid within the microchannel was dependent on flow rate and ranged from 1.50-1.59 s. The production of fibers was continuous with consistent shape, and the sheath fluid was easily removed using an aqueous collection bath.

5.2.1.1 Photopolymerization models

In the presence of a photoinitiator and a suitable light source, photopolymerization of PEG-acrylates proceeds by a chemistry analogous to the free radical polymerization of any vinyl monomer. However, the kinetics of this process are complex and have two distinct phases because the viscous and diffusive properties of the system rapidly change after the onset of gelation.[293, 294] Immediately after the onset of polymerization, the viscosity of the solution rapidly increases resulting in a

phenomenon known as autoacceleration, where diffusion of propagating centers, which act as terminators by coupling with other centers, becomes much slower than diffusion of smaller PEG-based macromers, leading to an increased rate of reaction. As the network becomes more robust throughout the polymerization eventually the diffusion of monomer also becomes limited, leading to a decreased polymerization rate known as autodeceleration. Since this polymerization is occurring at low concentrations in an aqueous environment exposed to atmospheric oxygen, other termination/inhibition processes are also likely affecting the polymerization.[295]

For high crosslink-density, *i.e.* monomer conversion in flow, cure depth was analyzed by modified photolithography equations.[296] The kinetics of the photohydrogel systems have been studied extensively in recent years. Several parameters are found to influence the final monomer-to-polymer conversions of these systems, such as temperature, light intensity, monomer functionality and reactivity, and photoinitiator concentration. However, the roles of these exact same parameters on cure depth, as opposed to overall bond conversion, have not been fully examined specifically with thiol-ene hydrogels. The pre-production analysis of both methacrylate photopolymerization and thiol-ene photopolymerization helped narrow the tested flow rate ratios, energy dose and polymer concentrations. It is the effect of photoinitiator concentration and light intensity on cure depth will definitively determine whether or not cells can viably undergo the in-flow photopolymerization process. Several hydrogels that are used in tissue engineering are non-toxic derivatives of acrylates, and the cross-linking abilities of multifunctional acrylates are often exploited in these scenarios.[297] When designing the immobilization matrices, the initiation of the polymerization must be carefully considered. For instance, excessive heat during immobilization processing could kill bacteria, as could exposure to certain chemicals; ultraviolet light (UV) can cause intracellular mutations or death in high doses or

energies. Any of these issues could cause bacterial stress, causing false positive signals in the biosensor. Most photopolymers utilize visible light or UV to crosslink the monomers used in the formation of the encapsulation matrices; therefore, it was critical to examine the photopolymerization process to minimize both the UV exposure and photoinitiator chemical concentration.

Multifunctional acrylate are used in a range of applications from lithography to surface coatings, so their photopolymerization kinetics have been extensively studied.[298–300] In photopolymerization, radicals are generated from the initiator through photodisassociation. A photon from the light source separates the photoinitiator into groups of highly energized radicals. The radicals then react with the resident monomer in solution and initiate the thermoset polymerization. This initiation procedure is commensurate to the typical thermal initiation of free radical polymerization, so the conversion of monomer-to-polymer can be analyzed by simple kinetic equations, Eq. 5.1 and Eq. 5.2:

$$-\frac{d[M]}{dt} = R_i + R_p \approx R_p \tag{5.1}$$

and

$$R_p = k_p[M][M^*] \tag{5.2}$$

where R_p is the rate of polymerization, R_i is the rate of free radical initiation, [M] is the monomer concentration, [M*] is the radical chain concentration, and k_p is the kinetic rate constant for propagation. Assuming the steady-state approximation:

$$R_p = k_p[M]\left(\frac{R_i}{2k_t}\right)^{1/2} \tag{5.3}$$

where k_t is the kinetic rate constant for termination.

For bifunctional initiators, the initiation rate is related to the photonic flux and concentration of initiator. According to Einstein's photonic flux and the Beer-Lambert law, the rate of photodissociation and consequently the rate of initiation is determined as [301]:

$$R_i = 2\phi\epsilon[PI]I_z \tag{5.4}$$

where

$$I_z = I_0(10^{-\epsilon[PI]z}), \tag{5.5}$$

ϕ is the quantum yield of the photoinitiator, ϵ is the molar extinction coefficient ($M^{-1}l^{-1}$), [PI] is the photoinitiator molar concentration (M), and I_z is the photonic intensity at depth, z related to the laser intensity at the surface, I_0 by Eq. 5.5. Thus, the combination of Eq. 5.3 and Eq. 5.4 can be rewritten as:

$$-\frac{d[M]}{dt} \approx R_p = k_p[M]\left[\frac{\phi\epsilon I_0[PI](=I_0(10^{-\epsilon[PI]z})}{k_t}\right]^{1/2}. \tag{5.6}$$

Assuming no time dependence of UV penetration depth and by integrating Eq. 5.6, the resultant equation determines the degree of polymerization, $\overline{x}_n$[296]:

$$ln\frac{[M]_0}{[M]} = \left[\frac{k_p^2\phi\epsilon I_0[PI](=I_0(10^{-\epsilon[PI]z})}{k_t}\right]^{1/2} t, \tag{5.7}$$

where

$$\frac{[M]_0}{[M]} = \overline{x}_n. \tag{5.8}$$

The degree of polymerization, $\overline{x}_n$, is related to the extent of polymerization:

$$\overline{x}_n = \frac{1}{1-p}, \tag{5.9}$$

where p can be considered the gel point, the critical threshold of monomer conversion where an insoluble gel is formed. By reorganizing, Eq. 5.7 and Eq. 5.8 the constants of the chemical system can be grouped, and the UV dose parameters are coupled into the maximum exposure such that:

$$\left[\frac{k_t[ln(1-p_c)]^2 chNP_L}{k_p^2 \phi \epsilon \lambda W_0^2 (2\pi)^{1/2}}\right]\left[\frac{1}{E^2}\right] = [PI](10^{-\epsilon[PI]z}), \tag{5.10}$$

where c is the speed of light (m/s), h is Planck's constant, N is Avogadro's number, P_L is the photocuring light power, W_0 is the width of the photocuring beam, E is the maximum energy exposure, and λ is the wavelength of the initiating photon. Ultimately, Eq. 5.10 organizes the chemical and photo constants to determine both the required photoinitiator concentration to achieve a specific extent of polymerization.

The chemical constants have been previously determined, and a photoinitiator known to be non-toxic to mammalian cells, 4-(2-hydroxyethoxy) phenyl-(2-propyl) ketone (HEPPK, Irgacure 2959) was used both for modeling and in the later experiments as the photoinitiator for the polymerization of poly(ethylene glycol) dimethacrylate (PEGDMA). The dissociation of HEPPK is illustrated in Figure 5.8. HEPPK is an ultraviolet light activated photoinitiator, but it is sensitive to visible light, which makes it a good candidate for curing in the violet spectral region of the electromagnetic spectrum.[302–304] Curing times are typically longer when using the lower frequencies, but they are less detrimental to the overall well-being of the cells being encapsulated, so the peak wavelength used for modeling and photocuring was $\lambda =$ 365 nm. For determination of the ideal photoinitiator concentration and UV does, the extent of polymerization will be considered at a gel point $\overline{x}_n$, which Paul Flory described as the monomer conversion dependent on the functionality of the monomer as:

parameter	value	reference
ϕ	0.6 $\frac{radicals}{photon}$	[302, 304]
ϵ_{365nm}	6.7 $m^{-2} \cdot mol^{-1}$	[303]
I_0	0.1 W/cm^2	-
k_p	400 (l / mol · s)	[298, 299]
k_t	5 x 10^5 (l / mol · s)	[299]
$\overline{x}_{l-diacrylate}$	0.33	-
$\overline{x}_{c-diacrylate}$	0.57	-

Table 5.1: Parameters used in determining optimized photoinitiator concentration and cure depth.

$$\overline{x}_l \approx \frac{1}{(f-1)},\ \overline{x}_c \approx \sqrt{\frac{1}{(f-1)}}, \tag{5.11}$$

where f is the functionality of the monomer, $\overline{x}_l$ assumes no cyclization and $\overline{x}_c$ assumes cyclization of monomers. The kinetic parameters and experimental constants are summarized in Table 5.1. The rates of propagation and termination are affected by diffusion limitations and thus they may vary at different times during the reaction; however, for simplification, the rate of diffusion is deemed negligible under laminar flow of the microfluidic device, therefore rate constants can be held constant. Loss of radicals to oxygen, known as oxygen inhibition, is a problem that is pervasive in polymerization involving radicals; however, oxygen inhibition is also diffusion limited. Making the same limited diffusion assumption for laminar flow, there should be little consumption of radicals by oxygen. By applying the simplifying assumptions that there is continuous irradiation with no oxygen, and the total live radical concentration is at steady state.

By applying Eq. 5.10, optimized gel depth can be determined as a function of photoinitiator concentration and UV-dosage. The rate constants and conversion cut-off value for HEPPK have been previously determined and provide the necessary parameters for predicting a critical gel depth. Figures 5.6a is a plot of critical

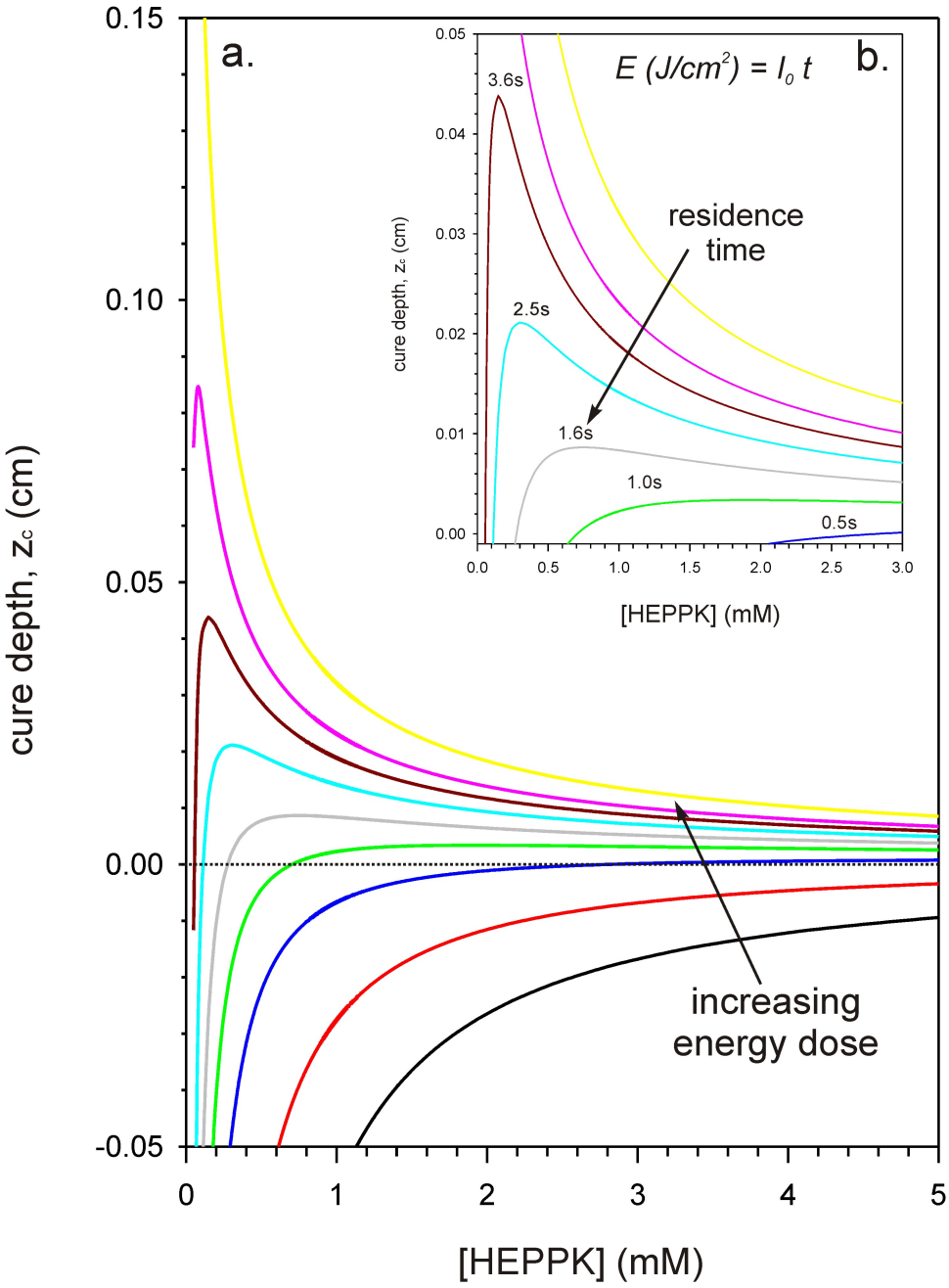

Figure 5.6: Critical cure depth as a function of (a) photoinitiator concentration [HEPPK] and energy dose and (b) an expanded plot illustrating the local maxima effect due to photoinitiator absorbance. The minimal applied energy dose at low [HEPPK] is only realized at cure times > 0.5s.

gel depth as a function of initiator concentration for varied energy doses (negligible oxygen termination is assumed). A similar plot was reported by Ilhan Aksay *et al.* for a deoxygenated acrylate system using the stead- state model and reported a similar peak in the cure depth located at lower photoinitiator concentrations.[296] Figure5.6b shows an expanded plote of the reaction simulation of a dimethacrylate curing photopolymerization utilizing HEPPK initiator concentrations in the range of 0.25-8 wt%. The varying energy doses shown are the product of the incident intensity of 0.1 W/cm^2 and varied exposure time. In general, the values of k_p for free-radical polymerizations are between 10^1 and 10^3 l / mol $\cdot$ s, and those for kt are in the range of 10^3 to 10^5 l / mol $\cdot$ s.[293, 298, 299] For each energy dose in Figure 5.6b, as the initiator concentration is increased, the cure depth reaches a clear maximum; this is caused by the absorptivity of HEPPK at increased concentrations and shows a trend that the typical stereolithography models cannot provide without experimental data for each one of the experimental conditions.[296, 305, 306] By confining the dimensions of the volume of monomer by microfluidic shaping, the smaller microflow results in a a smaller critical cure depth (z_c), so the system can operate at both lower initiator concentration and lower energy doses. The resultant gel is a polymer structure that should be fully crosslinked, allowing the capture of many cells inside a robust fiber.

5.2.2 Acrylate fibers

Common polymer fiber production methods include melt extrusion, casting, and electrospinning. The methods often require cytotoxic chemicals, procedures incompatible with maintaining cell viability, or complex processing tools. The melt extrusion process produces unique fibers with intricate dies; however, highly-crosslinked, physically robust hydrogels are incompatible with melt processing. Casting fibers us-

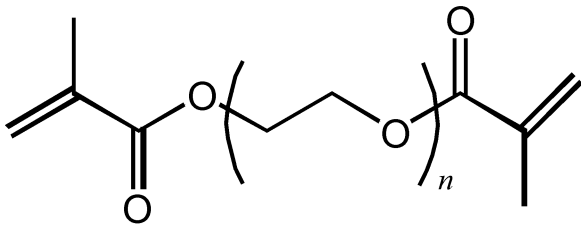

Figure 5.7: Structure of poly(ethylene glycol) dimethacrylate (PEGDMA).

ing fused silica capillaries as molds is limited by its poor reproducibility and small batch production. Electrospinning has been adopted as a popular method to produce biohybrid fibers; however, electrospinning is not suitable for the in situ encapsulation of viable cells. Electrospinning with post-fabrication crosslinking has been reported to induce bacterial cell death of up to 50% of the cells, and has also been shown to be incompatible with maintaining any viability of mammalian cultures post encapsulation Recent alternatives for fabrication of polymer fibers utilize in-flow processing, *e.g.* hydrodynamic extrusion or microfluidic casting. Although hydrodynamic extrusion circumvents the cytotoxic parameters of melt extrusion, this process is still restricted by complex dies, and limited chemistries. Microfluidic casting provides a facile route for producing complex shaped fibers, but this process utilizes cytotoxic organic solvents. For a viable, microfluidic production route of cell-laden fibers, the microsystem must avoid organic solvents, harsh polymerization conditions, and large concentration gradients. The pre-gel solution utilized as the core fluid was composed of poly(ethylene glycol dimethacrylate) M_n = 750 (PEGDMA), and the biocompatible, water-soluble photoinitiator Irgacure 2959 (HEPPK).[297, 303] Structures of PEGDMA and HEPPK are shown in Figure 5.7 and Figure 5.8, respectively. PEGDMA was chosen as the initial hydrogel due its rapid polymerization kinetics and the breadth of literature on its synthesis, previously reviewed in Chapter 5.1.2.[268, 307–309] PEGDMA is appropriate for the systematic exploration of cell

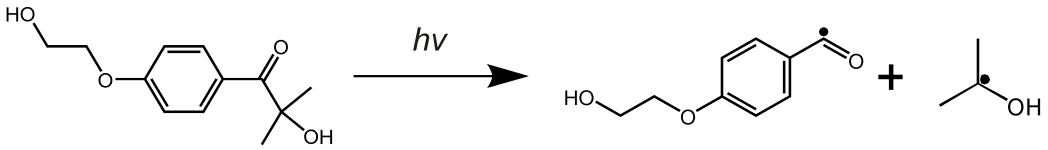

Figure 5.8: Photodisassociation of HEPPK.

response to specific alterations in the methods for fabricating the hydrogel scaffold. In addition, pure PEGDMA hydrogels function as blank slates in biological systems; they are resistant to nonspecific adsorption of plasma proteins, and minimal cell interactions between the hydrogel and the mesh occur unless reactive functional groups are incorporated.[275, 310] In this case, cell immobilization is strictly based on physical encapsulation within the hydrogel matrix. The sheath was an aqueous solution of poly(ethylene glycol) $M_n = 400$, selected to approximately match the viscosity and hydrophilicity of the pre-gel solutions.

Fibers were produced from pre-gel solutions of 75, 50 and 25% (w/w) PEGDMA. Varying the ratio of the sheath-to-core flow rates controlled the dimensions of the fiber. Optical and scanning electron microscopies were employed to characterize the size and morphology of the hydrogel fibers (Figure 5.9). An illustrative, interconnected network of pores was observed on the surface of the fibers (Figure 5.9d-f). Evaporative drying of hydrogels causes internal pore collapse; therefore, to accurately quantify the mesh size, laser scanning confocal microscopy was used to visualize the internal mesh in the water-swollen state (Figure 5.22). Reducing the concentration of PEGDMA increased the observed mesh size from 3.0 $\pm$ 1.9 μm to 31.4 $\pm$ 6.3 μm. Table summarizes the porosity analysis of the PEGDMA data. The dependence of mesh size on the ratio of PEGDMA:water is indicative of phase separation during polymerization.[311, 312] Consequently, both the flow rates of the fluids and the concentrations of the pre-gel solution can be used to tune the final morphology and

PEGDMA % (w/w)	mean pore area (μm^2)	Feret diameter (μm)
75	5.3±3.7	2.4 - 7.8
50	205.1±48.5	12.0 - 20.1
25	1002.3±284.3	21.7 - 43.4

Table 5.2: Porosity determined by laser scanning confocal microscopy.

porosity of the fibers.

Syringe pumps were used for injection of both the sheath and the sample fluid. The core (75, 50 or 25 % (w/w) PEGDMA/PBS) and sheath solution (PEG400 diluted with water) were prepared to have the similar viscosity and to be entirely miscible. The flow of sheath solution was initiated first in order to minimize contact of the acrylate with the channel walls. Into this flow, a steady stream of the acrylate solution was introduced, and focused by the 5 grooves. The outlet was submerged inside a beaker filled with water, such that the microfluidic device was normal to the collection bath surface. Three light-guides (diameter = 3 mm) of the UV lamp (Bluewave 200 UV Light Curing Spot Lamp, Dymax) were aligned along the microchannel approximately 1 inch away from the surface of the channel. The lamp provided an intensity of 100 mW/cm^2 at the centroid of the microchannel. The light intensity was calibrated with a UV Intensity Radiometer (Accu-Cal 50 Radiometer, Dymax). Optical micrographs of the produced fibers are shown in Figure5.10. By decreasing the flow rate of the core fluid and holding the sheath flow rate constant, the long axis of the ribbon-like fibers was decreased from ≈500 μm to ≈100 μm, as shown with optical micrographs in Figure 5.10.

For the fibers to be effectively used for applications, they must be physically and thermally robust, confine the cells, and permit both transport of nutrients/targets and the egress of waste.[275, 313] For biohybrid applications, the PEG length and the

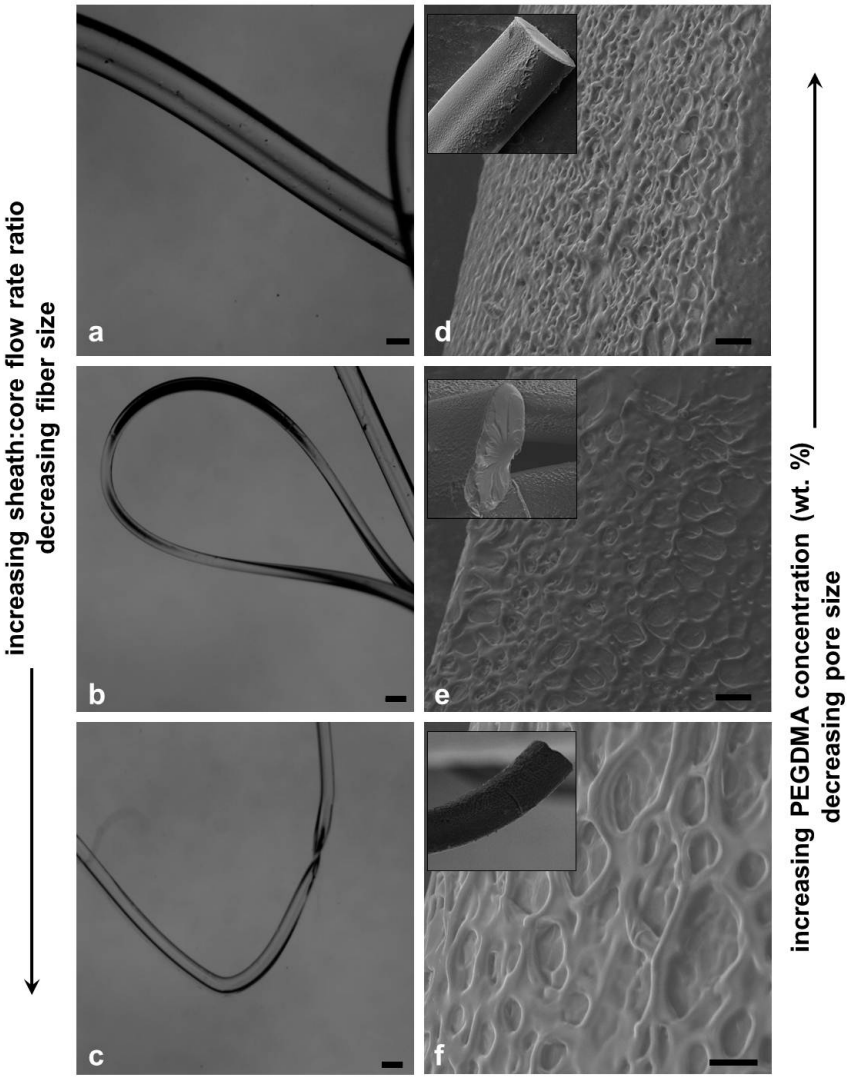

Figure 5.9: Optical and scanning electron micrographs of PEGDMA fibers. (a-c) During the fabrication process, the dimensions of the fiber are controlled by varying the sheath:core flow rate ratios (16:1, 32:1, 80:1). Increasing the sheath:core flow rate ratio decreases the cross-sectional area. Fibers shown were produced from a pre-gel solution of 75% (w/w) PEGDMA. Scale bars: 100μm (a-c). Hydrogel porosity was controlled by varying the concentration of PEGDMA in the pre-gel solution. (d-f) Increasing concentrations of PEGDMA decreases mesh size. The mean Feret diameters and standard deviation (n=6) for 75, 50, and 25% (w/w) PEGDMA fibers were 3.0 $\pm$ 1.9, 16.7 $\pm$ 2.8 and 31.4 $\pm$ 6.3 μm, respectively. Inset images are representative fibers at sheath:core flow rate of 800:25 μL/min. Scale bars: 20 μm (d-f).

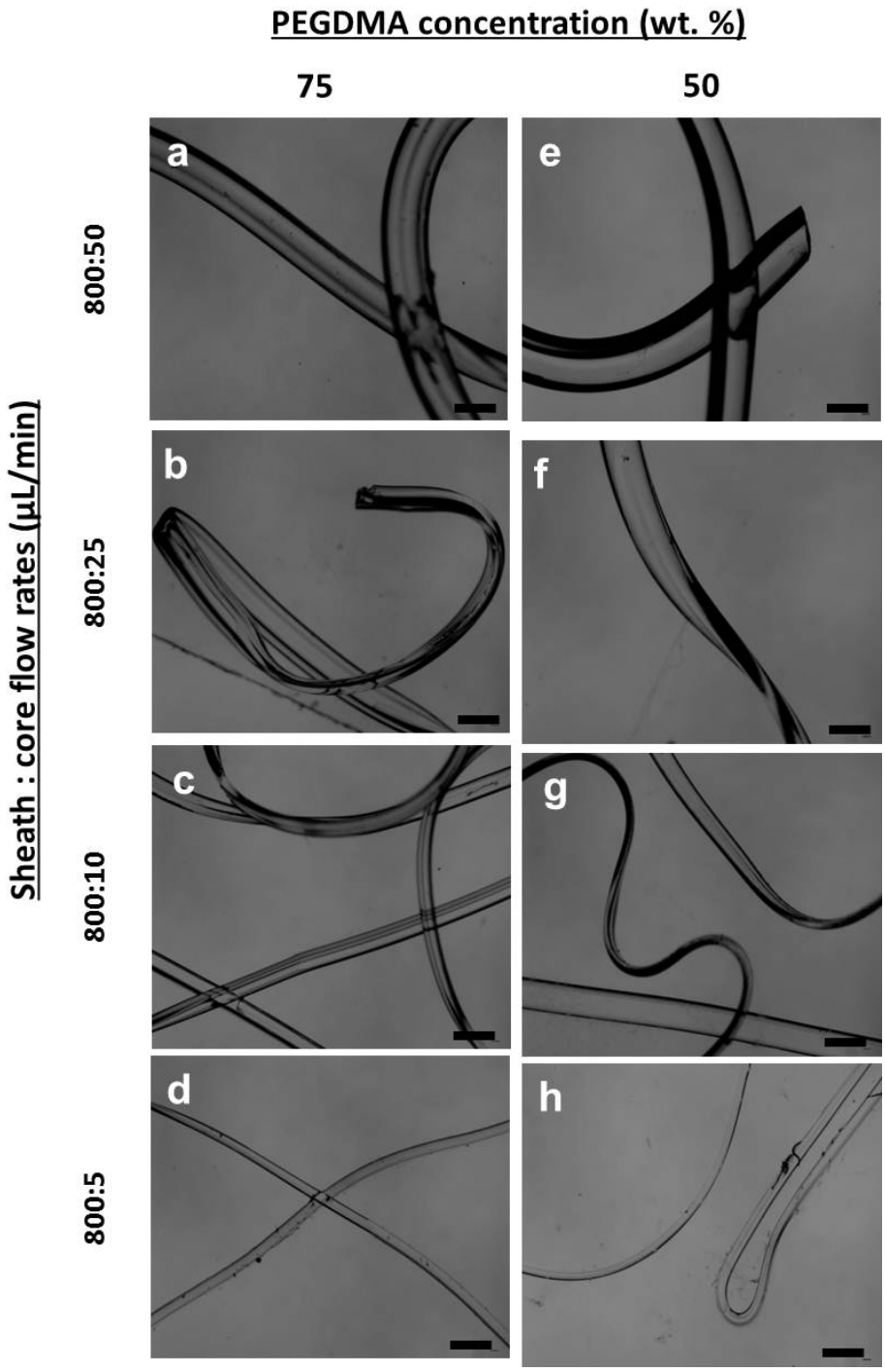

Figure 5.10: Optical micrographs of PEGDMA fibers are shown at 2x magnification. (a-d) Fibers synthesized from a polymer solution of 75% (w/w) PEGDMA. (e-h) Fibers synthesized from a polymer solution of 50% (w/w) PEGDMA. Fibers were produced at different sheath:core flow rates, from 800:50 to 800:5 μL/min. All scale bars indicate 500 μm.

initial concentration of pre-gel are used most commonly to alter the network structure. Increasing the initial macromer concentration or decreasing PEG length results in higher cross-linking, decreased swelling, increased mechanical modulus, and decreased apparent diffusivity of molecules within the gels. These properties alone can affect the behavior of cells within hydrogel.[314, 315] The thermal and hydration properties of the PEGDMA hydrogel fibers were determined using thermogravimetric analysis (TGA) and differential scanning calorimetry (DSC). After fabrication, fibers were immersed in water overnight to swell with water and remove unreacted prepolymer. For TGA, the initial weight loss of samples corresponds to the evaporation of water from the fibers. For pre-gel concentrations of 75, 50, and 25 % (w/w) PEGDMA and sheath:core flow rates of 800:50 μL/min (flow-rate ratio = 16:1), the water contents were 38%, 50%, and 77%, respectively (Figure 5.11).

The network structure of PEGDMA hydrogels is distinct from traditional polymer networks that are formed by cross-linking preformed polymer chains or by copolymerizing monomer with a small fraction of a cross-linker. PEGDMA hydrogels are formed typically from a single component that serves both as cross-linker and crosslinked chain. The resulting network consists of PEG chains esterified to dense, multifunctional cross-link regions; physical chain entanglements also contribute to the network. Numerous studies have attempted to develop effective strategies to control PEGDMA gel properties, including increasing the ratio of PEGDMA to water at the time of polymerization or decreasing the PEG chain length. These approaches result in decreased hydrogel swelling, increased mechanical modulus, and decreased effective transport of non-gaseous molecules through the hydrogel.[316–319] Researchers have also attempted to estimate the molecular weight between cross-links and the mesh size from swelling and mechanical data using variations on the Flory-Rehner model.[320, 321] These models provide estimates that generally correlate well with

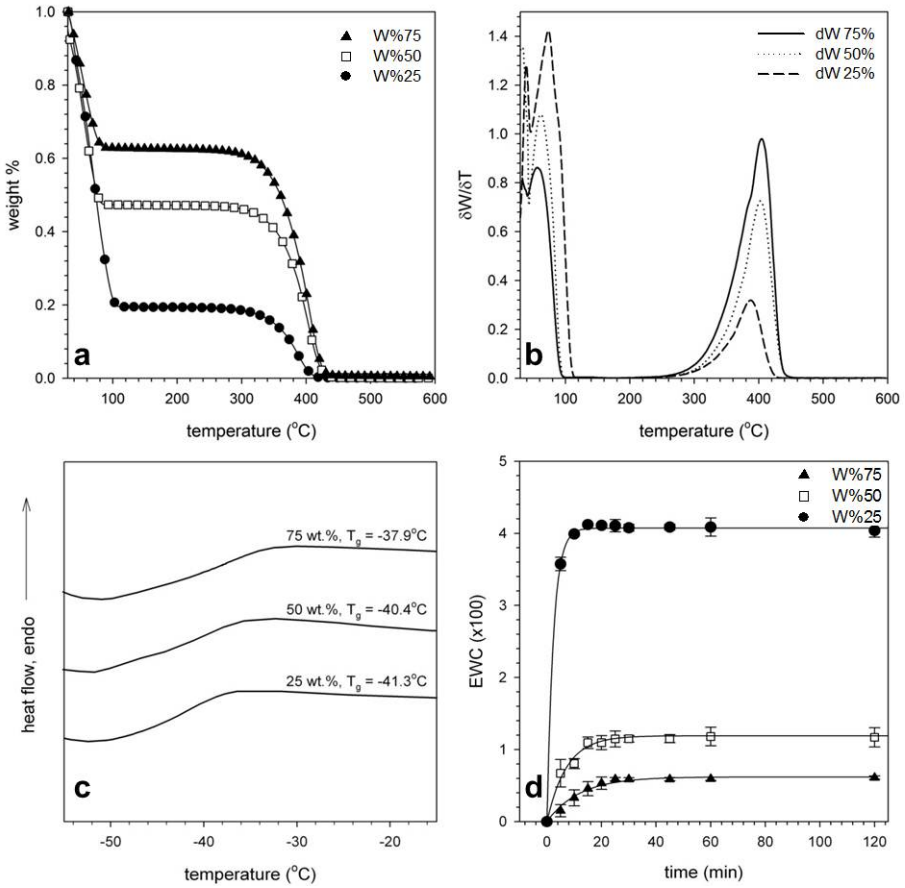

Figure 5.11: Original data from fiber characterization: (a) TGA thermogram of 800:50 μL/min fibers produced from different concentration of PEGDMA pre-polymer solutions show increased concentration of PEGDMA in the pre-polymer solutions decreases water uptake. (b) Differential thermograms with respect to temperature. (c) DSC thermograms of fibers produced from different concentrations of PEGDMA in the pre-polymer solution show a single T_g, which decreases with decreasing amounts of PEGDMA. (d) EWC v. time plot shows lower PEGDMA concentrations increase the rate of hydration.

observed physical properties; however, by using equations derived for networks formed with long polymers with tetra-functional junctions these analyses neglect the complex nature of the PEGDA network. For PEGDMA macromers, the net result of this complicated polymerization process is the formation of an interconnected PEG-network. This network contains poly(PEG-esterified) kinetic chains that form multifunctional cross-linking nodes bridged by PEG cross-link chains, and these cross-linking points aggregate into dense microdomains.[322] During polymerization, PEG chains can entangle to form additional cross-link nodes. The network also contains other defects, including partially unreacted macromer and cyclic structures, that do not contribute to the effective network.[323] The difficulty in accurately predicting PEGDMA hydrogel properties lies in the the inherent heterogeneity of dimethacrylate networks caused by the aforementioned polymerization kinetics. The heterogeneity stems from many factors, including self-cyclization (where a growing chain crosslinks with a pendant functional group from the main chain), the stochastic nature of polymerization and functional group distribution. To better understand the hydrogel microstucture, a battery of thermal analysis was applied to examine degradation, glass transition, swelling and porosity of the produced hydrogel microfibers.

The thermal degradation temperature of fibers indicates their stability in the common temperature range for biological use. After the evolution of water (>100°C), TGA showed no weight loss until temperatures between 375°C and 400°C were reached. This matched the expected temperature range for decomposition of a crosslinked network of poly(ethylene glycol).[311, 324] Accordingly, differential thermograms showed proportionally increasing decomposition rates for higher concentrations of PEGDMA. DSC confirmed the uniformity of gelation of the fibers. Dried fibers exhibited a single glass-transition temperature (T_g) dependent on the concentration of PEGDMA in the pre-gel solution. The corresponding T_g were -37.9, -40.4,

and -41.9 °C for 75, 50, and 25% (w/w) PEGDMA, respectively. By increasing the concentration of PEGDMA in the pre-gel solution, the T_g was increased. The data corroborated previous reports that water acts as a plasticizer/extender in the hydrogel network: during polymerization, water increases the free volume between polymer chains and causes increased chain mobility.[312] Figures 5.12a and 5.12c are the thermograms of fibers produced from sheath:core flow rate ratios of 800:25 and 800:10 μL/min, respectively. Figures 5.12b and 5.12d are the differential thermograms of fibers produced from sheath:core flow rate ratios of 800:25 and 800:10 μL/min, respectively. The increased rate of the evolution of water from the fibers, as shown in the differential thermograms (Figures 5.12b, 5.12d) is attributed to increased mesh size in fibers produced from solutions of lower concentration of PEGDMA. It was possible to tune the T_g and hydration of the fibers by controlling the relative concentration of pre-gel to carrier fluid. It is foreseen that T_g and hydration can also be tailored by controlling the PEG molecular weight between methacrylate end groups. Monomers with long chains tend to exhibit lower T_g than those with n-methyl groups or other bulky groups adjacent to the unsaturated bond in the monomer. The higher relative concentration of ethylene-oxide would also increase hydration. By carefully exploiting the interplay of these two effects, the T_g and hydration of PEGDMA networks can be adjusted.

The concentration of PEGDMA in the pre-gel solution and corresponding morphology of the derived fibers will also affect EWC (Figure 5.13). To analyze EWC, fibers were lyophilized for 24 h, transferred to a buffer solution, and incubated at 25°C for periods of up to 2 hours. Aqueous solutions of 0.1 M phosphate and 0.15 M saline were adjusted to pH 4, 7 and 10. The fiber samples were blotted with wet filter paper to remove excess water and weighed. EWC was calculated from Equation 5.12 where m_0 and m_t are the mass of the sample after drying and after hydration,

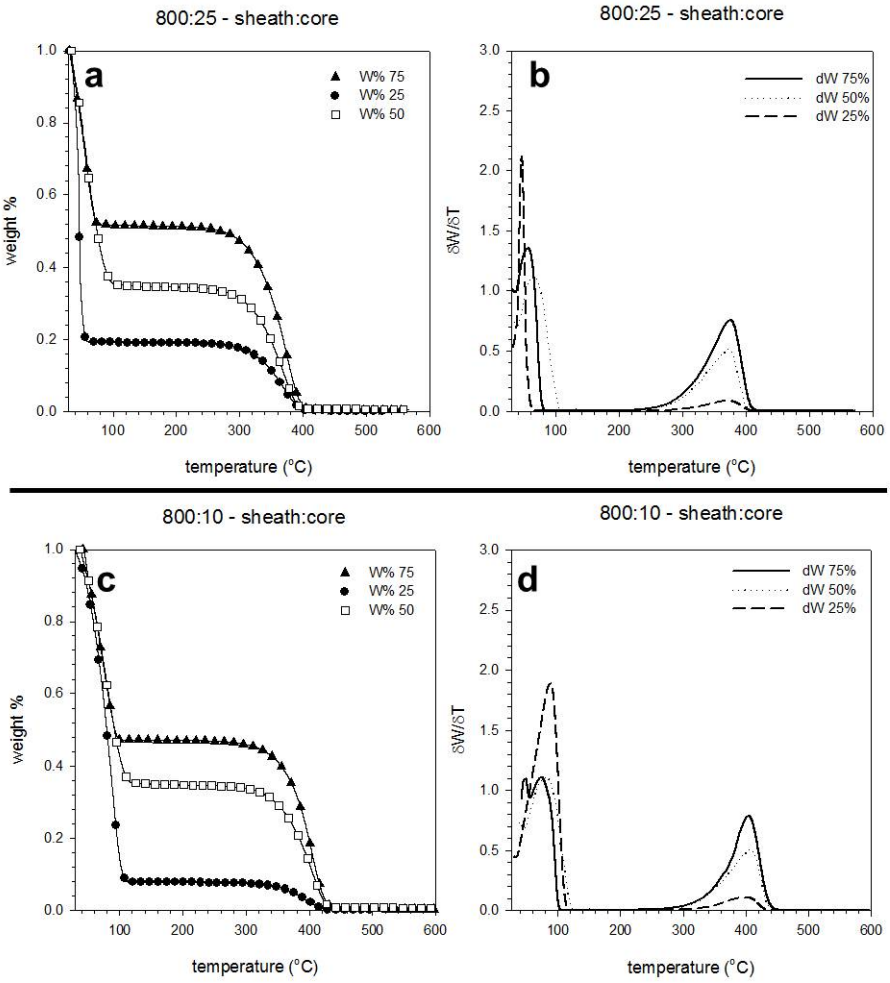

Figure 5.12: (a,c) Thermograms of fibers produced with sheath:core flow rates of 800:25 μL/min and 800:10 μL/min. (b,d) Differential thermograms of fibers produced with sheath:core flow rates of 800:25 μL/min and 800:10 μL/min.

respectively.

$$EWC = \frac{m_t - m_0}{m_0} \tag{5.12}$$

Fibers produced from a pre-gel solution containing 25% (w/w) PEGDMA reached EWC of 400% in less than 10 min. Fibers produced from a pre-gel solution containing 50% (w/w) and 75% (w/w) PEGDMA achieved EWC of 120% and 60%, respectively, in as little as 5 min. The pH of the hydrating solution caused no significant effect on EWC. Poly(ethylene glycol) is a neutral polymer at low molecular weights; therefore, pH should not affect its hydration properties.[317] The rate of hydration is critical for providing a uniform and equilibrium state for the encapsulated cells. Either exceedingly rapid or slow hydration of the fibers would ultimately prove detrimental to the encapsulated cells.

5.2.3 Thiol-ene and Thiol-yne fibers

Thiol-click chemistries were also explored as Cu-free routes to biohybrid fibers. Three-systems were investigated: 1) a poly-thiol PEG (PEG_{4SH}) with PEGDMA, 2) a poly-thiol (pentaerythritol tetrakis(3-mercaptopropionate) (PETMP) with a poly-alkyne PEG (PEG_{4yne}), and 3) PEG_{4SH} with PEG_{4yne}. Thiol- based PEG fibers were produced in a similar manner to the PEGDMA fibers; however, the sheath solution was 100% PEG_{400} to maintain miscibility with PETMP. The chemical structures of these constituents are shown in Figure 5.14.

The PEG_{4SH}/PEGDMA system is a traditional thiol-ene photopolymerization, as previously discussed. The PETMP/PEG_{4yne} is derived from a newer click chemistry, the radical mediated thiol-yne reactions.[325] The thiol-yne reaction and mechanism is shown in Figure 5.15. Thiol-yne reactions exhibit attributes typically associated with highly efficient thiol-ene chemistry, and investigators have explored

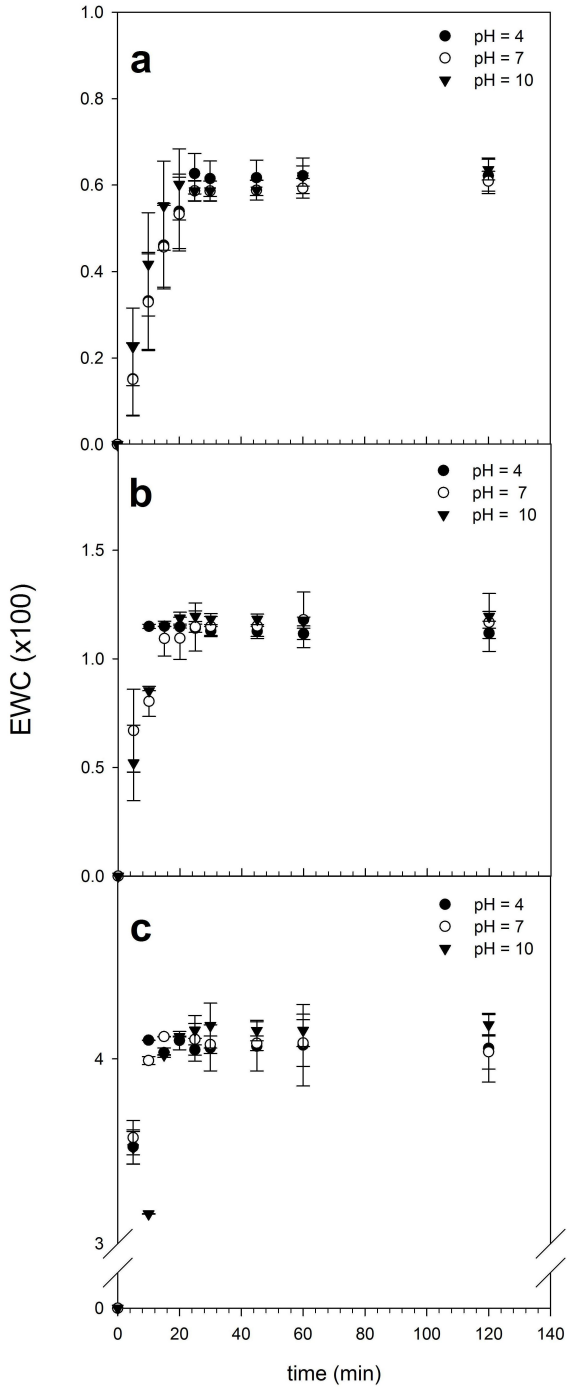

Figure 5.13: Fibers produced from different concentrations of PEGDMA were equilibrated at pH = 4, 7, 10. The fibers were produced from solutions of (a) 75%, (b) 50%, and (c) 25% (w/w) PEGDMA at sheath:core flow rates of 800:50 μL/min. Data points are the mean and error bars are the standard deviations of the samples (n=3).

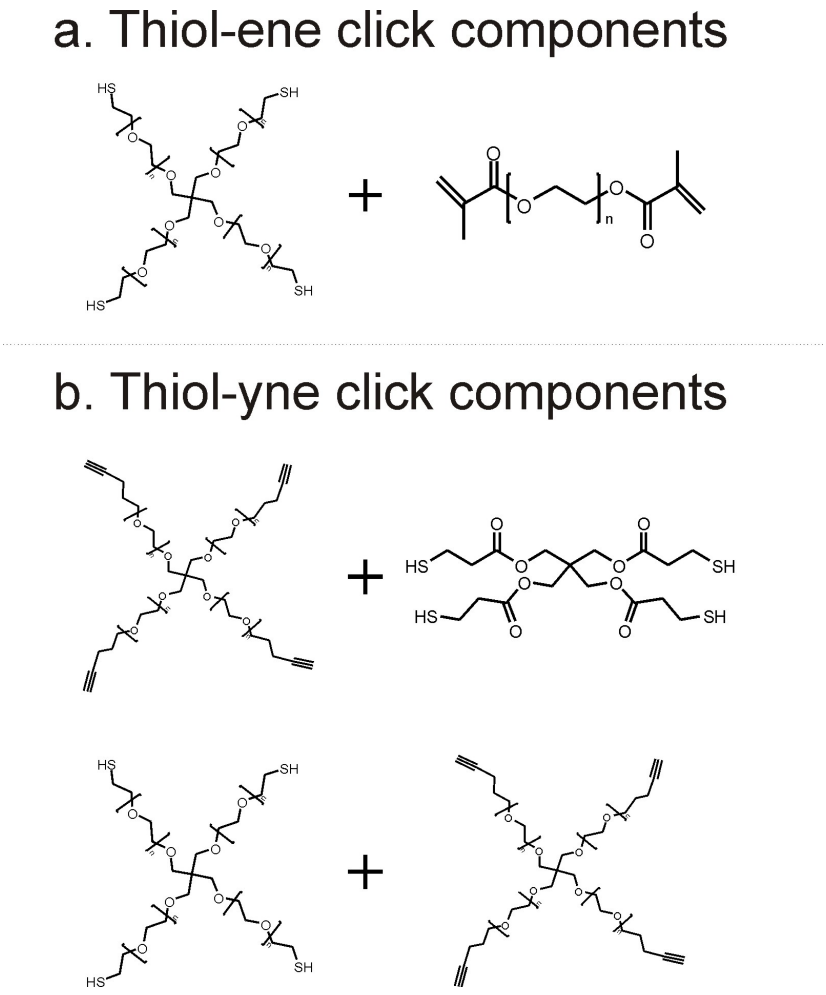

Figure 5.14: (a)Thiol-ene and (b) thiol-yne click components utilized to produced hydrogel microfibers. The thiol-ene reaction contained a thiol-ated PEG and PEGDMA. The thiol-yne reaction contained an alkyne-PEG and PETMP or a PEG-based system of PEG_{4SH}) with PEG_{4yne}.

thiol-yne reactions as a chemical platform for materials synthesis involving polymer functionalization and hydrogel synthesis.[259, 326–328] Each -yne moiety reacts first with a single thiol to form a vinyl sulfide followed by subsequent reaction of the vinyl sulfide with a second thiol to yield the 1,2-disubstituted adduct. Under stoichiometric (2 thiols: 1-yne) conditions the reaction was found to give rise to the mono-substituted vinyl sulfide moiety (a 1,2-disubstituted -ene) which, after being formed, was approximately three times more reactive with the thiols than the -yne moiety from which it was formed. When thiols were present in a stoichiometric excess, no vinyl sulfide reactant was found. However, when the alkyne was in stoichiometric excess, varying amounts of homopolymerization of the -yne and vinyl sulfide moieties were observed. The initial polymerization kinetics exhibited nearly first order (0.8 power) dependence on the thiol concentration and nearly zero-order dependence on the alkyne concentration (0.1 power), indicative of the chain transfer step being slower than the propagation step and rate limiting in this alternating, cyclical process.[325, 327] Clearly, the capability of each alkyne moiety to form 1,2-sulfide linkages rather than a single one as with each -ene has a dramatic impact on the potential of these reactions to yield highly crosslinked polymeric materials, which significantly enhances the maximum possible crosslink density and degree of substitution in these polymers as compared to more traditional thiol-ene reactions.

Illustrative SEM images of the produced from the PEG_{4SH}-PEGDMA, PETMP-PEG_{4yne}, and PEG_{4SH}-PEG_{4yne} systems are shown in Figure 5.16a, b and c, respectively. The PEGDMA incorporated fibers showed a predicted, large-open porosity that may be present due to the homopolymerization of the PEGDMA component (Figure 5.16a). In the thiol-yne systems, the porosity is reduced, and unexpectedly is completely absent in the PEG_{4SH}-PEG_{4yne} system (Figure 5.16c). Although the lack of visible porosity may be due to pore collapse during drying, examination of the net-

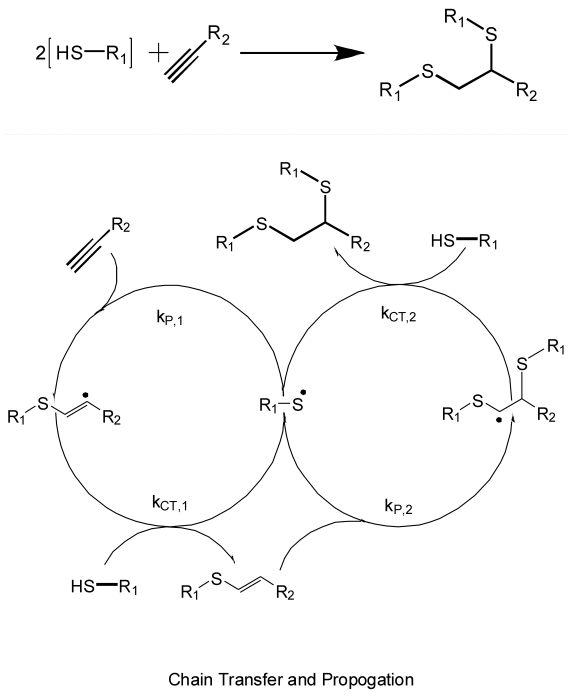

Figure 5.15: Thiol-yne polymerization mechanism.

work formation in thiol-click fibers is still necessary. Reaction of purely difunctional monomers results in a linear polymer system (thermoplastic), while the inclusion of monomers with higher functionality results in crosslinked network polymers, or thermosets. Mono-functional monomers simply act as chain terminators. However, the majority of the studies typically analyze one or two mechanical properties at most, generally with DMA. But since the thermo-mechanical properties of a material are a critical parameter in the design of a device for any application, a fuller understanding of the total behavior of thiol-ene polymers is necessary. To achieve full monomer conversion, a stoichiometric ratio of thiol and -ene functional groups is necessary. At this point, thiol-click fibers need to be further explored for their capabilities as biohybrid scaffolds, specifically their hydration and porosity components. Accordingly, biohybrid fibers would be produced utilizing the methacrylate-based PEGDMA system

seeing as it fit all the requirements as a click reaction.

5.2.4 Production of biohybrid fibers

Before encapsulation of cells in the hydrogel fibers, the effects of long-wave UV irradiation and photoinitiator on cell viability (Figure 5.17) were examined. Gram-positive *Bacillus cereus* (B.cereus) and Gram-negative *Escherichia coli* (E.coli) bacteria were chosen as models for biohybrid fiber fabrication. They are well-characterized organisms and have been reported as viable candidates for genetically engineered whole-cell sensors, a potential application for these biohybrid fibers.[329, 330] The effects of the photoinitiator (HEPPK) and the UV radiation (λ_{peak} = 365 nm, 100 mW/cm^2, 10s) on the viability and subsequent growth rate were evaluated. In multi-well plate growth experiments, B.cereus and E.coli cells were irradiated with UV in the presence and absence of the photoinitiator, and optical density (OD) readings were taken periodically over 15 hours at 600 nm. The growth curve in the absence of any treatment served as a reference. Timed comparisons of B.cereus cell growth as determined by OD600 measurements after treatment demonstrated that the photoinitiator and UV exposure have no significant effect on B.cereus viability and growth profile. In contrast, consistent with a previous report by Hollaender *et al.*,[331] UV-treated E.coli grew at a decelerated rate and to a 17% lower cell density than untreated or photoinitiator-treated E.coli. The prolongation of the "lag-phase" of E.coli, and the decreased cell density indicate a slight impact on the growth of E.coli after UV irradiation.

To evaluate bacterial encapsulation efficiency of the hydrogel photopolymerization process, B.cereus cells were pre-stained with Invitrogen LIVE/DEAD BacLight fluorescent dyes (L-7012) (Figure 5.18) and suspended directly in a PEGDMA pre-

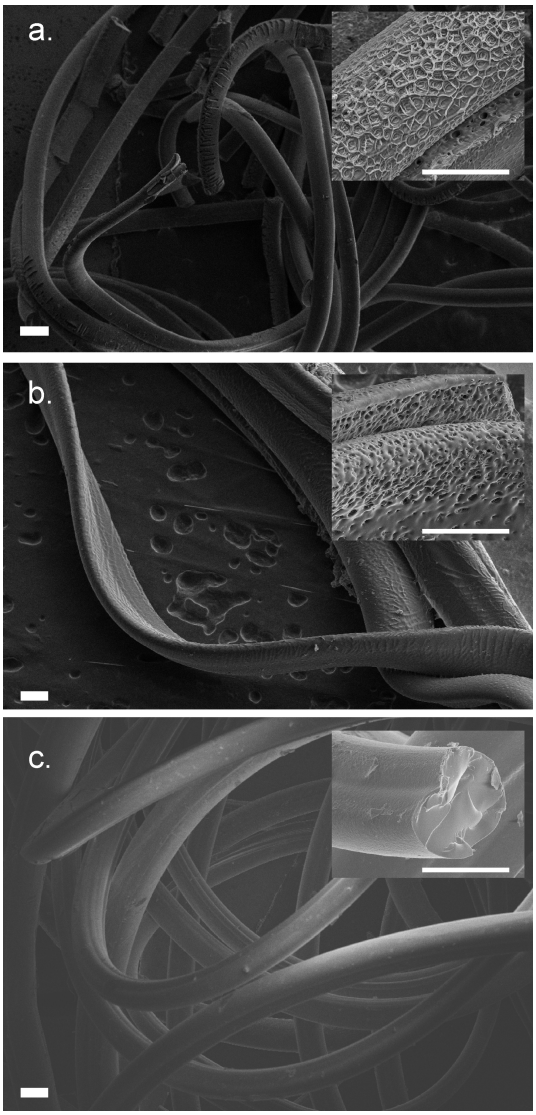

Figure 5.16: Thiol-click fibers produced from (a) a poly-thiol PEG (PEG_{4SH}) with PEGDMA, (b) a poly-thiol (pentaerythritol tetrakis(3-mercaptopropionate) (PETMP) with a poly-alkyne PEG (PEG_{4yne}), and (c) PEG_{4SH}) with PEG_{4yne}.

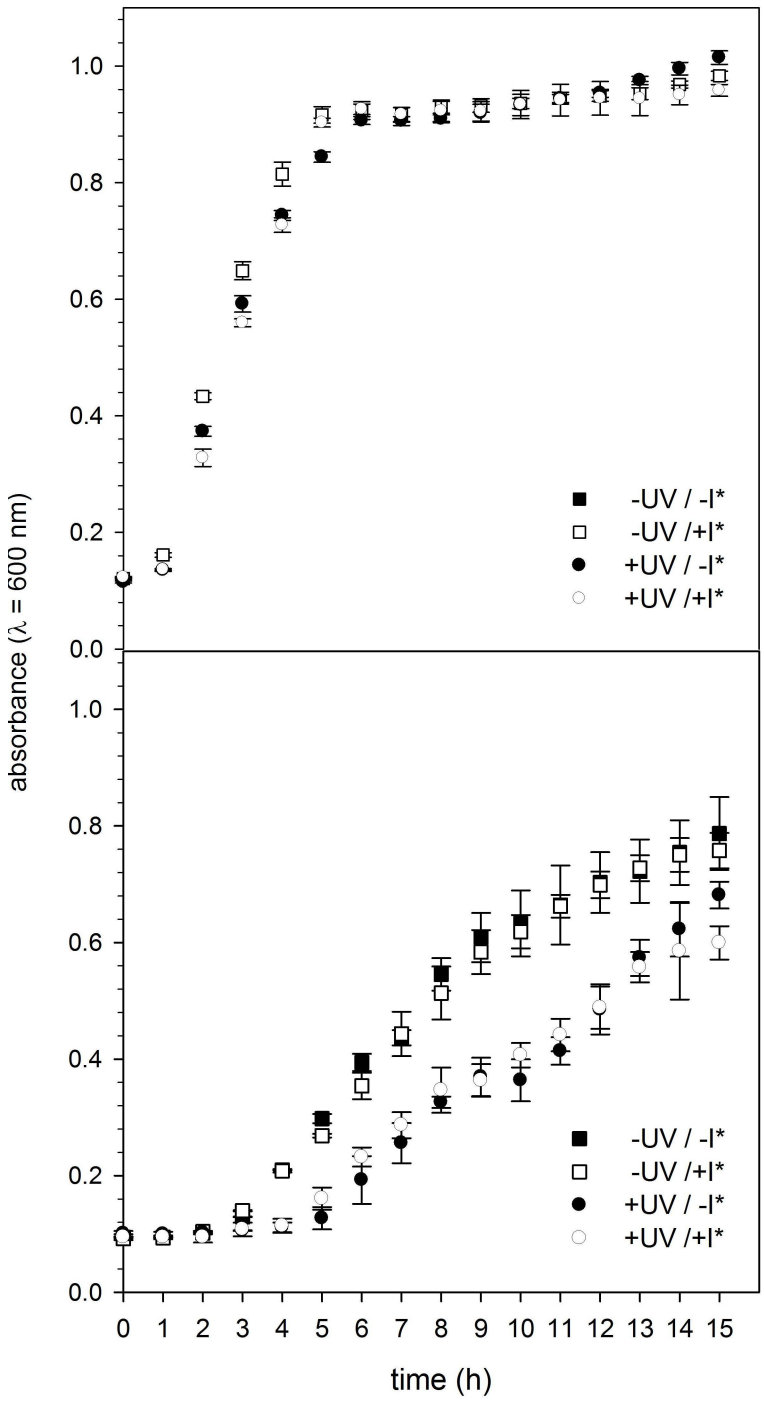

Figure 5.17: Exponential growth of (a) Gram-positive *Bacillus cereus* and (b) Gram-negative *Escherichia coli* in the presence of photoinitiator (+I*) or UV irradiation (+UV). Samples absent of photoinitiator or UV irradiation are labeled -I* and -UV, respectively.

polymer solution (6 x 10^6 cells/mL). For all biohybrid fibers, the core fluid contained PEGDMA diluted with PBS (pH=7.4). The fluid was injected at 800:50 μL/min sheath:core flow rates. The labeled bacteria were imaged post-fiber production on an inverted confocal microscope. Fluorescence micrographs of the fibers showed that bacterial cells were uniformly dispersed throughout the length and breadth of the hydrogel microfibers (Figure 5.18b, c).

As it is critical that the encapsulation process does not compromise cell viability, metabolic activity and growth assays were performed with different bacterial cell populations to determine not only the biocompatibility of the hydrogel scaffold but also the impact of both the chemistry and processing on cell viability and proliferation. B.cereus and E.coli bacteria were each encapsulated into hydrogel microfibers, and the number of viable cells within the 3-D scaffold was visualized with the vital stain 5-cyano-2,3-ditolyl tetrazolium chloride (CTC). In contrast to LIVE/DEAD stains that indicate the status of membrane integrity as opposed to "true" viability, CTC dyes react with electrons produced from redox reactions of actively respiring bacteria to form a red fluorescent formazan product signaling a working metabolism.[332] A green fluorescent probe (SYTO24) was used as a counterstain to identify all cells. Figure 5.18d-i shows representative images of the bacteria in the pre-gel solution and post-fiber production. E.coli and B.cereus, in solution and in fibers, show active cellular respiration as indicated by the red fluorescent formazan precipitation. A small population (<10%) of the cells of either species exhibited the green fluorescence of SYTO24 (Figure 5.18e, f, h, and i), indicating that both Gram-positive and Gram-negative cells survive the fiber production processing and retain metabolic activity. Micrographs showed >90% viable cells, which is highly significant in contrast to electrospinning, which generates <50% cell survival rate.

To further demonstrate the suitability of the hydrodynamically shaped fibers

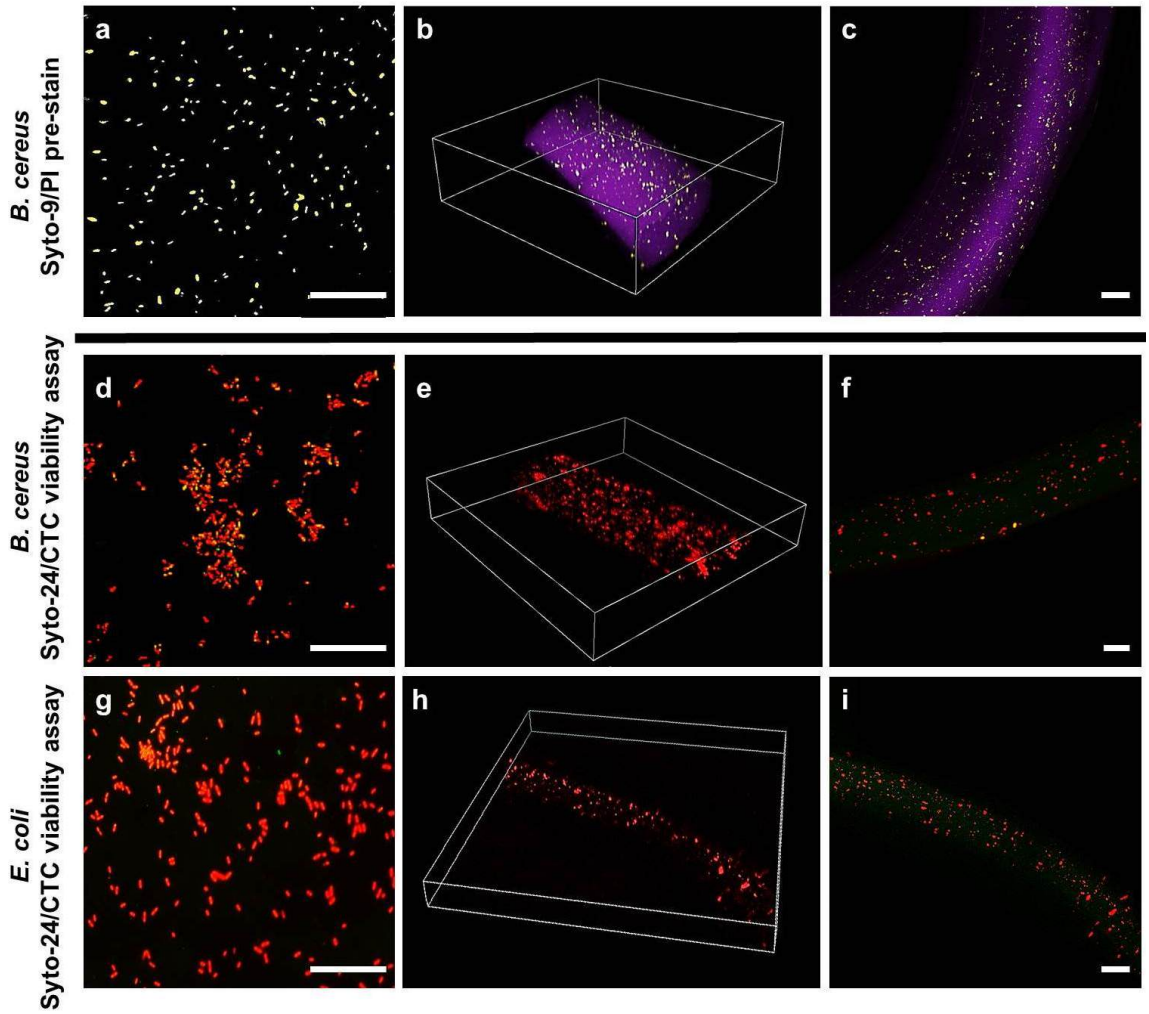

Figure 5.18: (a,d,g) Confocal micrographs of pre-stained bacteria in the pre-gel solutions and (b,c,e,f,h,i) encapsulated in fiber. (a-c) *Bacillus cereus* were pre-stained with green fluorescent SYTO9 (all bacteria) and propidium iodide (PI; non-viable cells only) to evaluate encapsulation efficiency and distribution of cells in the fiber. (d-f) B. cereus and (g-i) *Escherichia coli* treated with CTC to determine metabolic activity, as indicated by red fluorescent formazan product. SYTO24 was used as counterstain. (b,e,h) Images are z-stack confocal images of the entire thickness of the fibers. (c,f,i) Images are z-stack compressions of approximately half the fiber thickness to illustrate the density and uniformity of encapsulated cells. Scale bars: (a,d,g) = 50μm; (c,f,i) = 100μm.

as hosts for the bacterial cells, a recombinant E. coli strain harboring pRSET-B/mCherry was encapsulated into the hydrogel fibers, and confocal images were taken immediately after fiber production and after four hours of incubation in growth media. The expression of fluorescent protein ($\lambda_{ex}/\lambda_{em} = 587/610$) was used to monitor cell growth within fibers. The number of bacteria increased more than three times the initial density within the fiber after four hours of incubation in growth media, indicating that the fibers were sufficiently porous for efficient nutrient diffusion and waste exchange. To determine if the bacteria were inhibited from movement through the fibrous scaffold, fibers containing the cells were plated and cultured on standard agar plates. Significant bacterial colony formation about the fibers (Figure 5.19c, d) was observed. Furthermore, the spreading of a mass of cells (Figure 5.19a) to a more uniform distribution through the fiber (Figure 5.19b) suggests bacterial migration within the hydrogel scaffolding. Taken together, these results demonstrate that the morphology and hydration properties of these PEGDMA fibers not only support efficient nutrient exchange to promote cell growth and proliferation, but also allow cell mobility within the microfibers.

5.3 Conclusions

A simple one-step strategy using a single microfluidic device that continuously produces hydrogel fibers of various sizes containing viable cells is reported. Compared to nozzle-in-channel devices that create core-sheath flow to control fiber diameter, hydrogels and cells passing through the nozzle are subjected to cytotoxic shear forces.[333] Such shear stress was significantly reduced during fiber shaping by employing a core and sheath laminar flow using grooves in the channel walls to hydrodynamically focus the core within the sheath fluid. This approach enables the

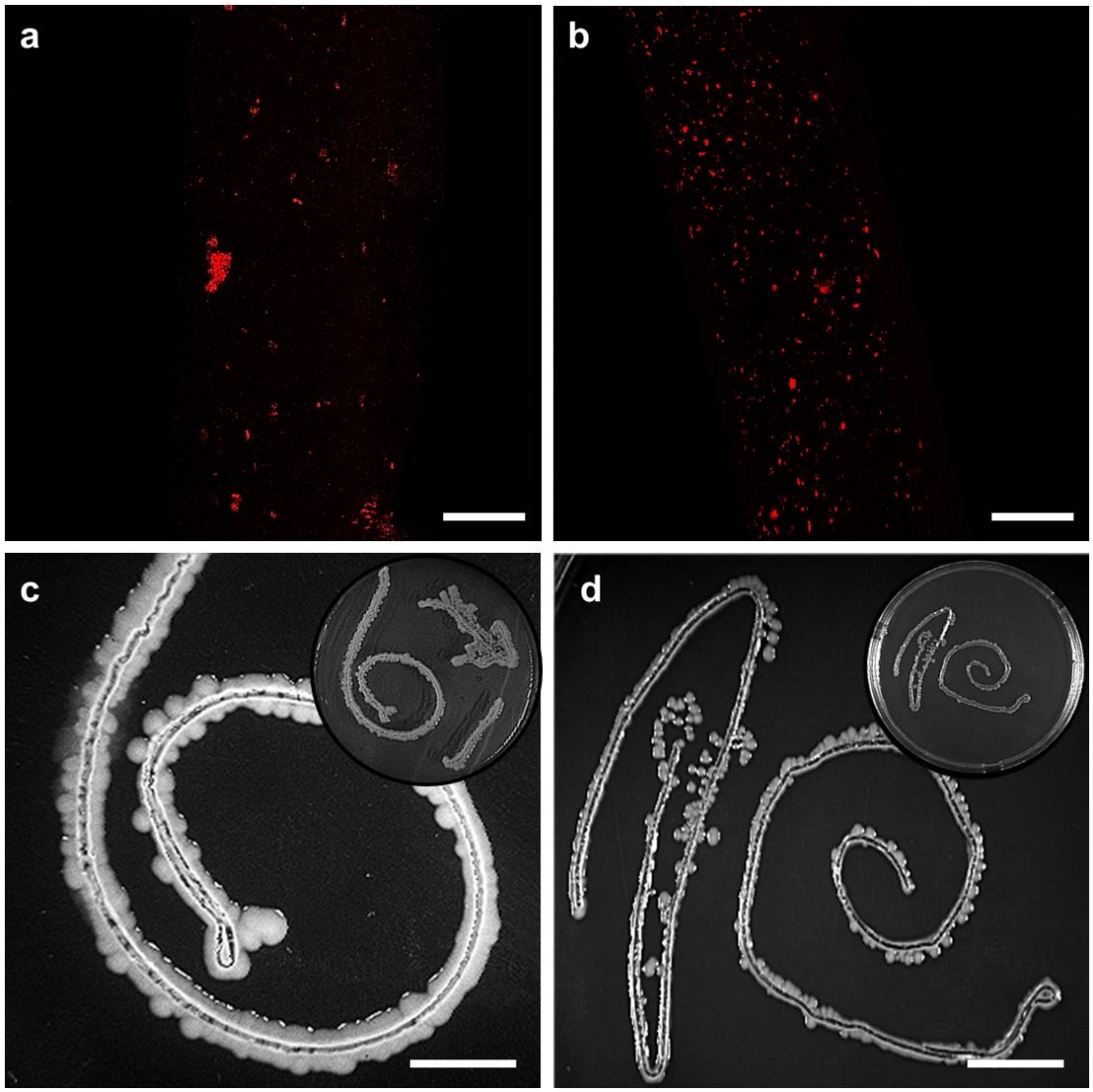

Figure 5.19: Confocal micrographs show the proliferation and distribution of fluorescent recombinant E.coli cells that are encapsulated in a fiber. (a) Image of cells immediately after fiber production, (t = 0 h) and (b), after incubation in liquid growth media (t = 4 h). Scale bars = 100 μm. Fibers with encapsulated (c) B.cereus and (d) E.coli show outgrowth from within the hydrogel fibers onto the surrounding agar surface. Inset is an image of the whole plate, diameter = 100 mm. Images (c) and (d) are magnification of the inset images. Scale bars: 10 mm.

injection of viscous pre-polymer reagents infused with biological constituents with minimal clogging. Compared to microfluidic casting approaches, the rapid photoinitiated polymerization in the microfluidic channel avoids the cytotoxicity caused by organic solvents as well as osmotic pressure changes. In the continuous single-step process reported here, cells are localized in the hydrodynamically constrained core flow, and upon exposure to light, the core forms a crosslinked biohybrid fiber. In addition, the sheath stream can shape the fibers prior to polymerization; this provides the ability to fabricate larger flat fibers that may have increased strength and higher surface area:volume than round fibers with the same cross-sectional area. The laminar flow and photopolymerization conditions maintain the viability of the cells during the fiber fabrication process.

By adjusting pre-polymer solutions and flow rates within the microchannel, the morphology, hydration, and thermal properties of the fibers were tuned. The methodology produced hydrogel fibers that sustained viable cells as demonstrated by the encapsulation and subsequent proliferation of B. cereus and E. coli. The described method differs from other hydrodynamic methods by removing the problematic needle-in-channel or "concentric annuli" form factors. Using integrated, shaping features and laminar flow reduces common fabrication problems like clogging or axial diffusion. Moreover, the hydrodynamic focusing within the microfluidic channel can provide a continuous process for *in situ* gelation. The flexibility in fiber size, shape and composition, coupled with benign photopolymerization conditions, surpasses other reported biohybrid fiber fabrication methods in terms of ease of the fabrication and resultant cell viability.

5.4 Experimental Details

5.4.1 Materials

PEGDMA and Irgacure 2959 (2-Hydroxy-4-(2-hydroxyethoxy)-2-methyl-propiophenone (HEPPK)) were purchased from Sigma Aldrich (St. Louis, MO). Prior to mixing pre-gel solutions, the hydroquinone inhibitor was removed from the PEGDMA using an inhibitor removal column (column SDHR-4 from Scientific Polymer Products, Inc., Ontario, NY). Deionized water was obtained from a Millipore Sapphire System and exhibited a resistivity of 1 x 10^{18} ohm^{-1} cm^{-1}.

5.4.2 Microfluidic channel production and microfluidic simulations

The microchannel was direct-milled into a cyclic-olefin-copolymer (COC) to the dimensions, 2.54 mm x 1.68 mm (width x height). The dimensions of the 5 diagonal grooves were 0.64 mm x 0.84 mm (width x depth) and were spaced 3 mm apart.

5.4.2.1 COMSOL fluid dynamic simulations

All simulations of fluid flow in the microchannel were carried out using COMSOL Multiphysics (COMSOL, Inc.). Steady-state solutions of incompressible Navier-Stokes flow were solved first for each simulation, and the solution obtained was then used to calculate the convection and diffusion concentration profile of the fluids in the system. Simulations were carried out for different flow-rate ratios between the sheath and sample streams. An adaptive meshing technique was applied for the simulation

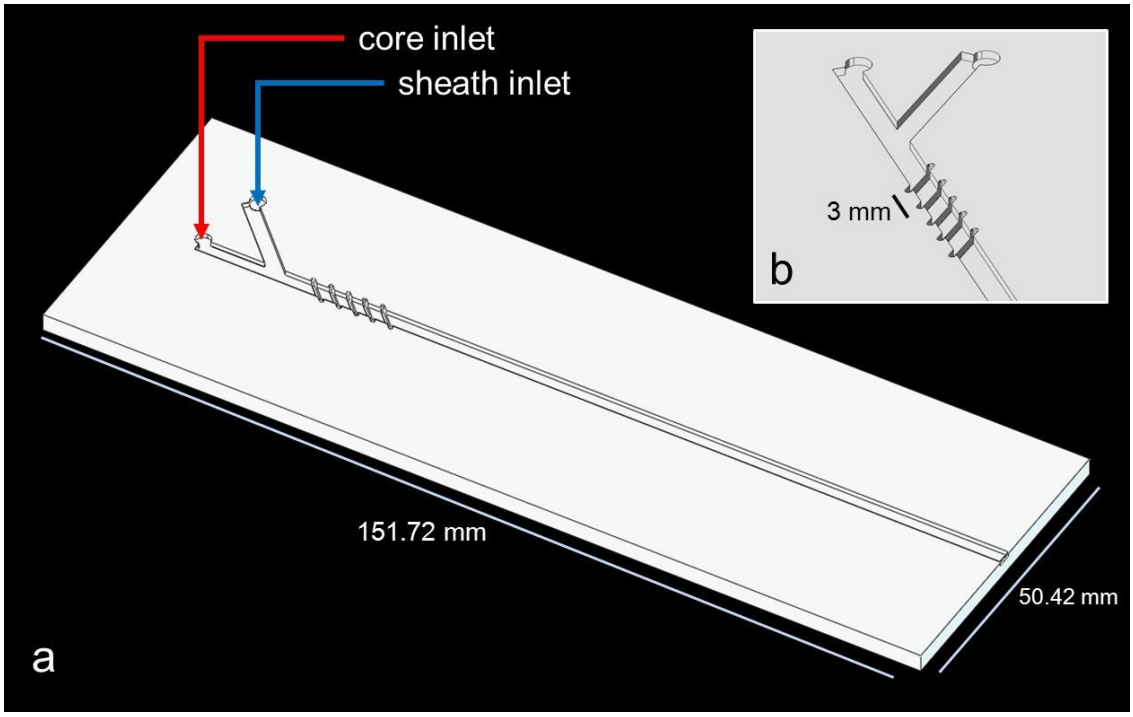

Figure 5.20: An illustration of the microchannel device. (a) Half the microchannel device. (b) Expanded view of the shaping features of the microfluidic device.

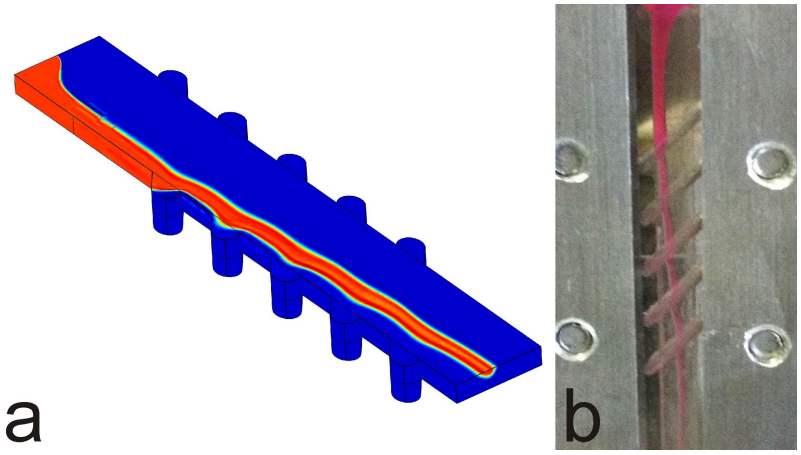

Figure 5.21: Example fluid-shaping in microfluidic device from (a) simulation (b) dyed-core fluid.

of the concentration profile. Due to the device's symmetry, only half of the fluid was modeled. A non-slip boundary condition was applied to the channel walls, and the symmetry condition was applied at a horizontal symmetry plane through the center of the channel. A diffusion coefficient of 1 x 10^{-9} m^2s^{-1} was used, and the fluid was modeled with the density (1.1 g/mL) and viscosity blend index (≈3.6 cP) for the PEGDMA 50% (w/w) pre-polymer solution. The diffusion coefficient of PEGDMA in water was estimated from the diffusion coefficients of precise PEG oligomers in pure water.[334, 335] Simulations were carried out at the following sheath:core flow rates (μL/min): 800:50, 800:25, 800:10, and 800:5 (corresponding to flow-rate ratios of 16:1, 32:1, 80:1, and 160:1). Cross-sectional images were obtained at ≈20 mm downstream from the last shaping groove. This is the approximate start of the UV-exposure window. Cross-sectional images were mirrored along the horizontal symmetry plane to provide visualization of the entire channel as presented in Figure 5.5 and Figure 5.21.

The sheath flow device had two inlets, adjacent to the channel, for the sheath and sample fluid. The device footprint was 151.72 x 50.42 mm. The channel was 2.54 mm x 1.68 mm (width x height). The width and depth of the grooves were 0.64

mm and 0.84 mm, respectively. The grooves penetrated the wall 0.64 mm, and they were spaced 3 mm apart. The halves of the microchannel were clamped together with aluminum plates. The inlets for sample and sheath fluids were integrated on the base aluminum clamp connected with flat bottom PEEK nuts (P-283) with corresponding ferrules.

5.4.2.2 Confocal imaging of porosity

An inverted laser scanning confocal microscope with transmission detector was used to image the interior of the fibers. Confocal images were processed with ImageJ software (Bethesda, MD).[336] First, a fast Fourier transform bandpass filter was applied to the images to delineate edge features. Afterward, a minimum bandpass filter was used to smooth the image. The thresholding function was used to create a binary image of the layer of the fiber in which the PEGDMA appeared white and pores appeared black. The watershed function was used to separate merged pores. The particle analysis function in ImageJ was used to count and measure the pore area and Feret diameter. The mean Feret diameter is the range of means across the sample (n=6) (Table 5.2). Z-stack images were acquired at 0.5 μm intervals at 60x magnification, scanned from the bottom up, and compiled.

5.4.3 Microbe encapsulation in hydrogel fibers

E. coli XL-1 Blue (Agilent Technologies, Santa Clara, CA) was cultured in Luria-Bertani broth (Difco BD Microbiology Systems, Sparks, MD) containing 12 ug/mL tetracycline at 37 °C. E. coli XL-1 Blue/pRSET-B mCherry was cultured in LB broth containing 100μg/mL ampicillin at 37 °C. B. cereus (ATCC, Manassas, VA) was cultured in Tryptic Soy Broth (Difco BD) at 30 °C. For growth profiles, cells

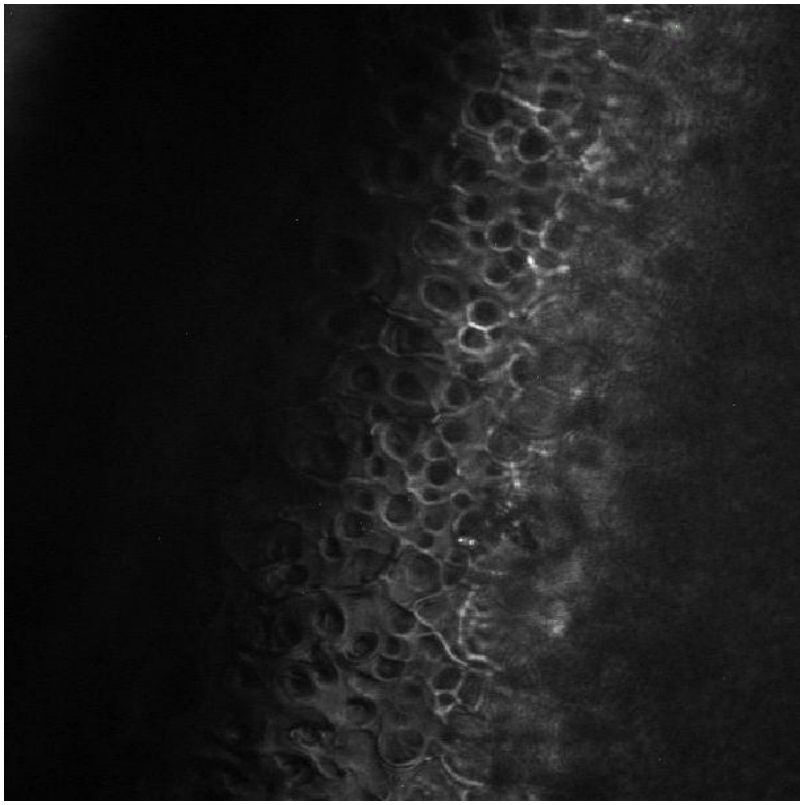

Figure 5.22: Confocal z-stack through a fiber produced from a solution of 75% (w/w) PEGDMA.

overnight cultures were inoculated in multi-well plates at a final OD600 ≈0.10. Individual wells were treated with photoinitiator, irradiated with UV, or both. Growth profiles were obtained over a 15 h period. For encapsulation studies, overnight cultures were washed three times in phosphate buffered saline (PBS) and suspended in PBS prior to fiber production. Final concentrations of cells in the pre-gel solution were $\approx 10^6$ cells/mL. The pre-gel solution was prepared in PBS by mixing PEGDMA (75, 50, 25% (w/w)) and I2959 (0.1% (w/w)). For the encapsulation of cells, a suspension of cells in PBS (6 x 10^6 cells/mL) was incorporated into the core solution. The sheath solution was prepared by mixing PEG $M_n = 400$ and water (50% (v/v)). Sheath and core fluids were injected into the microchannel via syringe pumps. Cellular activity of bacteria was determined by the BacLight RedoxSensor CTC vitality assay (Molecular Probes, Eugene, OR) following manufacturer's instruction. This fluorometric assay is based on the ability of cells to convert 5-cyano-2,3-ditolyl tetrazolium chloride (CTC) into an insoluble, red fluorescent formazan product, and is an indicator of the level of respiratory activity of bacterial populations. Green fluorescent SYTO 24 was used as a counterstain. Fibers containing cells were incubated in the solution for 30 minutes and visualized under a confocal microscope. A cell count comparison for Figure 5.197a and Figure 5.197b was calculated with the ImageJ software. The thresholding function was used to create a binary image. The watershed function was used to separate cell masses. The particle analysis function in ImageJ was used to count cells.

5.4.4 Thermal analysis

Thermogravimetric analysis was performed at a heating rate of 10 °C/min in a nitrogen atmosphere up to 600 °C with a Thermal Analysis 2900 TGA instrument.

The mass of the samples varied from 5 to 9 mg. The water/polymer content was determined at the onset of the first derivative of weight loss with respect to temperature reaching zero. Thermal degradation temperature values reported were taken at the peak maximum of the first derivative of weight loss with respect to temperature. Differential scanning calorimetry was performed from -65 °C to 20 °C at a rate of 5 °C/min with a Thermal Analysis 2920 DSC equipped with R40 refrigerant cooling accessory. The carrier gas was nitrogen at a flow rate of 50 mL/min. All DSC samples were hermetically sealed and cycled thrice, with reported values taken from the third cycle. Reported T_g values were taken at the peak maximum in the curve of the first derivative of heat flow.

5.5 Attributions

Cell growth and viability assessments were conducted with the aid of Dr. Stella H. North. Synthesis of PEG_{4SH} was aided by Dr. Jawad Naciri. The results presented in Chapter 5 were conducted under the advisement and aid of Dr. Andre A. Adams and Dr. Francis S. Ligler at the U.S. Naval Research Laboratory (NRL). Portions of this work have been submitted for publication as Daniele *et al.*, *Rapid and Continuous Hydrodynamically Controlled Fabrication of Biohybrid Microfibers.* Advanced Materials, 2012. The author thanks Dr. Igor L. Medintz for providing the E. coli pRSET-B mCherry used herein. The author's tenure at NRL was supported by George Mason University. This work was supported by the NRL and the Office of Naval Research (ONR) 6.1 work unit MA041-06-4286. The views expressed here represent those of the author and do not reflect those of NRL, the Navy, or the Department of Defense.

CHAPTER 6

Concluding Remarks

6.1 Summary

The objective of the presented work was to explore a new paradigm in the synergy of materials science, biological sciences and engineering technologies *via* click chemistry. This paradigm posits that the application of click chemistry to materials science is an ideal platform in which new materials can be built to harness biosystems to produce materials capable of sensing, isolating, and converting biosystems into applicable technologies. To this end, novel materials and techniques have been developed on the small-molecule, nanoscale and microscale. The following summary of results illustrates the potential capabilities of employing click chemistry and materials science to harness biosystems:

Building small-molecule bioprobes. In the vein of the original purpose for the CuCAAC reaction, small-molecule FRET pairs were built and utilized as an enzyme probe. a simple diagnostic tool was presented that employed a coupled donor/acceptor pair that was formed through a click transformation. A thorough examination of the optoelectronic properties of the different FRET pairs was undertaken by rigor-

ous simulations and photoluminescence spectroscopy to explicate the energy transfer mechanism between lobes of the clicked FRET dyads. Both *ab initio* HF and DFT calculations allowed predicted the spectral response of the FRET pairs and aided in designing the optimal FRET pairs.The FRET pair exhibited a significant variation in PL response with exposure to the lysate of *Pseudomonas resinovorans* CA10, an organism which can degrade variants of both the donor and acceptor fluorophores. This general approach can be tailored for a range of metabolic processes and be employed as a method for single-cell metabolomic studies.

At the design stage, increased computational power would allow for precise calculations of molecular orbitals and more accurate predictions of both electron excitation and emission energies. Time-dependent density-functional theory (TDDFT) would provide a rigorous formalism for the calculations of excitation energies. The excitation energies can be readily obtained from a TDDFT calculation by knowing how the system responds to a small time-dependent perturbation. Despite the successes of DFT in describing the electronic structure of complex molecular systems, the treatment of electronic correlation within DFT is only approximate. Therefore, one needs to resort to alternative approaches as the more costly wave function based methods. Most importantly, transitional dipole calculations, which would be beneficial in analyzing the dipole-dipole or quadripole-quadripole interactions present in a FRET system and would provide a "real" orientation factor.

Quantum chemical calculations can also provide a valuable tool in describing the experienced interactions between ATBC and the CARDO enzymes. The unreliability of density-functional-based approaches to accurately describe photoexcitation of biomolecules means any computational approaches would rely on expanding the wave function in Slater determinants and, as the system size increases and the energies of the single-particle orbitals become closely spaced, the space of orbitals which

must be included to recover a significant fraction of electronic correlation grows enormously. Therefore, when these approaches are applied to large biomolecules, compromises must be taken as in the use of a small atomic basis or a reduced space of active orbitals. Consequently, while highly-correlated quantum chemical approaches are accurate for small systems where these techniques can be pushed to their limits, the same level of accuracy cannot in general be guaranteed when going to a large biosystem.

Functionalization of nanoparticles as bio-active ligand carriers. Nanoparticles were efficiently modified with bioactive moieties as tools to harvest enzymes. Functionalized nanoparticles can be utilized in an array of biotechnologies, *e.g.* medical assays, therapeutics, and diagnostics. In this case, a tool was developed and presented for a critical component of commercialized biotechnologies for bioseparation. The ability to target and extract biomolecules of interest from a natural source with ease and efficiency is critical for understanding and ultimately developing useful technologies from these systems.

Initially, a model system was utilized to show the efficacy of synthesizing a "baited" nanoparticle to capture and recycle enzymes from lysate. Enzyme trapping and recycling was illustrated with the CARDO systems, an enzyme important in bioremediation and natural product synthesis. The enzymes were baited with an azide modified carbazolyl-moiety attached to a PA nanoparticle. The bait products is well dispersed in water and buffers, a property that is independent of selected ligand, but a result of their attachment to PA particles. These results establish a universal model applicable to concentrating and extracting known substrate protein pairs, but it can be an invaluable tool in recognizing unknown protein-ligand affinities. Despite the widespread availability of genome sequences, according to the shear multitude of

metabolites the selectivity of many metabolic enzymes are still veiled, this procedure goes a long way toward cultivating large banks of recyclable metabolic enzymes and probing enzyme selectivity.

The ability to create a clickable nano-surface was easily achieved with propargyl acrylate nanoparticles because of the inherent presence of alkynes; however, the addition of click functionality to inorganic nanoparticles seemed like a sizable challenge. By again employing propargyl acrylate, that addition of a clickable copolymer to an inorganic surface was successfully demonstrated and characterized as a general methodology for producing magnetic nanoclusters with an elevated alkyne functionality. The functional nanoclusters were formed by the adsorption of poly(AA-co-PA), which provides both colloidal stability and surface functionality. Complicated synthesis routes previously required for the surface functionalization of SPIONs are circumvented by designing the copolymer stabilizer prior to nanocluster formation. By copolymerizing acrylic acid with propargyl acrylate we synthesized a *clickable* coating, that would be anchored to the SPION. We also showed the size of the nanoclusters and thickness of the polymer coating was controlled by tailoring the molecular weight of the adsorbed polymer with the use of a chain transfer agent during synthesis. For the first time, the complex susceptibility measurements of the particles was utilized to investigate the nanoparticles clustering formation. Nanoclusters exhibited a relaxation time dominated by Brownian relaxation, confirming that the particles coat with polymer and then bridge to form clusters. The availability of accessible alkyne groups on the surface of the aqueous-phase nanocluster allowed for the surface modification of the particles CuCAAC click reaction with an azide-modified ICG. We expect to extend this method to the synthesis of clinically viable hyperthermia nanoclusters, which exploit the CuAAC click reaction for the targeting of nanoclusters, and direct delivery of therapeutic agents.

Although both the bioseparation colloids and clickable-SPION demonstrate routes to clickable biofunctionality, they are a mere drop in the bucket of opportunities that the convergence of nanomaterials and biotechnology present. Even within the CARDO system, the bioseparation colloids can be further developed to incorporate targeting ligands to generate *in vivo* bait particles. Comparatively, the clickable-SPION were evaluated only for their fluorescence imaging capabilities; a more in-depth analysis of their magnetic properties would provide for a better understanding of the the additional imaging (MRI contrast) and therapeutic (hyperthermia, drug delivery) properties afforded by superparamagnetic particles.

Production of cell encapsulating materials in-flow. Microfluidics and hydrodynamic focusing provided a method for the continuous production of biohybrid fibers. By adjusting pre-polymer solutions and flow rates within the microchannel, we were able to tune the morphology, hydration, and thermal properties of the fibers. The methodology produced hydrogel fibers that sustained viable cells as demonstrated by the encapsulation and subsequent proliferation of B.cereus and E.coli. The described method differs from other hydrodynamic methods by removing the problematic needle-in-channel or "concentric annuli" form factors. Using integrated, shaping features and laminar flow reduces common fabrication problems like clogging or axial diffusion. Moreover, the hydrodynamic focusing within the microfluidic channel can provide a continuous process for in situ gelation. The flexibility in fiber size, shape and composition, coupled with benign photopolymerization conditions, surpasses other reported biohybrid fiber fabrication methods in terms of ease of the fabrication and resultant cell viability.

The view that continuous flow processing is only useful for commodity products has changed over the last 20 years as the advent of nano- and biotechnology has

scaled production methods down to the lab bench and smaller. Flow processing not only provides low-end assembly-line benefits but also has value for high-margin products because of the heat-transfer, mixing, and flow-alignment attributes conveyed by micro-reactors. Compared to nozzle-in-channel devices that create core-sheath flow to control fiber diameter, hydrogels and cells passing through the nozzle are subjected to cytotoxic shear forces.[333] The presented microfluidic device negates such shear stress during fiber shaping by employing a core and sheath laminar flow using grooves in the channel walls to hydrodynamically focus the core within the sheath fluid. This approach enabled the injection of viscous pre-polymer reagents infused with biological constituents with minimal clogging. Compared to microfluidic casting approaches, the rapid photoinitiated polymerization in the microfluidic channel avoids the cytotoxicity caused by organic solvents as well as osmotic pressure changes. In the continuous single-step process reported here, cells are localized in the hydrodynamically constrained core flow, and upon exposure to light, the core forms a crosslinked biohybrid fiber. In addition, the sheath stream can shape the fibers prior to polymerization; this provides the ability to fabricate larger flat fibers that may have increased strength and higher surface area:volume than round fibers with the same cross-sectional area. The laminar flow and photopolymerization conditions maintain the viability of the cells during the fiber fabrication process.

Since the requirement of a Cu(I)-catalyst precludes the use of the CuCAAC reaction within living systems, many copper-free alternatives to CuCAAC exist. Along with the thiol-ene and thiol-yne reactions, the Staudinger ligation of phosphines with azides and strain-promoted cycloaddition of cyclo-octynes with azides, may provide alternative click routes to producing hydrogels for biohybrid materials. Initially, the thiol-ene and thiol-yne PEG fibers can be explored as cell immobilization materials, and future results will dictate the most suitable polymer chemistry for producing

biohybrid fibers in flow.

6.2 Theoretical implications and recommendations for future research

Since the renaissance of Huisgen's 1,3-dipolar cycloaddition of azides and terminal alkynes catalyzed by Cu(I), this reaction has become a favorite ligation tool of polymer and materials scientists, proving particularly useful in areas as diverse as polymer synthesis, molecular biology and nanoelectronics. Far beyond the selected examples included here, click chemistry has developed into an important tool set for materials scientists, and it is not difficult to predict that the range of potential applications, especially in the life sciences, will continue to grow. On the other hand, it can be expected that the continuous push for designer materials will lead to the identification of additional chemical reactions that can be reframed within the concept of click chemistry; a framework of chemical versatility and control. Nevertheless, there are still limitations of the CuCAAC reaction that must be considered for biological applications. The further development of metal-free reactions or "click-methods," like microfluidic reactors, are potential solutions.

Click chemistries provide a future for materials science, that will be required to address the gap between sophisticated material function and the limited chemical control offered by many of the currently available synthetic processes. Current synthetic macromolecules are randomly and haphazardly combined in comparison to many proteins or nucleic acids. The more complex a macromolecular structure is, the more important it is to have a simple pathway for its preparation. And since Nature has optimized its chemistry *via* evolution, it is hubris to attempt duplication; rather,

it is the discovery and selection of the proper tools to harness and exploit Nature's methods that is essential for the rapid advancement of our philosophy.

Appendices

Appendix A Glossary

°C	degrees Celsius
β	The second letter of the greek alphabet
ϵ	molar absorptivity
η	viscosity
μm	micrometer
π	transcendental number (≈ 3.1415)
ϕ	quantum efficiency
τ_B	Brownian relaxation time (s)
τ_N	Néel relaxation time (s)
AA	acrylic acid
AA-PA	poly(acrylic acid-*co*-propargyl acrylate)
ABA	2-amino-benzoic acid
AIBN	2,2'-azobisisobutyronitrile
$\overrightarrow{B}$	magnetic field induction
B.cereus	*Bacillus cereus*
BSA	bovine serum albumin
E	energy
EA	9-ethyl anthracene
c	speed of light (2.99792458 m/s)
C6	coumarin-6
CA10	*Pseudomonas resinovorans* CA10
CAR	9H-carbazole
CARDO	carbazole 1,9a-dioxygenase
CuCAAC	Cu(I)-catalyzed azide-alkyne cycloaddition
CTA	chain transfer agent
DET	Dexter energy transfer
DFT	density functional theory
DLS	dynamic light scattering
E.coli	*Escherichia col*
EGDMA	ethylene glycol dimethacrylate
f	frequency (Hz)

FRET	Förster resonance energy transfer
FT-IR	Fourier transform infrared spectroscopy
h	Planck's constant (6.626068 x 10^{-34} m^2kg/s)
$\overrightarrow{H}$	magnetic field
HF	Hartree-Fock
ICG	indocyanine green
m	meter
M	magnetization
MALDI-TOF	matrix-assisted laser desorption/ionization time-of-flight mass spectroscopy
MeOH	methanol
MRI	magnetic resonance imaging
MPn	Müller-Plesset correlation with n degrees
N	Avogadro's number (6.02 x 10^{23})
nm	nanometer
NMR	nuclear magnetic resonance
PA	propargyl acrylate
PAAC	poly(propargyl acrylate)-*mod*-AC nanoparticles
PC	pyrocatechol
PEG	poly(ethylene glycol)
PEG_{4yne}	4-star poly(ethylene glycol) with alkyne functionality
PEG_{4SH}	4-star poly(ethylene glycol) with thiol functionality
PEGDMA	poly(ethylene glycol) dimethacrylate
PETMP	pentaerythritol tetrakis(3-mercaptopropionate)
PL	photoluminescence
RAFT	reversible addition-fragmentation chain transfer polymerization
ROMP	ring-opening metathesis polymerization
s	second
SDS-PAGE	sodium dodecyl sulfate polyacrylamide gel electrophoresis
SEM	scanning electron microscopy
SPION	superparamagnetic iron oxide nanoparticle
TEM	transmission electron microscopy
THF	tetrahydrofuran

Appendix B Copyright Permissions

JOHN WILEY AND SONS LICENSE
TERMS AND CONDITIONS

Jun 03, 2012

This is a License Agreement between Michael Daniele ("You") and John Wiley and Sons ("John Wiley and Sons") provided by Copyright Clearance Center ("CCC"). The license consists of your order details, the terms and conditions provided by John Wiley and Sons, and the payment terms and conditions.

All payments must be made in full to CCC. For payment instructions, please see information listed at the bottom of this form.

License Number	2911451388753
License date	May 17, 2012
Licensed content publisher	John Wiley and Sons
Licensed content publication	Photochemistry and Photobiology
Licensed content title	Manipulation of Förster Energy Transfer of Coupled Fluorophores Through Biotransformation by Pseudomonas resinovorans CA10
Licensed content author	Michael A. Daniele,Yuriy P. Bandera,Stephen H. Foulger
Licensed content date	Dec 16, 2011
Start page	129
End page	134
Type of use	Dissertation/Thesis
Requestor type	Author of this Wiley article
Format	Print and electronic
Portion	Full article
Will you be translating?	No
Order reference number	
Total	0.00 USD
Terms and Conditions	

TERMS AND CONDITIONS

This copyrighted material is owned by or exclusively licensed to John Wiley & Sons, Inc. or one of its group companies (each a "Wiley Company") or a society for whom a Wiley Company has exclusive publishing rights in relation to a particular journal (collectively WILEY"). By clicking "accept" in connection with completing this licensing transaction, you agree that the following terms and conditions apply to this transaction (along with the billing and payment terms and conditions established by the Copyright Clearance Center Inc., ("CCC's Billing and Payment terms and conditions"), at the time that you opened your Rightslink account (these are available at any time at http://myaccount.copyright.com)

JOHN WILEY AND SONS LICENSE
TERMS AND CONDITIONS

Jun 03, 2012

This is a License Agreement between Michael Daniele ("You") and John Wiley and Sons ("John Wiley and Sons") provided by Copyright Clearance Center ("CCC"). The license consists of your order details, the terms and conditions provided by John Wiley and Sons, and the payment terms and conditions.

All payments must be made in full to CCC. For payment instructions, please see information listed at the bottom of this form.

License Number	2911451137830
License date	May 17, 2012
Licensed content publisher	John Wiley and Sons
Licensed content publication	Small
Licensed content title	Substrate-Baited Nanoparticles: A Catch and Release Strategy for Enzyme Recognition and Harvesting
Licensed content author	Michael A. Daniele,Yuriy P. Bandera,Deepti Sharma,Parul Rungta,Ryan Roeder,Michael G. Sehorn,Stephen H. Foulger
Licensed content date	Apr 24, 2012
Start page	n/a
End page	n/a
Type of use	Dissertation/Thesis
Requestor type	Author of this Wiley article
Format	Print and electronic
Portion	Full article
Will you be translating?	No
Order reference number	
Total	0.00 USD
Terms and Conditions	

TERMS AND CONDITIONS

This copyrighted material is owned by or exclusively licensed to John Wiley & Sons, Inc. or one of its group companies (each a "Wiley Company") or a society for whom a Wiley Company has exclusive publishing rights in relation to a particular journal (collectively WILEY"). By clicking "accept" in connection with completing this licensing transaction, you agree that the following terms and conditions apply to this transaction (along with the billing and payment terms and conditions established by the Copyright Clearance Center Inc., ("CCC's Billing and Payment terms and conditions"), at the time that you opened your Rightslink account (these are available at any time at http://myaccount.copyright.com)

Bibliography

[1] K. B. Sharpless. Searching for new reactivity. *Angewandte Chemie-International Edition*, 41(12):2024–2032, 2002.

[2] H. C. Kolb, M. G. Finn, and K. B. Sharpless. Click chemistry: Diverse chemical function from a few good reactions. *Angewandte Chemie-International Edition*, 40(11):2004–2021, 2001.

[3] Q. Wang, T. R. Chan, R. Hilgraf, V. V. Fokin, K. B. Sharpless, and M. G. Finn. Bioconjugation by copper(i)-catalyzed azide-alkyne 3+2 cycloaddition. *Journal of the American Chemical Society*, 125(11):3192–3193, 2003.

[4] K. Nwe and M. W. Brechbiel. Growing applications of "click chemistry" for bioconjugation in contemporary biomedical research. *Cancer Biotherapy and Radiopharmaceuticals*, 24(3):289–302, 2009.

[5] J. F. Lutz and Z. Zarafshani. Efficient construction of therapeutics, bioconjugates, biomaterials and bioactive surfaces using azide-alkyne "click" chemistry. *Advanced Drug Delivery Reviews*, 60(9):958–970, 2008.

[6] V. Hong, S. I. Presolski, C. Ma, and M. G. Finn. Analysis and optimization of copper-catalyzed azide-alkyne cycloaddition for bioconjugation. *Angewandte Chemie-International Edition*, 48(52):9879–9883, 2009.

[7] G. Hermanson. *Bioconjugate Techniques*. Academic Press, London, UK, 2nd edition, —2008—.

[8] J. E. Hudak, R. M. Barfield, G. W. de Hart, P. Grob, E. Nogales, C. R. Bertozzi, and D. Rabuka. Synthesis of heterobifunctional protein fusions using copper-free click chemistry and the aldehyde tag. *Angewandte Chemie-International Edition*, 51(17):4161–4165, 2012.

[9] J. Kalia and R. T. Raines. Advances in bioconjugation. *Current Organic Chemistry*, 14(2):138–147, 2010.

[10] K. W. Dehnert, J. M. Baskin, S. T. Laughlin, B. J. Beahm, N. N. Naidu, S. L. Amacher, and C. R. Bertozzi. Imaging the sialome during zebrafish development with copper-free click chemistry. *Chembiochem*, 13(3):353–357, 2012.

[11] Xinghai Ning, Jun Guo, Margreet A. Wolfert, and Geert-Jan Boons. Visualizing metabolically labeled glycoconjugates of living cells by copper-free and fast huisgen cycloadditions. *Angewandte Chemie-International Edition*, 47(12):2253–2255, 2008.

[12] G. C. Tron, T. Pirali, R. A. Billington, P. L. Canonico, G. Sorba, and A. A. Genazzani. Click chemistry reactions in medicinal chemistry: Applications of the 1,3-dipolar cycloaddition between azides and alkynes. *Medicinal Research Reviews*, 28(2):278–308, 2008.

[13] J. Lahann. *Click Chemistry for Biotechnology and Materials Science*. John Wiley & Sons Ltd., West Sussex, UK, —2009—.

[14] V. V. Rostovtsev, L. G. Green, V. V. Fokin, and K. B. Sharpless. A stepwise huisgen cycloaddition process: Copper(i)-catalyzed regioselective "ligation" of azides and terminal alkynes. *Angewandte Chemie-International Edition*, 41(14):2596–+, 2002.

[15] R. Huisgen. Cycloadditions: Definition, classification and characterization. *Angewandte Chemie-International Edition*, 7(5):321, 1968.

[16] C. W. Tornoe, C. Christensen, and M. Meldal. Peptidotriazoles on solid phase: 1,2,3 -triazoles by regiospecific copper(i)-catalyzed 1,3-dipolar cycloadditions of terminal alkynes to azides. *Journal of Organic Chemistry*, 67(9):3057–3064, 2002.

[17] F. Himo, T. Lovell, R. Hilgraf, V. V. Rostovtsev, L. Noodleman, K. B. Sharpless, and V. V. Fokin. Copper(i)-catalyzed synthesis of azoles. dft study predicts unprecedented reactivity and intermediates. *Journal of the American Chemical Society*, 127(1):210–216, 2005.

[18] Morten Meldal and Christian Wenzel Tornoe. Cu-catalyzed azide-alkyne cycloaddition. *Chemical Reviews*, 108(8):2952–3015, 2008.

[19] V. O. Rodionov, V. V. Fokin, and M. G. Finn. Mechanism of the ligand-free cu-i-catalyzed azide-alkyne cycloaddition reaction. *Angewandte Chemie-International Edition*, 44(15):2210–2215, 2005.

[20] L. Zhang, X. G. Chen, P. Xue, H. H. Y. Sun, I. D. Williams, K. B. Sharpless, V. V. Fokin, and G. C. Jia. Ruthenium-catalyzed cycloaddition of alkynes and organic azides. *Journal of the American Chemical Society*, 127(46):15998–15999, 2005.

[21] S. Oppilliart, G. Mousseau, L. Zhang, G. C. Jia, P. Thuery, B. Rousseau, and J. C. Cintrat. 1-protected 5-amido 1,2,3-triazoles via ruthenium-catalyzed [3+2] cycloaddition of azides and ynamides. *Tetrahedron*, 63(34):8094–8098, 2007.

[22] M. M. Majireck and S. M. Weinreb. A study of the scope and regioselectivity of the ruthenium-catalyzed [3+2]-cycloaddition of azides with internal alkynes. *Journal of Organic Chemistry*, 71(22):8680–8683, 2006.

[23] L. K. Rasmussen, B. C. Boren, and V. V. Fokin. Ruthenium-catalyzed cycloaddition of aryl azides and alkynes. *Organic Letters*, 9(26):5337–5339, 2007.

[24] W. G. Lewis, F. G. Magallon, V. V. Fokin, and M. G. Finn. Discovery and characterization of catalysts for azide-alkyne cycloaddition by fluorescence quenching. *Journal of the American Chemical Society*, 126(30):9152–9153, 2004.

[25] P. L. Golas, N. V. Tsarevsky, B. S. Sumerlin, and K. Matyjaszewski. Catalyst performance in "click" coupling reactions of polymers prepared by atrp: Ligand and metal effects. *Macromolecules*, 39(19):6451–6457, 2006.

[26] C. Barner-Kowollik, F. E. Du Prez, P. Espeel, C. J. Hawker, T. Junkers, H. Schlaad, and W. Van Camp. "clicking" polymers or just efficient linking: What is the difference? *Angewandte Chemie-International Edition*, 50(1):60–62, 2011.

[27] J. A. Johnson, M. G. Finn, J. T. Koberstein, and N. J. Turro. Construction of linear polymers, dendrimers, networks, and other polymeric architectures by copper-catalyzed azide-alkyne cycloaddition "click" chemistry (vol 29, pg 1052, 2008). *Macromolecular Rapid Communications*, 29(16):1421–1421, 2008.

[28] Wolfgang H. Binder and Robert Sachsenhofer. 'click' chemistry in polymer and material science: An update. *Macromolecular Rapid Communications*, 29(12-13):952–981, 2008.

[29] H. Nandivada, X. W. Jiang, and J. Lahann. Click chemistry: Versatility and control in the hands of materials scientists. *Advanced Materials*, 19(17):2197–2208, 2007.

[30] Yi Liu, David D. Diaz, Adrian A. Accurso, K. Barry Sharpless, Valery V. Fokin, and M. G. Finn. Click chemistry in materials synthesis. iii. metal-adhesive polymers from cu(i)-catalyzed azide-alkyne cycloaddition. *Journal of Polymer Science Part a-Polymer Chemistry*, 45(22):5182–5189, 2007.

[31] Craig J. Hawker, Valery V. Fokin, M. G. Finn, and K. Barry Sharpless. Bringing efficiency to materials synthesis: The philosophy of click chemistry. *Australian Journal of Chemistry*, 60(6):381–383, 2007.

[32] T. Zhang, Z. H. Zheng, X. Cheng, X. B. Ding, and Y. X. Peng. "click" chemistry in materials science. *Progress in Chemistry*, 20(7-8):1090–1101, 2008.

[33] C. J. Hawker and K. L. Wooley. The convergence of synthetic organic and polymer chemistries. *Science*, 309(5738):1200–1205, 2005.

[34] D. D. Diaz, S. Punna, P. Holzer, A. K. McPherson, K. B. Sharpless, V. V. Fokin, and M. G. Finn. Click chemistry in materials synthesis. 1. adhesive polymers from copper-catalyzed azide-alkyne cycloaddition. *Journal of Polymer Science Part a-Polymer Chemistry*, 42(17):4392–4403, 2004.

[35] P. Wu, A. K. Feldman, A. K. Nugent, C. J. Hawker, A. Scheel, B. Voit, J. Pyun, J. M. J. Frechet, K. B. Sharpless, and V. V. Fokin. Efficiency and fidelity in a click-chemistry route to triazole dendrimers by the copper(i)-catalyzed ligation of azides and alkynes. *Angewandte Chemie-International Edition*, 43(30):3928–3932, 2004.

[36] R. A. Evans. The rise of azide-alkyne 1,3-dipolar 'click' cycloaddition and its application to polymer science and surface modification. *Australian Journal of Chemistry*, 60(6):384–395, 2007.

[37] Wolfgang H. Binder and Robert Sachsenhofer. 'click' chemistry in polymer and materials science. *Macromolecular Rapid Communications*, 28(1):15–54, 2007.

[38] P. L. Golas and K. Matyjaszewski. Marrying click chemistry with polymerization: expanding the scope of polymeric materials. *Chemical Society Reviews*, 39(4):1338–1354, 2010.

[39] V. O. Rodionov, S. I. Presolski, D. D. Diaz, V. V. Fokin, and M. G. Finn. Ligand-accelerated cu-catalyzed azide-alkyne cycloaddition: A mechanistic report. *Journal of the American Chemical Society*, 129(42):12705–12712, 2007.

[40] S. I. Presolski, V. Hong, S. H. Cho, and M. G. Finn. Tailored ligand acceleration of the cu-catalyzed azide-alkyne cycloaddition reaction: Practical and mechanistic implications. *Journal of the American Chemical Society*, 132(41):14570–14576, 2010.

[41] P. L. Golas, N. V. Tsarevsky, B. S. Sumerlin, L. M. Walker, and K. Matyjaszewski. Multisegmented block copolymers by 'click' coupling of polymers prepared by atrp. *Australian Journal of Chemistry*, 60(6):400–404, 2007.

[42] K. Matyjaszewski and N. V. Tsarevsky. Nanostructured functional materials prepared by atom transfer radical polymerization. *Nature Chemistry*, 1(4):276–288, 2009.

[43] M. Semsarilar and S. Perrier. 'green' reversible addition-fragmentation chain-transfer (raft) polymerization. *Nature Chemistry*, 2(10):811–820, 2010.

[44] F. A. Leibfarth, M. Kang, M. Ham, J. Kim, L. M. Campos, N. Gupta, B. Moon, and C. J. Hawker. A facile route to ketene-functionalized polymers for general materials applications. *Nature Chemistry*, 2(3):207–212, 2010.

[45] Kaushik Patel, Sarah Angelos, William R. Dichtel, Ali Coskun, Ying-Wei Yang, Jeffrey I. Zink, and J. Fraser Stoddart. Enzyme-responsive snap-top covered silica nanocontainers. *Journal of the American Chemical Society*, 130(8):2382–2383, 2008.

[46] Rachel K. O'Reilly, Maisie J. Joralemon, Craig J. Hawker, and Karen L. Wooley. Facile syntheses of surface-functionalized micelles and shell cross-linked nanoparticles. *Journal of Polymer Science Part a-Polymer Chemistry*, 44(17):5203–5217, 2006.

[47] D. A. Fleming, C. J. Thode, and M. E. Williams. Triazole cycloaddition as a general route for functionalization of au nanoparticles. *Chemistry of Materials*, 18(9):2327–2334, 2006.

[48] M. A. White, J. A. Johnson, J. T. Koberstein, and N. J. Turro. Toward the syntheses of universal ligands for metal oxide surfaces: Controlling surface functionality through click chemistry. *Journal of the American Chemical Society*, 128(35):11356–11357, 2006.

[49] R. K. O'Reilly, M. J. Joralemon, K. L. Wooley, and C. J. Hawker. Functionalization of micelles and shell cross-linked nanoparticles using click chemistry. *Chemistry of Materials*, 17(24):5976–5988, 2005.

[50] L. D. Pachon, J. H. van Maarseveen, and G. Rothenberg. Click chemistry: Copper clusters catalyse the cycloaddition of azides with terminal alkynes. *Advanced Synthesis and Catalysis*, 347(6):811–815, 2005.

[51] M. J. Joralemon, R. K. O'Reilly, C. J. Hawker, and K. L. Wooley. Shell click-crosslinked (scc) nanoparticles: A new methodology for synthesis and orthogonal functionalization. *Journal of the American Chemical Society*, 127(48):16892–16899, 2005.

[52] D. Evanoff, S. Foulger, and et al. Functionalization of crystalline colloidal arrays through click chemistry. *Advanced Materials*, 19:3507–3512, 2007.

[53] P. Rungta, Y. P. Bandera, V. Tsyalkovsky, and S. H. Foulger. Designing fluoroprobes through forster resonance energy transfer: Surface modification of nanoparticles through "click" chemistry. *Soft Matter*, 6:6083–6095, 2010.

[54] Christian Wendeln and Bart Jan Ravoo. Surface patterning by microcontact chemistry. *Langmuir*, 28(13):5527–5538, 2012.

[55] Scott R. Schricker, Manuel L. B. Palacio, and Bharat Bhushan. Designing nanostructured block copolymer surfaces to control protein adhesion. *Philosophical Transactions of the Royal Society a-Mathematical Physical and Engineering Sciences*, 370(1967):2348–2380, 2012.

[56] Peter K. B. Palomaki and Peter H. Dinolfo. A versatile molecular layer-by-layer thin film fabrication technique utilizing copper(i)-catalyzed azide alkyne cycloaddition. *Langmuir*, 26(12):9677–9685, 2010.

[57] Sascha Reuter, Karsten Busse, Ute Radics, Hans-Joachim Niclas, and Joerg Kressler. Langmuir monolayers and langmuir-blodgett films of 1-acyl-1,2,4-triazoles. *Journal of Colloid and Interface Science*, 340(2):276–284, 2009.

[58] Hernan R. Rengifo, Cristian Grigoras, Benjamin I. Dach, Xia Li, Nicholas J. Turro, Hae-Jeong Lee, Wen-Li Wu, and Jeffrey T. Koberstein. Solid phase synthesis of polymacromer and copolymacromer brushes. *Macromolecules*, 45(9):3866–3873, 2012.

[59] J. Lahann, M. Balcells, T. Rodon, J. Lee, I. S. Choi, K. F. Jensen, and R. Langer. Reactive polymer coatings: A platform for patterning proteins and mammalian cells onto a broad range of materials. *Langmuir*, 18(9):3632–3638, 2002.

[60] J. Lahann, I. S. Choi, J. Lee, K. F. Jenson, and R. Langer. A new method toward microengineered surfaces based on reactive coating. *Angewandte Chemie-International Edition*, 40(17):3166–+, 2001.

[61] B. J. Adzima, Y. H. Tao, C. J. Kloxin, C. A. DeForest, K. S. Anseth, and C. N. Bowman. Spatial and temporal control of the alkyne-azide cycloaddition by photoinitiated cu(ii) reduction. *Nature Chemistry*, 3(3):256–259, 2011.

[62] H. C. Kolb and K. B. Sharpless. The growing impact of click chemistry on drug discovery. *Drug Discovery Today*, 8(24):1128–1137, 2003.

[63] T. H. Li, L. N. Guo, Y. Zhang, J. J. Wang, Z. H. Li, L. Lin, Z. X. Zhang, L. Li, J. P. Lin, W. Zhao, J. Li, and P. G. Wang. Design and synthesis of o-glcnacase inhibitors via 'click chemistry' and biological evaluations. *Carbohydrate Research*, 346(9):1083–1092, 2011.

[64] J. W. Yang and G. R. Chen. A unique and rapid approach toward the efficient development of novel protein tyrosine phosphatase (ptp) inhibitors based on 'clicked' pseudo-glycopeptides. *Bioorganic & Medicinal Chemistry Letters*, 21(4):1092–1096, 2011.

[65] M. J. Giffin, H. Heaslet, A. Brik, Y. C. Lin, G. Cauvi, C. H. Wong, D. E. McRee, J. H. Elder, C. D. Stout, and B. E. Torbett. A copper(i)-catalyzed 1,2,3-triazole azide-alkyne click compound is a potent inhibitor of a multidrug-resistant hiv-1 protease variant. *Journal of Medicinal Chemistry*, 51(20):6263–6270, 2008.

[66] R. Srinivasan, J. Li, S. L. Ng, K. A. Kalesh, and S. Q. Yao. Methods of using click chemistry in the discovery of enzyme inhibitors. *Nature Protocols*, 2(11):2655–2664, 2007.

[67] A. E. Speers and B. F. Cravatt. Profiling enzyme activities in vivo using click chemistry methods. *Chemistry & Biology*, 11(4):535–546, 2004.

[68] A. E. Speers, G. C. Adam, and B. F. Cravatt. Activity-based protein profiling in vivo using a copper(i)-catalyzed azide-alkyne [3+2] cycloaddition. *Journal of the American Chemical Society*, 125(16):4686–4687, 2003.

[69] K. Kizjakina, J. M. Bryson, G. Grandinetti, and T. M. Reineke. Cationic glycopolymers for the delivery of pdna to human dermal fibroblasts and rat mesenchymal stem cells. *Biomaterials*, 33(6):1851–1862, 2012.

[70] S. Averick, E. Paredes, W. W. Li, K. Matyjaszewski, and S. R. Das. Direct dna conjugation to star polymers for controlled reversible assemblies. *Bioconjugate Chemistry*, 22(10):2030–2037, 2011.

[71] M. M. Rowland, H. E. Bostic, D. H. Gong, A. E. Speers, N. Lucas, W. H. Cho, B. F. Cravatt, and M. D. Best. Phosphatidylinositol 3,4,5-trisphosphate activity probes for the labeling and proteomic characterization of protein binding partners. *Biochemistry*, 50(51):11143–11161, 2011.

[72] V. Hong, N. F. Steinmetz, M. Manchester, and M. G. Finn. Labeling live cells by copper-catalyzed alkyne-azide click chemistry. *Bioconjugate Chemistry*, 21(10):1912–1916, 2010.

[73] M. P. Lutolf and J. A. Hubbell. Synthesis and physicochemical characterization of end-linked poly(ethylene glycol)-co-peptide hydrogels formed by michael-type addition. *Biomacromolecules*, 4(3):713–722, 2003.

[74] C. C. Lee, G. Grandinetti, P. M. McLendon, and T. M. Reineke. A polycation scaffold presenting tunable "click" sites: Conjugation to carbohydrate ligands and examination of hepatocyte-targeted pdna delivery. *Macromolecular Bioscience*, 10(6):585–598, 2010.

[75] S. Srinivasachari and T. M. Reineke. Versatile supramolecular pdna vehicles via "click polymerization" of beta-cyclodextrin with oligoethyleneamines. *Biomaterials*, 30(5):928–938, 2009.

[76] S. Hvilsted. Facile design of biomaterials by click' chemistry. *Polymer International*, 61(4):485–494, 2012.

[77] S. K. Mamidyala and M. G. Finn. In situ click chemistry: probing the binding landscapes of biological molecules. *Chemical Society Reviews*, 39(4):1252–1261, 2010.

[78] Maarten van Dijk, Dirk T. S. Rijkers, Rob M. J. Liskamp, Cornelus F. van Nostrum, and Wim E. Hennink. Synthesis and applications of biomedical and pharmaceutical polymers via click chemistry methodologies. *Bioconjugate Chemistry*, 20(11):2001–2016, 2009.

[79] M. L. Flenniken, D. A. Willits, S. Brumfield, M. J. Young, and T. Douglas. The small heat shock protein cage from methanococcus jannaschii is a versatile nanoscale platform for genetic and chemical modification. *Nano Letters*, 3(11):1573–1576, 2003.

[80] N. W. Li and W. H. Binder. Click-chemistry for nanoparticle-modification. *Journal of Materials Chemistry*, 21(42):16717–16734, 2011.

[81] P. Rungta, Y. P. Bandera, R. D. Roeder, Y. C. Li, W. S. Baldwin, D. Sharma, M. G. Sehorn, I. Luzinov, and S. H. Foulger. Selective imaging and killing of cancer cells with protein-activated near-infrared fluorescing nanoparticles. *Macromolecular Bioscience*, 11(7):927–937, 2011.

[82] M. Shi, J. Lu, and M. S. Shoichet. Organic nanoscale drug carriers coupled with ligands for targeted drug delivery in cancer. *Journal of Materials Chemistry*, 19(31):5485–5498, 2009.

[83] J. Lu, M. Shi, and M. S. Shoichet. Click chemistry functionalized polymeric nanoparticles target corneal epithelial cells through rgd-cell surface receptors. *Bioconjugate Chemistry*, 20(1):87–94, 2009.

[84] S. Srinivasachari, K. M. Fichter, and T. M. Reineke. Polycationic beta-cyclodextrin "click clusters": Monodisperse and versatile scaffolds for nucleic acid delivery. *Journal of the American Chemical Society*, 130(14):4618–4627, 2008.

[85] K. Deuschle, B. Chaudhuri, S. Okumoto, I. Lager, S. Lalonde, and W. B. Frommer. Rapid metabolism of glucose detected with fret glucose nanosensors in epidermal cells and intact roots of arabidopsis rna-silencing mutants. *Plant Cell*, 18(9):2314–2325, 2006.

[86] E. V. Bichenkova and K. T. Douglas. Detection of nucleic acids in situ: novel oligonucleotide analogues for target-assembled dna-mounted exciplexes. *Organic & Biomolecular Chemistry*, 5(7):1039–1051, 2007.

[87] E. V. Bichenkova and K. T. Douglas. Target-assembled tandem oligonucleotide systems based on exciplexes for detecting dna mismatches and single nucleotide polymorphisms. *Biochemical and Biophysical Research Communications*, 332(4):956–964, 2005.

[88] E. V. Bichenkova, A. Sardarian, H. E. Savage, C. Rogert, and K. T. Douglas. An exciplex-based, target-assembled fluorescence system with inherently low background to probe for specific nucleic acid sequences. *Assay and Drug Development Technologies*, 3(1):39–46, 2005.

[89] M. Kadirvel, B. Arsic, S. Freeman, and E. V. Bichenkova. Exciplex and excimer molecular probes: detection of conformational flip in a myo-inositol chair. *Organic & Biomolecular Chemistry*, 6(11):1966–1972, 2008.

[90] Z. H. Zhou and C.J. Fahrni. A fluorogenic probe for the copper(i)-catalyzed azide-alkyne ligation reaction: modulation of the fluorescence emission via 3(n,pi)-1(pi,pi) inversion. *Journal of the American Chemical Society*, 126(29):3, 2004.

[91] L. Du, N. Ni, M. Li, and B. Wang. A fluorescent hydrogen peroxide probe based on a "click" modified coumarin fluorophore. *Tetrahedron Letters*, 51(8):2, 2010.

[92] A. T. Brunger, P. Strop, M. Vrljic, S. Chu, and K. R. Weninger. Three-dimensional molecular modeling with single molecule fret. *Journal of Structural Biology*, 173(3):497–505, 2011.

[93] N.S. Sariciftci, L. Smilowitz, A.J. Heeger, and F. Wudl. Photoinduced electron-transfer from a conducting polymer to a buckminsterfullerine. *Science*, 258:1474, 1992.

[94] J. L. Bredas, D. Beljonne, V. Coropceanu, and J. Cornil. Charge-transfer and energy-transfer processes in pi-conjugated oligomers and polymers: A molecular picture. *Chemical Reviews*, 104:4971, 2004.

[95] E. Haas, E. Katchalski-Katzir, and I.Z. Steinberg. Effect of the orientation of donor and acceptor on the probability of energy transfer involving electronic transitions of mixed polarization. *Biochemistry*, 17(23):6, 1978.

[96] B. N. G. Giepmans, S. R. Adams, M. H. Ellisman, and R. Y. Tsien. Review - the fluorescent toolbox for assessing protein location and function. *Science*, 312(5771):217–224, 2006.

[97] M. Fehr, W. B. Frommer, and S. Lalonde. Visualization of maltose uptake in living yeast cells by fluorescent nanosensors. *Proceedings of the National Academy of Sciences of the United States of America*, 99(15):9846–9851, 2002.

[98] D. E. Prasuhn, A. Feltz, J. B. Blanco-Canosa, K. Susumu, M. H. Stewart, B. C. Mei, A. V. Yakovlev, C. Loukov, J. M. Mallet, M. Oheim, P. E. Dawson, and I. L. Medintz. Quantum dot peptide biosensors for monitoring caspase 3 proteolysis and calcium ions. *ACS Nano*, 4(9):5487–5497, 2010.

[99] A. Amantonico, P. L. Urban, and R. Zenobi. Analytical techniques for single-cell metabolomics: state of the art and trends. *Analytical and Bioanalytical Chemistry*, 398(6):2493–2504, 2010.

[100] I. Nobeli, A. D. Favia, and J. M. Thornton. Protein promiscuity and its implications for biotechnology. *Nature Biotechnology*, 27(2):157–167, 2009.

[101] K. Hult and P. Berglund. Enzyme promiscuity: mechanism and applications. *Trends in Biotechnology*, 25(5):231–238, 2007.

[102] L. C. James and D. S. Tawfik. Conformational diversity and protein evolution - a 60-year-old hypothesis revisited. *Trends in Biochemical Sciences*, 28(7):361–368, 2003.

[103] A. Aharoni, L. Gaidukov, O. Khersonsky, S. M. Gould, C. Roodveldt, and D. S. Tawfik. The 'evolvability' of promiscuous protein functions. *Nature Genetics*, 37(1):73–76, 2005.

[104] S. D. Copley. Enzymes with extra talents: moonlighting functions and catalytic promiscuity. *Current Opinion in Chemical Biology*, 7(2):265–272, 2003.

[105] L. C. James and D. S. Tawfik. Catalytic and binding poly-reactivities shared by two unrelated proteins: The potential role of promiscuity in enzyme evolution. *Protein Science*, 10(12):2600–2607, 2001.

[106] L. C. James and D. S. Tawfik. The specificity of cross-reactivity: Promiscuous antibody binding involves specific hydrogen bonds rather than nonspecific hydrophobic stickiness. *Protein Science*, 12(10):2183–2193, 2003.

[107] R. A. Jensen. Enzyme recruitment in evolution of new function. *Annual Review of Microbiology*, 30:409–425, 1976.

[108] M. Suarez, P. Tortosa, M. M. Garcia-Mira, D. Rodriguez-Larrea, R. Godoy-Ruiz, B. Ibarra-Molero, J. M. Sanchez-Ruiz, and A. Jaramillo. Using multi-objective computational design to extend protein promiscuity. *Biophysical Chemistry*, 147(1-2):13–19, 2010.

[109] P. J. O'Brien and D. Herschlag. Catalytic promiscuity and the evolution of new enzymatic activities. *Chemistry & Biology*, 6(4):R91–R105, 1999.

[110] O. Khersonsky and D. S. Tawfik. Enzyme promiscuity: A mechanistic and evolutionary perspective. *Annual Review of Biochemistry*, 79:34, 2010.

[111] F. H. Arnold, P. L. Wintrode, K. Miyazaki, and A. Gershenson. How enzymes adapt: lessons from directed evolution. *Trends in Biochemical Sciences*, 26(2):100–106, 2001.

[112] S. C. Rothman and J. F. Kirsch. How does an enzyme evolved in vitro compare to naturally occurring homologs possessing the targeted function? tyrosine aminotransferase from aspartate aminotransferase. *Journal of Molecular Biology*, 327(3):593–608, 2003.

[113] H. Nojiri, J. W. Nam, M. Kosaka, K. I. Morii, T. Takemura, K. Furihata, H. Yamane, and T. Omori. Diverse oxygenations catalyzed by carbazole 1,9a-dioxygenase from Pseudomonas sp strain CA10. *Journal of Bacteriology*, 181(10):3105–3113, 1999.

[114] G. E. Johnson. Intramolecular excimer formation in carbazole double molecules. *Journal of Chemical Physics*, 61(8):3002–3008, 1974.

[115] K. Ray, D. Bhattacharjee, and T. N. Misra. Photophysical characteristics of 9-cyanoanthracene molecules organised in langmuir-blodgett films. *Journal of the Chemical Society-Faraday Transactions*, 93(22):4041–4045, 1997.

[116] K. Ray and T. N. Mishra. Energy transfer between carbazole and anthracene moieties organised in langmuir-blodgett films. *Journal of Physics and Chemistry of Solids*, 60(3):401–405, 1999.

[117] J. Guan, D. E. Kyle, L. Gerena, Q. A. Zhang, W. K. Milhous, and A. J. Lin. Design, synthesis, and evaluation of new chemosensitizers in multi-drug-resistant plasmodium falciparum. *Journal of Medicinal Chemistry*, 45(13):2741–2748, 2002.

[118] Q. Xiao, R. T. Ranasinghe, A. M. P. Tang, and T. Brown. Naphthalenyl- and anthracenyl-ethynyl dt analogues as base discriminating fluorescent nucleosides and intramolecular energy transfer donors in oligonucleotide probes. *Tetrahedron*, 63:3483–3490, 2007.

[119] M. M. Bradford. Rapid and sensitive method for quantitation of microgram quantities of protein utilizing principle of protein-dye binding. *Analytical Biochemistry*, 72(1-2):248–254, 1976.

[120] A. Miller and J. Tanner. *Essentials of Chemical Biology: Structure and Dynamics of Biological Macromolecules*. John Wiley & Sons Ltd., West Sussex, UK, —2008—.

[121] R. Ghosh. *Principles of Bioseparation Engineering*. World Scientific Publishing Co., London, UK, second ed. edition, —2010—.

[122] G. Walsh. Biopharmaceutical benchmarks. *Nature Biotechnology*, 24(7):769–776, 2006.

[123] T. Przybycien, N. Pujar, and L. Steele. lternative bioseparation operations: life beyond packed-bed chromatography. *Current Opinions in Biotechnology*, 15(5):469–478, 2004.

[124] B. Kelley. Very large scale monoclonal antibody purification: the case for conventional unit operations. *Biotechnology Progress*, 23(5):995–1008, 2007.

[125] L. Borisjuk, S. Walenta, H. Weber, W. Mueller-Klieser, and U. Wobus. High-resolution histographical mapping of glucose concentrations in developing cotyledons of vicia faba in relation to mitotic activity and storage processes: glucose as a possible developmental trigger. *Plant Journal*, 15(4):583–591, 1998.

[126] E. M. Farre, A. Tiessen, U. Roessner, P. Geigenberger, R. N. Trethewey, and L. Willmitzer. Analysis of the compartmentation of glycolytic intermediates, nucleotides, sugars, organic acids, amino acids, and sugar alcohols in potato tubers using a nonaqueous fractionation method. *Plant Physiology*, 127(2):685–700, 2001.

[127] K. Jungermann and T. Kietzmann. Zonation of parenchymal and nonparenchymal metabolism in liver. *Annual Review of Nutrition*, 16:179–203, 1996.

[128] A. J. Karley, R. A. Leigh, and D. Sanders. Where do all the ions go? the cellular basis of differential ion accumulation in leaf cells. *Trends in Plant Science*, 5(11):465–470, 2000.

[129] D. Altschuh, S. Oncul, and A. P. Demchenko. Fluorescence sensing of intermolecular interactions and development of direct molecular biosensors. *Journal of Molecular Recognition*, 19(6):459–477, 2006.

[130] C. Schultz. Fluorescent revelations. *Chemistry & Biology*, 16(2):107–111, 2009.

[131] X. J. Zhao, L. R. Hilliard, S. J. Mechery, Y. P. Wang, R. P. Bagwe, S. G. Jin, and W. H. Tan. A rapid bioassay for single bacterial cell quantitation using bioconjugated nanoparticles. *Proceedings of the National Academy of Sciences of the United States of America*, 101(42):15027–15032, 2004.

[132] M. Fehr, S. Okumoto, K. Deuschle, I. Lager, L. L. Looger, J. Persson, L. Kozhukh, S. Lalonde, and W. B. Frommer. Development and use of fluorescent nanosensors for metabolite imaging in living cells. *Biochemical Society Transactions*, 33:287–290, 2005.

[133] A. Baki, A. Bielik, L. Molnar, G. Szendrei, and G. M. Keseru. A high throughput luminescent assay for glycogen synthase kinase-3 beta inhibitors. *Assay and Drug Development Technologies*, 5(1):75–83, 2007.

[134] Ching-Ching Yu, Yu-Ying Kuo, Chien-Fu Liang, Wei-Ting Chien, Huan-Ting Wu, Tsung-Che Chang, Fan-Dan Jan, and Chun-Cheng Lin. Site-specific immobilization of enzymes on magnetic nanoparticles and their use in organic synthesis. *Bioconjugate Chemistry*, 23(4):714–24, 2012.

[135] X. W. Yang, Z. W. Cai, Z. M. Ye, S. Chen, Y. Yang, H. F. Wang, Y. F. Liu, and A. N. Cao. In situ synthesis of porous silica nanoparticles for covalent immobilization of enzymes. *Nanoscale*, 4(2):414–416, 2012.

[136] A. Beloqui, M. E. Guazzaroni, F. Pazos, J. M. Vieites, M. Godoy, O. V. Golyshina, T. N. Chernikova, A. Waliczek, R. Silva-Rocha, Y. Al-ramahi, V. La Cono, C. Mendez, J. A. Salas, R. Solano, M. M. Yakimov, K. N. Timmis, P. N. Golyshin, and M. Ferrer. Reactome array: Forging a link between metabolome and genome. *Science*, 326(5950):252–257, 2009.

[137] Niels Jonker, Jeroen Kool, Hubertus Irth, and Wilfried M. A. Niessen. Recent developments in protein-ligand affinity mass spectrometry. *Analytical and Bioanalytical Chemistry*, 399(8):2669–2681, 2011.

[138] Brett Lomenick, Richard W. Olsen, and Jing Huang. Identification of direct protein targets of small molecules. *ACS Chemical Biology*, 6(1):34–46, 2011.

[139] Cuatreca.P, M. Wilchek, and C. B. Anfinsen. Selective enzyme purification by affinity chromatography. *Proceedings of the National Academy of Sciences of the United States of America*, 61(2):636–649, 1968.

[140] Andrew K. Johnson, Anna M. Zawadzka, Lee A. Deobald, Ronald L. Crawford, and Andrzej J. Paszczynski. Novel method for immobilization of enzymes to magnetic nanoparticles. *Journal of Nanoparticle Research*, 10(6):1009–1025, 2008.

[141] Amirali Popat, Sandy Budi Hartono, Frances Stahr, Jian Liu, Shi Zhang Qiao, and Gao Qing Lu. Mesoporous silica nanoparticles for bioadsorption, enzyme immobilisation, and delivery carriers. *Nanoscale*, 3(7):2801–2818, 2011.

[142] J. Kim, J. Lee, H. B. Na, B. C. Kim, J. K. Youn, J. H. Kwak, K. Moon, E. Lee, J. Park, A. Dohnalkova, H. G. Park, M. B. Gu, H. N. Chang, J. W. Grate, and T. Hyeon. A magnetically separable, highly stable enzyme system based on nanocomposites of enzymes and magnetic nanoparticles shipped in hierarchically ordered, mesocellular, mesoporous silica. *Small*, 1(12):1203–1207, 2005.

[143] B. M. Brena, J. Lidholm, F. Batista-Viera, and J. Carlsson. Selective removal of enzymes from substrate and products. an alternative to immobilization for enzymes acting on macromolecular or solid substrates. *Applied Biochemistry and Biotechnology*, 75(2-3):323–341, 1998.

[144] Caterina Longo and Lance A. Liotta. A novel biomarker harvesting nanotechnology identifies bak as a candidate melanoma biomarker in serum. *Experimental Dermatology*, 20(1):29–34, 2011.

[145] Caterina Longo, Alexis Patanarut, Tony George, Barney Bishop, Weidong Zhou, Claudia Fredolini, Mark M. Ross, Virginia Espina, Giovanni Pellacani, III Petricoin, Emanuel F., Lance A. Liotta, and Alessandra Luchini. Core-shell hydrogel particles harvest, concentrate and preserve labile low abundance biomarkers. *Plos One*, 4(3), 2009.

[146] Alessandra Luchini, Caterina Longo, Virginia Espina, III Petricoin, Emanuel F., and Lance A. Liotta. Nanoparticle technology: Addressing the fundamental roadblocks to protein biomarker discovery. *Journal of Materials Chemistry*, 19(29):5071–5077, 2009.

[147] J. Kalisiak, S. A. Trauger, E. Kalisiak, H. Morita, V. V. Fokin, M. W. W. Adams, K. B. Sharpless, and G. Siuzdak. Identification of a new endogenous metabolite and the characterization of its protein interactions through an immobilization approach. *Journal of the American Chemical Society*, 131(1):378–386, 2009.

[148] M. J. van der Werf, R. H. Jellema, and T. Hankemeier. Microbial metabolomics: replacing trial-and-error by the unbiased selection and ranking of targets. *Journal of Industrial Microbiology & Biotechnology*, 32(6):234–252, 2005.

[149] Natsumi Saito, Yoshiaki Ohashi, Tomoyoshi Soga, and Masaru Tomita. Unveiling cellular biochemical reactions via metabolomics-driven approaches. *Current Opinion in Microbiology*, 13(3):358–362, 2010.

[150] Andrew D. Patterson, Frank J. Gonzalez, and Jeffrey R. Idle. Xenobiotic metabolism: A view through the metabolometer. *Chemical Research in Toxicology*, 23(5):851–860, 2010.

[151] W. B. Dunn, N. J. C. Bailey, and H. E. Johnson. Measuring the metabolome: current analytical technologies. *Analyst*, 130(5):606–625, 2005.

[152] Chirayu Desai, Hilor Pathak, and Datta Madamwar. Advances in molecular and "-omics" technologies to gauge microbial communities and bioremediation at xenobiotic/anthropogen contaminated sites. *Bioresource Technology*, 101(6):1558–1569, 2010.

[153] Rima Kaddurah-Daouk, Bruce S. Kristal, and Richard M. Weinshilboum. Metabolomics: A global biochemical approach to drug response and disease. In *Annual Review of Pharmacology and Toxicology*, volume 48 of *Annual Review of Pharmacology and Toxicology*, pages 653–683. —2008—. Times Cited: 75.

[154] D. H. Pieper and W. Reineke. Engineering bacteria for bioremediation. *Current Opinion in Biotechnology*, 11(3):262–270, 2000.

[155] J. Widada, H. Nojiri, and T. Omori. Recent developments in molecular techniques for identification and monitoring of xenobiotic-degrading bacteria and their catabolic genes in bioremediation. *Applied Microbiology and Biotechnology*, 60(1-2):45–59, 2002.

[156] P. Rajakumar, K. Sekar, V. Shanmugaiah, and N. Mathivanan. Synthesis of novel carbazole based macrocyclic amides as potential antimicrobial agents. *European Journal of Medicinal Chemistry*, 44(7):3040–3045, 2009.

[157] A. A. Pieper, S. H. Xie, E. Capota, S. J. Estill, J. N. Zhong, J. M. Long, G. L. Becker, P. Huntington, S. E. Goldman, C. H. Shen, M. Capota, J. K. Britt, T. Kotti, K. Ure, D. J. Brat, N. S. Williams, K. S. MacMillan, J. Naidoo, L. Melito, J. Hsieh, J. De Brabander, J. M. Ready, and S. L. McKnight. Discovery of a proneurogenic, neuroprotective chemical. *Cell*, 142(1):39–51, 2010.

[158] J. R. Vandermeer, W. M. Devos, S. Harayama, and A. J. B. Zehnder. Molecular mechanisms of genetic adaptation to xenobiotic compounds. *Microbiological Reviews*, 56(4):677–694, 1992.

[159] H. Ochman, J. G. Lawrence, and E. A. Groisman. Lateral gene transfer and the nature of bacterial innovation. *Nature*, 405(6784):299–304, 2000.

[160] K. Maeda, H. Nojiri, M. Shintani, T. Yoshida, H. Habe, and T. Omori. Complete nucleotide sequence of carbazole/dioxin-degrading plasmid pcar1 in pseudomonas resinovorans strain ca10 indicates its mosaicity and the presence of large catabolic transposon tn4676. *Journal of Molecular Biology*, 326(1):21–33, 2003.

[161] S. Harayama. Polycyclic aromatic hydrocarbon bioremediation design. *Current Opinion in Biotechnology*, 8(3):268–273, 1997.

[162] H. Nojiri, H. Sekiguchi, K. Maeda, M. Urata, S. I. Nakai, T. Yoshida, H. Habe, and T. Omori. Genetic characterization and evolutionary implications of a car gene cluster in the carbazole degrader Pseudomonas sp strain CA10. *Journal of Bacteriology*, 183(12):3663–3679, 2001.

[163] H. M. Tan. Bacterial catabolic transposons. *Applied Microbiology and Biotechnology*, 51(1):1–12, 1999.

[164] M. Tsuda and T. Iino. Genetic-analysis of a transposon carrying toluene degrading genes on a tol plasmid pwwo. *Molecular & General Genetics*, 210(2):270–276, 1987.

[165] M. Tsuda, H. M. Tan, A. Nishi, and K. Furukawa. Mobile catabolic genes in bacteria. *Journal of Bioscience and Bioengineering*, 87(4):401–410, 1999.

[166] W. Arber. Genetic variation: molecular mechanisms and impact on microbial evolution. *Fems Microbiology Reviews*, 24(1):1–7, 2000.

[167] K. C. Loh and Y. G. Yu. Kinetics of carbazole degradation by pseudomonas putida in presence of sodium salicylate. *Water Research*, 34(17):4131–4138, 2000.

[168] E. Frimmersdorf, S. Horatzek, A. Pelnikevich, L. Wiehlmann, and D. Schomburg. How pseudomonas aeruginosa adapts to various environments: a metabolomic approach. *Environmental Microbiology*, 12(6):1734–1747, 2010.

[169] D. C. Bressler and P. M. Fedorak. Bacterial metabolism of fluorene, dibenzofuran, dibenzothiophene, and carbazole. *Canadian Journal of Microbiology*, 46(5):397–409, 2000.

[170] H. Nojiri and T. Omori. Molecular bases of aerobic bacterial degradation of dioxins: Involvement of angular dioxygenation. *Bioscience Biotechnology and Biochemistry*, 66(10):2001–2016, 2002.

[171] L. M. Gieg, A. Otter, and P. M. Fedorak. Carbazole degradation by Pseudomonas sp ld2: Metabolic characteristics and the identification of some metabolites. *Environmental Science and Technology*, 30(2):575–585, 1996.

[172] S. I. Sato, J. W. Nam, K. Kasuga, H. Nojiri, H. Yamane, and T. Omori. Identification and characterization of genes encoding carbazole 1,9a-dioxygenase in Pseudomonas sp. strain CA10. *Journal of Bacteriology*, 179(15):4850–4858, 1997.

[173] S. Sato, N. Ouchiyama, T. Kimura, H. Nojiri, H. Yamane, and T. Omori. Cloning of genes involved in carbazole degradation of Pseudomonas sp. strain CA10: Nucleotide sequences of genes and characterization of meta-cleavage enzymes and hydrolase. *Journal of Bacteriology*, 179(15):4841–4849, 1997.

[174] N. Ouchiyama, Y. Zhang, T. Omori, and T. Kodama. Biodegradation of carbazole by pseudomonas spp ca06 and ca10. *Bioscience Biotechnology and Biochemistry*, 57(3):455–460, 1993.

[175] S. K. Ahuja, G. M. Ferreira, and A. R. Moreira. Utilization of enzymes for environmental applications. *Critical Reviews in Biotechnology*, 24(2-3):125–154, 2004.

[176] J. S. Seo, Y. S. Keum, and Q. X. Li. Bacterial degradation of aromatic compounds. *International Journal of Environmental Research and Public Health*, 6(1):278–309, 2009.

[177] X. Wang, Z. H. Gai, B. Yu, J. H. Feng, C. Y. Xu, Y. Yuan, Z. X. Lin, and P. Xu. Degradation of carbazole by microbial cells immobilized in magnetic gellan gum gel beads. *Applied and Environmental Microbiology*, 73(20):6421–6428, 2007.

[178] A. L. Larentis, H. C. C. Sampaio, C. C. Carneiro, O. B. Martins, and T. L. M. Alves. Evaluation of growth, carbazole biodegradation and anthranilic acid production by Pseudomonas stutzeri. *Brazilian Journal of Chemical Engineering*, 28(1):37–44, 2011.

[179] D. Waldau, A. Mikolasch, M. Lalk, and F. Schauer. Derivatization of bioactive carbazoles by the biphenyl-degrading bacterium ralstonia sp strain sbug 290. *Applied Microbiology and Biotechnology*, 83(1):67–75, 2009.

[180] D. Waldau, K. Methling, A. Mikolasch, and F. Schauer. Characterization of new oxidation products of 9h-carbazole and structure related compounds by biphenyl-utilizing bacteria. *Applied Microbiology and Biotechnology*, 81(6):1023–1031, 2009.

[181] H. Habe, K. Ide, M. Yotsumoto, H. Tsuji, H. Hirano, J. Widada, T. Yoshida, H. Nojiri, and T. Omori. Preliminary examinations for applying a carbazole-degrader, Pseudomonas sp strain CA10, to dioxin-contaminated soil remediation. *Applied Microbiology and Biotechnology*, 56(5-6):788–795, 2001.

[182] J. W. Nam, H. Nojiri, H. Noguchi, H. Uchimura, T. Yoshida, H. Habe, H. Yamane, and T. Omori. Purification and characterization of carbazole 1,9a-dioxygenase, a three-component dioxygenase system of Pseudomonas resinovorans strain CA10. *Applied and Environmental Microbiology*, 68(12):5882–5890, 2002.

[183] E. Lallana, E. Fernandez-Megia, and R. Riguera. Surpassing the use of copper in the click functionalization of polymeric nanostructures: A strain-promoted approach. *Journal of the American Chemical Society*, 131(16):5748–5750, 2009.

[184] D. D Evanoff, Jr., J. R. Lawrence, C. E. Huebner, J. M. Houchins, B. J. Stevenson, A. L. Foguth, J. B. Carroll, and S. H. Foulger. Copolymers of 2-(9h-carbazol-9-yl)ethyl 2-methylacrylate and 4-[5-(4-tert-butylphenyl)-1,3,4-oxadiazol-2-yl]phenyl 2-methylacrylate: Correlating hole drift mobility and electronic structure calculations with electroluminescence. *ACS Applied Materials & Interfaces*, 1:875–881, 2009.

[185] D. D Evanoff, Jr., J. B. Carroll, R. D. Roeder, Z. J. Hunt, J. R. Lawrence, and S. H. Foulger. Poly(methyl methacrylate) copolymers containing pendant carbazole and oxadiazole moieties for applications in single-layer organic light emitting devices. *Journal of Polymer Science Part A-Polymer Chemistry*, 46(23):7882–7897, 2008.

[186] A. Voronov and O. Shafranska. Synthesis of chemically grafted polystyrene "brushes" and their influence on the dewetting in thin polystyrene films. *Langmuir*, 18(11):4471–4477, 2002.

[187] H. Nojiri, H. Habe, and T. Omori. Bacterial degradation of aromatic compounds via angular dioxygenation. *Journal of General and Applied Microbiology*, 47(6):279–305, 2001.

[188] W. Klopffer. Transfer of electronic excitation energy in polyvinyl carbazole. *J. Chem. Phys.*, 50(6):2337–2343, 1969.

[189] W. Tungittiplakorn, C. Cohen, and L. W. Lion. Engineered polymeric nanoparticles for bioremediation of hydrophobic contaminants. *Environmental Science and Technology*, 39(5):1354–1358, 2005.

[190] L. Li, P. Xu, and H. D. Blankespoor. Degradation of carbazole in the presence of non-aqueous phase liquids by Pseudomonas sp. *Biotechnology Letters*, 26(7):581–584, 2004.

[191] L. Li, Q. G. Li, F. L. Li, Q. Shi, B. Yu, F. R. Liu, and P. Xu. Degradation of carbazole and its derivatives by a Pseudomonas sp. *Applied Microbiology and Biotechnology*, 73(4):941–948, 2006.

[192] J. O. Lay. MALDI-TOF mass spectrometry of bacteria. *Mass Spectrometry Reviews*, 20(4):172–194, 2001.

[193] Y. Ashikawa, Z. Fujimoto, H. Noguchi, H. Habe, T. Omori, H. Yamane, and H. Nojiri. Crystallization and preliminary x-ray diffraction analysis of the electron-transfer complex between the terminal oxygenase component and ferredoxin in the rieske non-haem iron oxygenase system carbazole 1,9a-dioxygenase. *Acta Crystallogr Sect F Struct Biol Cryst Commun*, 61(Pt 6):577–80, 2005.

[194] H. Nojiri and T. Omori. Structure of the terminal oxygenase component of angular dioxygenase, carbazole 1,9a-dioxygenase. *Journal of Molecular Biology*, 351(2):355–370, 2005.

[195] Lisong Xiao, Jiangtian Li, Dermot F. Brougham, Eoin K. Fox, Neus Feliu, Alexey Bushmelev, Annette Schmidt, Natascha Mertens, Fabian Kiessling, Martin Valldor, Bengt Fadeel, and Sanjay Mathur. Water-soluble superparamagnetic magnetite nanoparticles with biocompatible coating for enhanced magnetic resonance imaging. *ACS Nano*, 5(8):6315–6324, 2011.

[196] Y. T. Wang, F. H. Xu, C. F. Zhang, D. Lei, Y. H. Tang, H. Xu, Z. J. Zhang, H. Y. Lu, X. X. Du, and G. Y. Yang. High mr sensitive fluorescent magnetite nanocluster for stem cell tracking in ischemic mouse brain. *Nanomedicine-Nanotechnology Biology and Medicine*, 7(6):1009–1019, 2011.

[197] S. J. H. Soenen, U. Himmelreich, N. Nuytten, and M. De Cuyper. Cytotoxic effects of iron oxide nanoparticles and implications for safety in cell labelling. *Biomaterials*, 32(1):195–205, 2011.

[198] A. J. Cole, V. C. Yang, and A. E. David. Cancer theranostics: the rise of targeted magnetic nanoparticles. *Trends in Biotechnology*, 29(7):323–332, 2011.

[199] R. Hao, R. J. Xing, Z. C. Xu, Y. L. Hou, S. Gao, and S. H. Sun. Synthesis, functionalization, and biomedical applications of multifunctional magnetic nanoparticles. *Advanced Materials*, 22(25):2729–2742, 2010.

[200] N. Miguel-Sancho, O. Bomati-Miguel, G. Colom, J. P. Salvador, M. P. Marco, and J. Santamaria. Development of stable, water-dispersible, and biofunctionalizable superparamagnetic iron oxide nanoparticles. *Chemistry of Materials*, 23(11):2795–2802, 2011.

[201] L. Babes, B. Denizot, G. Tanguy, J. J. Le Jeune, and P. Jallet. Synthesis of iron oxide nanoparticles used as mri contrast agents: A parametric study. *Journal of Colloid and Interface Science*, 212(2):474–482, 1999.

[202] H. Bin Na, G. Palui, J. T. Rosenberg, X. Ji, S. C. Grant, and H. Mattoussi. Multidentate catechol-based polyethylene glycol oligomers provide enhanced stability and biocompatibility to iron oxide nanoparticies. *ACS Nano*, 6(1):389–399, 2012.

[203] C. H. Dodd, R. Weissleder, and J. M. Mountz. Normal t-cell response and in vivo magnetic resonance imaging of t cells loaded with hiv transactivator-peptide-derived superparamagnetic nanoparticles. *Journal of Immunological Methods*, 256(1-2):89–105, 2001.

[204] G. F. Goya, V. Grazu, and M. R. Ibarra. Magnetic nanoparticles for cancer therapy. *Current Nanoscience*, 4(1):1–16, 2008.

[205] M. K. Yu, Y. Y. Jeong, J. Park, S. Park, J. W. Kim, J. J. Min, K. Kim, and S. Jon. Drug-loaded superparamagnetic iron oxide nanoparticles for combined cancer imaging and therapy in vivo. *Angewandte Chemie-International Edition*, 47(29):5362–5365, 2008.

[206] R. Massart. Preparation of aqueous magnetic liquids in alkaline and acidic media. *IEEE Transactions on Magnetics*, 17(2):1247–1248, 1981.

[207] C. Ravikumar and Rajdip Bandyopadhyaya. Mechanistic study on magnetite nanoparticle formation by thermal decomposition and coprecipitation routes. *Journal of Physical Chemistry C*, 115(5):1380–1387, 2011.

[208] D. K. Kim, Y. Zhang, W. Voit, K. V. Rao, and M. Muhammed. Synthesis and characterization of surfactant-coated superparamagnetic monodispersed iron oxide nanoparticles. *Journal of Magnetism and Magnetic Materials*, 225(1-2):30–36, 2001.

[209] S. Santra, C. Kaittanis, J. Grimm, and J. M. Perez. Drug/dye-loaded, multifunctional iron oxide nanoparticles for combined targeted cancer therapy and dual optical/magnetic resonance imaging. *Small*, 5(16):1862–1868, 2009.

[210] R. Roeder, P. Rungta, Y. P. Bandera, V. Tsyalkovskyy, and S. H. Foulger. Colloidal templating: Seeded emulsion polymerization of a soluble shell with controlled alkyne surface density. *Soft Matter*, 23(8):5492–5500, 2012.

[211] P. Penzkofer, A. Baumler, W. Szeimies, and C. Abels. Absorption and fluorescence spectroscopic investigation of indocyanine green. *Journal of Photochemistry and Photobiology A*, 96:137–148, 1996.

[212] K. Sauda, T. Imasaka, and N. Ishibashi. Determination of protein in human-serum by high-performance liquid-chromatography with semiconductor-laser fluorometric detection. *Analytical Chemistry*, 58:2649–2653, 1986.

[213] C. L. Lin, C. F. Lee, and W. Y. Chiu. Preparation and properties of poly(acrylic acid) oligomer stabilized superparamagnetic ferrofluid. *Journal of Colloid and Interface Science*, 291(2):411–420, 2005.

[214] J. L. Viota, J. de Vicente, J. D. G. Duran, and A. Delgado. Stabilization of magnetorheological suspensions by polyacrylic acid polymers. *Journal of Colloid and Interface Science*, 284(2):527–541, 2005.

[215] S. Y. Mak and D. H. Chen. Fast adsorption of methylene blue on polyacrylic acid-bound iron oxide magnetic nanoparticles. *Dyes and Pigments*, 61(1):93–98, 2004.

[216] K. Y. Yoon, C. Kotsmar, D. R. Ingram, C. Huh, S. L. Bryant, T. E. Milner, and K. P. Johnston. Stabilization of superparamagnetic iron oxide nanoclusters in concentrated brine with cross-linked polymer shells. *Langmuir*, 27(17):10962–10969, 2011.

[217] A. Ditsch, P. E. Laibinis, D. I. C. Wang, and T. A. Hatton. Controlled clustering and enhanced stability of polymer-coated magnetic nanoparticles. *Langmuir*, 21(13):6006–6018, 2005.

[218] G. F. Dalelio and R. C. Evers. Linear polymers of some vinyl monomers containing a terminal acetylenic group. *Journal of Polymer Science Part 1: Polymer Chemistry*, 5(5):999, 1967.

[219] George G. Odian. *Principles of polymerization*. Wiley-Interscience, Hoboken, N.J., 4th edition, —2004—.

[220] K. Tao, S. Song, J. Ding, H. J. Dou, and K. Sun. Carbonyl groups anchoring for the water dispersibility of magnetite nanoparticles. *Colloid and Polymer Science*, 289(4):361–369, 2011.

[221] J. Liu, Z. K. Sun, Y. H. Deng, Y. Zou, C. Y. Li, X. H. Guo, L. Q. Xiong, Y. Gao, F. Y. Li, and D. Y. Zhao. Highly water-dispersible biocompatible magnetite particles with low cytotoxicity stabilized by citrate groups. *Angewandte Chemie-International Edition*, 48(32):5875–5879, 2009.

[222] M. Racuciu, D. E. Creanga, and A. Airinei. Citric-acid-coated magnetite nanoparticles for biological applications. *European Physical Journal E*, 21(2):117–121, 2006.

[223] J. T. Keiser, C. W. Brown, and R. H. Heidersbach. The oxidation of fe3o4 on iron and steel surfaces. *Corrosion*, 38(7):357–360, 1982.

[224] L. Tu, Y. Jing, Y. P. Li, and J. P. Wang. Real-time measurement of brownian relaxation of magnetic nanoparticles by a mixing-frequency method. *Applied Physics Letters*, 98(21), 2011.

[225] B. Fischer, B. Huke, M. Lucke, and R. Hempelmann. Brownian relaxation of magnetic colloids. *Journal of Magnetism and Magnetic Materials*, 289:74–77, 2005.

[226] P. C. Fannin, B. K. P. Scaife, and S. W. Charles. The measurement of the frequency-dependent susceptibility of magnetic colloids. *Journal of Magnetism and Magnetic Materials*, 72(1):95–108, 1988.

[227] O. A. Valenzuela, J. M. Aquino, R. B. Galindo, O. R. Fernandez, P. C. Fannin, and A. T. Giannitsis. Synthesis and complex magnetic susceptibility characterization of magnetic fluids in different liquid carriers. *Journal of Applied Physics*, 97(10), 2005.

[228] P. C. Fannin, C. Mac Oireachtaigh, L. Cohen-Tannoudji, E. Bertrand, and J. Bibette. Complex susceptibility measurements of a suspension of magnetic beads. *Journal of Magnetism and Magnetic Materials*, 300(1):E210–E212, 2006.

[229] R. Kotitz, P. C. Fannin, and L. Trahms. Time-domain study of brownian and neel relaxation in ferrofluids. *Journal of Magnetism and Magnetic Materials*, 149(1-2):42–46, 1995.

[230] P. C. Fannin, B. K. P. Scaife, and S. W. Charles. A study of the complex susceptibility of ferrofluids and rotational brownian-motion. *Journal of Magnetism and Magnetic Materials*, 65(2-3):279–281, 1987.

[231] Peter J. W. Debye. *Polar molecules*. The Chemical Catalog Company, Inc., New York,, —1929—.

[232] L. A. Su, W. Z. Jia, C. J. Hou, and Y. Lei. Microbial biosensors: A review. *Biosensors & Bioelectronics*, 26(5):1788–1799, 2011.

[233] S. Rodriguez-Mozaz, M. J. L. de Alda, M. P. Marco, and D. Barcelo. Biosensors for environmental monitoring - a global perspective. *Talanta*, 65(2):291–297, 2005.

[234] S. F. D'Souza. Microbial biosensors. *Biosensors & Bioelectronics*, 16(6):337–353, 2001.

[235] N. Nassif, O. Bouvet, M. N. Rager, C. Roux, T. Coradin, and J. Livage. Living bacteria in silica gels. *Nature Materials*, 1(1):42–44, 2002.

[236] A. F. Collings and F. Caruso. Biosensors: recent advances. *Reports on Progress in Physics*, 60(11):1397–1445, 1997.

[237] L. Bousse. Whole cell biosensors. *Sensors and Actuators B-Chemical*, 34(1-3):270–275, 1996.

[238] M. J. Dennison and A. P. F. Turner. Biosensors for environmental monitoring. *Biotechnology Advances*, 13(1):1–12, 1995.

[239] R. P. John, R. D. Tyagi, S. K. Brar, R. Y. Surampalli, and D. Prevost. Bio-encapsulation of microbial cells for targeted agricultural delivery. *Critical Reviews in Biotechnology*, 31(3):211–226, 2011.

[240] M. A. Heitkamp and W. P. Stewart. A novel porous nylon biocarrier for immobilized bacteria. *Applied and Environmental Microbiology*, 62(12):4659–4662, 1996.

[241] M. A. Heitkamp, V. Camel, T. J. Reuter, and W. J. Adams. Biodegradation of para-nitrophenol in an aqueous waste stream by immobilized bacteria. *Applied and Environmental Microbiology*, 56(10):2967–2973, 1990.

[242] M. D. Pease, L. ShriverLake, and F. S. Ligler. Adaptation of a fiber-optic biosensor for use in environmental monitoring. *Biosensor and Chemical Sensor Technology*, 613:33–43, 1995.

[243] O. Bretschger, J. B. Osterstock, W. E. Pinchak, S. Ishii, and K. E. Nelson. Microbial fuel cells and microbial ecology: Applications in ruminant health and production research. *Microbial Ecology*, 59(3):415–427, 2010.

[244] J. Heo, K. J. Thomas, G. H. Seong, and R. M. Crooks. A microfluidic bioreactor based on hydrogel-entrapped e. coli: Cell viability, lysis, and intracellular enzyme reactions. *Analytical Chemistry*, 75(1):22–26, 2003.

[245] K. Vijayaraghavan and Y. S. Yun. Bacterial biosorbents and biosorption. *Biotechnology Advances*, 26(3):266–291, 2008.

[246] M. B. Cassidy, H. Lee, and J. T. Trevors. Environmental applications of immobilized microbial cells: A review. *Journal of Industrial Microbiology*, 16(2):79–101, 1996.

[247] H. Ben-Yoav, S. Melamed, A. Freeman, Y. Shacham-Diamand, and S. Belkin. Whole-cell biochips for bio-sensing: integration of live cells and inanimate surfaces. *Critical Reviews in Biotechnology*, 31(4):337–353, 2011.

[248] C. Z. Wu, S. Bai, M. B. Ansorge-Schumacher, and D. Y. Wang. Nanoparticle cages for enzyme catalysis in organic media. *Advanced Materials*, 23(47):5694–5699, 2011.

[249] K. W. Wang, K. G. Lee, T. J. Park, Y. C. Lee, J. W. Yang, D. H. Kim, S. J. Lee, and J. Y. Park. Organoclay-assisted interfacial polymerization for microfluidic production of monodisperse peg-microdroplets and in situ encapsulation of e. coli. *Biotechnology and Bioengineering*, 109(1):289–294, 2012.

[250] D. Zaytseva-Zotova, V. Balysheva, A. Tsoy, M. Drozdova, T. Akopova, L. Vladimirov, I. Chevalot, A. Marc, J. L. Goergen, and E. Markvicheva. Biocompatible smart microcapsules based on chitosan-poly(vinyl alcohol) copolymers for cultivation of animal cells. *Advanced Engineering Materials*, 13(12):B493–B500, 2011.

[251] J. C. Jewett and C. R. Bertozzi. Cu-free click cycloaddition reactions in chemical biology. *Chemical Society Reviews*, 39(4):1272–1279, 2010.

[252] P. V. Chang, J. A. Prescher, E. M. Sletten, J. M. Baskin, I. A. Miller, N. J. Agard, A. Lo, and C. R. Bertozzi. Copper-free click chemistry in living animals. *Proceedings of the National Academy of Sciences of the United States of America*, 107(5):1821–1826, 2010.

[253] C. E. Hoyle and C. N. Bowman. Thiol-ene click chemistry. *Angewandte Chemie-International Edition*, 49(9):1540–1573, 2010.

[254] C. E. Hoyle, T. Y. Lee, and T. Roper. Thiol-enes: Chemistry of the past with promise for the future. *Journal of Polymer Science Part a-Polymer Chemistry*, 42(21):5301–5338, 2004.

[255] M. J. Kade, D. J. Burke, and C. J. Hawker. The power of thiol-ene chemistry. *Journal of Polymer Science Part a-Polymer Chemistry*, 48(4):743–750, 2010.

[256] J. Ma, C. Cheng, and K. L. Wooley. The power of raft for creating polymers having imbedded side-chain functionalities: Norbornenyl-functionalized polymers and their transformations via romp and thiol-ene reactions. *Australian Journal of Chemistry*, 62(11):1507–1519, 2009.

[257] M. W. Jones, G. Mantovani, S. M. Ryan, X. X. Wang, D. J. Brayden, and D. M. Haddleton. Phosphine-mediated one-pot thiol-ene "click" approach to polymer-protein conjugates. *Chemical Communications*, (35):5272–5274, 2009.

[258] K. L. Killops, L. M. Campos, and C. J. Hawker. Robust, efficient, and orthogonal synthesis of dendrimers via thiol-ene "click" chemistry. *Journal of the American Chemical Society*, 130(15):5062–+, 2008.

[259] J. W. Chan, B. Yu, C. E. Hoyle, and A. B. Lowe. Convergent synthesis of 3-arm star polymers from raft-prepared poly(n,n-diethylacrylamide) via a thiol-ene click reaction. *Chemical Communications*, (40):4959–4961, 2008.

[260] K. M. Schreck, D. Leung, and C. N. Bowman. Hybrid organic/inorganic thiol-ene-based photopolymerized networks. *Macromolecules*, 44(19):7520–7529, 2011.

[261] A. K. O'Brien, N. B. Cramer, and C. N. Bowman. Oxygen inhibition in thiol-acrylate photopolymerizations. *Journal of Polymer Science Part a-Polymer Chemistry*, 44(6):2007–2014, 2006.

[262] N. B. Cramer, J. P. Scott, and C. N. Bowman. Photopolymerizations of thiol-ene polymers without photoinitiators. *Macromolecules*, 35(14):5361–5365, 2002.

[263] T. Posner. Beitrage zur kenntniss der ungesättigten verbindungen. ii. ueber die addition von mercaptanen an ungesattigte kohlenwasserstoffe. *Ber. Dtsch. Chem. Ges.*, 38:11, 1905.

[264] C.R. Morgan, A.D. Ketley, and F. Magnotta. Thiol/ene photocurable polymers. *Journal of Polymer Science: Polymer Chemistry Edition*, 15(3):18, 1977.

[265] T. Y. Lee, T. M. Roper, E. S. Jonsson, C. A. Guymon, and C. E. Hoyle. Thiol-ene photopolymerization kinetics of vinyl acrylate/multifunctional thiol mixtures. *Macromolecules*, 37(10):3606–3613, 2004.

[266] T. M. Roper, C. A. Guymon, E. S. Jonsson, and C. E. Hoyle. Influence of the alkene structure on the mechanism and kinetics of thiol-alkene photopolymerizations with real-time infrared spectroscopy. *Journal of Polymer Science Part a-Polymer Chemistry*, 42(24):6283–6298, 2004.

[267] N. B. Cramer, T. Davies, A. K. O'Brien, and C. N. Bowman. Mechanism and modeling of a thiol-ene photopolymerization. *Macromolecules*, 36(12):4631–4636, 2003.

[268] J. Elisseeff, W. McIntosh, K. Anseth, S. Riley, P. Ragan, and R. Langer. Photoencapsulation of chondrocytes in poly(ethylene oxide)-based semi-interpenetrating networks. *Journal of Biomedical Materials Research*, 51(2):164–171, 2000.

[269] H. Uludag, P. De Vos, and P. A. Tresco. Technology of mammalian cell encapsulation. *Advanced Drug Delivery Reviews*, 42(1-2):29–64, 2000.

[270] O. Smidsrod and G. Skjakbraek. Alginate as immobilization matrix for cells. *Trends in Biotechnology*, 8(3):71–78, 1990.

[271] M. Z. Lu, H. L. Lan, and F. F. Wang. Cell encapsulation with alginate and alpha-phenoxycinnamylidene-acetylated poly(allylamine). *Biotechnology and Bioengineering*, 70(5):479–483, 2000.

[272] D. L. Hern and J. A. Hubbell. Incorporation of adhesion peptides into nonadhesive hydrogels useful for tissue resurfacing. *Journal of Biomedical Materials Research*, 39(2):266–276, 1998.

[273] M. P. Lutolf, J. L. Lauer-Fields, H. G. Schmoekel, A. T. Metters, F. E. Weber, G. B. Fields, and J. A. Hubbell. Synthetic matrix metalloproteinase-sensitive hydrogels for the conduction of tissue regeneration: Engineering cell-invasion characteristics. *Proceedings of the National Academy of Sciences of the United States of America*, 100(9):5413–5418, 2003.

[274] E. W. Merrill, K. A. Dennison, and C. Sung. Partitioning and diffusion of solutes in hydrogels of poly(ethylene oxide). *Biomaterials*, 14(15):1117–1126, 1993.

[275] S. J. Bryant and K. S. Anseth. Hydrogel properties influence ecm production by chondrocytes photoencapsulated in poly(ethylene glycol) hydrogels. *Journal of Biomedical Materials Research*, 59(1):63–72, 2002.

[276] B. K. Mann, A. S. Gobin, A. T. Tsai, R. H. Schmedlen, and J. L. West. Smooth muscle cell growth in photopolymerized hydrogels with cell adhesive and proteolytically degradable domains: synthetic ecm analogs for tissue engineering. *Biomaterials*, 22(22):3045–3051, 2001.

[277] K. S. Masters, D. N. Shah, L. A. Leinwand, and K. S. Anseth. Crosslinked hyaluronan scaffolds as a biologically active carrier for valvular interstitial cells. *Biomaterials*, 26(15):2517–2525, 2005.

[278] P. Martens and K. S. Anseth. Characterization of hydrogels formed from acrylate modified poly(vinyl alcohol) macromers. *Polymer*, 41(21):7715–7722, 2000.

[279] D. A. Ossipov and J. Hilborn. Poly(vinyl alcohol)-based hydrogels formed by "click chemistry". *Macromolecules*, 39(5):1709–1718, 2006.

[280] M. Malkoch, R. Vestberg, N. Gupta, L. Mespouille, P. Dubois, A. F. Mason, J. L. Hedrick, Q. Liao, C. W. Frank, K. Kingsbury, and C. J. Hawker. Synthesis of well-defined hydrogel networks using click chemistry. *Chemical Communications*, (26):2774–2776, 2006.

[281] S. Yigit, R. Sanyal, and A. Sanyal. Fabrication and functionalization of hydrogels through "click" chemistry. *Chemistry-an Asian Journal*, 6(10):2648–2659, 2011.

[282] C. C. Lin, A. Raza, and H. Shih. Peg hydrogels formed by thiol-ene photo-click chemistry and their effect on the formation and recovery of insulin-secreting cell spheroids. *Biomaterials*, 32(36):9685–9695, 2011.

[283] L. M. Campos, I. Meinel, R. G. Guino, M. Schierhorn, N. Gupta, G. D. Stucky, and C. J. Hawker. Highly versatile and robust materials for soft imprint lithography based on thiol-ene click chemistry. *Advanced Materials*, 20(19):3728–+, 2008.

[284] C. D. Pritchard, T. M. O'Shea, D. J. Siegwart, E. Calo, D. G. Anderson, F. M. Reynolds, J. A. Thomas, J. R. Slotkin, E. J. Woodard, and R. Langer. An injectable thiol-acrylate poly(ethylene glycol) hydrogel for sustained release of methylprednisolone sodium succinate. *Biomaterials*, 32(2):587–597, 2011.

[285] Cole A. DeForest, Brian D. Polizzotti, and Kristi S. Anseth. Sequential click reactions for synthesizing and patterning three-dimensional cell microenvironments. *Nature Materials*, 8(8):659–664, 2009.

[286] D. C. Duffy, J. C. McDonald, O. J. A. Schueller, and G. M. Whitesides. Rapid prototyping of microfluidic systems in poly(dimethylsiloxane). *Analytical Chemistry*, 70(23):4974–4984, 1998.

[287] B. G. Chung, K. H. Lee, A. Khademhosseini, and S. H. Lee. Microfluidic fabrication of microengineered hydrogels and their application in tissue engineering. *Lab on a Chip*, 12(1):45–59, 2012.

[288] Jeremy L. Steinbacher and D. Tyler McQuade. Polymer chemistry in flow: New polymers, beads, capsules, and fibers. *Journal of Polymer Science Part a-Polymer Chemistry*, 44(22):6505–6533, 2006.

[289] Holger Becker and Claudia Gaertner. Polymer microfabrication technologies for microfluidic systems. *Analytical and Bioanalytical Chemistry*, 390(1):89–111, 2008.

[290] M. Hu, R. S. Deng, K. M. Schumacher, M. Kurisawa, H. Y. Ye, K. Purnamawati, and J. Y. Ying. Hydrodynamic spinning of hydrogel fibers. *Biomaterials*, 31(5):863–869, 2010.

[291] M. Hu, M. Kurisawa, R. Deng, C. M. Teo, A. Schumacher, Y. X. Thong, L. Wang, K. M. Schumacher, and J. Y. Ying. Cell immobilization in gelatin-hydroxyphenylpropionic acid hydrogel fibers. *Biomaterials*, 30(21):3523–3531, 2009.

[292] M. Yamada, S. Sugaya, Y. Naganuma, and M. Seki. Microfluidic synthesis of chemically and physically anisotropic hydrogel microfibers for guided cell growth and networking. *Soft Matter*, 8(11):3122–3130, 2012.

[293] K. S. Anseth, L. M. Kline, T. A. Walker, K. J. Anderson, and C. N. Bowman. Reaction-kinetics and volume relaxation during polymerizations of multiethylene glycol dimethacrylates. *Macromolecules*, 28(7):2491–2499, 1995.

[294] J. A. Burdick, T. M. Lovestead, and K. S. Anseth. Kinetic chain lengths in highly cross-linked networks formed by the photoinitiated polymerization of divinyl monomers: A gel permeation chromatography investigation. *Biomacromolecules*, 4(1):149–156, 2003.

[295] D. L. Kurdikar and N. A. Peppas. A kinetic-study of diacrylate photopolymerizations. *Polymer*, 35(5):1004–1011, 1994.

[296] J. H. Lee, R. K. Prud'homme, and I. A. Aksay. Cure depth in photopolymerization: Experiments and theory. *Journal of Materials Research*, 16(12):3536–3544, 2001.

[297] K. T. Nguyen and J. L. West. Photopolymerizable hydrogels for tissue engineering applications. *Biomaterials*, 23(22):4307–4314, 2002.

[298] K. S. Anseth, C. N. Bowman, and N. A. Peppas. Polymerization kinetics and volume relaxation behavior of photopolymerized multifunctional monomers producing highly cross-linked networks. *Journal of Polymer Science Part a-Polymer Chemistry*, 32(1):139–147, 1994.

[299] K. S. Anseth, C. M. Wang, and C. N. Bowman. Reaction behavior and kinetic constants for photopolymerizations of multi(meth)acrylate monomers. *Polymer*, 35(15):3243–3250, 1994.

[300] C. N. Bowman and N. A. Peppas. A kinetic gelation method for the simulation of free-radical polymerizations. *Chemical Engineering Science*, 47(6):1411–1419, 1992.

[301] George G. Odian. *Principles of polymerization*. McGraw-Hill, New York, NY, —1970—.

[302] C. G. Williams, A. N. Malik, T. K. Kim, P. N. Manson, and J. H. Elisseeff. Variable cytocompatibility of six cell lines with photoinitiators used for polymerizing hydrogels and cell encapsulation. *Biomaterials*, 26(11):1211–1218, 2005.

[303] S. J. Bryant, C. R. Nuttelman, and K. S. Anseth. Cytocompatibility of uv and visible light photoinitiating systems on cultured nih/3t3 fibroblasts in vitro. *Journal of Biomaterials Science-Polymer Edition*, 11(5):439–457, 2000.

[304] N. S. Allen, M. C. Marin, M. Edge, D. W. Davies, J. Garrett, F. Jones, S. Navaratnam, and B. J. Parsons. Photochemistry and photoinduced chemical crosslinking activity of type i & ii co-reactive photoinitiators in acrylated prepolymers. *Journal of Photochemistry and Photobiology a-Chemistry*, 126(1-3):135–149, 1999.

[305] A. Boddapati, S. B. Rahane, R. P. Slopek, V. Breedveld, C. L. Henderson, and M. A. Grover. Gel time prediction of multifunctional acrylates using a kinetics model. *Polymer*, 52(3):866–873, 2011.

[306] T. Y. Lee, T. M. Roper, E. S. Jonsson, I. Kudyakov, K. Viswanathan, C. Nason, C. A. Guymon, and C. E. Hoyle. The kinetics of vinyl acrylate photopolymerization. *Polymer*, 44(10):2859–2865, 2003.

[307] Anestis Papadopoulos, David A. Bichara, Xing Zhao, Shinichi Ibusuki, Mark A. Randolph, Kristi S. Anseth, and Michael J. Yaremchuk. Injectable and photopolymerizable tissue-engineered auricular cartilage using poly(ethylene glycol) dimethacrylate copolymer hydrogels. *Tissue Engineering Part A*, 17(1-2):161–169, 2011.

[308] J. L. Drury and D. J. Mooney. Hydrogels for tissue engineering: scaffold design variables and applications. *Biomaterials*, 24(24):4337–4351, 2003.

[309] N. Garagorri, S. Fermanian, R. Thibault, W. M. Ambrose, O. D. Schein, S. Chakravarti, and J. Elisseeff. Keratocyte behavior in three-dimensional photopolymerizable poly(ethylene glycol) hydrogels. *Acta Biomaterialia*, 4(5):1139–1147, 2008.

[310] W. G. Koh, A. Revzin, and M. V. Pishko. Poly(ethylene glycol) hydrogel microstructures encapsulating living cells. *Langmuir*, 18(7):2459–2462, 2002.

[311] J. A. Killion, L. M. Geeuer, D. M. Deuine, J. E. Kennedy, and C. L. Higginbotham. Mechanical properties and thermal behaviour of pegdma hydrogels for potential bone regeneration application. *Journal of the Mechanical Behavior of Biomedical Materials*, 4(7):1219–1227, 2011.

[312] Y. H. Wu, H. B. Park, T. Kai, B. D. Freeman, and D. S. Kalika. Water uptake, transport and structure characterization in poly(ethylene glycol) diacrylate hydrogels. *Journal of Membrane Science*, 347(1-2):197–208, 2010.

[313] J. A. DiRamio, W. S. Kisaalita, G. F. Majetich, and J. M. Shimkus. Poly(ethylene glycol) methacrylate/dimethacrylate hydrogels for controlled release of hydrophobic drugs. *Biotechnology Progress*, 21(4):1281–1288, 2005.

[314] S. J. Bryant, R. J. Bender, K. L. Durand, and K. S. Anseth. Encapsulating chondrocytes in degrading peg hydrogels with high modulus: Engineering gel structural changes to facilitate cartilaginous tissue production. *Biotechnology and Bioengineering*, 86(7):747–755, 2004.

[315] S. R. Peyton, C. B. Raub, V. P. Keschrumrus, and A. J. Putnam. The use of poly(ethylene glycol) hydrogels to investigate the impact of ecm chemistry and mechanics on smooth muscle cells. *Biomaterials*, 27(28):4881–4893, 2006.

[316] A. N. Buxton, J. Zhu, R. Marchant, J. L. West, J. U. Yoo, and B. Johnstone. Design and characterization of poly(ethylene glycol) photopolymerizable semi-interpenetrating networks for chondrogenesis of human mesenchymal stem cells. *Tissue Engineering*, 13(10):2549–2560, 2007.

[317] N. C. Padmavathi and P. R. Chatterji. Structural characteristics and swelling behavior of poly(ethylene glycol) diacrylate hydrogels. *Macromolecules*, 29(6):1976–1979, 1996.

[318] K. B. Keys, F. M. Andreopoulos, and N. A. Peppas. Poly(ethylene glycol) star polymer hydrogels. *Macromolecules*, 31(23):8149–8156, 1998.

[319] N. Ravi, A. Mitra, P. Hamilton, and F. Horkay. Characterization of the network properties of poly(ethylene glycol)-acrylate hydrogels prepared by variations in the ethanol-water solvent composition during crosslinking copolymerization. *Journal of Polymer Science Part B-Polymer Physics*, 40(23):2677–2684, 2002.

[320] M. Quesada-Perez, J. A. Maroto-Centeno, J. Forcada, and R. Hidalgo-Alvarez. Gel swelling theories: the classical formalism and recent approaches. *Soft Matter*, 7(22):10536–10547, 2011.

[321] P. J. Flory and J. Rehner. Statistical mechanics of cross-linked polymer networks ii swelling. *Journal of Chemical Physics*, 11(11):521–526, 1943.

[322] S. Lin-Gibson, R. L. Jones, N. R. Washburn, and F. Horkay. Structure-property relationships of photopolymerizable poly(ethylene glycol) dimethacrylate hydrogels. *Macromolecules*, 38(7):2897–2902, 2005.

[323] Nicholas A. Peppas. *Hydrogels in medicine and pharmacy*. CRC Press, Boca Raton, Fla., —1986—.

[324] H. Q. Lin, E. Van Wagner, J. S. Swinnea, B. D. Freeman, S. J. Pas, A. J. Hill, S. Kalakkunnath, and D. S. Kalika. Transport and structural characteristics of crosslinked poly(ethylene oxide) rubbers. *Journal of Membrane Science*, 276(1-2):145–161, 2006.

[325] A. B. Lowe, C. E. Hoyle, and C. N. Bowman. Thiol-yne click chemistry: A powerful and versatile methodology for materials synthesis. *Journal of Materials Chemistry*, 20(23):4745–4750, 2010.

[326] C. E. Hoyle, A. B. Lowe, and C. N. Bowman. Thiol-click chemistry: a multifaceted toolbox for small molecule and polymer synthesis. *Chemical Society Reviews*, 39(4):1355–1387, 2010.

[327] B. D. Fairbanks, T. F. Scott, C. J. Kloxin, K. S. Anseth, and C. N. Bowman. Thiol-yne photopolymerizations: Novel mechanism, kinetics, and step-growth formation of highly cross-linked networks. *Macromolecules*, 42(1):211–217, 2009.

[328] S. P. Zustiak and J. B. Leach. Hydrolytically degradable poly(ethylene glycol) hydrogel scaffolds with tunable degradation and mechanical properties. *Biomacromolecules*, 11(5):1348–1357, 2010.

[329] A. Date, P. Pasini, and S. Daunert. Construction of spores for portable bacterial whole-cell biosensing systems. *Analytical Chemistry*, 79(24):9391–9397, 2007.

[330] K. Yagi. Applications of whole-cell bacterial sensors in biotechnology and environmental science. *Applied Microbiology and Biotechnology*, 73(6):1251–1258, 2007.

[331] A. Hollaender. Effect of long ultraviolet and short visible radiation (3500 to 4900 angstrom) on escherichia coli. *Journal of Bacteriology*, 46(6):10, 1943.

[332] R. Zimmermann, R. Iturriaga, and J. Beckerbirck. Simultaneous determination of total number of aquatic bacteria and number thereof involved in respiration. *Applied and Environmental Microbiology*, 36(6):926–935, 1978.

[333] Su-Jung Shin, Ji-Young Park, Jin-Young Lee, Ho Park, Yong-Doo Park, Kyu-Back Lee, Chang-Mo Whang, and Sang-Hoon Lee. "on the fly" continuous generation of alginate fibers using a microfluidic device. *Langmuir*, 23(17):9104–9108, 2007.

[334] K. P. Chin, S. F. Y. Li, Y. J. Yao, and L. S. Yue. Infinite dilution diffusion-coefficients of poly(ethylene glycol) and poly(propylene glycol) in water in the temperature-range 303-318k. *Journal of Chemical and Engineering Data*, 36(3):329–331, 1991.

[335] K. Shimada, H. Kato, T. Saito, S. Matsuyama, and S. Kinugasa. Precise measurement of the self-diffusion coefficient for poly(ethylene glycol) in aqueous solution using uniform oligomers. *Journal of Chemical Physics*, 122(24), 2005.

[336] W.S. Rasband. Imagej. *U.S. National Institutes of Health*, Bethesda, MD, USA, 1997.

Vitae

Michael Angelo-Anthony Daniele was born on November 6, 1986 to Carmine and Annamaria Elizabeth Daniele (née Dellanno) in Ridgewood, NJ. He grew up at 34 Passaic Street, Paterson, NJ and graduated from Hawthorne High School in 2004. Michael attended the United States Naval Academy (Annapolis, MD) and graduated *magna cum laude* from Rutgers, The State University of New Jersey (New Brunswick, NJ) with a Bachelors of Science degree in Materials Science and Engineering and a minor in English Literature. In 2009, Michael enrolled at Clemson University (Clemson, SC) pursuing a doctorate in Materials Science and Engineering with a concentration in Polymers, under the supervision of Professor Stephen Hans Foulger. During his doctoral candidacy, he traveled to the United States Naval Research Laboratory (Washington, D.C.) to study the development of bio-hybrid materials, under the supervision of Dr. André Antonio Adams and Dr. Frances Smith Ligler. Upon completion of his degree, Michael will be returning to the United States Naval Research Laboratory as an awardee of the National Research Council Postdoctoral Associateship.